Modelling the role of doping elements in metal oxides for photocatalytic organic wastewater treatment

Vivek Christhunathan, IM.Sc. Physics (First Class Hons)

Thesis presented for fulfilment of the degree of

Doctor of Philosophy (Ph.D.)

OLLSCOIL NA GAILLIMHE
UNIVERSITY OF GALWAY

Mechanical Engineering, School of Engineering

College of Science and Engineering

University of Galway, Ireland

July 2023

Supervisor: Dr. Mingming Tong

Co-Supervisor: Dr. Pau Farràs

Table of Contents

Acknowledgements

This thesis is the result of four and a half years of dedicated research. It would not have been possible without the help and support of many people. I am grateful to my primary supervisor, Dr. Mingming Tong, for accepting me as his PhD student. I sincerely thank him for his skilled guidance, his insights, and his ability to always push this thesis work in the right direction. I would like to express my sincere gratitude to my co-supervisor, Dr. Pau Farràs, for his invaluable guidance, support, and encouragement throughout my research journey. His expertise and insights have been instrumental in shaping my work, and I am grateful for his unwavering commitment to my academic and personal development. I am fortunate to have had the opportunity to work under their supervision and am grateful for the knowledge and skills I have gained from both. I wish to thank every member of my ChemLight group for their useful discussion.

I express my sincere gratitude to Prof. Max Garcia-Melchor for the invitation and opportunity to join his research group, Computational Catalysis and Energy Materials (CCEM), Trinity College Dublin (TCD), Ireland, to learn advanced computational modelling on metal-oxide surfaces, as well as for having instilled in me their love of research. It would not have been possible for me to finish my final tasks for this thesis without the assistance and support of Prof. Garcia-Melchor and his group members.

I would like to thank the members of my Graduate Research Committee, Prof. Sean Leen, Dr. Rory Monaghan, and Dr. Martina Kelly, for providing helpful and constructive feedback during annual reviews, which informed the overall progress of my research work. Special thanks to Anna Ciotti from CCEM, TCD, for patiently answering my queries on modelling calculations during and after the research visit at CCEM. I would like to extend special thanks to Dr. Wenming Tong for his invaluable feedbacks and suggestions to my research work. I am also grateful to Ms. Hanka Besic, Mr. Levente Nagy, Dr. Wenming Tong and Dr. Pau Farràs for their experimental results. Their contribution was essential to my research, and I greatly appreciate their collaboration.

I would like to express my deepest gratitude to the Irish Centre for High-End Computing (ICHEC). Without their exceptional support in providing me with access to state-of-the-art supercomputer facilities and invaluable computational resources, my modelling calculations would not have been possible. Their generosity and dedication to scientific research have been instrumental in the success of my work, and for that, I am truly thankful.

I kindly acknowledge the College of Science and Engineering (previously College of Engineering and Informatics) and Higher Education Authority (HEA) costed extension for funding this research to the end, the Royal Society of Chemistry grand fellowship, and the European Union's Horizon 2020 (grant agreement No. 862453) for providing me with the financial support for the research visit to the TCD. I would also like to thank the research students and staff at the University of Galway for enhancing my research experience. My special thanks to Mr. Dermot McDermott for providing guidance during laboratory demonstrations. I would like to express my heartfelt gratitude to my former supervisor, Prof. Ravindran P., for his unwavering support and guidance throughout my research journey. His timely assistance has been invaluable to me.

My parents, Mrs. Alpponsmary C. and the late Mr. Christhunathan M., and my brothers, Mr. Punitharaj C., Mr. Pugal C., Mr. Nepoliyan C. and my sisters-in-law, Mrs. Gnana Lusiya Mary P., Mrs. Ugin Pricilla P., and Mrs. Suguna N. receive my deepest gratitude and love for their dedication and the many years of support during my studies that provided the foundation for this work. My heartfelt gratitude to Mrs. Shanmuga Priya VC for her unwavering encouragement and support throughout my career. I dedicate this doctorate degree to the cherished memory of my late father, Mr. Christhunathan. His unwavering belief in the power of education and his legacy of hard work continue to inspire me every day. This degree is a tribute to his memory and the values he instilled in me.

I would like to extend my sincere appreciation to my colleagues and friends Dr. Ashwin Kishor, Dr. Arunkumar S., Mr. Jeyavelan A.M., Mr. Rashid Rafeek V., Mrs. Madhumathi R., Mrs. Subhashini U., Mr. Manik Lochan, Mr. Nirumal Kumar

GV., Mr. Selva Kumar S., Mr. Hari Subhramaniyan CR., and Miss. Susmita Halder as well as friends from the University of Galway and the Central University of Tamil Nadu, India, for all their moral support and advice. I would like to acknowledge all the teachers I have learned from since my childhood.

Any omission in this brief acknowledgement does not mean a lack of gratitude.

Abbreviations

ASE	Atomic Simulation Environment
Å	Angstrom
B3LYP	Becke, 3-parameter, Lee–Yang–Parr
BZ	Brillouin zone
b/w	Between
CB	Conduction band
CBM	Conduction band minima
CCD	Charge Density Difference
Dff.	Difference
DFT	Density functional theory
DOS	Density of states
E_{ads}	Adsorption energy
E_f	Fermi energy level
E_{form}	Formation energy
E_{gap}	Energy bandgap
E_{sur}	Surface energy
E_{ads}	Adsorption energy
Eqn.	Equation
eV	Electron Volt
GGA	Generalized gradient approximation
GW	Green function (G) and screened Coulomb interaction (W)
HSE	Heyd–Scuseria–Ernzerhof
IELs	Impurity energy levels
LS	Spin-orbit coupling
MB	Methylene blue
MO	Methylene orange
MG	Methylene green
PAW	Projector augmented wave
PBE	Perdew-Burke-Ernzerhof
PDOS	Partial density of states
QE	Quantum ESPRESSO code

RhB	Rhodamine B
SCF	Self-consistency field
TDDFT	Time-dependent density functional theory
TDOS	Total density of states
TM	Transition metals
U	Hubbard-U
UV	Ultraviolet
UV-Vis	Ultraviolet-Visible
USPP	Ultrasoft pseudopotential
VASP	Vienna ab-initio simulation package
VB	Valence band
VBM	Valence band minima
VESTA	Visualization for Electronic and Structural Analysis
vdW	Van der Waals
VL	Visible light
XC	Exchange and Correlation
Γ	Gamma
$\boldsymbol{\mu_m}$	Magnetic moment
$\Delta \boldsymbol{E_{sur}}$	Surface energy difference

Affidavit

I, Vivek Christhunathan (Student ID: 18236145), a PhD researcher in the School of Engineering, hereby declare that the work presented in my PhD thesis, "Modelling the role of doping elements in metal oxides for photocatalytic organic wastewater treatment" is a result of my own independent research, which I completed on my own and submitted with the help of Dr. Mingming Tong and Dr. Pau Farràs.

The contents of this thesis have not served as the foundation for awarding any degrees or titles at this university, any other university, or other institutions of higher learning.

All references to other works of literature are cited consistently throughout the thesis and are listed at the end.

Vivek Christhunathan.

Abstract

The thesis presents research on visible light-harvesting photocatalysts for wastewater treatment, with a specific focus on the design of an advanced photocatalyst capable of efficiently generating electron-hole (e^--h^+) pairs and harnessing a broader range of the visible light spectrum. To achieve this, first-principles computational modelling is employed to quantify the impact of chemical modifications on the structural and electronic properties of the photocatalysts.

The primary focus of the thesis revolves around modelling the photocatalytic degradation of methylene blue (MB) molecules using metal oxides. Notably, the research encompasses the exploration of thin film metal oxide (MO) photocatalysts through density functional theory (DFT) modelling, unravelling the intricate processes of organic molecule adsorption and subsequent degradation mechanisms. The successful modelling of undoped and Cu-doped $CaWO_4$ thin films serves as a pioneering milestone in this field. By comprehensively examining the interactions of MB-loaded thin films, this research promises profound insights into the photocatalytic mechanisms crucial for wastewater treatment techniques, with significant implications for industries such as pharmaceuticals, cosmetics, food, and energy harvesting.

In terms of structure, the thesis consists of eight chapters. Chapters 1–3 provide the necessary background, the research aims and objectives, and an overview of the modelling methods employed in the project. Chapters 4 and 5 delve into the modelling of doping bulk metal oxides with transition metals (TMs). Chapter 6 focuses on the modelling of doping metal oxide thin films using metal ions. Chapter 7 centres around the modelling of the interaction between methylene blue and the metal oxide thin film. Lastly, Chapter 8 offers concluding remarks summarising the key findings and implications of the research.

Chapter 1 is a general introduction to the thesis and the PhD project.

Chapter 2 presents the aim, research questions and objectives of the project.

Chapter 3 presents the principles of density functional theory (DFT) and an overview of its related applications. The general methodology used throughout the thesis is given here.

Chapter 4 presents the computational modelling results of the effect of Zn^{2+} and La^{3+} ions on the photocatalytic properties of bulk anatase TiO_2 regarding the chemical modification of doping or co-doping the metal oxide. The chapter interprets the impact of dopants (such as Zn^{2+} and La^{3+}) in TiO_2 such as the electronic band structure, relative stability, and photocatalytic activities. The optimal doping concentration was predicted. It was found that the Zn^{2+}-La^{3+} co-doped TiO_2 system, which has a composition of 6.25 at.% Zn and 2.08 at.% La, exhibit notable absorption activity within the visible light range of 400 to 540 nm. This behaviour can be attributed to the limited influence of La-4f orbitals on the band edge levels.

Chapter 5 presents the computational modelling results of the chemically modified bulk $CaWO_4$ that are doped using Cu^{2+} cations. The modelling results of the photocatalytic properties of the modified bulk $CaWO_4$ (e.g. absorption spectra), thermostability, and electronic properties (such as density of states (DOS), charge density difference (CDD), electronic band structure) are analysed to understand how and why Cu^{2+} doping could have such influence.

Chapter 6 presents the computational modelling results of doping the $CaWO_4$ thin film using Cu^{2+}, focusing on the electronic and photocatalytic properties. Interestingly, the $CaWO_4$ thin film at the (101) exposed surface effectively decreases the bandgap value by 0.39 eV when compared to the corresponding bulk material.

Chapter 7 presents the computational modelling results of the interaction between methylene blue (MB) and undoped and Cu-doped $CaWO_4$ thin films, in

relation to the MB absorption and oxidation behaviour as well as the electronic properties of the oxide. Moreover, to examine the electrochemical potential of the thin-film, the adsorption of small molecules such as O_2, H_2, and H_2O on the Ca-terminated surface of $CaWO_4$ was analyzed using the computational method. The work on the adsorption of MB with various orientations on $CaWO_4$ surface revealed several new findings for the first time, including (i) the MB molecule would react strongly to the surface of the oxide in the presence of Ca^{2+} ions due to the charge transfer from the reduced surface to the oxidized molecule, (ii) doping the (101) surface of $CaWO_4$ thin film with a low concentration of Cu-cation can effectively improve the oxidation of MB without compromising surface Ca's reduction, and (iii) doping the (101) surface of $CaWO_4$ thin film with a high concentration of Cu^{2+} cation can inhibit MB oxidation while promoting surface Ca^{2+}'s partial oxidation on the $CaWO_4$ thin film.

Chapter 8 presents the comprehensive conclusions of the project as well as specific answers to the research questions.

Chapter 1: Introduction

1.1 The pollution to water

Water is a crucial resource for all living things, including humans, animals, and plants. With the advancements in science and technology, the chemical, petrochemical, pharmaceutical, mining, semiconductor, and microelectronics industries are rapidly expanding worldwide. These industries process a massive amount of water and discharge harmful organic pollutants, leading to increased environmental contamination and health implications due to the growing volume of wastewater produced by human activities[1]. For instance, in Ireland, over a billion litres of wastewater are collected daily by public sewers and processed at more than 1,100 treatment facilities[2], with antibiotics like ciprofloxacin, azithromycin, and cefalexin found in this wastewater. These antibiotics are toxic and carcinogenic and pollute aquatic ecosystems. To meet the world's growing food demand, pesticides and herbicides are used in agriculture, further depleting clean water[1]. Besides that, the use of organic dyes for various fields such as medical, textile, cosmetics, paper, leather, rubber, printing, and agriculture, due to their availability and affordability compared to natural colors[3], causes a significant amount of water pollution, which can be harmful to organisms.

To maintain a safe environment for humans, environmental regulations are tightening, and scientists and engineers are developing novel or improved water purification processes to combat water pollution.

1.2 Overview of wastewater treatment

Industrial wastewater containing organic pollutants has become a major concern in many countries around the globe due to its hazardous nature[4] to human beings and animals, causing symptoms like abdominal discomfort, nausea, vomiting, diarrhoea, and irritation[5]. Over 10,000 different dyes are commercially available and widely used in various industries as mentioned above leading to severe contamination[6]. Every year, more than 700,000 tons of dyes are produced globally, with 12% wasted during manufacturing, and 20% of these wasted dyes end up polluting the environment[7]. Therefore, it is essential to develop effective

wastewater treatment methods to remove organic matter such as these dyes from water and prevent environmental damage.

The increasing importance of addressing issues such as organic dye pollution and wastewater management has led to a search for cost-effective and environmentally friendly methods for the remediation of organic pollutants. In recent decades, methods such as activated carbon, reverse osmosis, activated sludge, thermochemical cycles, biological treatment (including biosorption and biodegradation, and enzymes and microbes), and advanced oxidation processes (including ionization, electrochemical, photo-Fenton, and photocatalysis) have been employed in wastewater treatment[3,8].

Among the various techniques employed for wastewater treatment, advanced oxidation processes (AOPs) have gained significant prominence. AOPs are being increasingly recognized as a simple, cost-effective, highly stable, and environmentally friendly approach to pollutant degradation. Notably, photocatalysis, a key AOP method, utilizes sunlight as an energy source to facilitate the decomposition of organic contaminants [9,10].

Regarding harvesting solar energy, related methods include photovoltaic or photothermal electricity production from solar panels, photocatalytic and photo-electrocatalytic water splitting for hydrogen production, and photocatalytic wastewater treatment[11]. Particularly, the utilization of solar energy for photocatalytic wastewater treatment presents a desirable, economical, and environmentally sustainable solution to the global energy and environmental crisis. By utilizing a steady source of solar energy, we can effectively remediate organic pollutants such as organic dye in wastewater using the photocatalysis approach.

Principles of photocatalysis/Photocatalytic mechanism: Photocatalytic materials have the unique ability to transform light into a source of energy that can be consumed[10]. The underlying principle of the photocatalytic process is that, upon absorbing photons with energies equal to or greater than its bandgap energy

(E_{gap}), the electrons (e^-s) in the valence band (VB) energy levels are promoted to the conduction band (CB) energy levels, leaving the holes (h^+s) in the VB. This generates electron-hole (e^--h^+) pairs (where, h^+ are oxidising and e^- are reducing, and their production depends on the materials and band edge energy positions), effectively acting as a catalyst under light irradiation. The resulting e^--h^+ pairs migrate to the surface of the photocatalyst, where they combine with H_2O and O_2 to generate strong oxidizing agents ($OH^\bullet$ and $O_2^{\bullet-}$) that can degrade organic molecules. Figure 1.1 schematically illustrates this entire photocatalytic degradation process[12].

During the process of photocatalytic wastewater treatment, a complex sequence of events is happening simultaneously that directly affects the efficiency of the reactions. These steps are photon absorption by the photocatalyst, production of charge carriers, separation of charges, trapping/recombination of charges, migration of the charges to the surface, and transfer of charges to organic and inorganic compounds or any other target molecules. The wastewater remediation by photocatalysis is influenced by all these[13–15].

1.3 Semiconductor photocatalysts

In general, semiconductor materials are suitable for photocatalytic applications due to their favourable light absorption nature, charge transport abilities, charge lifespan at an excited state and the electronic structure (which includes filled VBs and empty CBs that can help to create e^--h^+ pairs required to drive chemical redox reactions).

The VB includes low-energy electron orbitals that are fully occupied, whereas the CB includes high-energy electron orbitals where electrons can freely transfer between atoms when excited. The energy difference between the conduction band and valence band is referred to as bandgap energy (E_{gap}). Since different semiconductors have different bandgap energies (as well as band edge positions), the applied energy that is needed to move an e^- to the conduction band minimum (CBM) from the valence band maximum (VBM) can be different. This is referred

to as the photogeneration of the e^--h^+ pair when an electron jumps from VBM to partially filled CBM. For more clarification, the photogeneration process of the e^--h^+ pair in a semiconductor is schematically shown in Figure 1.2.

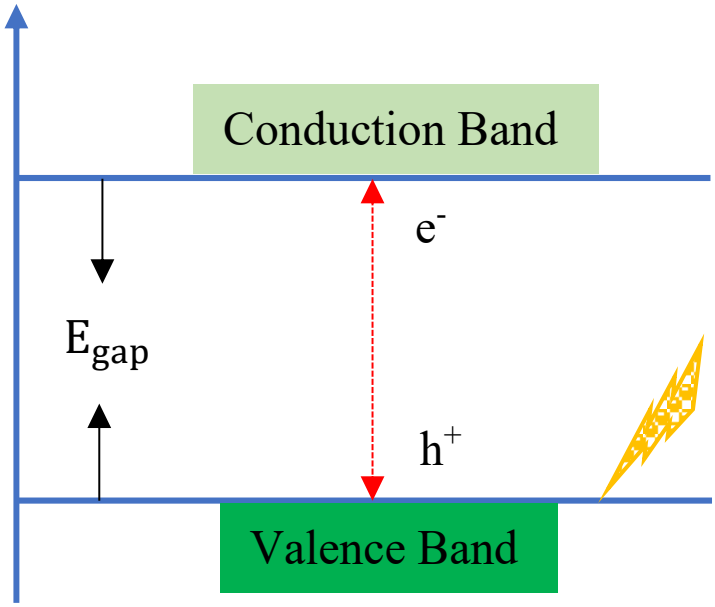

Figure 1.2: photogeneration of e^--h^+ pair, where ΔE_{gap} is the bandgap energy (eV).

The equation (1.1) can be used to determine the required threshold wavelength (λ in nm) of photons using the energy bandgap value (E_{gap} in eV) of a semiconductor.

$$\lambda_{nm} = {}^{1240}/_{E_{gap}} \qquad 1.1$$

Photons of applied energy must have a wavelength that is either equal to or smaller than the semiconductor's threshold wavelength for the semiconductor to be activated. Equation (1.1) means that a semiconductor with a low bandgap energy value is beneficial because it could be effectively stimulated by long wavelength light (e.g., visible light).

In general, photocatalysis is a chemical process in which a catalyst accelerates a reaction when exposed to light. In solar concentration methods for wastewater remediation, photocatalytic wastewater treatment has emerged as an increasingly

important research field[16]. In one of the first examples in the literature, Fujishima and Honda[17] conducted photoelectrochemical research in 1972 using TiO_2 as their photocatalyst to generate hydrogen and oxygen. After seminal work by Fujishima and Honda, TiO_2 emerged as a preferred photocatalyst semiconductor, leading to numerous studies in the literature between 1980 and 2000[18]. The objective of these investigations was to enhance our understanding of the photocatalytic properties exhibited by TiO_2, including its electronic and optical properties, and to answer fundamental scientific questions such as the nature of the oxidant, the preferred sites where the catalytic reaction occurs, how to enhance photocatalytic efficiency[18].

The majority of available photocatalysts are UV-active and could be divided into a variety of categories, such as metal-oxides[19] (i.e., TiO_2, WO_3, Fe_2O_3, ZnO), non-metal (i.e., g-C_3N_4), sulphides (i.e., ZnS, CdS), and other non-oxide (i.e., β-Ge_3N_4) photocatalysts. Among all semiconductor materials that have been examined in laboratories up to date, TiO_2 turned out to be the most widely employed in environmental applications[20–22]. On the other hand, however, TiO_2 photocatalyst can only use ultraviolet (UV) light with a wavelength of less than 400 nm. This means it cannot use visible light (VL) in photocatalytic reactions, which accounts for 48% of the sunlight reaching the Earth's surface[11], compared to only 6% for UV light[23].

There is a great demand for developing advanced photocatalysts that can effectively harness visible light supporting the photocatalytic reactions[11]. Although some photocatalysts have energy bandgaps that are small enough to capture photons from visible light, they are either unstable or exhibit low reactivity. To make better use of solar energy, tremendous initiatives have been undertaken to develop photocatalysts that can effectively function when exposed to visible light. Achieving this requires significant modifications to the photocatalyst's electronic structure, including reducing the bandgap, engineering the band positions to drive relevant reactions, and sustaining the chemical reactions with long-lived carriers. Such modifications are crucial to optimize the

photocatalytic efficiency and utilize the large amount of VL that constitutes (48%)[23] of the solar radiation reaching the Earth's surface.

Over the past two decades, numerous experimental findings have paved the way for the adoption of several common approaches to rendering photocatalysts active under visible light[24]. These techniques aim to modify the electronic structure of photocatalysts, thereby enhancing their photocatalytic activity[25] when subjected to visible light irradiation. Notable methods include:

i. Metal or/and non-metal ion doping (i.e., single and co-doping)[26,27]: In this approach, metal or non-metal ions are introduced into the lattice of the photocatalyst, effectively narrowing its bandgap. This modification leads to improved absorption of visible light by introducing new energy levels within the bandgap.
ii. Coupling wide bandgap and low bandgap semiconductors (solid solution development)[28]: This enhances the efficiency of photocatalysts. Wide bandgap semiconductors provide stability, whereas narrow bandgap semiconductors exhibit superior absorption of visible light owing to their wider spectral range. By combining these materials, the catalyst's performance is improved through red-shifted absorption spectra and manipulation of the photocatalyst's band structure.
iii. Dye sensitization[29–32]: Through the sensitization of UV-light-active photocatalysts with dyes, it becomes feasible to harness visible light, expanding their photocatalytic capabilities.
iv. Bandgap engineering[33,34]: This technique focuses on the development of novel single-phase photocatalysts that are specifically engineered to exhibit enhanced activity under visible light by manipulating the bandgap.

These approaches, based on extensive experimental findings, hold great promise for advancing the field of photocatalysis and facilitating the efficient utilization of visible light for various applications.

1.4 Chemical modification of photocatalysts

The photocatalysis performance of photocatalysts can be improved by doping the catalyst using other elements which can change its lattice structure and electronic band structure. Oxidation of pollutants requires stable semiconductors under oxidising conditions, therefore metal oxides are preferred over other types of materials. Consequently, there has been a growing focus on researching different metal oxide-based photocatalyst materials due to their significant potential in addressing water pollution caused by organic pollutants. In related experimental research, model organic compounds such as methylene blue (MB), Rhodamine B (RhB), and methyl orange (MO)[35] have been employed to mimic the organic pollutants (such as antibiotics)[36].

There has been extensive research on chemical modifications of TiO_2 to improve its photocatalytic properties. They include the single/co-doping of transition metal (TM) atoms into TiO_2, surface deposition, carbon (C) coating, and creating composite materials by combining TiO_2 with metals and/or different types of semiconductors. A summary of these approaches can be seen in Table 1.1 All this research on TiO_2 was undertaken with the intention of making TiO_2 useable in visible irradiation for the effective decomposition of organic pollutants that are present in the wastewater of many industries.

Table 1.1: Type of chemical modification of TiO_2

Type of chemical modification approaches on TiO_2	Chemically modified TiO_2 compounds	Remediate pollutants by a modified TiO_2	Degradation percentage (%) per time	Irradiation
Transition metal atoms single/co-doping	Sb-doped[37]	MB	98.4 % in 42 min	UV
	Ag, Sn or Zn-doped[38]	MB and MO	- 85.6 % (for Ag) in 600 min	UV

			- 96 % (for Sn) in 480 min - 99.6 % (for Zn) in 300 min	
	N-doped[39]	MB	32.9 % in 180 min	Vis-light
	Sn-doped[40]	RhB	94 % in 100 min	Vis-light
	Zn/La co-doped[41]	Formaldehyde	HCHO is nearly removed within 120 min	Xe-arc lamp
	Zn-N co-doped[42]	MB	85 % in 180 min	Vis-light
Surface deposition	Cu deposition[43]	MO	79.3 % in 300 min	UV
	Au deposition[44]	MO	72.11 % in 60 min	UV
Carbon (C) coating on the surface of TiO_2	C-Coated[45]	MO, 4-chlorophenol (4-CP) and Cr^{VI} reduction	MO=10.11 4-CP=~3.86 Cr^{VI} =~10.35 (in 180 min)	UV
	N-doped graphene quantum dots coated[46]	RhB	94 % in 120 min	Vis-light
Making TiO_2 as composite material	MnO_2/TiO_2 nanocomposite[47]	MB	90 % in 120 min	Vis-light
	Graphene oxide/TiO_2 composites[48]	MO	~35 % in 180 min	Vis-light

In addition to TiO_2, various semiconductors such as other metal oxides and sulfides (e.g., ZnO, ZnS, Fe_2O_3, and CdS) have been extensively studied and are commercially available for photocatalytic applications[1]. These semiconductors exhibit different properties that make them suitable for different applications. For instance, CdSe, GaP, Fe_2O_3, CdS, SiC, $SrTiO_3$, WO_3, ZnO, ZnS, and SnO_2 have specific wavelengths of 730 nm, 551 nm, 539 nm, 496 nm, 413 nm, 388 nm, 388 nm, 388 nm, 344 nm, and 326 nm, respectively. The corresponding bandgap energy values for these materials are 1.7 eV, 2.25 eV, 2.3 eV, 2.5 eV, 3.0 eV, 3.2 eV, 3.2 eV, 3.2 eV, 3.6 eV, and 3.8 eV. These properties play a crucial role in determining the suitability of these semiconductors for different photocatalytic processes. The similar chemical modifications described above have been applied to these semiconductor photocatalysts to increase their photocatalytic activity at the visible light range. A summary of these semiconductors and their chemical modifications can be seen in Table 1.2.

Table 1.2: A summary of existing research on different semiconductors that underwent various chemical modifications for the decomposition of diverse organic contaminants.

Semiconductor	Type of chemical modification approaches	Remediate pollutants by modified photocatalyst	Degradation percentage under visible light radiation
ZnO	C-doped[49]	MB	98.2 %
	P-doped[50]	RhB	99 %
	Cu-doped[51]	Direct Blue 15 dye	70 %
	La-doped[52]	Paracetamol	99 %
ZnS	Fe-doped[53]	Turquoise Blue H5G	71.2 %
	Ym-doped[53]		31.2 %
	Mn-doped[53]		58.6 %
Fe_2O_3	Sm-doped[54]	MB	99.8 %
$FeVO_4$	Zn-doped[55]	MB	~99 %

	Mn-doped[55]		~99 %
	Ti-doped[55]		~80 %
MWCNT-TiO_2-SiO_2	Composite[56]	Acetaminophen	~81.6 %
Ag_2O/AgBr-CeO_2	Composite[57]	Tetracycline	93.23 %
MoS_2/CdS	Nanodots-on-nanorod[58]	RhB	99.11 %
G-Bi_2WO_6	Composite[59]	RhB	68-98 %
FeO/ZnO@PANI	Nanocomposites[60]	3-aminophenol	92 %
TiO_2-Fe_2O_3	Nanocomposites[61]	MB	87%
CNTs/$InVO_4$	Nanocomposite[62]	RhB	92.3 %

On one hand, a wide variety of photocatalysts have been successfully developed that are active under visible light by using chemical modification approaches that alter the electronic band structure. To further emphasize the potential of photocatalysts, it is worth noting that they can also be utilized for the photocatalytic degradation of toxic chemicals and pathogens, making them a powerful tool for treating even more complicated wastes[63,64]. On the other hand, however, these photocatalysts normally have a high charge carrier recombination rate, which has a negative impact on the efficiency of photocatalytic organic waste degradation. Therefore, there is high demand in improving the photogenerated charge carrier separation while decreasing the rate of recombination.

Scheelite calcium tungstate ($CaWO_4$) has aroused particular interest among semiconductor physicists because of its stable physicochemical properties, unique light response characteristics and high density relative to other metal oxide semiconductor materials[65,66]. $CaWO_4$ nanoparticles exhibit low photoinduced e^--h^+ pair recombination rate, and advantageous light absorption and dispersion properties[67]. Moreover, $CaWO_4$ is inexpensive and non-toxic[68,69], giving it an advantage for use in industrial applications. For all of these reasons, $CaWO_4$ has become a promising photocatalysis for the remediation of organic pollutants in recent years.

However, $CaWO_4$ has some limitations. For example, it has a large bandgap (around 3.9 – 5.6 eV), leaving its main photocatalytic activity within the ultraviolet spectrum (UV, <380 nm). Another issue is that despite having a low rate of recombination[70], e^--h^+ pair recombination occurs readily in native $CaWO_4$, which annihilates the photogenerated charge carriers reducing its overall photocatalytic performance. Therefore, there is room to improve the photocatalytic response of $CaWO_4$, for example by modulating its electronic structure to effectively generate e^--h^+ pairs upon visible light illumination as well as to reduce the recombination rate.

1.5 Research method regarding photocatalyst materials

In Table 1.3, a comprehensive overview of methodologies is presented, offering valuable insights into the photocatalytic properties of materials. Researchers across various fields have consistently relied on these methods for their experimental analyses. Furthermore, diverse computational simulations, employing techniques like Quantum Dynamics, Monte Carlo, Molecular Dynamics, and Multiscale/Multiphysics modelling, have been conducted using an array of modelling codes (i.e., VASP[71], CASTEP[72,73], CRYSTAL06[74], QE[75], etc) and functionals (i.e., GGA[76], GGA+U[77], HSE06[78], etc).

These methodologies not only facilitate a deeper understanding of materials but also empower scientists to explore their electronic and optical behaviour with precision, contributing to advancements in the world of materials science and beyond.

Table 1.3: Methodologies for investigating photocatalytic properties of materials (Vienna Ab-initio Simulation Package (VASP), Quantum Espresso (QE), CAmbridge Serial Total Energy Package (CASTEP)).

Compounds	**Experimental**	**Computational**	
	Synthesis method	**Software**	**Method**
Nb_2O_5 [79]	Sol-gel	-	-

$LaNiO_3$ [80]	Mechanochemical route	-	-
$TmVO_4$ [81]	Pechini	-	-
Ce-doped $YMnO_3$ [82]	Polyacrylamide gel	-	-
Ce-Cu co-doped MoO_3 [83]	Spray Pyrolysis route	-	-
TiO_2 [84]	Electrochemical	-	-
SnO_2 [85]	Pulsed laser deposition	-	-
Bi_2S_3 [86]	Microwave irradiation	-	-
$ZnIn_2S_4$ [87]	Polymeric precursor	-	-
$BiOBr/Bi_2S_3$ [88]	Molten salt	-	-
$CdS–Ag_2S$ [89]	Ultrasound-assisted precipitation	-	-
MVO (M=Bi, Fe, Zn) [90]	Hydrothermal	-	-
$NaTaO_3$ [91]	Hydrothermal	CASTEP	GGA
$ZnGa_2O_4$ [92]	Aerosol-assisted chemical vapor deposition	VASP	HSE06
$CaWO_4$ [93]	Hydrothermal	CRYSTAL06	B3LYP
Mg-doped ZnO [94]	Solution combustion	WIEN2K	FP-LAPW
$BiVO_3$ [95]	-	VASP	GGA+U
$NiTiO_3$ [96]	-	QE	GGA+U
$ZnCo_2O_4$ [97]	-	QE	GGA+U
SiPAs [98]	-	VASP, QE, Phonopy, Wannier90	GGA, HSE06, GW
C_2P_2 monolayers [99]	-	VASP	GW+BSE
Zn–Fe layered double hydroxide [100]	Co-precipitation	BIOVIA Materials Studio	Monte Carlo

SiPAs [98]	-	VASP	Ab initio molecular dynamics
C_2P_2 monolayers [99]	-	VASP	Ab initio molecular dynamics
ZnO/Montmorillonite [101]	Co-precipitation	Materials Studio 2017	Molecular dynamics
Al cluster [102]	-	-	Multiscale modelling
La-doped CuO [103]	Sol-gel	COMSOL	Multiphysics modelling

1.6 State-of-the-art research on $CaWO_4$

$CaWO_4$ nanoparticles produced using citric acid exhibited approximately 93% MB dye degradation through photocatalytic activity under UV-light irradiation for 60 min[104]. The degradation capacity of $CaWO_4$ photocatalysts with regard to RhB solution was measured to be approximately 96% after 200 min under UV-C illumination (200 – 280 nm)[105]. The research on $CaWO_4$ showed that the MO degradation was about 63% after 90 min illumination of UV light[106]. The degradation of MB and carmine (CR) under UV irradiation was carried out using the nanoscale $CaWO_4$ material [67] that was synthesized through one-step coprecipitation. Under UV light, it demonstrated strong absorption capabilities and photoelectric response features [67].

Neto et al.[70] synthesized transition metal (TM) ion (Ag^+ and Zn^{2+}) co-doped $CaWO_4$ nanoparticles and tested their influence on the decomposition of MB under sunlight (Ultraviolet region). It was identified that Ag and Zn cations occupy levels near the $CaWO_4$ conduction band, and the internal strains formed by Ag and Zn cations obstruct the movement of photogenerated e^--h^+ pairs, which enhances the photocatalytic activity of $CaWO_4$. The research also shows that co-doping the

metal oxide can be a great approach to effectively degrade the MB while maintaining the crystal lattice structure of the metal oxide[70].

Ayappan et al.[66] found that $CaWO_4$ combined with other photocatalyst materials improves the photocatalytic effectiveness of photocatalysts by increasing the photogenerated e^--h^+ pair separation and minimizing charge carrier recombination. They synthesized a $CaWO_4$/α-Ag_2WO_4 nano-composite and evaluated its performance in terms of the photocatalytic decomposition of MB under VL illumination. The reduction of its bandgap to 2.79 eV was observed, and as a result, the nanocomposite exhibited a higher photocatalytic activity of 85% MB dye degradation under VL illumination for 105 minutes[66]. Using Ag-AgBr/ $CaWO_4$ composite under VL irradiation, the photodegradation of the azo dye Acid Red 18 (AR18) was examined experimentally. It was discovered that, after 70 min of reaction, about 91% of the dye could be degraded[107].

Density functional theory (DFT) methods, which utilize the concept of electronic density, have been employed to explore the geometrical properties, electronic properties, and optical properties of $CaWO_4$ from a theoretical perspective[93,108–112]. Extensive DFT studies have been undertaken on the $CaWO_4$ semiconductor to comprehend its structural and electronic characteristics for diverse applications, such as photoluminescence and photocatalysis. For instance, J.A.S. Laranjeira *et al.*[113] investigated the surface stability of scheelite-type ABO_4 (A = Ca and B = Mo and W) molybdate or tungstate and determined that it is predominantly influenced by the A^{2+} cation. By varying surface energy values, they successfully generated a comprehensive map depicting the morphological transformations in $CaXO_4$ compounds. This map serves as a valuable tool for comprehending changes in morphology, controlling growth, and unravelling the mechanisms underlying photocatalysis through the utilisation of DFT simulations. These valuable insights greatly contribute to the analysis of microscopy results and the interpretation of experimental findings. H. Wu *et al.*[114] performed theoretical calculations to investigate the electronic structures of phosphors. The results demonstrated that the doped phosphor exhibits the characteristics of an n-type semiconductor. Moreover, the analysis of the charge difference in $CaWO_4$: Tb^{3+}, Sm^{3+}/$CaWO_4$: Tb^{3+} phosphors provided further evidence that the presence of Sm^{3+} ions in the co-

doped phosphors allows for energy sharing with the matrix, leading to a reduction in the luminescence of Tb^{3+}.

1.7 Progress to make beyond the state-of-the-art

Upon conducting a literature review, it was discovered that $CaWO_4$ lacks sufficient e^--h^+ pair separation and is only photoactive in the UV region due to its relatively large bandgap value. The absence of an efficient visible-light-response is one of the major limitations of using $CaWO_4$ as a photocatalyst. While there has been some experimental research on improving the photocatalytic activity of $CaWO_4$, the overall available methods used for designing the $CaWO_4$ based photocatalysts are all based on trial and error. To date, there has been no systematic research that quantitatively explains how and why chemical modification alters the electronic bandgap of the parent compound, $CaWO_4$, in the application of photocatalysis.

In this thesis, we endeavour to improve the photocatalytic properties of metal oxides (MOs) by using computational modelling research on the chemical modifications of related photocatalysts. The research focuses on two key aspects. Firstly, computational modelling is employed to predict the electronic and photocatalytic properties of chemically modified metal oxides, namely titanium dioxide (TiO_2) and calcium tungstate ($CaWO_4$). Properties such as geometry, the density of state (DOS), electronic band structure, charge density difference, and absorption spectra are computationally predicted to investigate the effects of chemical modifications. Moreover, a model pollutant MB is used in DFT modelling to computationally predict how the photocatalysts, including undoped and Cu-doped $CaWO_4$ thin films, can interact with the functional groups of MB. The obtained modelling results shed light on the underlying mechanisms governing the photocatalytic properties of the investigated catalysts. Secondly, the computational modelling research aims to identify the optimal composition of dopants in the chemically modified metal oxide photocatalysts. By systematically varying the dopant concentrations in the computational modelling, the thesis seeks to find the composition that the most improves the photocatalytic properties of the metal oxides. On top of these, this thesis provides deep insight into the

fundamental photocatalysis mechanisms of metal oxides and their influence on the degradation process of MB.

Overall, this thesis employs computational modelling to implement chemical modifications to improve the photocatalytic efficiency of metal oxides. On one hand, the research outcomes make contribution to the body of knowledge regarding fundamental mechanisms of related photocatalysis processes. On the other hand, the outcomes can help the material scientists and engineers to find the optimal composition of chemically modified related photocatalysts for the purpose of organic waste degradation.

1.8 Properties under investigation

This thesis undertakes a thorough exploration of numerous properties found within semiconductor materials, with a particular focus on their crucial involvement in photocatalytic processes. The investigation includes the following:

- **Structural analysis:** The investigation extends to the geometrical properties of these materials. This includes the determination of lattice parameters, analysis of bonding nature, measurement of bond lengths, identification of crystallographic phases, and an exploration of lattice defects. Insights into materials' morphological features and crystalline structures are documented.
- **Electronic band structure:** This section offers profound insight into the electronic band structure of the semiconductor materials under scrutiny. Detailed information is provided about band edge positions, types of electron transitions occurring within the material, categorization of the bands as valence or conduction, and precise quantification of the materials' bandgap energies. The electronic band structure is analysed in-depth to uncover the subtleties of charge transport and electronic behaviour.
- **Density of states:** Exploring these materials' electronic properties, a comprehensive examination of the density of states (DOS) is undertaken. This analysis differentiates atomic orbitals' contributions to the electronic

band structure, revealing their widths and influence on band formation. It also uncovers intricate inter-band interactions and hybridization among these orbitals. Insights into the distribution of electron energy levels are documented, providing a holistic view of the material's electronic properties.

- **Charge density mapping:** The study extends to the spatial distribution of electron density within the material. Utilizing advanced computational techniques, precise charge density maps are created, revealing the localization of charge carriers, electron cloud variations, and electron delocalization phenomena. This mapping aids in understanding the materials' electronic behaviour, charge transport, and potential charge trapping sites.
- **Absorption spectra analysis:** The optical characteristics of these materials are examined in detail through the analysis of absorption spectra. Investigation focuses on the materials' ability to absorb and utilize visible light for photocatalytic purposes. Spectral features, such as absorption peaks, band transitions, and the influence of material properties on light absorption, are thoroughly investigated.
- **Formation energy:** To ascertain the stability of these materials under various conditions, an exploration of formation energy calculations is conducted. This includes an evaluation of their thermal stability, chemical reactivity, and potential phase transformations. The data provides critical insights into the materials' durability and suitability for photocatalytic applications.
- **Adsorption analysis:** An extensive study is conducted to elucidate the complex dynamics of molecule-surface interactions on metal oxide surfaces. The investigation focuses on the adsorption behaviour, kinetics, and thermodynamics of molecules on semiconductor surfaces. This analysis sheds light on the mechanisms governing surface reactions, which are crucial for photocatalytic processes.
- **Magnetic property:** Finally, the inherent magnetic properties of these materials are comprehensively characterized. Exploration delves into their magnetic behaviour, such as ferromagnetism, antiferromagnetism, or

paramagnetism, and examines how these properties can influence their utility in specific photocatalytic applications.

This examination of the aforementioned properties provides an in-depth understanding of semiconductor materials, offering valuable insights into their potential applications in photocatalysis and contributing significantly to the scientific community's knowledge base.

Chapter 2:

Research aims and objectives

2.1 Thesis' scope and structure

The project aim is to design an advanced photocatalyst that can more effectively generate e^--h^+ pairs and avail of the wider visible-light spectrum to degrade organic wastes, by using computational modelling methods.

There are two objectives of the project. The first objective is to use computational modelling methods to predict the electronic and photocatalytic properties of pure and chemically modified anatase TiO_2. The modelling results of related tasks can be used to verify the modelling approach of the project. The second objective is to use computational modelling methods to predict the electronic and photocatalytic properties of pure and chemically modified $CaWO_4$.

Chapter 4 of the thesis presents the computational modelling results of the effect of doping or co-doping anatase TiO_2 using Zn^{2+} and La^{3+} ions. The modelling results are used to interpret the impact of doping Zn^{2+} and La^{3+} in TiO_2 on the oxide electronic band structure and predict the optimal doping concentration. The modelling results of pure TiO_2 are compared with related results of literature to verify the modelling approach.

Chapter 5 and Chapter 6 present the modelling results of electronic and photocatalytic properties of pristine and chemically modified $CaWO_4$ bulk mater or thin film which is doped with Cu^{2+} cations. Particularly, the modelling results are used to explain and interpret why doping with Cu cations can have such influence on the properties of $CaWO_4$ as well as why such influence can vary while the doping concentration of Cu^{2+} cations varies. The modelling results of the interaction between MB and pure or chemically modified $CaWO_4$ are presented in Chapter 7. It is the first time that DFT computational modelling has been used to explore the underlying mechanism of chemical modification of $CaWO_4$ (doping with Cu^{2+} cations) thin film and the interaction between the $CaWO_4$ surface and MB.

2.2 Thesis' research questions

By answering the following research questions, the thesis is making a contribution to the body of knowledge regarding the underlying mechanism of improving the photocatalytic properties of metal oxides by doping with metal ions. On the other hand, the research method that is presented in the thesis can be used as a toolbox by related material scientists and engineers to design novel advance photocatalytic materials for organic waste treatment applications.

Chapter 4:

What could be the optimal co-doping concentration for bulk anatase TiO_2 with Zn^{2+} and La^{3+}?

How and why does the co-doping using Zn^{2+} and La^{3+} metal cations influence TiO_2's photocatalytic properties?

Chapter 5:

What could be the impact of Cu-doping on the photocatalytic properties of bulk $CaWO_4$, and what is the underlying mechanism?

Chapter 6:

How does Cu-doping affect the electronic properties of $Ca_{48}(WO_4)_{48}$ with the (101) surface exposed, and what is the underlying mechanism?

Chapter 7:

What would be the interaction between the MB molecule and Cu-doped $Ca_{48}(WO_4)_{48}$ on the (101) surface?

How would the doping concentration of Cu affect the photocatalytic and adsorption properties of Cu-doped $Ca_{48}(WO_4)_{48}$ that is loaded with MB?

Chapter 3:

Theoretical background and computational methods

3.1 Schrödinger equation

Understanding the interactions between electrons and atomic nuclei helps us to comprehend the quantum mechanical properties of matter. This can be quantitatively described by the many-body Schrödinger equation, which was derived by Erwin Schrödinger in 1925. The time-independent, non-relativistic Schrödinger equation can be expressed in operator form[115] as

$$\hat{\mathrm{H}}\psi\left(\vec{\mathrm{r}}_{\mathrm{i}}, \vec{\mathrm{R}}_{\mathrm{j}}\right) = \mathrm{E}\psi\left(\vec{\mathrm{r}}_{\mathrm{i}}, \vec{\mathrm{R}}_{\mathrm{j}}\right) \qquad 3.1$$

where

$\hat{\mathrm{H}}$ – Hamiltonian operator;

E – operator's energy eigenvalue;

ψ – associated wave function;

$\vec{\mathrm{r}}_i$ – electron (i) coordinate

$\vec{\mathrm{R}}_j$ – nucleus (j) coordinate

The kinetic energies of the electrons and nuclei (T_e and T_n, respectively), the attractive electrostatic interaction between the electrons and nuclei (V_{ne}), and the repulsive potential resulting from the electron-electron (V_{ee}) and nucleus-nucleus interactions (V_{nn}) account for the Hamiltonian for an interacting many-body system[116]. The Hamiltonian of the system with M nuclei and N electrons can thus be represented as

$$\hat{\mathrm{H}} = \mathrm{T_e} + \mathrm{T_n} + \mathrm{V_{ne}} + \mathrm{V_{ee}} + \mathrm{V_{nn}} \qquad 3.2$$

where

$$T_e = \sum_{i=1}^{N} \frac{-\hbar^2}{2m_i} \nabla_i^2;\ T_n = \sum_{j=1}^{M} \frac{-\hbar^2}{2m_j} \nabla_j^2;\ V_{ne} = \sum_{i=1}^{N} \sum_{j=1}^{M} \frac{-Z_j e^2}{|\vec{r}_i - \vec{R}_j|};$$

$$V_{ee} = \sum_{i=1}^{N} \sum_{j>1}^{N} \frac{e^2}{|\vec{r}_i - \vec{r}_j|};\ V_{nn} = \sum_{i=1}^{M} \sum_{j>1}^{M} \frac{Z_i Z_j e^2}{|\vec{R}_i - \vec{R}_j|}$$

where

$\hbar\left(= {}^{h}/_{2\pi}\right)$ – the reduced Plank's constant;

m_i and m_j – the electron mass and nucleus mass;

$Z_i(\nabla_i)$ and $Z_j\left(\nabla_j\right)$ – the atomic number (Laplacian operator) of the electron and nucleus respectively. When atomic units are used, m_i, $\hbar$, and e are all equal to 1.

3.2 Born-Oppenheimer (BO) approximation

Max Born and J. Robert Oppenheimer came up with the Born-Oppenheimer (BO) approximation, which is one of the fundamental methods[117] for deriving the challenging Schrödinger equation for molecules. As is well known, electrons and nuclei are attracted to one another by the same force and momentum and have the same amount of charge. Then, a very low velocity will thus be experienced by the nucleus, whose mass is far greater than that of the electron. Therefore, in the Born-Oppenheimer approximation, it is believed that electrons are considered to rotate around stationary nuclei. The Hamiltonian in Eq. 3.2 then divides into two distinct parts: the nuclear portion (H_n) and the electronic portion (H_e). This division enables the separation of the motion of electrons and nuclei. The total wave function (ψ) is consequently divided into the following forms[118]:

$$\psi\left(\vec{r}_i, \vec{R}_j\right) = \psi_e^R(\vec{r}_i)\psi\vec{R}_j \qquad 3.3$$

where

$\psi_e^R(\vec{r}_i)$ – the electronic wavefunction with current nuclei positions;

$\psi\vec{R}_j$ – the wavefunction of the nuclei;

The system's total energy (E_{tot}) is then calculated by calculating the sum of the energy from nuclear and electronic components (E_N and E_e, respectively).

$$\mathrm{E}_{tot} = \mathrm{E}_N + \mathrm{E}_e \qquad 3.4$$

E_N is a constant in this instance, and Eq. 3.2 is simplified as[119,120]

$$\hat{\mathrm{H}}_\mathrm{e} = \frac{-1}{2}\sum_{\mathrm{i}=1}^{\mathrm{N}} \nabla_\mathrm{i}^2 + \sum_{\mathrm{i}=1}^{\mathrm{N}}\sum_{\mathrm{j}=1}^{\mathrm{M}} \frac{-\mathrm{Z}_\mathrm{j}}{\left|\vec{\mathrm{r}}_\mathrm{i} - \vec{\mathrm{R}}_\mathrm{j}\right|} + \sum_{\mathrm{i}=1}^{\mathrm{N}}\sum_{\mathrm{j}>1}^{\mathrm{N}} \frac{1}{\left|\vec{\mathrm{r}}_\mathrm{i} - \vec{\mathrm{R}}_\mathrm{j}\right|} \qquad 3.5$$

The BO approximation minimizes the amount of variables in Eq. 3.2, however in many practical systems, this computing burden still calls for additional approximations.

3.3 Hartree-Fock (HF) approximation

The simplest approximation that offers a remedy for interacting many-body systems is the Hartree approximation. In Equation 3.2, the potential depends on the positions of other electrons, and hence, it can be estimated by an average single-electron potential, commonly referred to as the Hartree potential. The Hartree potential is independent of the individual mobility of other electrons; however, the electrons interact with each other exclusively through the mean field Coulomb potential. As a result, this interaction gives rise to one-electron Schrödinger equations in the following form[121–123]

$$\left[\frac{-\hbar^2}{2m}(\nabla^2) + \mathrm{V}(\vec{\mathrm{r}})\right]\psi_i(\vec{\mathrm{r}}) = \epsilon_i\psi_i(\vec{\mathrm{r}}) \qquad 3.6$$

where

ψ_i – wave function of a single particle

$\mathrm{V}(\vec{\mathrm{r}})$ – the electron's Hartree potential, which incorporates nuclear−electron interaction;

$$V_{nucleus}(\vec{r}) = -Ze^2 \sum_R \frac{1}{|\vec{r} - \vec{R}|} \quad 3.7$$

and mean field originates from N-1 other electrons, which are smeared out into a continuous negative charge density $\rho(\vec{r})$. This leads to a potential of the form

$$V_{nucleus}(\vec{r}) = -e \int \rho(\vec{r}) \frac{1}{|\vec{r} - \vec{R}|} dr' \quad 3.8$$

where,

$$\rho(\vec{r}') = \sum_i^{occupied} |\psi(\vec{r})|^2 \quad 3.9$$

Despite the fact that it enables one to discover the answer to the one-electron Schrödinger equation, the Hartree approximation has just a few limitations. The Hartree approximation does not satisfy the Pauli-exclusion principle, which asserts that two electrons in an atom cannot have the same quantum number[124]. This is due to the fact that the wave function in Hartree's theory is not antisymmetric to electron permutation.

$$\psi(\vec{r}_1, \vec{r}_2, \ldots \vec{r}_N) = \prod_i^N \psi(\vec{r}_i) \quad 3.10$$

The Hartree-Fock (HF) approach overcomes the limitations of the Hartree approximation by approximating the electronic wave function with a single Slater determinant[118]. The approximation of the HF approach converts the many-body problem into a single-particle problem[118]. This approach correctly accounts for the antisymmetric nature of the trial wave functions. The self-consistent field approach (SCF), which is also known as the Hartree-Fock approximation, assumes that the final field computed from the charge distribution is "self-consistent" with the beginning field.

The variational principle states that the ground state wavefunction ψ yields the lowest possible energy expectation value when the system is in that state ψ.

$$E[\psi] = \frac{\langle\psi|\hat{\mathrm{H}}|\psi\rangle}{\langle\psi|\psi\rangle} \tag{3.11}$$

By substituting a Slater-determinant of one electron wavefunction for the wavefunction in Eq. 3.10

$$\psi(\vec{\mathrm{r}}_1, \vec{\mathrm{r}}_2, \ldots \vec{\mathrm{r}}_\mathrm{N}) = \frac{1}{\sqrt{N!}}\begin{bmatrix} \psi_1\vec{\mathrm{r}}_1 & \cdots & \psi_N\vec{\mathrm{r}}_1 \\ \vdots & \ddots & \vdots \\ \psi_1\vec{\mathrm{r}}_\mathrm{N} & \cdots & \psi_N\vec{\mathrm{r}}_\mathrm{N} \end{bmatrix} \tag{3.12}$$

This decouples the electrons resulting in a single particle Hartree-Fock[125] equation[126]:

$$\begin{aligned} &\frac{-\hbar^2}{2m}(\nabla^2)\psi_i(\vec{\mathrm{r}}) + [\mathrm{V}_{nucleus}(\vec{\mathrm{r}}) + \mathrm{V}_{electron}(\vec{\mathrm{r}})]\psi_i(\vec{\mathrm{r}}) \\ &\quad -\sum_j \int \frac{\psi_j^*(\vec{\mathrm{r}}')\psi_i^*(\vec{\mathrm{r}}')\psi_j(\vec{\mathrm{r}})}{|\vec{\mathrm{r}} - \vec{\mathrm{r}}'|}\mathrm{d}\mathrm{r}' = \epsilon_i\psi_i(\vec{\mathrm{r}}) \end{aligned} \tag{3.13}$$

Here, the kinetic energy is represented by the first term. In addition to the Hartree potentials as a second term (the electrostatic potential from the charge distribution of N electrons[127]), another potential called the exchange potential (final term) acts only on electrons with the same spin. Both potentials arise from the Slater-determinant form of the wavefunction. Moreover, there should be an electrostatic interaction between the electrons known as correlation interaction, which is not taken into account here. By subtracting the HF energy from the exact energy of the system, we can define the correlation energy.

3.4 Density functional theory (DFT)

The emergence of density functional theory (DFT) marks a pivotal moment in modern quantum mechanics[128]. Instead of using the many-body wavefunction to

derive the material properties, the DFT employs the density of electron ($\rho(\vec{r})$) as a primary variable. The electrons are indistinguishable, and the $\rho(\vec{r})$ measures the probability of an electron being present at a particular location[129].

$$\rho(\vec{r}) = \psi^*(\vec{r})\,\psi(\vec{r}) \qquad 3.14$$

The definition of density for a system with N particles is as follows:

$$\rho(\vec{r}) = \psi^*(\vec{r}_1, \vec{r}_2, \ldots \vec{r}_N)\,\psi(\vec{r}_1, \vec{r}_2, \ldots \vec{r}_N)\overrightarrow{dr_2} \ldots . \overrightarrow{dr_N} \qquad 3.15$$

i.e., the probability amplitude of detecting a particle in close proximity to a particular position $\vec{r}$ in space.

The first version of the DFT was developed by Thomas and Fermi in 1927[130,131] and called as Thomas-Fermi (TF) model, which gives the kinetic energy of a noninteracting electron at some specified external potential V(r) as a function of electron density. TF model, as comparable to Hartree-Fock (HF) approach, only included electron-electron interactions and ignored both exchange and correlation (XC).

3.4.1 Hohenberg-Kohn (HK) theorem

In 1964, Hohenberg and Kohn presented evidence suggesting that the TF formula can be regarded as an approximation to DFT[132]. The Hohenberg-Kohn (HK) theory is supported by two theorems that provide justification for employing the electron density $\rho(r)$ as a fundamental variable in determining the energy of the ground state in non-degenerate systems[118]. The HK theory depends on two theorems that justify the use of the electron density $\rho(r)$ as a fundamental variable to calculate the energy of the ground state for non-degenerate ground states. In accordance with the first HK theorem, the system's properties are determined primarily by the electron density. It claims that the electron density is uniquely determined for an interacting system of electrons with an external potential $V_{ext}(r)$. Thus, any ground state property can be expressed using the ground state $\rho(r)$. Consequently, the

energies due to the kinetic and electron-electron interactions will thus be expressed as functionals of the electron density[133], $F[\rho(\vec{r})]$, which yields electronic energy:

$$E = \int V_{ext}(\vec{r})\rho(\vec{r})\overrightarrow{dr} + F[\rho(\vec{r})] \qquad 3.16$$

The second HK theorem defines that the ground state (GS) energy of a system can be calculated using a formula called the functional[134], $F[\rho(\vec{r})]$. This formula will yield minimal energy if the supplied density is the actual GS density. For example, when the electron density matches the system's actual ground state, the functional reaches its minimal value.

3.4.2 Kohn-Sham (KS) theorem

The Hohenberg-Kohn theorem does not provide a complete explanation of the universal functional F[ρ(r)]. In 1965, Kohn and Sham applied the Hohenberg-Kohn theorems to propose the concept of a non-interacting reference system[135], aiming to approximate this functional[136]. The Kohn-Sham (KS) approximation allows for the non-interacting reference system's [135] kinetic energy to retain its real electron density ρ(r) which can be expressed as[118],

$$T_s = \frac{-1}{2}\sum_{i}^{N}\langle\phi_i|\nabla^2|\phi_i\rangle \qquad 3.17$$

where

ϕ_i – the single particle wave function (i.e., the so-called KS wave function);

T_s – the non-interacting kinetic energy (T) of the interacting system[137];

Therefore, Kohn and Sham addressed that by revising the universal functional as follows:

$$F[\rho] = T_s[\rho] + E[\rho] + E_{xc}[\rho] \qquad 3.18$$

Thus, $E[\rho]$ stands for the electrons' classical Hartree energy, while $E_{xc}[\rho]$ stands for the XC energy.

The system's potential energy and a portion of its kinetic energy are mostly contributed by the non-classical phenomena of exchange and correlation. With this approach, the many-body problem is thereby transformed onto an efficient single particle problem[118]. This results in the Kohn-Sham equation shown below, which works with any interacting systems with ground state density $\rho(r)$:

The expression for a non-interacting system with the same ground state density ρ(r) is.

$$\left[\frac{-1}{2}\nabla^2 + V_{eff}(\vec{r})\right]\phi_i = \epsilon_i\phi_i \qquad 3.19$$

where
ϵ_i – the Kohn-Sham eigen energies;
$V_{eff}(\vec{r})$ – the effective potential, which is a combination of the classical Coulomb potential, XC potential, and external potential[118] ($V_{eff}(\vec{r})$);

$$V_{eff}(\vec{r}) = \int \frac{\rho(\vec{r}')}{|\vec{r} - \vec{r}'|}\overrightarrow{dr'} + V_{xc}(\vec{r}) + V_{ext}(\vec{r}) \qquad 3.20$$

where the potential for exchange-correlation is expressed as,

$$V_{xc}(\vec{r}) = \frac{\delta E_{xc}[\rho]}{\delta\rho(\vec{r})} \qquad 3.21$$

This suggests that the $V_{xc}(\vec{r})$ is the functional derivative of $E_{xc}[\rho]$ with respect to the density[138]. In terms of KS orbitals, the density $\rho(\vec{r})$ of the real system can be defined as follows:

$$\rho(\vec{r}) = \sum_{i}^{N} |\phi_i(\vec{r})|^2 \qquad 3.22$$

In principle, if the precise forms of exchange-correlation energy E_{xc} and its corresponding potential V_{xc} can be determined, the Kohn-Sham method is the accurate method to obtain the optimum eigenvalue of the Hamiltonian operator of the Schrödinger equation. This results in enhanced approximations to E_{xc} and V_{xc}, which is the main objective of modern density functional theory.

3.5 Exchange-correlation (XC) functional

KS proposed the local density approximation (LDA), which is the fundamental approximation to the XC functional. LDA makes the simple assumption that the XC energies at a point r are identical[126] to those of a homogeneous electron gas with the same density[139] at that place[140]. It should be highlighted that this approximation is valid for systems with slowly fluctuating densities. The value of the E_{xc} in the LDA only depends on the local electron density $\rho(r)$. We are aware that the electron density can change as a function of *r*. According to LDA, ρ is single-valued, therefore the value of E_{xc} at *r* is unaffected by changes in ρ away from *r*.

$$E_{xc}^{LDA}[\rho] = \int \rho(\vec{r})\varepsilon_{xc}[\rho(\vec{r})]\,\overrightarrow{dr} \qquad 3.23$$

where $\varepsilon_{xc}(\rho)$ indicates the XC energy per particle of a uniform electron gas density ρ and $\varepsilon_{xc}(\rho)$ consists of two parts such as exchange $\varepsilon_x(\rho)$ and correlation $\varepsilon_c(\rho)$ part. Thus,

$$E_{xc}^{LDA}[\rho] = \int \rho(\vec{r})[\varepsilon_x(\rho(\vec{r})) + \varepsilon_c(\rho(\vec{r}))]\,\overrightarrow{dr} \qquad 3.24$$

The exchange component for the homogeneous electron gas system is anticipated to be,

$$\varepsilon_x(\rho) = \frac{-3}{4}[\frac{3\rho(\vec{r})}{\pi}]^{1/3} \quad 3.25$$

However, an explicit functional form like $\varepsilon_x(\rho)$ cannot describe the correlation portion, $\varepsilon_c(\rho)$. As a result, the XC potential, v_{xc}, can be stated as

$$v_{xc}(\vec{r}) = \frac{\delta E_{xc}^{LDA}}{\delta\rho(\vec{r})} = \varepsilon_{xc}[\rho(\vec{r})] + \rho(\vec{r})\frac{\partial\varepsilon_{xc}(\rho)}{\partial\rho} \quad 3.26$$

LDA has the drawback of ignoring corrections to the E_{xc} caused by inhomogeneities within the electron density around *r*. To tackle this, the generalised gradient approximation (GGA) is introduced, which takes into account the impacts of inhomogeneities by incorporating the gradient of the local electron density[141]. GGA is therefore dependent on both the gradient of $\rho(r)$ as well as the local density value at a point.

$$E_{xc}^{GGA}[\rho] = \int \rho(\vec{r})\varepsilon_{xc}[\rho(\vec{r}), \nabla\rho(\vec{r})]\,\overrightarrow{dr} \quad 3.27$$

The $E_{xc}^{GGA}[\rho]$ also comprises of exchange and correlation parts (E_x^{GGA} and E_c^{GGA}, respectively), similar to the LDA. But GGA enhances the solids' ground state properties as opposed to LDA. The literature contains a variety of GGA functionals that are named after their inventors, such as Liangreth-Mehl, Perdew-Wang, Perdew-Burke-Ernzerhof, etc. However, in this study, we utilised the GGA functional developed by Perdew-Burke-Ernzerhof (GGA-PBE)[76,142].

Both LDA and GGA approximation has the primary drawback of providing inaccurate bandgap. Hybrid functionals (HF) are a type of approximation to the XC energy functional in addition to LDA and GGA. It combines a portion of the HF theory's exchange with GGA, and the GGA fully accounts for the correlation function. For example, Hybrid functionals combine HF non-local exchange with GGA local exchange to address the self-interaction error present in LDA/GGA[78].

$$E_{xc}^{hybrid}[\rho] = \alpha E_{xc}^{GGA}[\rho] + (1-\alpha)E_x^{HF}[\rho] + E_c^{GGA}[\rho] \quad 3.28$$

where, the parameter α can be adjusted to match experimental data for molecules (approximately 0.75), or it can be obtained based on known properties. PBE0[143,144], B3LYP[145,146], and HSE06[78,147] are examples of well-known hybrid functionals.

The hybrid functional makes improvements in the bandgap, however, it still cannot match the bandgap values observed in experiments. Hence, the GW approximation is the next step[148]. A many-body system of electrons' self-energy is calculated using this approach. Since this method is based on perturbation theory, the reference Hamiltonian should be selected in a way that it offers the most accurate approximation for the electron 'Green function (G) and screened Coulomb interaction (W)'[149], which are generally taken from KS-DFT calculations.

$$G_0(r_1, r_2, \omega) = \sum_{nk} \frac{\phi_{nk}^{KS}(r_1)\phi_{nk}^{KS}(r_2)^*}{-\epsilon_{nk}^{KS} + i\eta sgn(\epsilon_{nk}^{KS} - \mu)} \qquad 3.29$$

The independent-particle or random phase approximation includes polarizability. The provided screened Coulomb interaction is

$$W_0(r_1, r_2, \omega) = \int dr_3 \frac{\epsilon^{-1}(r_1, r_2, \omega)}{|r_1 - r_3|} \qquad 3.30$$

and self-energy

$$\sum(r_1, r_2, \omega) = \frac{i}{2\pi} \int G_0(r_1, r_2, \omega - \omega')W_0(r_1, r_2, \omega)e^{-i\eta\omega'}d\omega' \qquad 3.31$$

All $e-e$ interactions are contained within the self-energy. This process can be repeated until self-consistency is achieved. It is possible to end the computation after just one GW iteration, which is known as a single-shot calculation (G_0W_0). This GW calculation is the simplest and most efficient in terms of computation. The G_0W_0 the approach typically has a bandgap precision of ~ 0.1–0.2 eV.

3.6 Computational methods

The advancement of efficient and accurate computer codes/programs, as well as computer technologies, has greatly expanded the spectrum of research questions that can be reliably solved using computational modelling. DFT is one of the most well-known quantum mechanical techniques that makes a significant advancement in material design as well as material property prediction for a vast variety of applications. The methods employed in this study to solve the below Kohn-Sham equation and calculate GS energy are briefly explained in the below sections.

$$\left[-\nabla^2 + V_{eff}(r)\right]\psi_i(r) = \epsilon_i\psi_i(r) \qquad 3.32$$

Using the following equation, one can determine the electron charge density $\rho(r)$

$$\rho(r) = \sum_{j=1}^{N} \left|\psi_j\right|^2 \qquad 3.33$$

Since the XC potential V_{xc} and electrostatic potential (Φ) both rely on $\rho(r)$, one can estimate a new $V_{eff}(r)$ utilising the LDA, GGA, hybrid functional, etc. for the XC and the Poisson equation for the electrostatic contribution[150]:

$$\nabla^2\Phi(r)_i = -4\pi \sum_{j=1, j\neq i}^{N} \left|\psi_j\right|^2 \qquad 3.34$$

The iterative process continues until self-consistency is achieved, meaning that the difference between $V_{eff}(r)$ in the current and previous iterations (m and m-1) is below a predefined threshold value indicating convergence[150]. The total energy of the system, consisting of electrons and nuclei, is calculated iteratively until self-consistency is achieved. This is accomplished by employing the total-energy equation which is described[150] in Equation 3.16.

3.6.1 Periodicity and crystal symmetry

Due to the impossibility of solving the KS equations for all of the electrons in the material, periodic symmetry makes the Kohn-Sham equation solution for crystalline solids easier. As the potential for an infinite crystal is periodical, it is possible to apply translational symmetry to the crystal to solve the equations in a smaller portion of the system, leading to the solution for the overall system [150].

$$V = (r + T) = V(r) \qquad 3.35$$

where,

$$T = m_1 a_1 + m_2 a_2 + m_3 a_3 \qquad 3.36$$

The vectors a_i are the real-space Bravais lattice vectors [150], while m_i are integers. According to Bloch's theorem, the eigenstates of the one-electron Hamiltonian can be expressed as a plane wave multiplied by a function exhibiting the periodicity of the Bravais lattice[150,151];

$$\psi_k(r + T) = e^{i\boldsymbol{k}.\boldsymbol{T}}\psi_{\boldsymbol{k}}(r) \qquad 3.37$$

where,
k – Bloch wave vector. Eq. 3.32 can now be reformulated as follows since the Bloch vector *k* now serves as a description of the one-electron function [150,151];

$$H_{eff}(r)\psi_n(k;r) = \epsilon_n(k)\psi_n(k;r) \qquad 3.38$$

where,
n – quantum number (it has taken the place of an index (*i*) in Eq. 3.32.);
ψ_n – one-electron wave function;
ϵ_n – associated eigenvalues [150,151];

When the wave vector is related to a reciprocal lattice vector according to the following formula [150], certain electronic states exhibit a phase factor value of 1.

$$G = 2\pi(n_1 b_1 + n_2 b_2 + n_3 b_3) \quad 3.39$$

where n_i and b_i are the reciprocal lattice's integers and basis vectors, respectively. i.e.,

$$(a_i . b_j) = \delta_{ij} \quad 3.40$$

For k = G

$$e^{i\boldsymbol{k}.\boldsymbol{T}} = e^{iG.T} = e^{2\pi i m_i n_i} = 1 \quad 3.41$$

As a result, the Bloch condition is satisfied by the electron state wave vector $k' = k + G$ since the periodicity in real space induces the periodicity in reciprocal space (k) [150,151]. The wave vectors existing within the Brillouin zone (BZ) can be taken into account when describing the electronic structure of a material. Since the crystal obeys rotational and translational symmetry, which can change the symmetry operation of one wave vector into some other wave vector. As a conclusion, we should first discover a solution for the Irreducible part of the BZ (IBZ) alone, which further simplifies the issue.

3.6.2 The projected augmented wave (PAW) method

The PAW approach is employed in this thesis. Blöchl[152] was those who initially developed and employed the PAW approach. However, Kresse and Joubert[153] have derived the formal connection between Vanderbilt-type ultrasoft pseudopotentials and the PAW approach. The rapidly oscillating valence wave functions around the ion cores require numerous Fourier components to correctly describe them, hence the PAW method helps to convert them into smooth wavefunctions. Here, I summarise the fundamentals of the PAW approach.

To do DFT calculations with greater computational efficiency, the PAW approach combines the principles of pseudopotential and linear augmented-plane wave

(LAPW) methods [150]. One electron wave function $|\psi\rangle$, also known as an orbital, is obtained from the pseudo-orbitals $|\tilde{\psi}\rangle$ by starting with a simple linear transformation[151].

$$|\psi\rangle = |\tilde{\psi}\rangle - \sum_{N,i} |\tilde{\phi}_{N,i}\rangle \langle \tilde{p}_{N,i}|\tilde{\psi}\rangle + \sum_{N,i} |\phi_{N,i}\rangle \langle \tilde{p}_{N,i}|\tilde{\psi}\rangle \qquad 3.42$$

All sites are covered by the index N, and the quantum numbers n, l, and m are covered by the index i. The local wave functions are represented by ϕ. The quantities associated with pseudo-wave functions are denoted by a tilde. The localised projector functions $\tilde{p}$ must satisfy the following requirement [150].

$$\sum_{i} |\tilde{\phi}\rangle \langle \tilde{p}_i| = 1 \qquad 3.43$$

The character $C_{N,i}$ describes [150] the contribution of an arbitrary wave function $\tilde{\psi}$ to the atomic site N.

$$C_{N,i} = \langle \tilde{p}_{N,i}|\tilde{\psi}\rangle \qquad 3.44$$

At an atomic site N, the pseudo- and all-electron wavefunctions can be simply generated using the plane-wave expanded pseudo-wave functions [150], as shown below.

$$|\tilde{\psi}_N\rangle = \sum_i |\tilde{\phi}_{N,i}\rangle C_{N,i} \qquad 3.45$$

and

$$|\psi_N\rangle = \sum_i |\phi_{N,i}\rangle C_{N,i} \qquad 3.46$$

Variational quantities that need to be calculated during the ground-state calculation are contained in the pseudo wave function $\tilde{\psi}$. Unlike "simple"

pseudopotential approaches, the operator A representing physical quantities must be consistently extended to their all-electron forms[151]:

$$\tilde{A} = A + \sum_{N,i,j} |\tilde{p}_{N,i}\rangle \left(\langle \phi_{N,i}|A|\phi_{N,j}\rangle - \langle \tilde{\phi}_{N,i}|A|\tilde{\phi}_{N,j}\rangle \right) \langle \tilde{p}_{N,j}| \qquad 3.47$$

The equation above holds true for both local and quasi-local operators like kinetic energy.

The valence-only PAW approach has been incorporated into the DFT package called VASP[71]. All calculations in relation to $CaWO_4$ of this thesis were done primarily using VASP. Only the calculations in Chapter 4 in relation to TiO_2 were completed using the Quantum ESPRESSO (QE) code[75].

3.6.3 Brillouin zone (BZ) integration

It is feasible to compute the charge density, total energy, forces, matrix components and response functions etc. by adding up the occupied states. As was stated in Section 3.6.1, this needs to be performed over the BZ for crystals. By considering crystal symmetry, calculations can be simplified by performing integration across the irreducible BZ's wedge. The eigenstates with corresponding eigenvalues $\epsilon_i(k)$ are filled starting from the lowest energy eigenvalue, following the variational principle of minimizing the total energy and considering the Pauli exclusion principle. The Fermi energy (E_F) corresponds to the energy of the most fully occupied eigenstate. The E_F can be determined from

$$N = \int_{-\infty}^{\epsilon_F} D(\epsilon) d\epsilon \qquad 3.48$$

where N is the valence electrons' total number and $D(\epsilon)$ refers to the DOS.

$$D(\epsilon) = \frac{2}{8\pi^3} \int_{S(\epsilon)} \frac{dS}{|\nabla \epsilon(K)|} \qquad 3.49$$

In the IBZ, the integration is conducted over the entire surface of constant energy, $S(\epsilon)$. The one-electron states that are of utmost importance for physical properties are those located near the E_F. As a result, these states play a crucial role in ensuring the crystal's stability and other aspects including transport properties. This integral needs to be calculated numerically at a discrete set of k-points within the BZ using wavefunctions and eigenvalues. Below is a brief discussion of the two most popular techniques.

3.6.3.1 Special k-points method

This approach performs the integration as a balanced sum over a grid of discrete k-points. While choosing a set of discrete k-points for Brillouin-zone sampling, three criteria must be taken into consideration: (i) To minimise the computational cost, there should be as few points as possible; (ii) To ensure uniform sampling, the points must be distributed evenly within the first Brillouin zone; (iii) While computed at these points, the k-points may also satisfy other conditions, such as orthogonality of a cluster of plane waves.

The mean-value point which uses only one point was suggested by Baldereschi[154]. A set of only a few special points that is suitable for semiconductors was proposed by Chadi and Cohen[155]. Later, Monkhorst and Pack offered a set of arguments that comprised the ideas put forth by Chadi and Cohen as well as a simple construction method shared by all space groups. The Monkhorst-Pack scheme has attracted prominence since it satisfies all the aforementioned requirements. Moreover, the linear tetrahedron approach has been integrated with it, broadening its applications.

3.6.3.2 Linear tetrahedron method

This approach involves applying interpolation in three phases. At first, nonoverlapping and space-filling tetrahedra are produced from the Brillouin zone. At the k-points on the tetrahedra's vertices, the wave functions $\psi_n(k)$, band

energies $\epsilon_n(k)$, and matrix elements $A_n(k)$ are calculated. Second, the difference of the band energies is then linearly interpolated between the vertices. In addition, quadratic techniques have also been applied. The Fermi energy is calculated using this linear interpolation. Finally, the analytical solutions for the integrals over all tetrahedra are then summed to calculate the Brillouin-zone integrals.

3.6.4 Popular software for the DFT modelling on semiconductor

A variety of software packages are available for the computation of electronic properties in crystalline solids, surfaces, molecules, liquids, and amorphous materials using DFT with a plane wave basis set. Prominent among these software packages are Vienna Ab-initio Simulation Package (VASP), Quantum Espresso (QE), CRYSTAL, CAmbridge Serial Total Energy Package (CASTEP), WIEN2k[156], Material Studio[157], and several others which are listed in the Table 1.3 of Chapter 1. It is noteworthy that VASP is widely used and preferred by researchers when compared to other available options. Its robust capabilities and versatility make it a primary choice for exploring the electronic properties of materials through first-principles calculations. In contrast, while calculations with the QE code may take a bit more time compared to VASP, the results are on par in terms of modelling accuracy. What's particularly noteworthy is that the QE code is accessible at no cost, thanks to its GNU license. This compelling combination of factors led us to primarily employ VASP in our project, with just one instance where we harnessed the power of the QE code. Moreover, the GGA method with the PBE functional is the prevailing choice for the entirety of this thesis. Its selection is based on its cost-effectiveness, making it particularly well-suited for projects involving simulation domains with several hundred atoms.

Chapter 4:

First-principles study of electronic properties of Zn and La-doped and co-doped anatase TiO_2

4.1. TiO_2 and its chemical modification

Titanium dioxide (TiO_2) is extensively used in many applications such as water splitting, air purification, and wastewater treatment due to its high oxidative power, high chemical stability, resistance to photo corrosion, nontoxic, and low cost [158–162]. Anatase TiO_2 effectively transforms organic pollutants into non-toxic substances and is suitable for decomposing substances that are difficult to treat by using other conventional biological or physical methods. The anatase phase TiO_2 shows better photocatalytic properties than its rutile phase. For example, anatase TiO_2 has an indirect bandgap which results in a longer lifetime of photoinduced electrons [163]. While these properties make anatase TiO_2 suitable for photocatalytic applications, there is room for improvement on its photocatalytic properties, in particular in reducing the relatively large bandgap (3.2 eV) from its main photocatalytic activity within the ultraviolet range (UV, <380 nm [164]) to the visible light range (> 400nm) of the solar spectrum. To effectively decompose organic waste, it is essential to effectively generate the electron-hole pairs (and hence the hydroxyl radical in the presence of water). The electron-hole pair recombination process in the native TiO_2 annihilates the photogenerated charge carriers and transforms them to heat and other forms of energy. As a result, it reduces the photocatalytic performance of the native TiO_2.

The properties of TiO_2 photocatalysts can be improved by doping this material using elements which can change its lattice and electronic band structure. This approach can enhance photocatalysis by capturing longer solar wavelengths and efficient photogeneration of charge carriers. Also, these chemical modifications can reduce the recombination rate by creating localized energy states in the bandgap [165,166]. Moreover, some of the doping metal ions in TiO_2 can prevent the phase transformation of anatase to rutile and can hence improve the thermal stability of the TiO_2 structure [167].

Chemical modification of TiO_2 has been extensively researched in the fields of (i) transition metal atoms doping [168]; (ii) surface deposition [169]; (iii) carbon coating on the surface of TiO_2 [170]; and (iv) making composite material by combining

metals and/or different types of semiconductors (such as MnO_2 [171], RuO_2 [172], and WO_3 [173]) with TiO_2. Most of these studies aimed to make TiO_2 usable in visible irradiation for their respective targeted applications [174].

Doping TiO_2 using Zn^{2+} can enhance the photocatalytic activity, resulting in a better degradation of Rhodamine B [175]. The optical absorption range of Zn-doped TiO_2 was expanded from 400 to 550 nm [176] compared with the pure TiO_2. Doping by La^{3+} proved to improve electron-hole separation, in which La^{3+} acts as a trapping centre for photogenerated electrons [177], as well as a significant inhibition on its phase transformation [178]. Moreover, La-doped TiO_2 can inhibit the recombination of photogenerated electron-hole pairs, leading to its enhanced photocatalytic activity [179].

The decomposition rate of HCHO on a Zn^{2+}-La^{3+} co-doped TiO_2 powder was higher than that on pure TiO_2 [180] since co-doping can modify the conduction band edge of TiO_2, which reduces its bandgap leading to a shift towards visible light absorption. Zn^{2+}-La^{3+} co-doped TiO_2 has a photocatalytic efficiency which could be twice as good as pure TiO_2 powder [180]. Introducing La^{3+} ions into synthesised Zn-TiO_2 material can result in a noticeable blue shift and increased optical absorption [181].

The literature review reinforces the understanding that the introduction of Zn cations effectively narrows down the bandgap value, forming new energy levels not only within the bands but also within the bandgap region. Conversely, the presence of La cations plays a significant role in inhibiting phase transfer and facilitating precise band edge engineering. These compelling insights form the foundation upon which this project has chosen to incorporate Zn and La cations as dopants in the chemical modification of anatase TiO_2.

While there has been extensive experimental research on single doping and co-doping TiO_2 using Zn^{2+} and La^{3+}, up to date, there has not been a systematic explanation regarding how and why the co-doping can have such influences. Furthermore, no research has been published in terms of trying to find the optimum composition of the co-doped material using these ions. This chapter of the thesis

presents the author's computational modelling research on predicting the electronic and absorption properties of anatase TiO_2 photocatalyst, doped and co-doped with Zn^{2+} and La^{3+} ions. The modelling results include crystal lattice structural properties, electronic band structure, the density of state (DOS), formation energy, charge density and absorption spectrum. The modelling results are used to interpret and explain the underlying mechanism of how the Zn^{2+} and La^{3+} co-doping may affect the properties of TiO_2, identifying their role in its electronic band structure and the optimum composition.

4.2. Computational methods

First-principles density functional theory (DFT) calculations for anatase TiO_2 were conducted by using Quantum Expresso code [75] with the generalized gradient approximation (GGA) method. The properties of the TiO_2 supercell doped and co-doped by Zn^{2+} and La^{3+} ions were studied using ultrasoft pseudopotential (USPP) with Perdew-Burke-Ernzerhof (PBE) exchange-correlation functional[76]. The calculated properties, including the lattice parameters, electronic band structure, DOS, charge density and absorption spectrum, were estimated using the GGA method.

The pseudopotentials of Ti, O, Zn, and La atoms for this study are taken from the Quantum Expresso database [182–185]. Anatase TiO_2 has a tetragonal structure with the space group body-centred crystal structure $I4_1/amd$. The anatase TiO_2 system, in the computation, contains 4 titanium (Ti) atoms and 8 oxygen (O) atoms in each unit cell. A 2×2×1 supercell of TiO_2 (which contains 16-Ti atoms, 32-O atoms, and a total of 48 atoms) is used in all computations of this chapter. The simulation domain measures 7.596 Å × 7.596 Å × 9.717 Å. One or multiple Ti atoms of the TiO_2 supercell are replaced by the 3d and 5d metal ions Zn^{2+} and La^{3+} in the DFT calculations for the doped and/or co-doped systems. The kinetic energy cut-off for wave functions of 60 Ry and the charge density cut-off of 600 Ry is used to expand the valence electronic wave function with valence configurations of Ti-$3d^2 4s^2$, and O-$2s^2 2p^4$ as well as to precisely incorporate the significant number of bands required to achieve convergence [186]. The Monkhorst-Pack scheme k-point grid of

2×2×2 is employed for the geometry optimization calculations of pure TiO_2 and its corresponding doped and co-doped systems after examining the k-point convergent test. The convergence threshold for self-consistency is set to 1.0×10^{-9} Ry to increase the accuracy of the modelling results. The turboEELS code from time-dependent density-functional theory (TDDFT) was used when doing the calculation of the absorption spectra[187]. The crystal lattice structure of the supercell is relaxed first until the pressure and forces of the supercell reach -0.06 kbar and 0.001 eV/Å, respectively. Then, the total energy, DOS, electronic band structures, charge density and absorption spectrum of pure TiO_2 and its chemically modified systems (Zn^{2+}-doped, La^{3+}-doped, and Zn^{2+}-La^{3+} co-doped systems) are analysed.

The entirety of this study primarily adheres to the GGA method for the reasons outlined above. Nevertheless, the DFT+U method was also employed in some calculations of Ti-3d orbitals in TiO_2 to examine the influence of Hubbard U (i.e., U = 8.5 eV [188]) correction on the results of calculation in terms of electronic band structure.

4.3. Results and discussion

4.3.1. Structural optimization

The supercell lattice structure of pure TiO_2 and its corresponding doped and co-doped systems are shown in Figure 4.1. For the convenience of presentation, only the supercell structures of 2.08 at.% La^{3+}-doped, 6.25 at.% Zn^{2+}-doped, and 8.33 at.% Zn^{2+}-La^{3+} co-doped TiO_2 systems (at.% = atomic percentages) are shown in this figure.

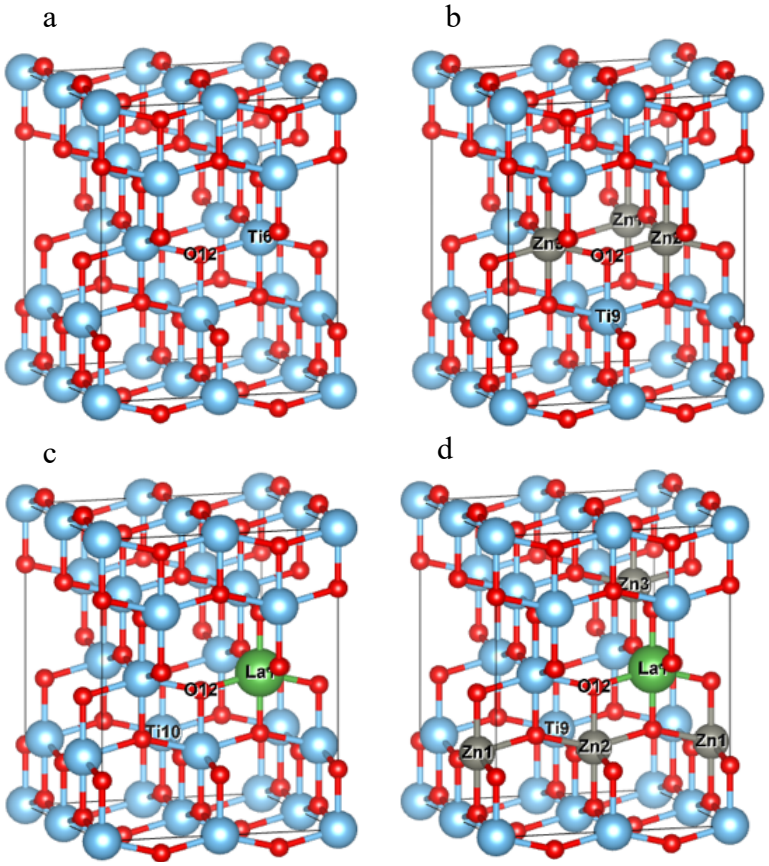

Figure 4.1: 2 x 2 x 1 supercell structure of the (a) pure anatase TiO_2, (b) Zn^{2+}-doped TiO_2, (c) La^{3+}-doped TiO_2 and (d) Zn^{2+}-La^{3+} co-doped TiO_2, where the red, blue, green and grey spheres indicate O, Ti, La, and Zn atoms respectively.

To analyse the influence of concentration of doping elements on the properties of chemically modified TiO_2, the following systems are employed in the computational modelling: (1) $Ti_{15}La_1O_{32}$, $Ti_{14}La_2O_{32}$, $Ti_{13}La_3O_{32}$, $Ti_{12}La_4O_{32}$, and $Ti_{11}La_5O_{32}$ for the La^{3+}-doped TiO_2, (2) $Ti_{15}Zn_1O_{32}$, $Ti_{14}Zn_2O_{32}$, $Ti_{13}Zn_3O_{32}$, $Ti_{12}Zn_4O_{32}$, and $Ti_{11}Zn_5O_{32}$ for the Zn^{2+}-doped TiO_2, (3) $Ti_{14}Zn_1La_1O_{32}$, $Ti_{13}Zn_2La_1O_{32}$, $Ti_{13}Zn_1La_2O_{32}$, $Ti_{12}Zn_3La_1O_{32}$, $Ti_{12}Zn_1La_3O_{32}$, $Ti_{11}Zn_4La_1O_{32}$, $Ti_{11}Zn_1La_4O_{32}$ for the Zn^{2+}-La^{3+} co-doped TiO_2. Table 4.1 shows the specific composition of these systems as well as their bandgap values computed using the GGA method. It can be seen that the bandgap value of La^{3+}-doped TiO_2 (4.17 at.%) is 2.13 eV (see Table 4.1), which is very close to the modelling results of Zhao and Liu (2.28 eV) [189].

Table 4.1: Composition of target materials and computational modelling results of bandgap value using the GGA method.

Bandgap values (eV) of optimized compositions			
Compounds	**Concentrations of doping elements (at.%)**	**Chemical formula**	**Modelling results of bandgap (eV)**
Pure TiO_2	-	$Ti_{16}O_{32}$	2.12
Zn^{2+}-doped TiO_2	2.08	$Ti_{15}Zn_1O_{32}$	2.15
	4.17	$Ti_{14}Zn_2O_{32}$	1.81
	6.25	$Ti_{13}Zn_3O_{32}$	**1.73**
	8.33	$Ti_{12}Zn_4O_{32}$	1.84
	10.41	$Ti_{11}Zn_5O_{32}$	1.97
La^{3+}-doped TiO_2	2.08	$Ti_{15}La_1O_{32}$	**1.92**
	4.17	$Ti_{14}La_2O_{32}$	2.13
	6.25	$Ti_{13}La_3O_{32}$	2.06
	8.33	$Ti_{12}La_4O_{32}$	2.63
	10.41	$Ti_{11}La_5O_{32}$	2.17
Zn^{2+}- La^{3+} co-doped TiO_2	4.17	$Ti_{14}Zn_1La_1O_{32}$	2.21
	6.25	$Ti_{13}Zn_2La_1O_{32}$	2.39
	6.25	$Ti_{13}Zn_1La_2O_{32}$	2.38
	8.33	$Ti_{12}Zn_3La_1O_{32}$	**1.85**
	8.33	$Ti_{12}Zn_1La_3O_{32}$	2.34
	10.41	$Ti_{11}Zn_4La_1O_{32}$	2.12
	10.41	$Ti_{11}Zn_1La_4O_{32}$	2.37

When doping or co-doping TiO_2 using Zn^{2+} and/or La^{3+}, the Ti atoms at different positions of the supercell, such as 5Ti, 7Ti, 8Ti, 11Ti, 12Ti, 14Ti, 15Ti and 16Ti, may have the opportunity to be replaced by Zn^{2+} and/or La^{3+} in theory. Table 4.2 summarises the distance between the two Zn^{2+} ions in the 4.17 at.% single-doped system, showing the great variation of inter-Zn^{2+} ion distance which may affect the electronic properties of the material.

Table 4.2: Position of doped Zn^{2+} ions at Ti sites in the 4.17 at.% Zn^{2+}-doped TiO_2 and corresponding modelling results of the distance between the first and second Zn^{2+} ion.

Position of Zn^{2+}	6Ti-5Ti	6Ti-7Ti	6Ti-8Ti	6Ti-11Ti	6Ti-12Ti	6Ti-14Ti	6Ti-15Ti	6Ti-16Ti
Distance (Å)	3.73	5.28	3.73	4.78	2.99	2.99	7.12	4.78

The energy of the relaxed systems that have respective configurations regarding the position of Zn^{2+} ions is analysed and presented in Table 4.2. It can be seen that the substitutions in positions 6Ti-5Ti (3.73 Å), 6Ti-8Ti (3.73 Å), 6Ti-11Ti (4.78 Å), and 6Ti-16Ti (4.78 Å) are favourable in terms of the energy. Hence, the positions of Ti atoms that are replaced by Zn^{2+} ions in the systems of single doping using Zn^{2+} ions with dopant concentrations of 4.17, 6.25, 8.33 and 10.42 at.% are (5Ti,6Ti), (5Ti,6Ti,8Ti), (5Ti,6Ti,8Ti,11Ti), and (5Ti,6Ti,8Ti,11Ti,16Ti) respectively. A similar approach is used to determine the position of Ti atoms that are replaced by either La^{3+} ions or Zn^{2+} as well as La^{3+} ions in the La^{3+}-doped TiO_2 and Zn^{2+}- La^{3+} co-doped TiO_2.

As can be seen in Table 4.1, La^{3+} doping at the concentration of 2.08 at.% (chemical formula $Ti_{15}La_1O_{32}$) results in the lowest bandgap value (1.92 eV) amongst all the La^{3+} single-doped systems that are studied in the thesis. In the case of Zn^{2+} single-doped systems, the dopant concentration of 6.25 at.% (formula $Ti_{13}Zn_3O_{32}$) has the most significant influence, resulting in the lowest bandgap value of 1.73 eV. When co-doping the TiO_2 simultaneously using Zn^{2+} ions as well as La^{3+} ions, the $Ti_{12}Zn_3La_1O_{32}$ system (i.e. 6.25 at.% Zn^{2+} and 2.08 at.% La^{3+}) results in the lowest bandgap of 1.85 eV almost all the co-doping systems that are analyzed in the thesis. It is due to the synergistic effect of the two dopant elements. The following sections mainly focus on $Ti_{15}La_1O_{32}$, $Ti_{13}Zn_3O_{32}$, Ti_{12} $Zn_3La_1O_{32}$ and $Ti_{16}O_{32}$.

Table 4.3 lists the lattice constants *a*, *c*, *c/a*, bond length (equatorial (d_{ep}: *Ti-O)* and apical *(d_{ap}: Ti-O)*) as well as the bond angle *2θ* (Ti-O-Ti) of the relaxed pure TiO_2 and its corresponding doped and co-doped systems. It can be seen that the

lattice parameters of TiO_2 change as a result of doping. The computational results of pure TiO_2 are very close to the corresponding experimental results (a = b = 3.784 Å, c = 9.512 Å, d_{ep} = 1.933 Å, d_{ap} = 1.979 Å, and 2θ = 156.230°) [190]. It can be seen that the lattice constants *a* and *c* increase (relative to TiO_2) when Ti^{4+} (0.86 Å) atoms are replaced by Zn^{2+} (0.75 Å) and La^{3+} (1.16 Å) ions that have a different ionic radius.

Table 4.3: Computational modelling results of the lattice constants of pure TiO_2, and its doped and co-doped systems with Zn^{2+} and La^{3+}.

Lattice Parameter	**$Ti_{16}O_{32}$**	**$Ti_{13}Zn_3O_{32}$**	**$Ti_{15}La_1O_{32}$**	**$Ti_{12}Zn_3La_1O_{32}$**
***a* (/Å)**	3.798	3.801	3.802	3.842
***c* (/Å)**	9.717	9.878	10.217	10.043
***c/a* (/Å)**	2.558	2.598	2.687	2.614
d_{ep} (/Å)	1.947	1.944	1.949	1.874
d_{ap} (/Å)	2.006	2.052	2.109	1.923
2θ	154.829°	152.503°	151.626°	155.214°
E_{form} (eV)	-	3.317	-4.210	-1.342

4.3.2. Electronic properties

4.3.2.1 Electronic band structure

a. Use GGA method:

The electronic bandgap value directly influences the photocatalytic properties of materials such as anatase TiO_2. Figure 4.2 shows the calculated electronic band structures of $Ti_{16}O_{32}$, $Ti_{13}Zn_3O_{32}$, $Ti_{15}La_1O_{32}$ and $Ti_{12}Zn_3La_1O_{32}$, of which the bandgap values are listed and compared with experimental and computational results of the literature in Table 4.4.

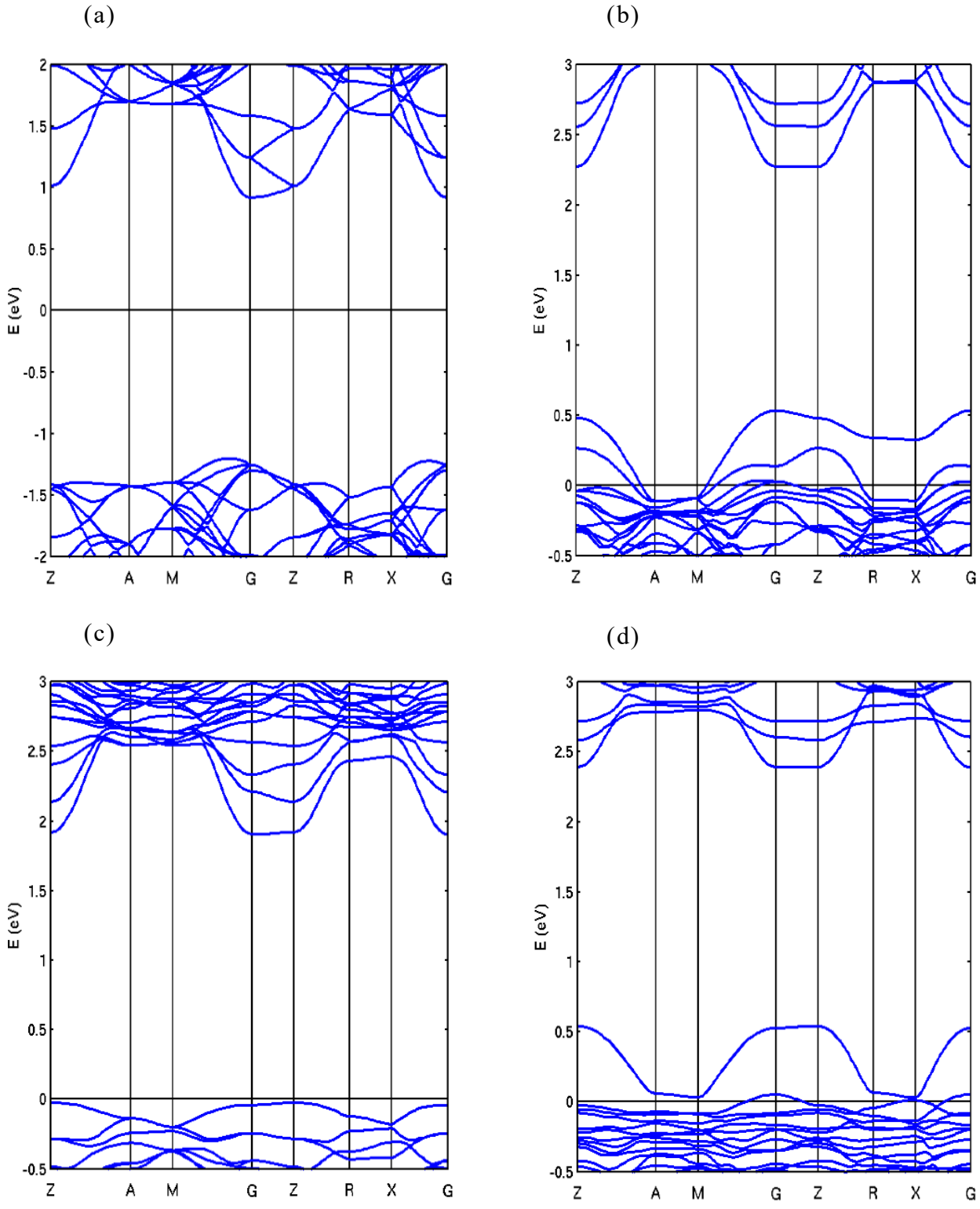

Figure 4.2: Computational modelling results of the electronic band structure of (a) pure $Ti_{16}O_{32}$, (b) $Ti_{13}Zn_3O_{32}$, (c) $Ti_{15}La_1O_{32}$ and (d) $Ti_{12}Zn_3La_1O_{32}$.

Table 4.4: Computational results of the bandgap value of related target materials, and the comparison with computational and experimental results of the literature where applicable.

Size of bandgap (eV)				
Systems	**This work**	**Difference in bandgap values of systems**	**Computational results of literature**	**Experimental results of the literature**
$Ti_{16}O_{32}$	2.12	0	2.21[191], 2.54 [189]	3.20 [192]
$Ti_{15}LaO_{32}$	1.92	0.20	2.28 [189]	3.15[193]
$Ti_{13}Zn_3O_{32}$	1.73	0.39	1.67[191]	3.00[194]
$Ti_{12}LaZn_3O_{32}$	1.85	0.27	n.a	n.a

Using the GGA method, the bandgap of $Ti_{16}O_{32}$ is estimated to be 2.12 eV, which is very close to related computational modelling results of 2.21 eV[191]. However, it's crucial to acknowledge that the GGA method tends to exhibit a tendency to underestimate bandgap values. This discrepancy becomes especially apparent when contrasting our findings with experimental data, where the bandgap is measured at 3.2 eV [191]. The root of this significant difference lies in the inherent limitations of the GGA method, particularly its inability to fully account for the self-interaction of electrons during calculations. This incomplete removal of self-interaction, in turn, leads to the underestimation of the bandgap value in our theoretical predictions. Furthermore, the GGA method is primarily designed to access ground-state properties and does not inherently incorporate the treatment of excited state electrons, as it follows the time-independent wave equation. As a result, bandgap underestimation typically hovers around 50% when compared to experimental data. In light of these considerations, our study provides valuable insights into the bandgap of $Ti_{16}O_{32}$ based on the GGA method, shedding light on its intrinsic limitations and emphasizing the importance of considering these factors when interpreting our computational results in the context of experimental data.

The La^{3+} doping into TiO_2 reduces the bandgap value from 2.12 to 1.92 eV, because of the shift of the valence band maxima (VBM). The conduction band minima (CBM) in La^{3+}-doped TiO_2 is not significantly affected. When replacing more Ti atoms using Zn^{2+} as the second doping element in the La^{3+} and Zn^{2+} co-doped TiO_2, the bandgap value is further reduced from 1.92 eV to 1.85 eV. This is due to the introduction of additional impurity energy levels (IELs) in the electronic band structure.

Figure 4.2a shows that the VBM of pure anatase TiO_2 lies approximately at -1.4 eV, whereas the VBM of Zn^{2+}-doped (Figure 4.2b) and La^{3+}-doped (Figure 4.2c) TiO_2 lies above VBM of pure TiO_2. Compared to pure TiO_2, single doping by using either Zn^{2+} or La^{3+} shifts the VBM from -1.4 eV to 0.49 eV and -1.4 eV to -0.1 eV, respectively. For the co-doped system (Figure 4.2d), the VBM further shifts to 0.51 eV, because the doping elements particularly Zn^{2+} directly contribute to the VBM by producing IELs in the valence band. Numerous IELs resulting from the presence of Zn^{2+} and La^{3+} also shift the CBM of the co-doped system, albeit La^{3+} plays a greater role in the shifting of CBM. Furthermore, since the Fermi level of the single-doped and co-doped materials (Figure 4.2d) move towards its VB region as a result of the VBM shift, it can be concluded that Zn^{2+} and La^{3+} co-doping ions convert TiO_2 from n-type to a p-type semiconductor.

Figure 4.2d shows the well-dispersed bands of the Zn^{2+}-La^{3+} co-doped TiO_2 at both VB and CB edges. When compared to a Zn^{2+}-doped material (Figure 4.2b), the VB of a co-doped system varies considerably owing to the introduction of a La^{3+} ion. The IELs formed by La^{3+} ion in the co-doped system is mostly located in the low energy region of VB, not in the region of the bandgap. These IELs due to doping with La^{3+} results in well-dispersed energy levels at the VB edge of the co-doped system [189] and shifts it just above the Fermi level (see Figure 4.2d). The narrow bandgap of the co-doped system facilitates photoexcited electrons to go from VBM to CBM with less energy than in the case of pure TiO_2[192]. The well-dispersed bands at both VBM and CBM (that can be seen in Figure 4.2d) due to co-doping using La^{3+} and Zn^{2+} act as a holder for the photoexcited carriers when the separation of photoexcited electron-hole pairs occurs. Hence it reduces the rate of recombination and increases the lifetime of photoinduced charge carriers [195].

The combination of these effects overall improves the photocatalytic activity of the co-doped material.

The electronic band structure (Figure 4.2d) reveals that the Zn^{2+}-La^{3+} co-doped TiO_2 has indirect bandgap behaviour since its electron transition occurs between the Z point of the top-most VB and the G point of the bottom-most CB of the Brillouin zone. Such indirect band transition favours the efficient separation of charge carriers and thus improves photocatalytic properties. Interestingly, the three doped materials feature a flat energy band between the G and Z points in the CBM. This dispersive flat band appears due to an increase in overlap interactions by the higher atomic weight substituents Zn^{2+} and La^{3+} at the Ti sites of TiO_2 and thus resulting in more effective mobility of the photoexcited carriers than in pure TiO_2 [195]. Particularly, the Zn^{2+}-La^{3+} co-doped system (Figure 4.2d) features the most distinctive flat band region at G−Z points in both VBM and CBM. This implies that when photoexcitation occurs, the holes remain in the flat band region of VBM whereas the electrons remain in the flat band region of CBM. This photogenerated electron-hole pair can help to decrease recombination rates and extend the lifetime of charge carriers.

b. Use GGA+U method:

To comprehend the influence of Hubbard U values on the modelling results of such as electronic band structure and bandgap properties, GGA+U method was employed in a separate set of DFT modelling of $Ti_{16}O_{32}$, $Ti_{15}LaO_{32}$, $Ti_{13}Zn_3O_{32}$, and $Ti_{12}LaZn_3O_{32}$, selected as the compounds with lowest bandgap energy as calculated using GGA. The modelling results of the bandgap values using the GGA method and separately using the GGA+U method are displayed in Table 4.5.

Table 4.5: Modelling results of the bandgap value using the GGA method and GGA+U method (U correction is 8.5 eV).

Materials	Overall doping at.%	Bandgap value (eV) calculated using the GGA method	Bandgap value (eV) calculated using the GGA+U method

$Ti_{16}O_{32}$	0.00	2.12	2.87
$Ti_{15}LaO_{32}$	2.08	1.92	2.76
$Ti_{13}Zn_3O_{32}$	6.25	1.73	2.60
$Ti_{12}LaZn_3O_{32}$	8.33	1.85	2.38

Notably, the findings demonstrate that the implementation of GGA+U method in calculations results in greater bandgap values in the modelling, relative to the modelling results using the GGA method, and the results are closer to related experimental results (see Table 4.4, difference between 0.33 – 0.41 eV).

Figure 4.3 illustrates the bandgap values calculated using the GGA method and separately using the GGA+U method for the Zn^{2+}-La^{3+} co-doped systems. It can be seen that the modelling results of bandgap value using the GGA+U method are consistently greater than the bandgap values calculated using the GGA method.

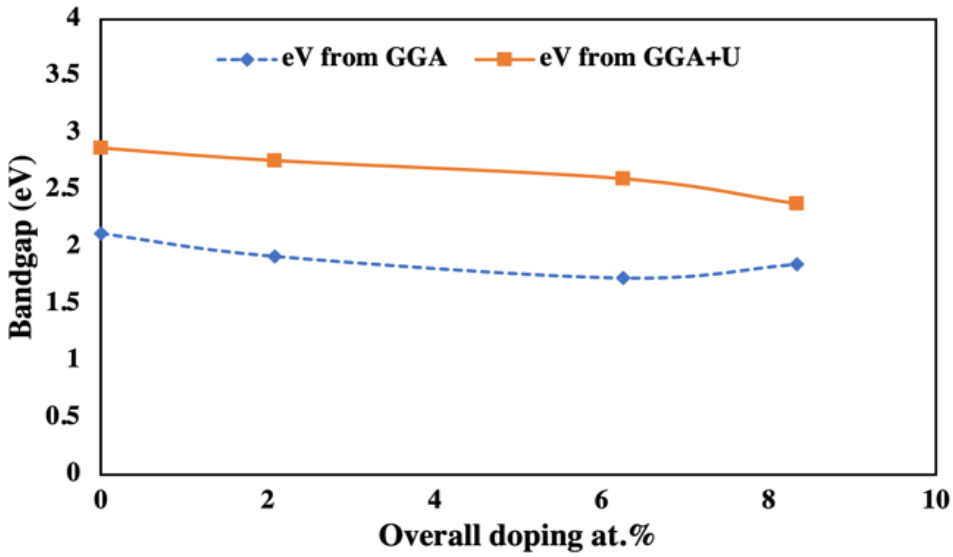

Figure 4.3: Comparison of GGA and GGA+U modelling results of bandgap value for the La (mentioned at doping concentration 2.08 at.%) and Zn (mentioned at doping concentration 6.25 at.%) single doped and co-doped (mentioned at doping concentration 8.33 at.%) systems.

The disparity between these two sets of modelling outcomes remains remarkably stable, observed consistently between 0 to 6.25 at.%, particularly in cases at ion doping levels of 2.08 at.% for La^{3+} and 6.25 at.% of Zn^{2+}. At relatively high combined doping concentrations of 8.33 at.% (i.e., 2.08 at.% from La^{3+} and 6.25

at.% from Zn^{2+}), the influence of exchange-correlation becomes more pronounced, resulting in a larger deviation between the two methods.

The electronic band structures obtained using the GGA+U method for both pure and Zn^{2+}-La^{3+} co-doped TiO_2 systems are depicted in Figure 4.4. Upon comparing Figure 4.4a and b with Figure 4.2a and d, it can be seen that the introduction of Hubbard U induces significant shifts of the band edges towards the higher energy level, particularly noticeable in the CBM of these systems. This explains why Hubbard U may affect the modelling results of bandgap value when the GGA+U is employed in the modelling. Overall, on one hand, the GGA method underestimates the bandgap values relative to the GGA+U method. On the other hand, however, the magnitude of underestimation is quite consistent over a relatively large range of dopant concentration. It means that the modelling results using the GGA method are still valid as a comparative tool between different doping elements and concentrations, while the fact that it may underestimate the bandgap values is acknowledged.

(a)

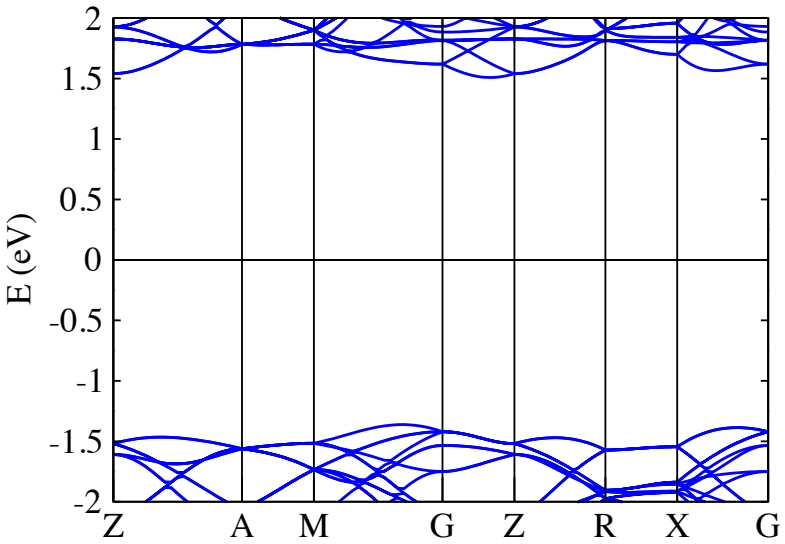

(b)

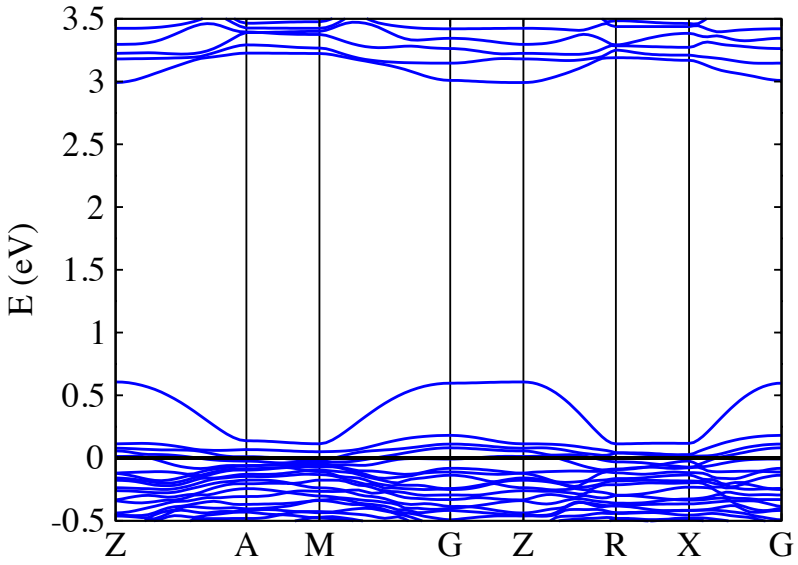

Figure 4.4: Electronic band structure predicted using GGA+U method: (a) pure $Ti_{16}O_{32}$, (b) $Ti_{12}Zn_3La_1O_{32}$.

Although the GGA+U method can provide theoretical results closer to experimental data, it works at the cost of very high computational cost. This is only worsened if a larger supercell is required to provide lower doping concentrations, as it was the objective of this manuscript. Therefore, the rest of computational properties have been calculated using the GGA method and only comparative analyses between the compounds are provided.

4.3.3. Density of states

To analyse the bonding behaviour and reason of bandgap reduction, the computational modelling results of the total density of states (TDOS) and partial density of states (PDOS) of $Ti_{16}O_{32}$, $Ti_{15}La_1O_{32}$, $Ti_{13}Zn_3O_{32}$ and $Ti_{12}Zn_3La_1O_{32}$ are shown in Figure 4.5. In Figure 4.5a, it can be seen that O-2p states mainly occupy the VB, whereas CB is mainly dominated by Ti-3d states. For La^{3+}-doped TiO_2 (Figure 4.5b), a very similar situation is observed where the contribution of La-5d states is minimal to both VB and CB, albeit the bandgap is reduced from 2.12 eV for pure $Ti_{16}O_{32}$ to 1.92 eV for $Ti_{15}LaO_{32}$. For Zn^{2+}-doped TiO_2, the VB is still primarily occupied by O-2p states, while there is a significant contribution from the lower energy states of Ti-3d and Zn-3d. The Ti-3d states dominate the CB with some contribution of O-2p states, as shown in Figure 4.5c. They reduce

the bandgap value from 2.12 eV of pure $Ti_{16}O_{32}$ to 1.73 eV of $Ti_{13}Zn_3O_{32}$. When TiO_2 is co-doped by both Zn and La elements, the combined effects of the two elements can be seen in Figure 4.5d. VB and CB bands are still mostly dominated by O-2p and Ti-3d states, respectively. However, Zn-3d states contribute to lower energy in the VB, whereas La-5d states contribute to higher energy in the CB. The La-5d contribution is more pronounced here than in the mono-doped $Ti_{15}LaO_{32}$ material. The combined effect can be seen in the bandgap value, which is reduced from 2.12 eV of pure $Ti_{16}O_{32}$ to 1.85 eV of $Ti_{12}LaZn_3O_{32}$. Figure 4.5d indicates that most of the hybridisation occurs between the 2p states of O atoms and the 3d states of Ti atoms.

For the Zn^{2+}-La^{3+} co-doped TiO_2, the reduction of the bandgap relates to the contribution of the d orbitals of Zn atoms as well as the p and d orbitals of O and Ti atoms. They significantly narrow the bandgap by changing the edges of both CBM and VBM.

(a)

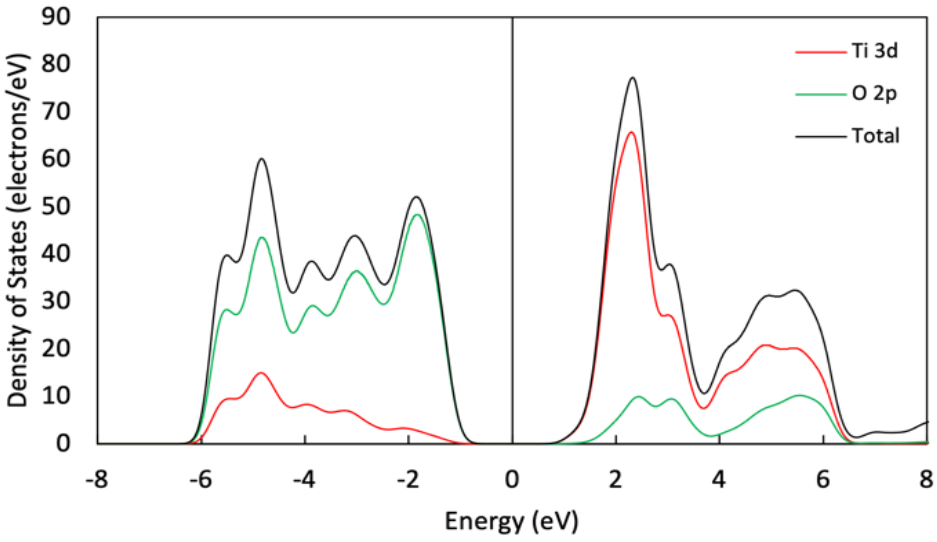

(b)

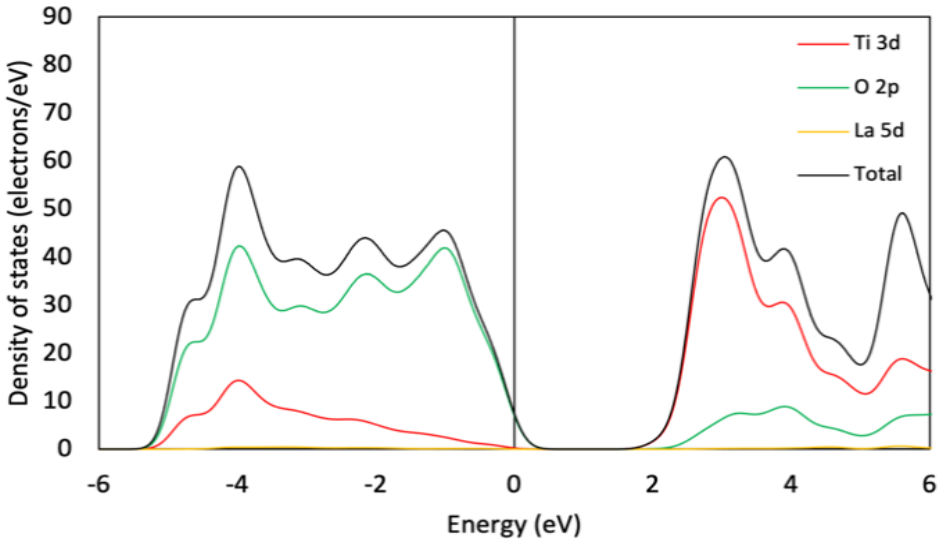

(c)

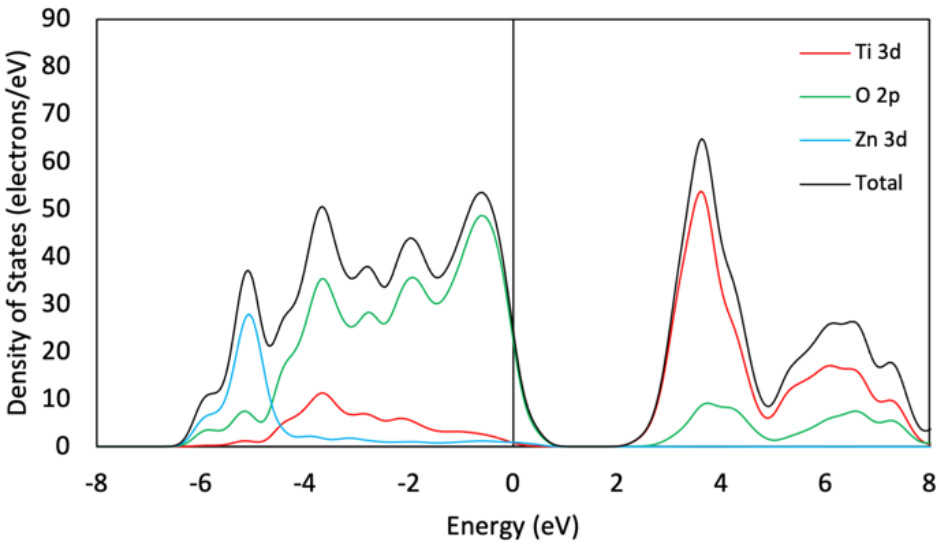

(d)

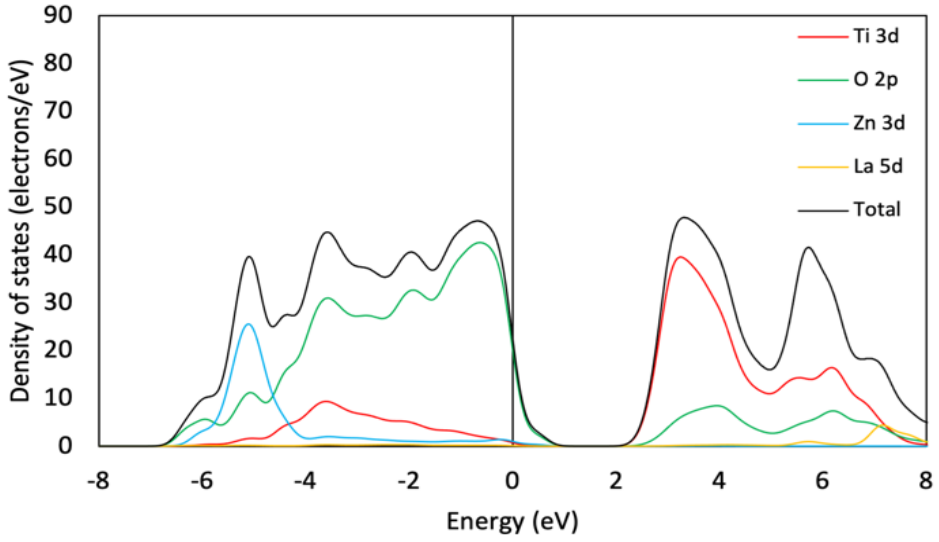

Figure 4.5: Computational modelling results of TDOS and PDOS of (a) pure $Ti_{16}O_{32}$, (b) $Ti_{15}La_1O_{32}$, (c) $Ti_{13}Zn_3O_{32}$, and (d) $Ti_{12}Zn_3La_1O_{32}$.

The 3d and 5d states of Zn and La atoms are localized in Zn^{2+}-La^{3+} co-doped TiO_2. The Zn and La cations affect the native bond lengths between them and neighbouring atoms of the co-doped TiO_2 and facilitate the formation of several IELs in the bands (VB and CB). The DOS profile of Zn^{2+}-La^{3+} co-doped TiO_2 (Figure 4.5d) is broader and smoother than the DOS profile of pure TiO_2 (Figure 4.5a). The IELs generated by the La-5d states are located in the higher energy level of CB (between 6.75 and 7.91 eV). However, these IELs are located at the lowest energy level of VB (between -0.09 and -6.15 eV). The IELs formed by Zn-3d states are predominantly located at the lowest energy level of VB (between -0.02 and -6.11 eV). However, the IELs of Zn-3d states facilitate the O-2p states in the formation of their VBM above the Fermi level.

In Figure 4.2d, the valence band is formed by the cluster of electron band energy levels, except for a single band energy level (also called as a single broad band) that arises just over the Fermi energy level which is noticeably detached from other bands. Although the La-5d states of this system are well away from the Fermi energy level, they play a significant role in this single band. Besides the La-5d orbitals, the hybridization of the Zn-3d orbital with the 3d and 2p orbitals of Ti and O atoms contributes to this single broad band detachment from other bands. The PDOS and electronic band structure analysis indicates that the CBM at the G point originates predominantly from the 3d states of Ti atoms. The VBM that can be found at the Z point mainly emerges from O-2p states hybridization with Ti-3d and Zn-3d. Conclusively, the La^{3+} cation associated orbital states contribute less to the VB or CB in the co-doped TiO_2 system, whereas the Zn, Ti, and O ions associated orbital states contribute more towards band edges. This might be the reason why Zn^{2+}-La^{3+} co-doped TiO_2 fails to outperform the Zn^{2+}-doped TiO_2, in the sense that the overall bandgap value of the co-doped system is greater than that of the Zn^{2+} single doped TiO_2.

As have been observed above, co-doping the TiO_2 using Zn^{2+} and La^{3+} ions can directly influence the material's photocatalytic properties by modifying its entire electronic band structure. Some of the Ti atoms in the anatase structure are replaced by Zn^{2+} and La^{3+} as presented in section 4.3.1. Based on the most stable structure, the Ti6 atom is replaced by a La^{3+} ion, and the Ti10, Ti12, and Ti14

atoms are replaced by Zn^{2+} ions, forming $Ti_{12}LaZn_3O_{32}$. In it, the VB width is expanded to 7.65 eV (± 0.05), which is greater than the VB size of the pure TiO_2 (5.59 eV (± 0.05)). As a result, the bandgap in the Zn^{2+}-La^{3+} co-doped TiO_2 is reduced. Therefore, the VB band width expansion of Zn^{2+}-La^{3+} co-doped TiO_2 is due to the combined influences of O-2p states and Zn-3d states. Furthermore, as seen in Figure 4.5d, the Fermi energy level of Zn^{2+}-La^{3+} co-doped TiO_2 drops downward into the VB region. This shift is mainly attributed to O-2p states, with minor contributions from Zn-3d and Ti-3d states. These findings suggest that the co-doping of TiO_2 with Zn^{2+} and La^{3+} cations makes the chemically modified TiO_2 a p-type semiconductor, while the pure anatase TiO_2 has an n-type semiconductor nature.

4.3.4. Formation energy

The impurity formation energy E_{form} is calculated to characterise the relative difficulty of forming the single-doped (Zn^{2+}/La^{3+} Equation 4.1) or co-doped (Zn^{2+}-La^{3+}, Equation 4.2) TiO_2, in which the metal ions (M) such as Zn^{2+} and La^{3+} replace some Ti^{4+} :

$$E_{form} = E_{M-doped} - E_{pure} - n_M\mu_M + n_{Ti}\mu_{Ti} \qquad 4.1$$

$$E_{form} = E_{M-codoped} - E_{pure} - n_{Zn}\mu_{Zn} - n_{La}\mu_{La} + n_{Ti}\mu_{Ti} \qquad 4.2$$

$E_{M-doped}$ is the total energy of TiO_2 that is doped with Zn^{2+} or La^{3+} ions, $E_{M-codoped}$ is the total energy of TiO_2 that is co-doped with Zn^{2+} and La^{3+} ions, E_{pure} is the energy of the pure TiO_2, n_{Ti} is the number of Ti atoms eliminated from the TiO_2, n_M (n_{Zn} or n_{La}) is the number of M (Zn or La) atoms inserted in the TiO_2, μ_M (μ_{Zn} or μ_{La}) and μ_{Ti} are the chemical potentials of M (Zn or La) and Ti, respectively. Generally, the formation energy of a system is correlated with the chemical potentials of Ti and O depending on the experimental growth conditions of the target material, which can be Ti-rich or O-rich (or anything in between).

Under the Ti-rich condition, the Ti is considered to be in thermodynamic equilibrium with its bulk solid phase, resulting in a fixed chemical potential value of μ_{Ti}. Meanwhile, the chemical potential of O is fixed by the growth condition:

$$\mu(TiO_2) = \mu_{Ti} + 2\mu_O \qquad 4.3$$

Under extreme O-rich condition, it is assumed that the O within the TiO_2 crystal lattice is in equilibrium with the O_2 gas molecule, and thus, its chemical potential can be determined by the energy of the triplet ground state O_2 gas molecule (i.e., $\mu_O = \frac{\mu(O_2)}{2}$). Meanwhile, Ti's chemical potential is fixed by Equation (4.3)[191,196].

Based on the formula below[191], the chemical potentials for metals (μ_M) are defined and computed:

$$\mu_M = (\mu_{M_mO_n} - n\mu_O)/m \qquad 4.4$$

Where, $\mu_{M_mO_n}$ is the most stable dopant oxide's ground state energy (at ambient temperature). For example, when dealing with a Zn doping at TiO_2 crystal lattice, a fixed value for the chemical potential of Zn atom (μ_{Zn}) is employed, which is obtained at the point where the formation energy of Zn_2O_2 is equal to zero using the formula (4.4)[191,197–199].

In this chapter, the formation energies (E_{form}) for the doped and co-doped models are determined under the O-rich condition and are shown in Table 4.3. Systems of La-doping and Zn-La co-doping have negative and lower formation energies than those of Zn-doping (see Table 4.3). It means that it is energetically much more favourable to substitute Ti with La ion than with Zn ions under O-rich growth conditions. The $Ti_{15}La_1O_{32}$ system has better stability and the $Ti_{13}Zn_3O_{32}$ system has worse stability compared with the $Ti_{12}Zn_3La_1O_{32}$ system.

4.3.5. Charge density

In Figures 4.6c and d, the contour of charge density is plotted on a plane that contains O–Zn–O bonds and their nearest-neighbouring atoms La and Ti. The contour of charge density for the Zn^{2+}-La^{3+} co-doped TiO_2 (Figure 4.6c) shows that the bond length of La-O is greater than that of Ti-O and Zn-O bonds (see Table 4.6) due to the larger ionic radius of the La^{3+} ion doped at the Ti site. It indicates that the La-O bonds have weaker covalent bonds than the Zn-O and Ti-O bonds because the overlapping of La-5d states with O-2p states has less effect than the overlapping of Zn-3d and Ti-3d states with the O-2p states. Hence, the electron fields are concentrated mostly between the bonding axis of the Zn and Ti atom (such as Zn-O and Ti-O directions), with less electron density between La-O which can be seen in Figure 4.6c.

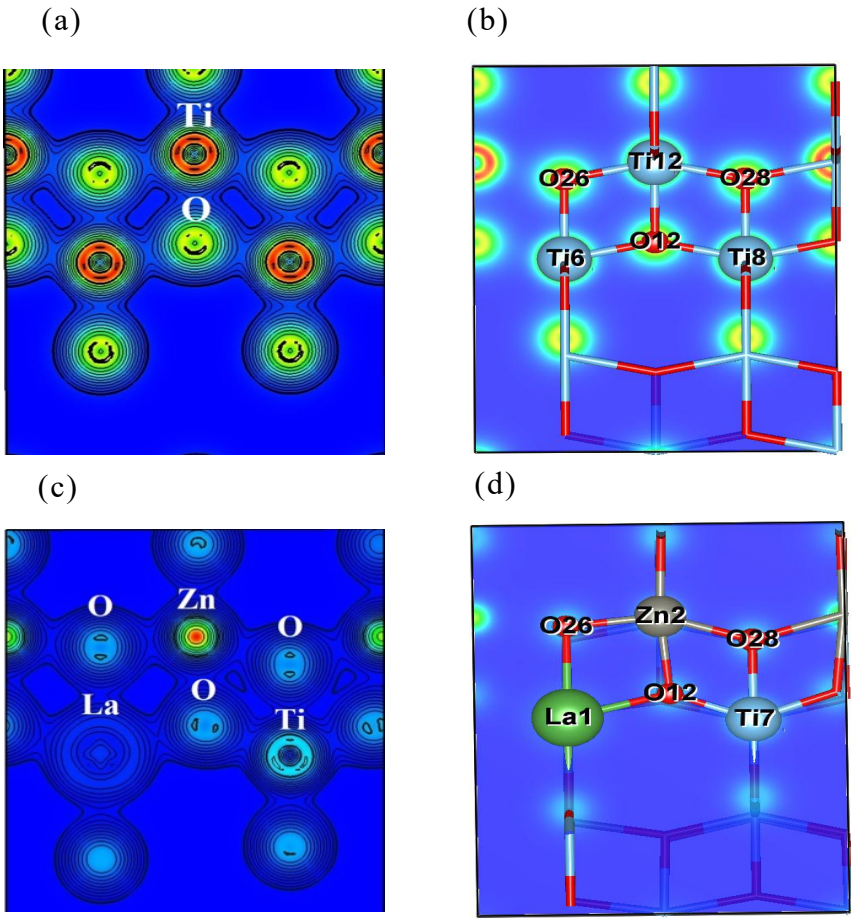

Figure 4.6: Computational modelling results of contour of charge density of pure $Ti_{16}O_{32}$ (a) and $Ti_{12}LaZn_3O_{32}$ (c), and crystal lattice structure of pure $Ti_{16}O_{32}$ (b) and $Ti_{12}LaZn_3O_{32}$ (d).

Table 4.6: Computational modelling results of bond length (Å) and volume (Å^3) of $Ti_{16}O_{32}$, $Ti_{13}Zn_3O_{32}$, $Ti_{15}LaO_{32}$and $Ti_{12}LaZn_3O_{32}$.

Bond length d_{ep} in A °	$Ti_{16}O_{32}$	$Ti_{13}Zn_3O_{32}$	$Ti_{15}LaO_{32}$	$Ti_{12}LaZn_3O_{32}$
Ti-O	1.95	1.94	1.93	1.98
Zn-O	-	1.96	-	-
La-O	-	-	2.35	-
Ti-O (O-near to La)	-	-	1.83	1.85
Ti-O (O near to Zn)	-	1.94	-	1.85
Zn-O (O-near to La)	-	-	-	1.96
La-O (O-near to Zn)	-	-	-	2.22
Volume in A °3	561.35	571.51	591.39	597.44

Furthermore, the larger ionic radius of the La^{3+} ion affects the bond lengths between Ti and O atoms (O- near La atom), reducing it and resulting in a strong chemical (covalent) bond between Ti and O atoms. The O atoms that were attached to Ti atoms are now bonded to the Zn atoms due to the orbital hybridisation of Zn-3d and O-2p states. This analysis further confirms the above discussion on PDOS of Zn^{2+}-La^{3+} co-doped TiO_2 (see section 4.3.3) that the Zn orbital states are overlapping with O orbital states in its VB.

It is to be noted that the Zn^{2+}-La^{3+} co-doped TiO_2 (Figure 4.6c, d) deforms its crystal structure relative to the pure TiO_2 (Figure 4.6a, b) due to the presence of the Zn^{2+} and La^{3+} ions. In the co-doped system, the lattice parameters are increased significantly with a volume expansion from 561.35 Å^3 of the pure TiO_2 to 597.44 Å^3 of the co-doped TiO_2, representing an increase of 6% (see Table 4.6).

4.3.6. Absorption spectrum

The optical absorption spectrum of pure, doped, and co-doped TiO_2 are computationally predicted using turboEELS code of TDDFT[187], and results are displayed in Figure 4.7, for $Ti_{16}O_{32}$, $Ti_{13}Zn_3O_{32}$, $Ti_{15}LaO_{32}$ and $Ti_{12}LaZn_3O_{32}$. The absorption edge of pure TiO_2 is approximately 380 nm, which agrees with related experimental results [200]. Moreover, Figure 4.7 reveals that there is no absorption in the visible light region for the pure TiO_2.

The absorption edge shifts towards the visible-light region when doping TiO_2 using Zn^{2+} or La^{3+} ions and co-doping the TiO_2 simultaneously using Zn^{2+} and La^{3+} ions, as shown in Figure 4.7.

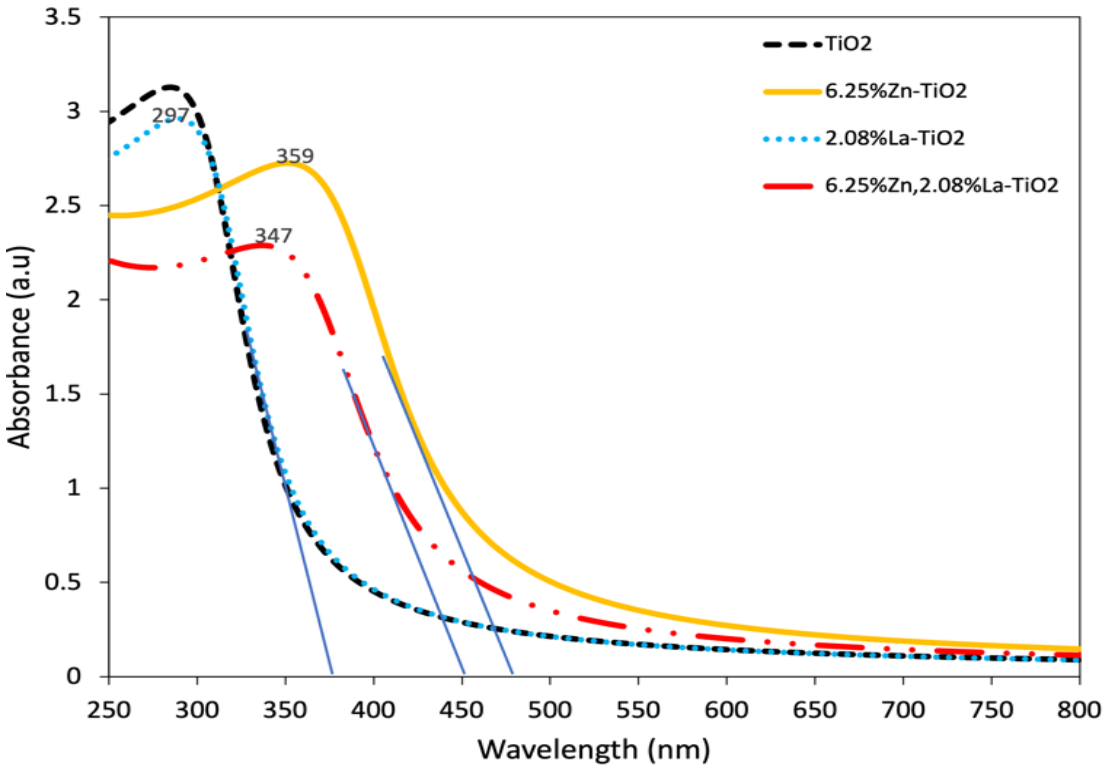

Figure 4.7: Computational results of absorption spectrum of (a) pure $Ti_{16}O_{32}$, (b) $Ti_{13}Zn_3O_{32}$, (c) $Ti_{15}LaO_{32}$ and (d) $Ti_{12}LaZn_3O_{32}$.

Regarding the TiO_2 doped with La^{3+} ion (2.08 at.% La), the absorption band edge is in the range between 380 to 400 nm, which agrees with related computational modelling results of other researchers [189], and its maximum absorption is at about 300 nm. For the Zn^{2+}-doped TiO_2 (6.25 at.% Zn), the absorption band edge is in the range between 420 nm and 580 nm, which agrees with related experimental results [201], and its maximum absorption is at 359 nm. The modelling results of Zn^{2+}-La^{3+} (6.25 at.% Zn, 2.08 at.% La) co-doped TiO_2 show a maximum absorption at 347 nm, and it has relatively active absorption activity in the region of visible light between 400 to 540 nm. It means that the Zn^{2+}-La^{3+} co-doped TiO_2 ($Ti_{12}LaZn_3O_{32}$) can harvest a wider spectrum of visible light. The electronic charge density redistribution of Zn^{2+}-La^{3+} co-doped TiO_2 could be the reason for the increase in absorption in the visible region, which is discussed in the above section

4.3.5. Figure 4.7 shows that the absorption of $Ti_{12}LaZn_3O_{32}$ progressively drops beyond 400 nm, which could be due to the intra-band transition of charge carriers in the IELs. Overall, it can be noted that the co-doped material $Ti_{12}LaZn_3O_{32}$ has better effective absorption than that of pure and La^{3+}-doped TiO_2.

4.4. Conclusions

The study aims to analyze the influence of chemical modification on the photocatalytic properties of anatase TiO_2 by doping the material using Zn^{2+} and La^{3+}. Lattice structural, electronic, charge density and optical properties of single-doped and co-doped TiO_2 with Zn^{2+} and La^{3+} were computationally predicted by using first-principles calculation based on DFT-GGA method. Additionally, the bandgap values of materials such as $Ti_{16}O_{32}$, $Ti_{15}LaO_{32}$, $Ti_{13}Zn_3O_{32}$, and $Ti_{12}LaZn_3O_{32}$ were examined using the GGA+U method to analyze the influence of U corrections on the modelling results of electronic band structure and particularly the bandgap values. The study shows that 6.25 at.% Zn^{2+} plus 2.08 at.% La^{3+} is optimum for a co-doped TiO_2. However, 6.25 at.% Zn^{2+} single-doped system turns out to be better than the co-doped system as it has the smallest bandgap among all the systems that are analysed in this chapter. As can be seen in Figure 4.7, the absorption edge for the co-doped and Zn^{2+} single-doped system is 347 nm and 359 nm respectively. The size of the bandgap of $Ti_{13}Zn_3O_{32}$ is also smaller than that of $Ti_{12}LaZn_3O_{32}$ by 0.12 eV. On the other hand, however, $Ti_{12}LaZn_3O_{32}$ (formation energy -1.342 eV) has better relative stability than $Ti_{13}Zn_3O_{32}$ (formation energy 3.317 eV).

Relative to pure TiO_2, the bandgap value of the co-doped material $Ti_{12}LaZn_3O_{32}$ (6.25 at.% Zn^{2+}, 2.08 at.% La^{3+}) is less than 12.7% . The modelling results of the electronic band structure and DOS reveal that it is easier for the oxide to migrate the photogenerated charge carriers to the CBM sites. The recombination rate can become lower due to the reduced bandgap value of $Ti_{12}LaZn_3O_{32}$, which ensures that the photocatalytic efficiencies of this system can be increased. Their VB and CB include numerous IELs, making the VBM and CBM well-dispersed. This can result in a longer lifetime of the photogenerated charge carriers. The photo-

absorption nature of the co-doped system $Ti_{12}LaZn_3O_{32}$ expands further into the region of visible light that can be seen from the optical absorption spectra analysis in Figure 4.7.

The bandgap of the pure TiO_2 can be effectively narrowed by co-doping the material using Zn^{2+} and La^{3+} ions. Overall, the DFT modelling results of this study provide a comprehensive explanation of how and why metal cation (Zn^{2+} and La^{3+}) co-doping influences the electronic properties and photocatalytic activities of the anatase TiO_2 photocatalyst.

Chapter 5:

Computational modelling of the Cu-doped bulk $CaWO_4$

5.1 Introduction

Chapter 4 presents the research on trying to enhance the photocatalytic properties of TiO_2 by co-doping it with Zn^{2+} and La^{3+} cations. The research outcomes demonstrate that such co-doping cannot achieve better photocatalytic properties of the oxide compared with single doping with Zn^{2+}. Although TiO_2 has been one of the most popular photocatalyst materials, increasingly extensive research recently has been carried out to develop other advanced photocatalysts. In particular, materials with different chemical structures, including photocatalysts having at least two different cations have been studied [70]. This has led to the increasingly wide experimental research on calcium tungstate ($CaWO_4$) by such as semiconductor physicists, as it possesses interesting structural and physicochemical characteristics[70], such as efficient luminescence, excellent optical properties [202], and high density[203] relative to other metal oxide materials [204]. As already been addressed in Chapters 1.4 and 1.5 of the thesis, the $CaWO_4$ nanoparticles exhibit low photoinduced e^--h^+ pair recombination rate, and advantageous light absorption and dispersion properties[67]. Overall, $CaWO_4$ has emerged as a novel photocatalyst in recent years with great potential for the remediation of organic pollutants.

The $CaWO_4$ is inexpensive and non-toxic[68,69]. In addition to its use as a catalyst, scheelite has garnered extensive use in multiple other fields, including the ceramics industry[205], lasers[206–208], lighting[209], medical devices[210], high-energy physics[211], and as a host for luminescent materials due to its higher chemical stability under high temperatures[212]. It is even used as a support in photographic emulsions[213]. Furthermore, scheelite is the main mineral ore utilized for extracting tungsten metal[214,215], which has an exceptionally high melting point and is commonly used in the form of filaments in light bulbs.

However, $CaWO_4$ has some limitations. For example, it has a large bandgap (around 3.9-7 eV) [216], leaving its main photocatalytic activity within the UV spectrum (e.g., having an absorption edge at 359 nm [217]). An additional challenge arises from the limited lifetime of photogenerated charges in native $CaWO_4$,

primarily attributed to its photoluminescent property[70,217], which annihilates the photogenerated charge carriers, compromising its photocatalytic performance.

Therefore, there is room to improve the photocatalytic response of $CaWO_4$, by modulating its electronic structure to generate electron-hole pairs and reduce the e^--h^+ recombination rate. The chemical modification, such as ion doping, can enhance the photocatalytic properties of $CaWO_4$ by improving the lifetime of photogenerated e^--h^+ pairs. This is achieved by decreasing the recombination rate [70,218–220] through the formation of internal strains[70]. The experimental characterisation of Zn^{2+} doped $CaWO_4$ showed absorption red-shift, energy-gap narrowing, and luminescence quenching when the Zn^{2+} concentration increases [221]. Co-doping the $CaWO_4$ with Er/Yb and Tm/Yb led to an increase in the O_2^- radicals generation of the compound [222]. The Bi-loaded $CaWO_4$ photocatalysts turned out to have more efficient charge separation and transfer as well as the absorption of visible light [223]. Moreover, the prior experimental research on Pr^{3+}-doped $CaWO_4$ [224], Ag–AgBr/$CaWO_4$ composite[107], and $Er^{3+}/Tm^{3+}/Yb^{3+}$ tridoped system ($CaWO_4$@(TiO_2/CaF_2))[225] demonstrated that the $CaWO_4$ could increase its photocatalytic performance by enhancing the photogenerated electron-hole pair separation and minimizing the recombination rate[217].

While most published research has been focused on the characterisation of electrochemical and photoluminescent properties of $CaWO_4$ using experimental methods, related underlying mechanisms are still not well-understood. Moreover, compared with research on doping with rare-earth elements, the published research on doping $CaWO_4$ with transition metals is very limited. Recently, Cu-doped materials have attracted wide interest of researchers worldwide, because Cu dopant can not only alter the valence band maxima (VBM) and conduction band minima (CBM) but also create intermediate energy levels (IELs) between them to reduce a photocatalyst's energy bandgap and electron-hole pair recombination rate [226]. Furthermore, it has been experimentally demonstrated that octahedral Cu^{2+} ions in crystal lattice structures are susceptible to a Jahn-Teller (JT) distortion that enables an electron transfer from O2p to Cu3d orbital, favouring the excitation. As a result, compounds containing Cu^{2+} cations have been reported to exhibit

better catalytic, structural, optical, and magnetic properties than the parent material without Cu^{2+} dopant[202].

Up to date, no computational modelling research has been published on the photocatalytic mechanism of $CaWO_4$ and the influence of doping with Cu^{2+} on it. Based on related computational modelling results, this chapter presents how and why the electronic and photocatalytic properties of $CaWO_4$ can be affected by doping with Cu^{2+}.

5.2 Computational methodology

The computational modelling uses the projector augmented wave (PAW) potentials [152] as implemented in the Vienna ab initio simulation package (VASP) [71] which is based on density functional theory (DFT). The generalized gradient approximation (GGA) along with Perdew-Burke-Ernzerhof (PBE) [76] exchange-correlation functional is used to predict the photocatalytic properties of undoped and Cu^{2+} ions doped $CaWO_4$. All atomic positions and lattice vectors have been optimized using a conjugate gradient algorithm to achieve an unstrained configuration. The $CaWO_4$ has a tetragonal structure with the space group of $I4_1/a$, and contains 4 calcium (Ca), 4 tungsten (W) and 16 oxygen (O) atoms in each unit cell (see Figure 5.1a). To achieve various dopant concentrations, a 2x2x2 supercell of $CaWO_4$ (see Figure 5.1b) is used which consists of 192 atoms in total (32-Ca, 32-W, and 128-O atoms). Because periodic boundary condition is employed in the a, b and c directions of the simulation domain, the supercell mimics an infinitely large bulk material. The valence electrons are referred to as $3s^23p^64s^2$ in calcium, $5p^65d^46s^2$ in tungsten, $2s^22p^4$ in oxygen, and $3p^63d^94s^2$ in copper. The periodic boundary condition is employed in the *a*, *b* and *c* directions. The following parameters of calculation are used in the geometry optimization calculations of undoped $CaWO_4$ (see Figures 5.1a and b) and its corresponding doped compounds (see Figure. S5.1 in Appendix-C5): (1) the cut-off energy 450 eV is employed in the plane-wave basis set, (2) it is determined that the Monkhorst-Pack scheme k-point mesh 5x5x3 is sufficient to achieve convergence of GGA-PBE calculations, (3) the overall energy convergence threshold is set to 10^{-6} eV, and (4) the atomic positions are

relaxed until their forces reached lesser than 0.01 eV/Å. The tetrahedron method with Blöchl corrections is used in the DOS calculation.

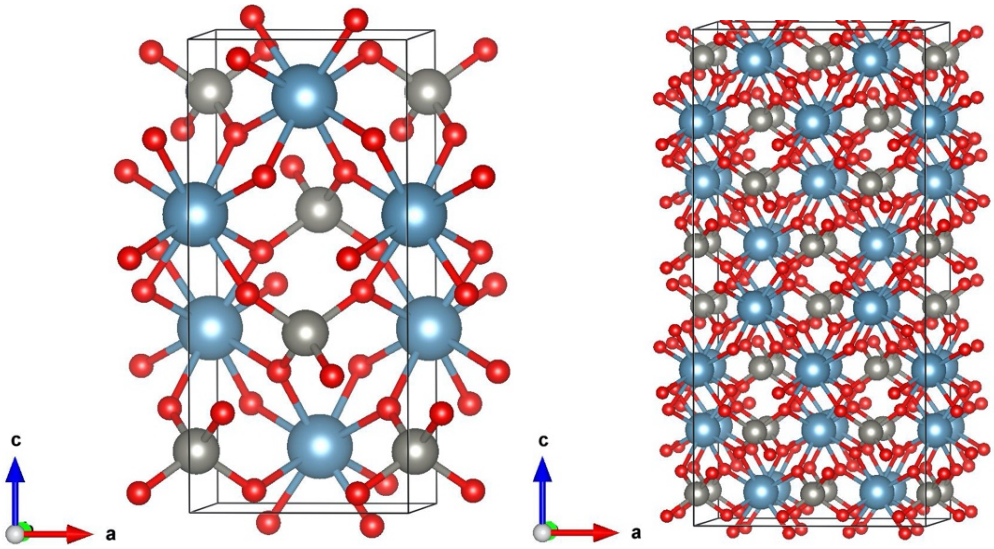

Figure 5.1: (a) Unit cell and (b) supercell (2x2x2) of pure $CaWO_4$.

5.3 Results and discussion

5.3.1 Structural properties

In this study, the lattice parameters of undoped $CaWO_4$ is determined using the Birch-Murnaghan equation of state. The optimized structure's lattice parameter is then utilized in related post-calculations and data analysis. The 2x2x2 supercell of undoped $Ca_{32}(WO_4)_{32}$ is constructed using this optimized $CaWO_4$ unit-cell and its lattice parameters are listed in Table 5.1 along with its corresponding doped systems. Doping with metal ions can change the lattice parameters of the $Ca_{32}(WO_4)_{32}$. The modelling results of the optimised latter parameters of undoped $Ca_{32}(WO_4)_{32}$ are $a = b = 5.279$ Å, $c = 11.474$ Å, $c/a = 2.174$ Å and volume (V) = 319.774 Å^3. They agree well with related experimental results [227]: a = b = 5.243 Å, c = 11.379 Å, $c/a = 2.17$ Å and volume (V) = 312.85 Å^3. Compared with undoped $Ca_{32}(WO_4)_{32}$, the lattice constants a and c decrease when transition metal (TM) ions with a smaller ionic radius, such as Cu^{2+}, substitute Ca atoms (see Table 5.1). The computational result of the bandgap value of the undoped $Ca_{32}(WO_4)_{32}$ is 4.07 eV. It appears that the obtained bandgap value of $Ca_{32}(WO_4)_{32}$ using PBE is underestimated in comparison to the experimental (4.94 eV[228]). Compared with the

PBE method, the HSE06 methodology is known to generate more precise results. This is because HSE06 tends to overestimate the bandgap value[108], resulting in greater accuracy [229]. However, it is important to note that the PBE method requires significantly less computational cost compared to HSE06.

Table 5.1: Lattice parameters of $Ca_{32}(WO_4)_{32}$, $Ca_{31}Cu(WO_4)_{32}$, $Ca_{30}Cu_2(WO_4)_{32}$, $Ca_{28}Cu_4(WO_4)_{32}$, $Ca_{25}Cu_7(WO_4)_{32}$, and $Ca_{24}Cu_8(WO_4)_{32}$ using PBE.

Systems	Cu^{2+} doping at%	*a* (/Å)	*b* (/Å)	*c* (/Å)	*c*/*a* (/Å)	*Volume* (Å^3)
$Ca_{32}(WO_4)_{32}$	0.0	5.279	5.279	11.474	2.174	319.774
$Ca_{31}Cu(WO_4)_{32}$	3.125	5.238	5.238	11.389	2.174	312.532
$Ca_{30}Cu_2(WO_4)_{32}$	6.25	5.286	5.306	11.514	2.178	322.945
$Ca_{28}Cu_4(WO_4)_{32}$	12.5	5.207	5.171	11.254	2.161	302.892
$Ca_{25}Cu_7(WO_4)_{32}$	21.875	5.230	5.176	11.302	2.161	305.985
$Ca_{24}Cu_8(WO_4)_{32}$	25.0	5.087	5.242	11.478	2.189	305.985

On the other hand, the obtained bandgap value of 4.07 eV agrees well with earlier theoretical studies (4.09 eV [230] and 4.03 eV[109]). To determine the optimal doping concentration, 3.125, 6.25, 12.5, 21.875, and 25.0 atomic percentages (at.%) of Cu^{2+} are used to dope $Ca_{32}(WO_4)_{32}$ in the computational modelling, which accounts for the systems of $Ca_{31}Cu(WO_4)_{32}$, $Ca_{30}Cu_2(WO_4)_{32}$, $Ca_{28}Cu_4(WO_4)_{32}$, $Ca_{25}Cu_7(WO_4)_{32}$, and $Ca_{24}Cu_8(WO_4)_{32}$, respectively. For the system of $Ca_{30}Cu_2(WO_4)_{32}$, i.e. replacing two Ca atoms using Cu^{2+} cations in the supercell (6.25 at.%), different sites of the Ca atoms are tested to find the optimal Ca-site for the Cu^{2+} substitution. For the higher concentrations of Cu^{2+} dopant, the aggregation doping strategy is used to select the Ca sites to be substituted by Cu^{2+} ions [229].

The doping of Cu^{2+} ions regulate the non-stoichiometry of $Ca_{32}(WO_4)_{32}$. The lattice volume and axis ratio (*c*/*a*) of $Ca_{32}(WO_4)_{32}$ and $Ca_{32-x}Cu_x(WO_4)_{32}$ system are shown in Figure 5.2 as a function of the dopant concentration of Cu^{2+}.

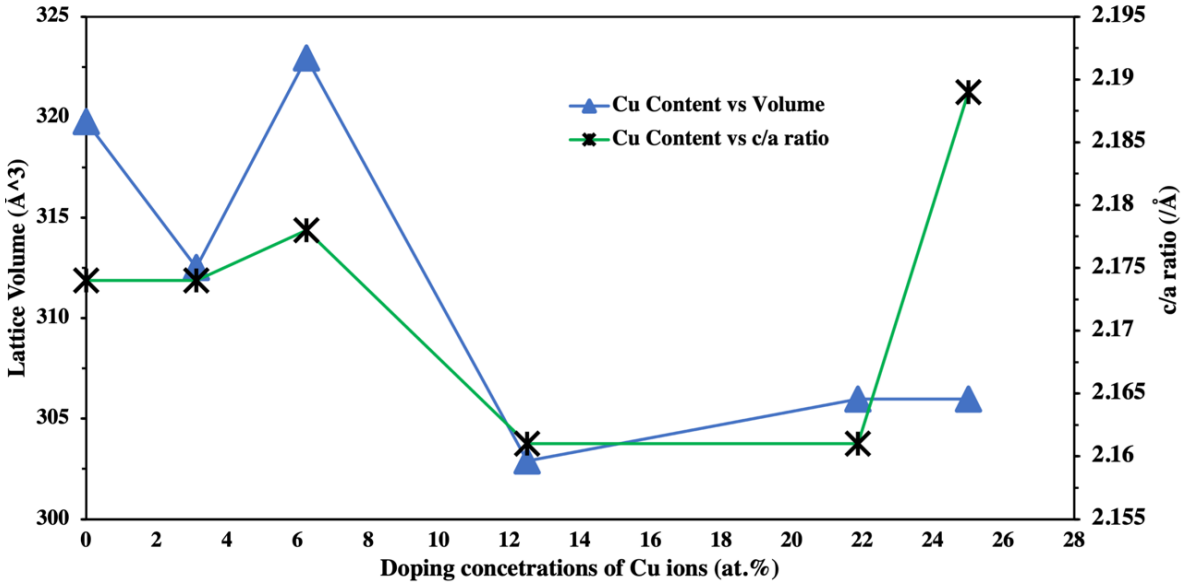

Figure 5.2: Lattice volume (Å^3) and axis ratio of c/a (Å) as a function of dopant concentrations of Cu^{2+} ions.

The lattice contraction happens while increasing the doping concentrations of Cu^{2+} ions from 0 to 12.5 at.%, which is reflected by a drop in the lattice volume. The lattice volume increases when the doping concentration increases further to 21.875 and 25 at.%. In the meanwhile, the *c*/*a* axis ratio remains relatively constant between 2.16 and 2.175 when the Cu^{2+} doping concentration increases from zero to 21.875 at.%, demonstrating the isotropic nature of the lattice contraction. Since high pressure usually results in lattice contraction, the bulk $Ca_{32}(WO_4)_{32}$'s high-pressure behaviour can be used to explain why the non-stoichiometry reveals isotropic lattice contraction [221]. The optimised structure of the $Ca_{32}(WO_4)_{32}$ with different doping concentrations of Cu^{2+} is shown in Figure. S5.1 in Appendix-C5.

The primary components of scheelite-typed $Ca_{32}(WO_4)_{32}$ are rigid WO_4 tetrahedra that resemble anions and they are enclosed by charge-balancing cations [231]. These tetrahedra units of the $Ca_{32}(WO_4)_{32}$ are exceedingly rigid and stable even under high pressure [230,231], whereas the Ca-O bond length compression is mostly responsible for the unit-cell contraction [111,221,232,233]. Moreover, the reduced Ca-O bond length when replacing the larger Ca^{2+} ions ($r_{Ca^{2+}}$ = 1.12 Å) by smaller Cu^{2+} ions ($r_{Cu^{2+}}$ = 0.73 Å) may cause the lattice to contract. In the presence of Cu dopants, distortion

of the lattice is expected, leading to strong bonding between numerous WO_4^{2-} units and Cu^{2+} as well as Ca^{2+}. This is likely to result in lattice shrinkage.

On the other hand, the cluster [CaO_8] is made up of Ca coupled with eight nearby oxygen atoms, which connects to the eight WO_4 tetragonal clusters in different orientations, including along the *a* and *c* directions. Ca^{2+} replacement with Cu^{2+} would shift the entire WO_4 unit in the direction of the initial Ca^{2+} site because of the physical rigidity of WO_4. This shift could be homogeneously contributed to the change of the *a*- and *c*- axis length of the lattice, which accounts for the constant *c*/*a* axis ratio of the different systems when the Cu^{2+} doping concentration changes between 0 and 21.875 at.%. At a composition of 25.0 at.%, the *c*/*a* axis ratio undergoes a significant increase (see Figure 5.2), suggesting that the shift is mainly concentrated in the *c* (as well as *b*) axis compared to the *a*-axis.

5.3.2 Absorption spectrum

On one hand, the $Ca_{32-x}Cu_x(WO_4)_{32}$ systems exhibit transparency in the visible spectrum. On the other hand, $Ca_{32-x}Cu_x(WO_4)_{32}$ systems show very significant band-to-band transmission in the UV region. Figure 5.3 shows that their absorption edge moves towards the greater wavelength as the Cu^{2+} doping concentration increases.

Since the optical transition of some $Ca_{32-x}Cu_x(WO_4)_{32}$ systems show an indirect type, the bandgap energy of the systems could not be estimated from the absorption edge. The $Ca_{32-x}Cu_x(WO_4)_{32}$ system has a strong red-shift as the Cu^{2+} concentration increases from 0 to 25 at.% which can be seen in Figure 5.3. Nonetheless, an intriguing deviation in the absorption peak behaviour has emerged, particularly notable in the case of $Ca_{30}Cu_2(WO_4)_{32}$ (with a Cu dopant concentration of 6.26 at.%). This unique observation is attributed to the absence of the Hubbard U correction in the calculations, which typically plays a pivotal role in dispersing the electron density among the atoms, thus influencing the material's both electronic and optical properties.

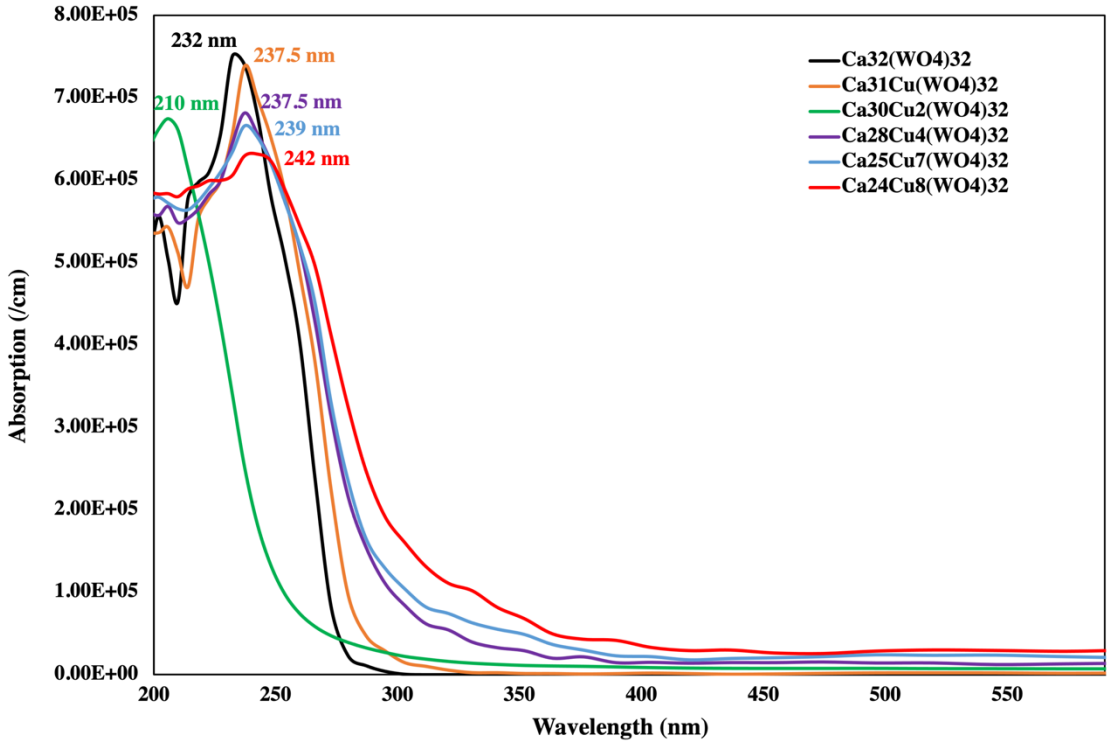

Figure 5.3: Absorption spectra of $Ca_{32}(WO_4)_{32}$, $Ca_{31}Cu(WO_4)_{32}$, $Ca_{30}Cu_2(WO_4)_{32}$, $Ca_{28}Cu_4(WO_4)_{32}$, $Ca_{25}Cu_7(WO_4)_{32}$ and $Ca_{24}Cu_8(WO_4)_{32}$.

In this perspective, the high concentrations of Cu^{2+} are most likely responsible for the red-shift of the absorption edge. The red shift in the absorption spectrum results from the narrowing of the bandgap in doped systems. The ionic radius of the Cu^{2+} ($r_{Cu^{2+}}$ = 0.73 Å[234]) is substantially less than that of the Ca^{2+} ($r_{Ca^{2+}}$ = 1.12 Å[108]). The following section provides a systematic analysis of how the electronic band structure of the $Ca_{32}(WO_4)_{32}$ system is influenced by various levels of Cu-doping concentration.

5.3.3 Electronic band structures

It is widely known that $Ca_{32}(WO_4)_{32}$ can be considered an insulating material or wide-bandgap semiconductor. The photocatalytic abilities of a compound like scheelite $CaWO_4$ is directly influenced by the size of the electronic bandgap. Figure 5.4a-f shows the electronic band structure of undoped and $Ca_{32-x}Cu_x(WO_4)_{32}$ systems. Table 5.2 displays the computational modelling results of the bandgap value of undoped and $Ca_{32-x}Cu_x(WO_4)_{32}$. The bandgap value of $Ca_{32}(WO_4)_{32}$ is 4.07

eV, and the bandgap value of $Ca_{31}Cu(WO_4)_{32}$ is 3.35 eV. A shift of the valence band maxima (VBM) and conduction band minima (CBM) resulting from the lattice distortions and the introduction of impurity energy levels (IELs) causes a reduction of the energy bandgap (E_{gap}). As the doping concentration increases, the bandgap value is 2.66, 2.35, 2.21, and 2.02 eV for the $Ca_{30}Cu_2(WO_4)_{32}$, $Ca_{28}Cu_4(WO_4)_{32}$, $Ca_{25}Cu_7(WO_4)_{32}$, and $Ca_{24}Cu_8(WO_4)_{32}$ systems, due to the formation of additional IELs within the CB, VB and bandgap of the oxides.

The direct electronic transition from the VBM to CBM is observed in the undoped $Ca_{32}(WO_4)_{32}$ at the Γ point. It is important to analyse the type of gaps for the materials with various Cu^{2+} doping concentrations as shown in Table 5.2. It can be seen that

- $Ca_{31}Cu(WO_4)_{32}$ exhibits indirect band transaction because its VBM and CBM are located at M and near Γ points, respectively.
- $Ca_{30}Cu_2(WO_4)_{32}$ exhibits direct band transaction because its VBM and CBM are located at the Γ point.
- $Ca_{28}Cu_4(WO_4)_{32}$ exhibits indirect band transaction because its VBM and CBM are located at M and near to Γ point.
- $Ca_{25}Cu_7(WO_4)_{32}$ exhibits direct band transaction because its VBM and CBM are located at the Γ point. $Ca_{24}Cu_8(WO_4)_{32}$ exhibits direct band transaction because its VBM and CBM are located at the Γ point.

The presence of distinct oxidation states of Cu atoms, such as Cu^{2+} or Cu^{+}, their abundance, and the variation in electron density between the identical oxidation states of Cu caused by the structure, may lead to a shift in the type of electron transaction as the concentration of Cu dopant increases.

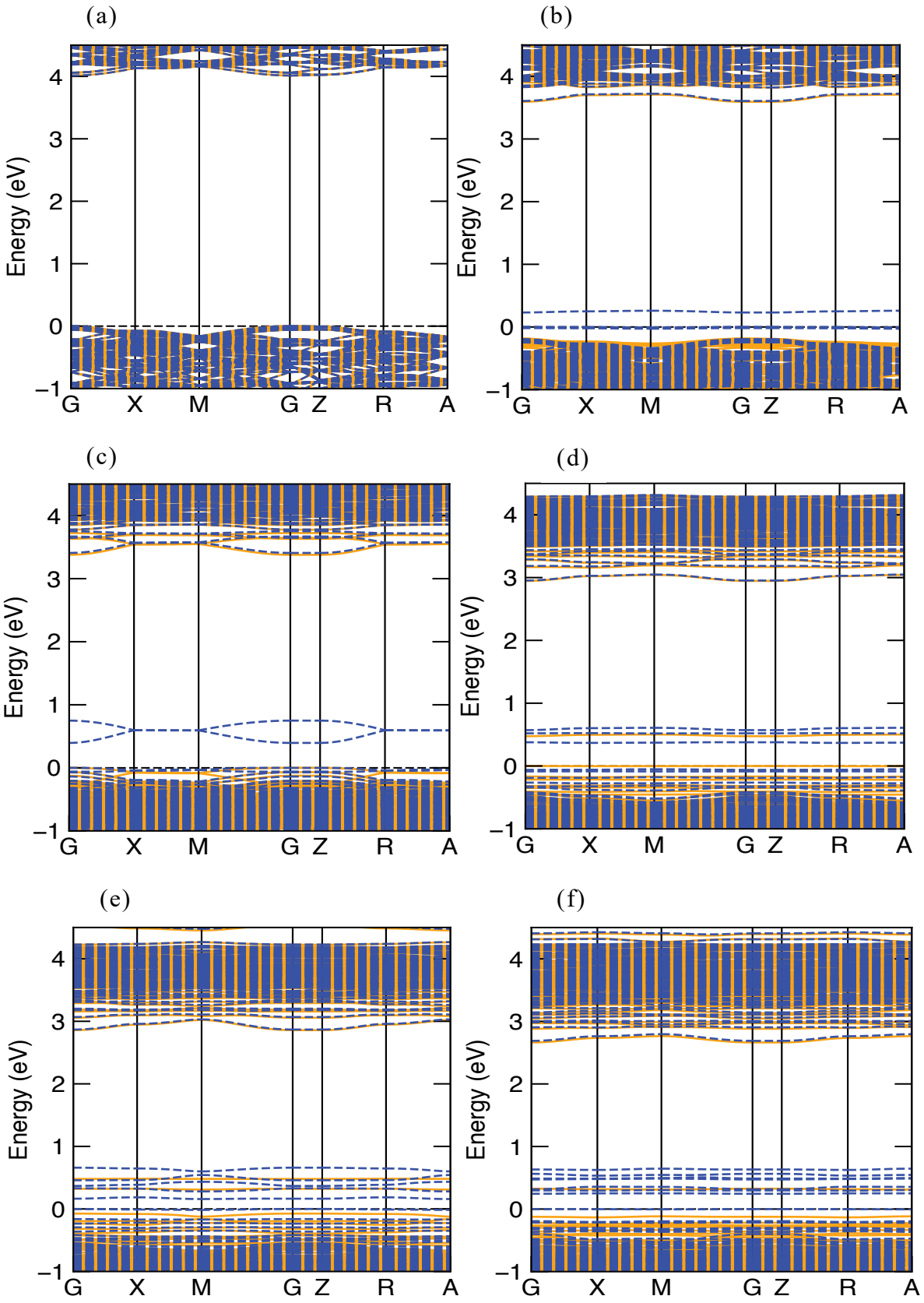

Figure 5.4: Electronic band structures of (a) $Ca_{32}(WO_4)_{32}$, (b) $Ca_{31}Cu(WO_4)_{32}$, (c) $Ca_{30}Cu_2(WO_4)_{32}$, (d) $Ca_{28}Cu_4(WO_4)_{32}$, (e) $Ca_{25}Cu_7(WO_4)_{32}$ and (f) $Ca_{24}Cu_8(WO_4)_{32}$.

The abundance of Cu-ions, either Cu^{2+} or Cu^{+}, in the $Ca_{32-x}Cu_x(WO_4)_{32}$ system may affect the electron transaction type. Indirect electron transaction occurs when the density of Cu^{2+} ions dominates the $Ca_{32-x}Cu_x(WO_4)_{32}$ system and forms either CuO or Cu_4O_3 oxide in it. Whereas, direct electron transaction occurs when the density of Cu^{+} ions dominates the $Ca_{32-x}Cu_x(WO_4)_{32}$ system and forms the Cu_2O oxide in it. In addition, earlier theoretical studies by C. Zhang et al.[229] demonstrated that varying the dopant concentration in the substitution doping procedure can cause the high symmetry point at VBM to transit from indirect to direct bandgap semiconductors.

Table 5.2: Electronic bandgap values, and the location (k-point) of valence band maxima (VBM) and conduction band minima (CBM) of undoped and $Ca_{32-x}Cu_x(WO_4)_{32}$ systems.

Materials	E_{gap} (eV)	k_{VBM}	k_{CBM}
$Ca_{32}(WO_4)_{32}$	4.07	Γ	Γ
$Ca_{31}Cu(WO_4)_{32}$	3.35	M	Γ
$Ca_{30}Cu_2(WO_4)_{32}$	2.66	Γ	Γ
$Ca_{28}Cu_4(WO_4)_{32}$	2.35	M	Γ
$Ca_{25}Cu_7(WO_4)_{32}$	2.21	Γ	Γ
$Ca_{24}Cu_8(WO_4)_{32}$	2.02	M	Γ

In Figure 5.4a, the VBM and CBM of the $Ca_{32}(WO_4)_{32}$ lie at approximately -0.03 eV and 4.02 eV. Compared to $Ca_{32}(WO_4)_{32}$,

- the $Ca_{31}Cu(WO_4)_{32}$ (Figure 5.4b) system shifts its VBM and CBM approximately from -0.03 eV to 0.26 eV and 4.02 eV to 3.61 eV, respectively.
- the $Ca_{30}Cu_2(WO_4)_{32}$ (Figure 5.4c) system shifts its VBM and CBM approximately from -0.03 eV to 0.75 eV and 4.02 eV to 3.41 eV.
- The $Ca_{28}Cu_4(WO_4)_{32}$ (Figure 5.4d) system shifts its VBM and CBM approximately from -0.03 eV to 0.6 eV and 4.02 eV to 2.95 eV.
- the $Ca_{25}Cu_7(WO_4)_{32}$ (Figure 5.4e) system shifts its VBM and CBM approximately from -0.03 eV to 0.66 eV and 4.02 eV to 2.87 eV.
- the $Ca_{24}Cu_8(WO_4)_{32}$ (Figure 5.4f) system shifts its VBM and CBM approximately from -0.03 eV to 0.14 eV and 4.02 eV to 3.09 eV.

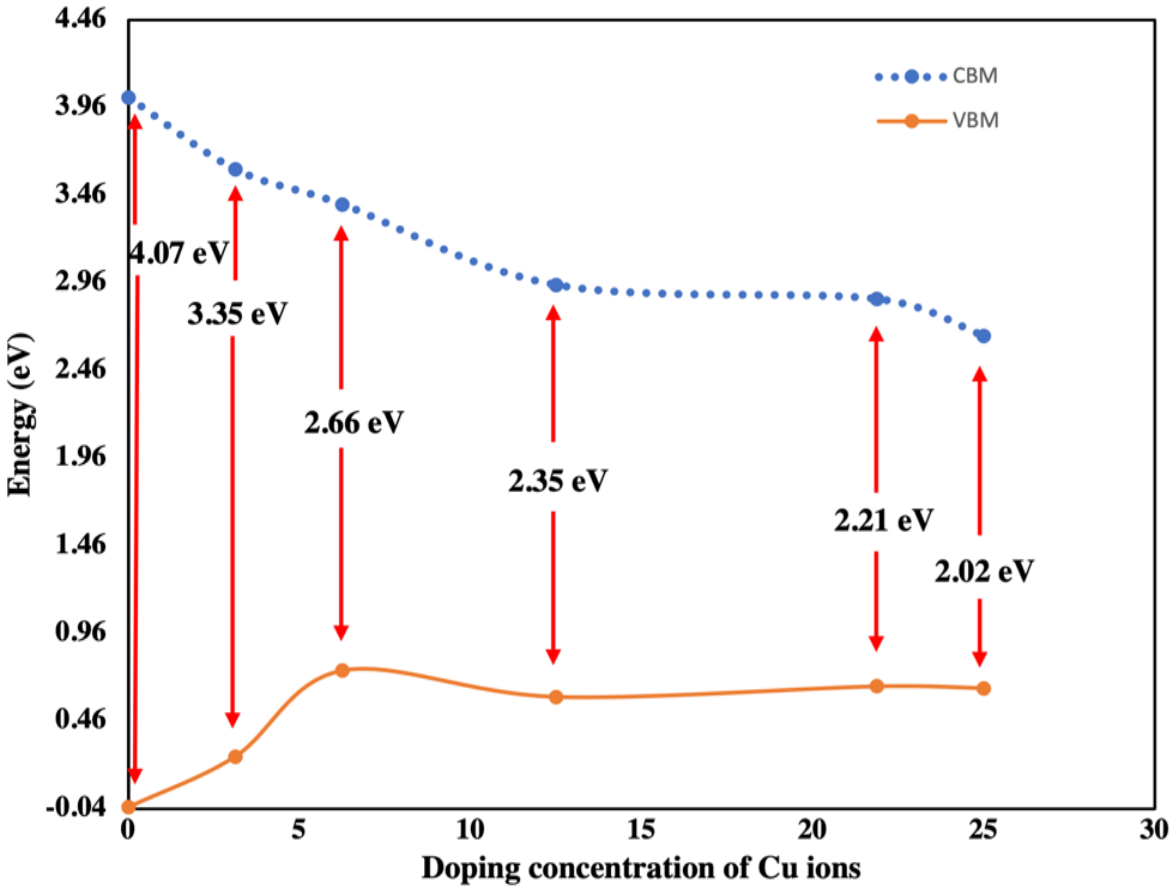

Figure 5.5: Energy vs Cu dopant's concentration

The computational modelling research of this project finds out that the IELs due to the Cu^{2+} dopants are mostly near the VBM of the oxides. As the doping concentration of Cu^{2+} increases, the CBM's position gradually moves to a lower energy level which can be seen in Figure 5.5. This behaviour affects the value of the bandgap, as the value of E_{gap} decreases in the order of: $Ca_{32}(WO_4)_{32}$ > $Ca_{31}Cu(WO_4)_{32}$ > $Ca_{30}Cu_2(WO_4)_{32}$ > $Ca_{28}Cu_4(WO_4)_{32}$ > $Ca_{25}Cu_7(WO_4)_{32}$ > $Ca_{24}Cu_8(WO_4)_{32}$. Consequently, the Fermi levels of all the Cu-doped systems shift into their VB regions due to the VBM shift resulting from the IELs and lattice distortion. Therefore, one can conclude that the n-type semiconductor nature of $Ca_{32}(WO_4)_{32}$ gets converted to the p-type semiconductor by Cu^{2+} doping.

As shown in Figure 5.6a, the computational modelling result of E_{gap} gradually decreases from 4.07 to 2.21 eV as the Cu^{2+} concentration increases from 0 to 21.875 at.%. This indicates that when dopant Cu^{2+} concentration increases, the e^--

h^+ pair separation process becomes easier to happen and the photogenerated e^--h^+ pair recombination process may decelerate.

(a)

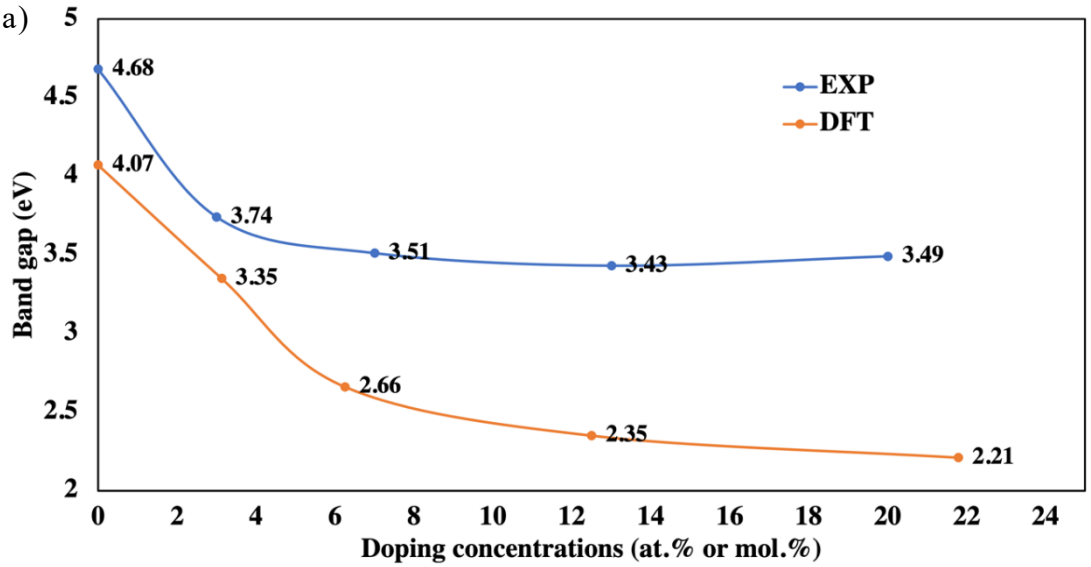

(b)

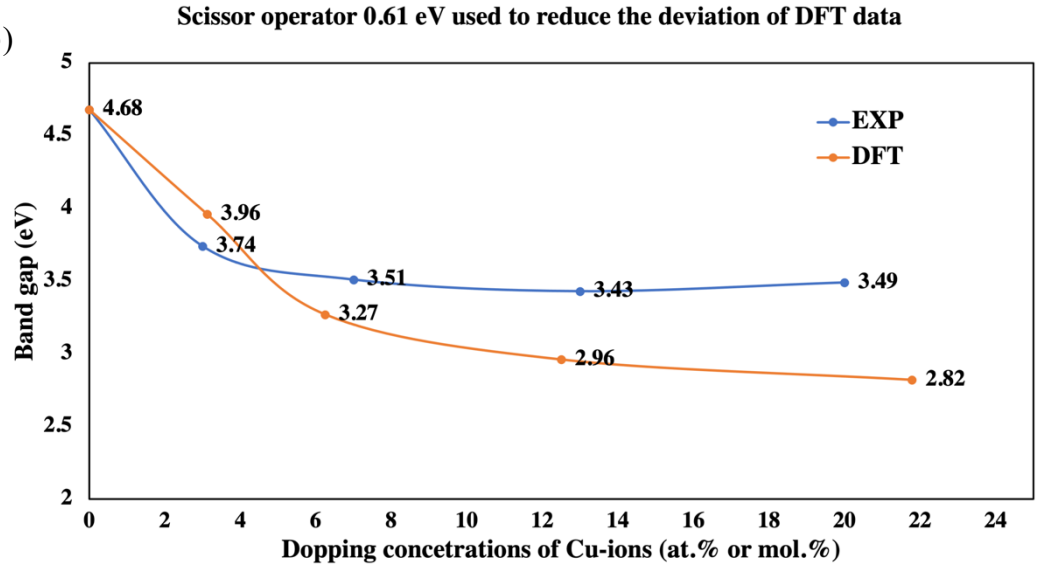

Figure 5.6: (a) Comparison of experimental and computational modelling results of the bandgap value E_{gap}, and (b) the comparison after the scissor operator of 0.61 eV is used. The experimental results were provided by Ms. Hanka Besic, Mr. Levente Nagy, Dr. Wenming Tong and Dr. Pau Farràs.

Relative to the bandgap value of $Ca_{32}(WO_4)_{32}$, the bandgap values of $Ca_{31}Cu(WO_4)_{32}$, $Ca_{30}Cu_2(WO_4)_{32}$, $Ca_{28}Cu_4(WO_4)_{32}$ and $Ca_{25}Cu_7(WO_4)_{32}$ are reduced

by 0.72, 1.41, 1.71, and 1.81 eV, respectively. The structural distortion around the WO_4 tetrahedron of $Ca_{32}(WO_4)_{32}$ crystal lattice and the IELs induced by Cu^{2+} ions in the VB and band region of the oxides result in such bandgap reduction[202].

Figure 5.6a also shows the difference between the experimental results and computational modelling results of bandgap values of the $Ca_{32}(WO_4)_{32}$ and the $Ca_{32-x}Cu_x(WO_4)_{32}$. Ms. Hanka Besic, Mr. Levente Nagy, Dr. Wenming Tong and Dr. Pau Farràs completed the material synthesis and characterisation using experimental methods as well as related data analysis.

In the realm of DFT modelling with the PBE functional, there's a consistent trend of underestimating the bandgap. To address this issue, the scissor operator[191] or rigid energy shift is employed in data analysis. This innovative method has proven highly effective, particularly for insulators and semiconductors, in fine-tuning the DFT bandgap discrepancies[235,236]. Generally, the scissor operator functions by adjusting the position of the conduction band relative to the valence band[237]. This correction mechanism demonstrates its true prowess when we possess precise experimental bandgap data for a material like $Ca_{32}(WO_4)_{32}$. In the case of pure $Ca_{32}(WO_4)_{32}$, the computational modelling yields a bandgap value of 4.07 eV, whereas the experimental result stands at 4.68 eV. To bridge this gap, the scissor operator is set at 0.61 eV.

The value of 0.61 eV is used as the scissor operator to adjust the modelling results of the bandgap values of all systems in Figure 5.6a to create Figure 5.6b. It can be seen that, in both the modelling result and the experimental results, the value of bandgap very rapidly decreases as the doping concentration of Cu cation slightly increases from zero. When the doping concentration becomes greater than approximately 4 at.%, the influence on the value of the bandgap becomes very limited.

5.3.4 Density of states

To investigate the impact of the Cu^{2+} cation doping on the electronic band structure of $Ca_{32}(WO_4)_{32}$, the density of states (DOS) analysis is used. The total density of

states (TDOS) and projected density of states (PDOS) of $Ca_{32}(WO_4)_{32}$ are shown in Figure 5.7. On one hand, the VB of $Ca_{32}(WO_4)_{32}$ is mainly dominated by O-2p orbitals with notable contribution by W-5d orbitals, and its VBM is primarily composed of O-2p (2py and 2px) orbitals. On the other hand, the first set of CB of $Ca_{32}(WO_4)_{32}$ is dominated by W-5d ($5dz^2$ and $5dx^2$) orbitals along with notable O-2p orbitals, while the second set of CB is primarily occupied by W-5dxz and W-5dyz orbitals. Of relevance, its CBM is primarily made up of W-$5dz^2$. Therefore, it reveals that local coordination plays a substantial role in the CB of $Ca_{32}(WO_4)_{32}$ which is mainly dominated by W-5d orbitals. Under light irradiation, $Ca_{32}(WO_4)_{32}$ uses photon energy to excite electrons from the O-2p (2py and 2px) orbitals to the W-5d ($5dz^2$) orbitals, where they then decay back to the O-2p orbitals.

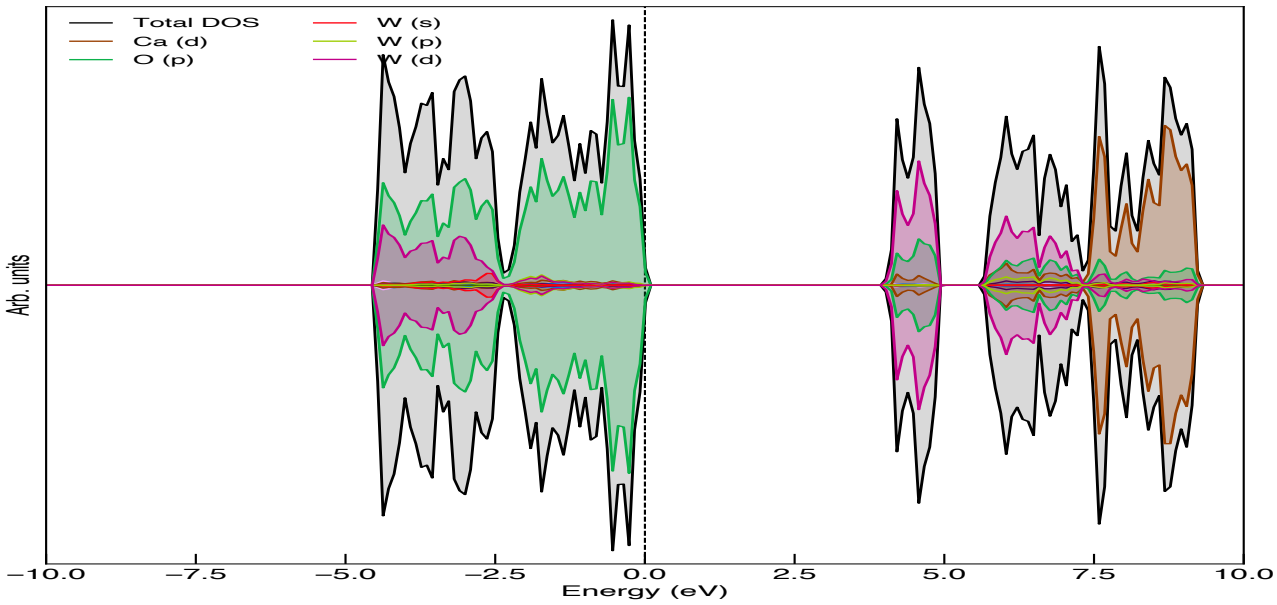

Figure 5.7: TDOS and PDOS of $CaWO_4$

Figure 5.8 shows the total density of states (TDOS) and projected density of states (PDOS) of $Ca_{32-x}Cu_x(WO_4)_{32}$ systems such as $Ca_{31}Cu(WO_4)_{32}$, $Ca_{30}Cu_2(WO_4)_{32}$, $Ca_{28}Cu_4(WO_4)_{32}$, $Ca_{25}Cu_7(WO_4)_{32}$, and $Ca_{24}Cu_8(WO_4)_{32}$.

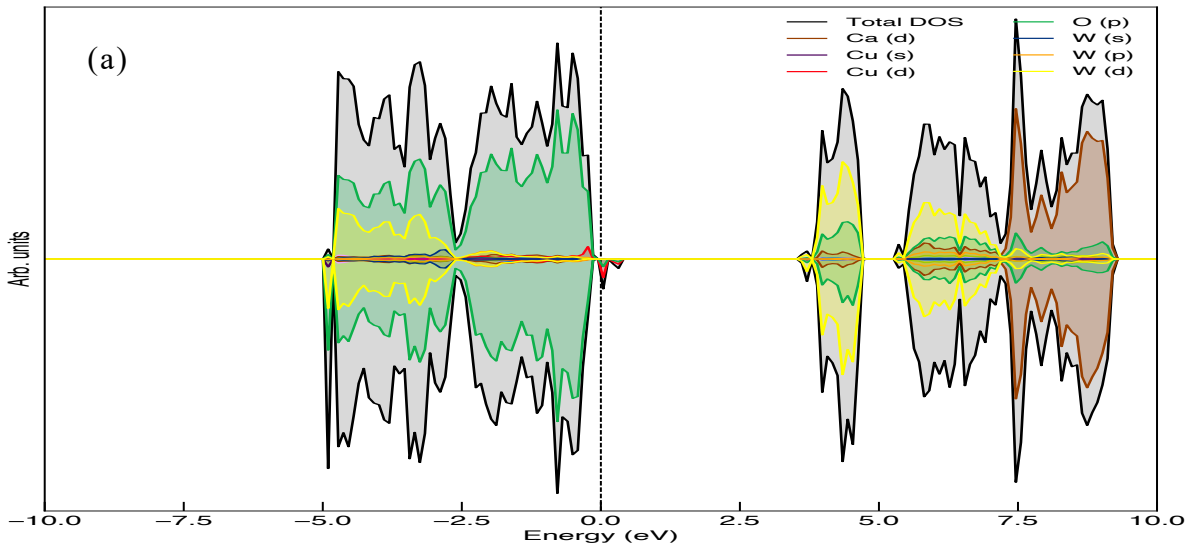
(a)
Total DOS
Ca (d)
Cu (s)
Cu (d)
O (p)
W (s)
W (p)
W (d)
Arb. units
−10.0
−7.5
−5.0
−2.5
0.0
2.5
5.0
7.5
10.0
Energy (eV)

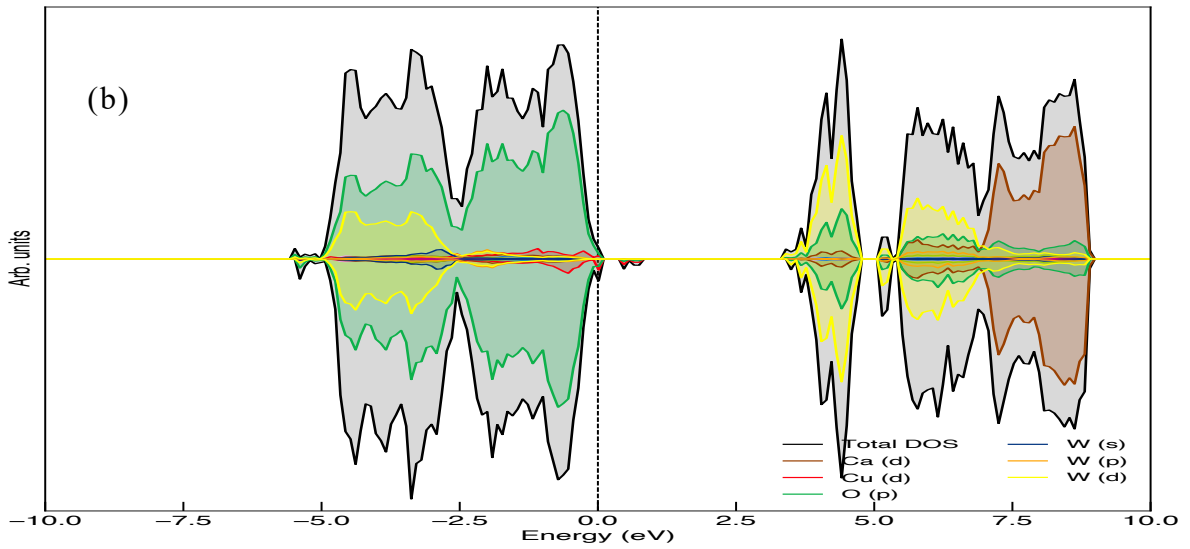
(b)
Total DOS
Ca (d)
Cu (d)
O (p)
W (s)
W (p)
W (d)
Arb. units
−10.0
−7.5
−5.0
−2.5
0.0
2.5
5.0
7.5
10.0
Energy (eV)

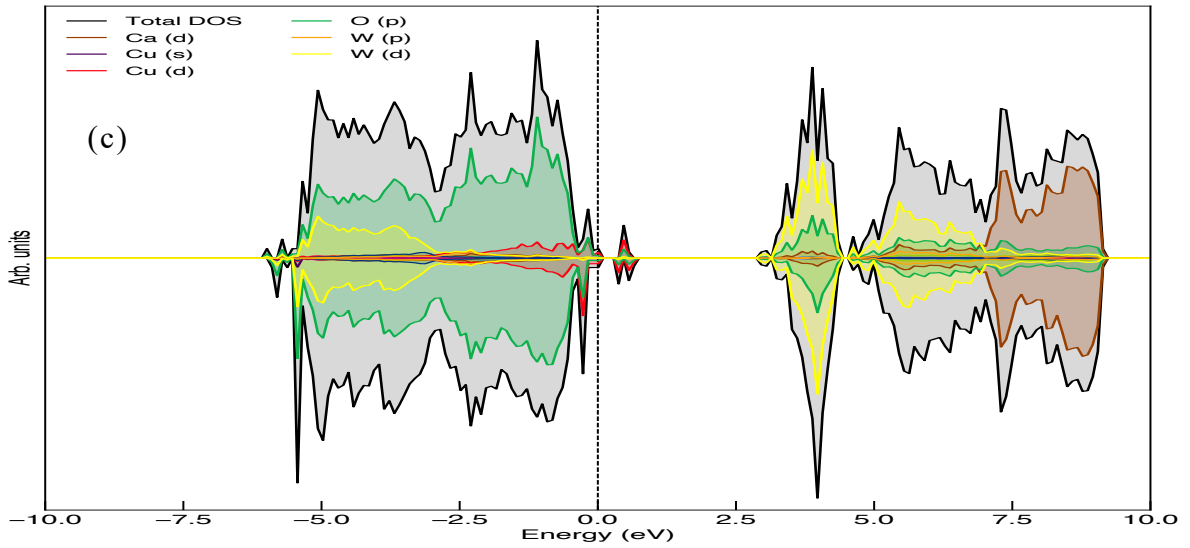
(c)
Total DOS
Ca (d)
Cu (s)
Cu (d)
O (p)
W (p)
W (d)
Arb. units
−10.0
−7.5
−5.0
−2.5
0.0
2.5
5.0
7.5
10.0
Energy (eV)

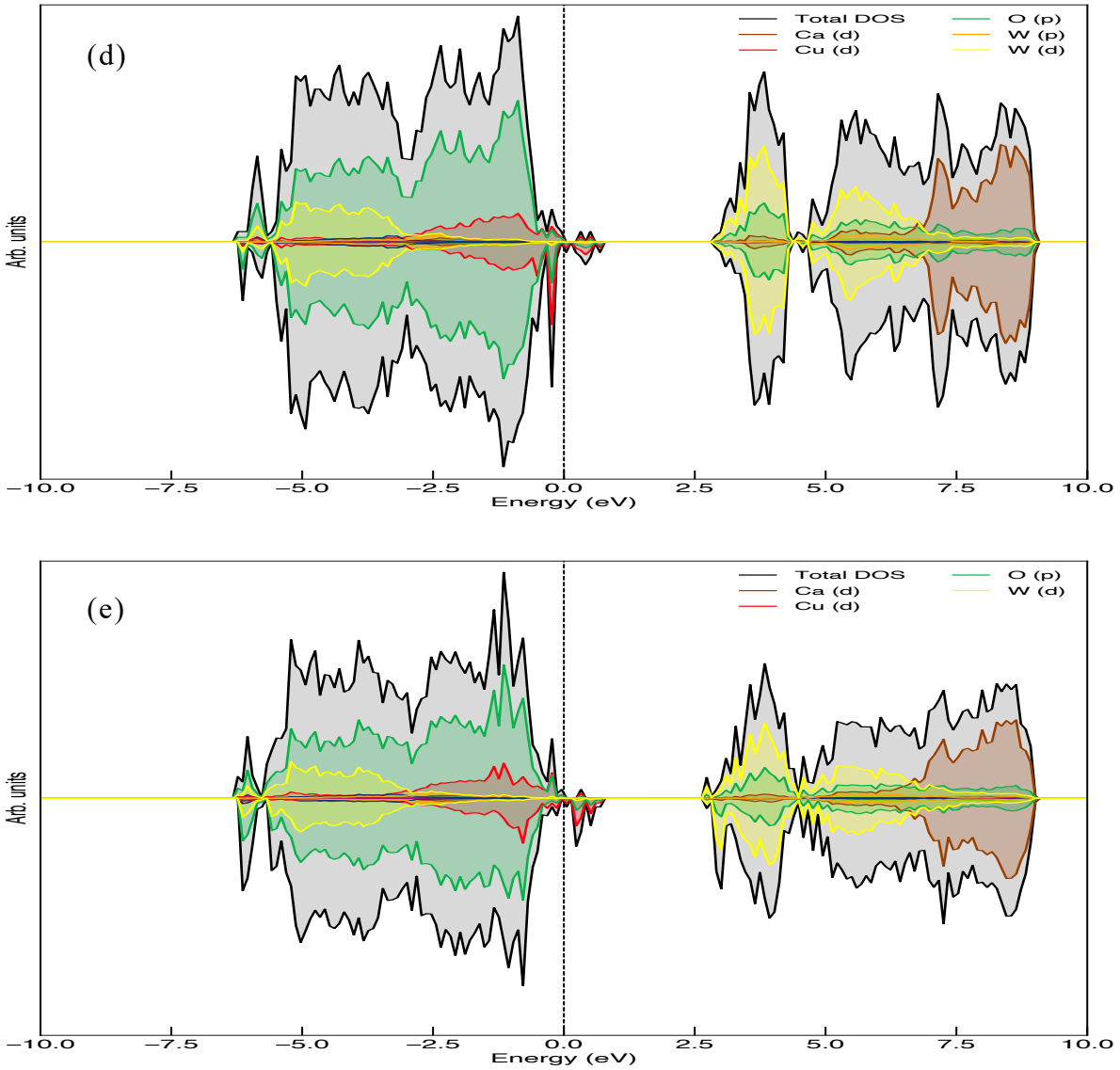

Figure 5.8: TDOS and PDOS of (a) $Ca_{31}Cu(WO_4)_{32}$, (b) $Ca_{30}Cu_2(WO_4)_{32}$, (c) $Ca_{28}Cu_4(WO_4)_{32}$, (d) $Ca_{25}Cu_7(WO_4)_{32}$, and (e) $Ca_{24}Cu_8(WO_4)_{32}$.

In Figure 5.8a, the VB of $Ca_{31}Cu(WO_4)_{32}$ is mainly dominated by O-2p orbitals along with a notable contribution from Cu-3d and W-5d orbitals. Its VBM is made up of Cu-3d orbitals that are effectively hybridised with O-2p at the Fermi level (E_f = 0 eV). Hence, there is a strong covalent bond nature between Cu and O atoms. W-5d and O-2p states dominate the CB. The bandgap of the material is reduced from 4.07 eV ($Ca_{32}(WO_4)_{32}$) to 3.35 eV ($Ca_{31}Cu(WO_4)_{32}$) by the newly formed Cu-3d energy levels which is hybridised with O-2p at the Fermi level. The $Ca_{30}Cu_2(WO_4)_{32}$, $Ca_{28}Cu_4(WO_4)_{32}$, $Ca_{25}Cu_7(WO_4)_{32}$, and $Ca_{24}Cu_8(WO_4)_{32}$ systems exhibit the same DOS characteristics as $Ca_{31}Cu(WO_4)_{32}$ regardless of the Cu-

doping concentrations. However, their VBM is located beyond the E_f (Figure 5.8b-e). Figure 5.8a-e illustrates that after the Cu ion replaces the Ca, the energy level of the Cu-3d orbital increases, and it becomes a dominant contributor to the VBM along with the O-2p orbital. In contrast, in the undoped system, the VBM is entirely dominated by the O-2p orbitals.

The bandgap value of $Ca_{30}Cu_2(WO_4)_{32}$, $Ca_{28}Cu_4(WO_4)_{32}$, $Ca_{25}Cu_7(WO_4)_{32}$, and $Ca_{24}Cu_8(WO_4)_{32}$ is lower than the bandgap value of $Ca_{32}(WO_4)_{32}$ by 2.66, 2.35, 2.21, and 2.02 eV. By comparing the DOS of the $Ca_{31}Cu(WO_4)_{32}$, $Ca_{30}Cu_2(WO_4)_{32}$, $Ca_{28}Cu_4(WO_4)_{32}$, $Ca_{25}Cu_7(WO_4)_{32}$, and $Ca_{24}Cu_8(WO_4)_{32}$ systems (see Figure 5.8a-e) with the electronic band structures of the corresponding system, as depicted in Figure 5.4b-f, it reveals that only a few energy levels emerge in the VB region of the electronic band structures as a result of the effective hybridization of the Cu-3d and O-2p orbitals, while the rest of the VBs remain relatively unaffected. One possible explanation for this phenomenon could be either a significant increase in the amount of charge transfer from Cu ions to O or a higher coordination number of Cu with nearby O atoms (i.e., Cu-O bonds can be seen in Table S5.1 of Appendix-C5). This highlights the crucial role played by the hybridization process in altering the electronic properties of the related systems. Compared to $Ca_{32}(WO_4)_{32}$, all three systems $Ca_{31}Cu(WO_4)_{32}$ and $Ca_{28}Cu_4(WO_4)_{32}$, and $Ca_{25}Cu_7(WO_4)_{32}$ exhibit a considerable reduction in bandgap.

$Ca_{25}Cu_7(WO_4)_{32}$ shows a more obvious decrease of bandgap compared to $Ca_{31}Cu(WO_4)_{32}$ and $Ca_{28}Cu_4(WO_4)_{32}$ due to a much higher density of newly formed IELs (i.e., hybridisation of Cu-3d and O-2p orbitals) in VB and bandgap regions and greater availability of empty Ca-3d and W-5d states in the CB region. As a result, $Ca_{25}Cu_7(WO_4)_{32}$ differs from the other two systems. As illustrated in Figure 5.8a-e, the majority of hybridization takes place between the 2p orbitals of O atoms and the 3d/5d states of Cu/W atoms, which are responsible for forming the VBM and CBM. Upon comparing the positions of their VBM, it becomes evident that $Ca_{24}Cu_8(WO_4)_{32}$ is situated further away from the energy level of E_f.

The compounds' VBM location moves away from their E_f when Cu-dopant concentrations rises. The position of the VBM in $Ca_{32}(WO_4)_{32}$ is at -0.03 eV. However, as the concentration of Cu dopant is gradually increased to 3.125, 6.25, 12.5, 21.875, and 25.0 at.%, the position of the VBM undergoes a significant shift, as previously discussed in detail in section 5.3.3. It proves once again that the presence of IELs at the VB and bandgap regions of all doped compounds cause changes in the locations of their VBM.

It was already found by other researchers for other materials that the amount of dopant ions affects a compound's band type besides the bandgap value[229]. The higher the concentration of Cu dopants, the greater the formation of Cu-oxides occurs through the bonding between Cu and O atoms within the lattice structure of the overall photocatalyst. Because the Cu-oxides are close to one another in the crystal lattice, there can be significant coulombic interactions between the Cu-oxides. In addition to the emergence of newly formed IELs resulting from the hybridization of Cu-3d and O-2p orbitals, the stronger interaction between Cu-oxides can also lead to a notable decrease in the bandgap value of the materials, particularly at high doping concentrations (such as $Ca_{25}Cu_7(WO_4)_{32}$ and $Ca_{24}Cu_8(WO_4)_{32}$). The energy level of the CBM, which comprises W-5d orbitals, is found to continuously decrease as the dopant concentration increases from 3.125 to 25.0 at.%. This reduction is attributed to the increased electrostatic interaction between the Cu-3d and W-5d orbitals as the Cu dopant concentration increases. As the CBM energy level decreases, it shifts towards the E_f, ultimately resulting in a decrease of the bandgap. As the concentration of Cu dopant increases, there is a gradual increase of the peak intensity of Cu-3d in the VB. Analysis of the PDOS (Figure 5.8a-e) reveals that the Cu-3d orbital's peak intensity is higher than that of O-2p orbitals at the VBM. Overall, all these findings indicate that Cu dopant has a significant impact on the VBM of the $Ca_{32-x}Cu_x(WO_4)_{32}$ system. Moreover, the VB width increases with the dopant concentration, accompanied by changes of both VBM and CBM.

5.3.5 Magnetic properties of Cu-doped systems

The magnetic moment (μ_B) of systems is analysed. $Ca_{32}(WO_4)_{32}$ is diamagnetic because its total μ_B is zero. On the other hand, the total μ_B of $Ca_{31}Cu(WO_4)_{32}$, $Ca_{30}Cu_2(WO_4)_{32}$, $Ca_{28}Cu_4(WO_4)_{32}$, $Ca_{25}Cu_7(WO_4)_{32}$, and $Ca_{24}Cu_8(WO_4)_{32}$ is 0.945, 1.867, 1.895, 2.848, and 5.709 μ_B, indicating the ferromagnetic property of the materials. In these Cu-doped systems, the magnetic properties are induced by the existence of unpaired spins of Cu^{2+} in the crystal field.

Each Cu^{2+} in a Cu-doped system makes the following contributions to the $Ca_{32-x}Cu_x(WO_4)_{32}$:

- Cu1 provides 0.608 μ_B to the $Ca_{31}Cu(WO_4)_{32}$ system;
- Cu1 and Cu2 each provide 0.605 μ_B to the $Ca_{30}Cu_2(WO_4)_{32}$ system;
- Cu1, Cu2, Cu3, and Cu4 provide -0.576, 0.612, 0.609, and 0.577 μ_B to $Ca_{28}Cu_4(WO_4)_{32}$ system;
- Cu1, Cu2, Cu3, Cu4, Cu5, Cu6 and Cu7 provide -0.571, -0.562, 0.594, 0.592, 0.598, 0.614, and 0.583 μ_B, respectively to the $Ca_{25}Cu_7(WO_4)_{32}$ system; and
- Cu1, Cu2, Cu3, Cu4, Cu5, Cu6 and Cu7 provide 0.592, 0.616, -0.581, 0.587, 0.599, 0.605, 0.620, and 0.608 μ_B, respectively to the $Ca_{24}Cu_8(WO_4)_{32}$ system.

The negative value of μ_B represents the magnetic moment contributed by spin-down electron. This finding implies that all Cu-doped derivatives exhibit magnetic properties.

Furthermore, as the concentration of Cu^{2+} cations increase in the scheelite lattice, adjacent Cu^{2+} cation sites can become occupied by electrons, leading to antiferromagnetically coupled spins. The spatial arrangement of Cu atoms in the crystal structure, as detailed in Table S5.2 (see Appendix-C5), clearly illustrates how these atoms draw closer to each other. This arrangement of proximity plays a critical role in facilitating the emergence of antiferromagnetic coupling between the spin states of the Cu atoms. As a consequence, this leads to a decrease in the value of μ_B and a reduction in the occurrence of Cu^{2+} oxidation states within the

lattice, particularly at higher doping concentrations, which is clearly shown in Figure 5.9. For example, the figure indicates that as the Cu concentration rises from 3.125 at.% to 25.0 at.%, the value of μ_B initially increases and plateaus before increasing again, reaching its maximum value of 5.709 μ_B at a doping level of 25.0 at.%. The plateau level between Cu doping concentrations of 6.25 and 12.5 at.% indicates an antiferromagnetically coupled spins behaviour. At higher doping concentrations, the Cu^{2+}-Cu^{2+} interaction becomes much more significant than the spin-orbit (LS) coupling, which can lessen the impact of the Cu^{2+} ion's orbital motion on the overall magnetic moment.

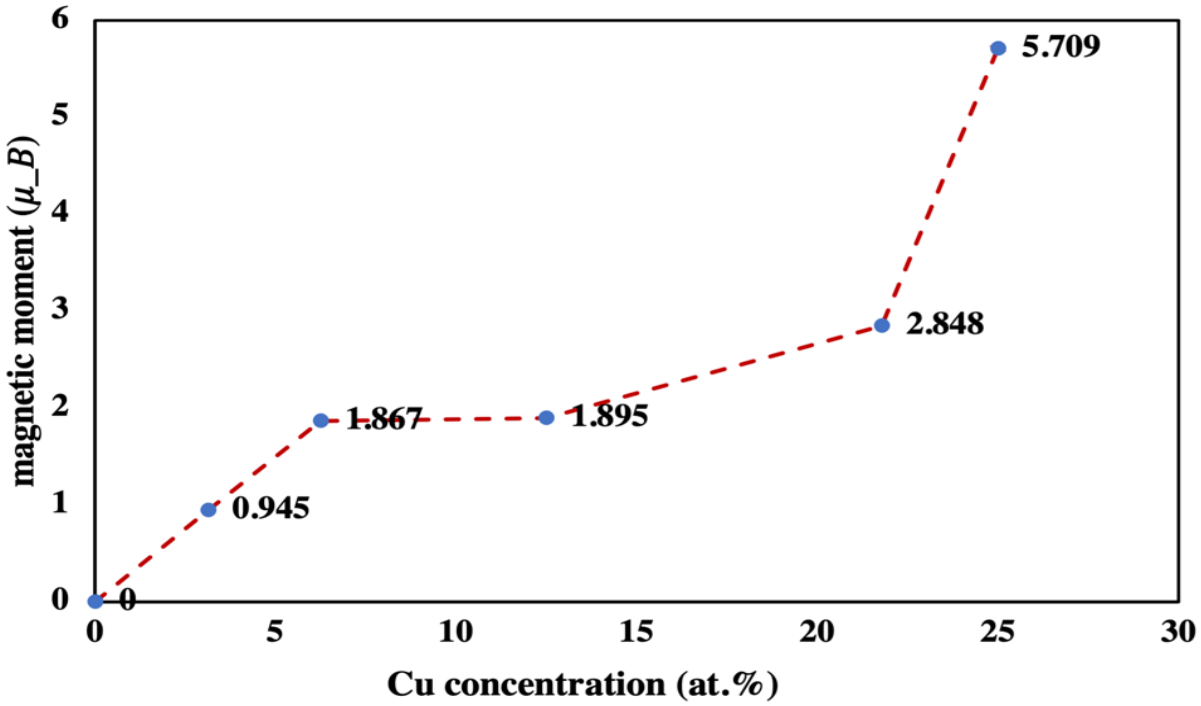

Figure 5.9: Variation of magnetic moment at various Cu doping concentrations from 0 to 25.0 at.%.

In Figure 5.10, the charge density contour plot is presented, which illustrates a significant amount of the Cu cation's electron spin density (represented by yellow colour clouds) is distributed over nearby O atoms. This distribution could potentially influence the overall magnetic moment of the supercells, along with the small magnetic moment induced by the unsaturated electrons in their O atoms. As Cu concentration increases, the hole's spin density (represented by light blue colour clouds) resulting from Cu oxidization becomes locally distributed among

the doped Cu cations (as can be seen in Fig. 5.10c-e). Such modelling results mean that there is interaction between the spins of Cu cations that are close to one another.

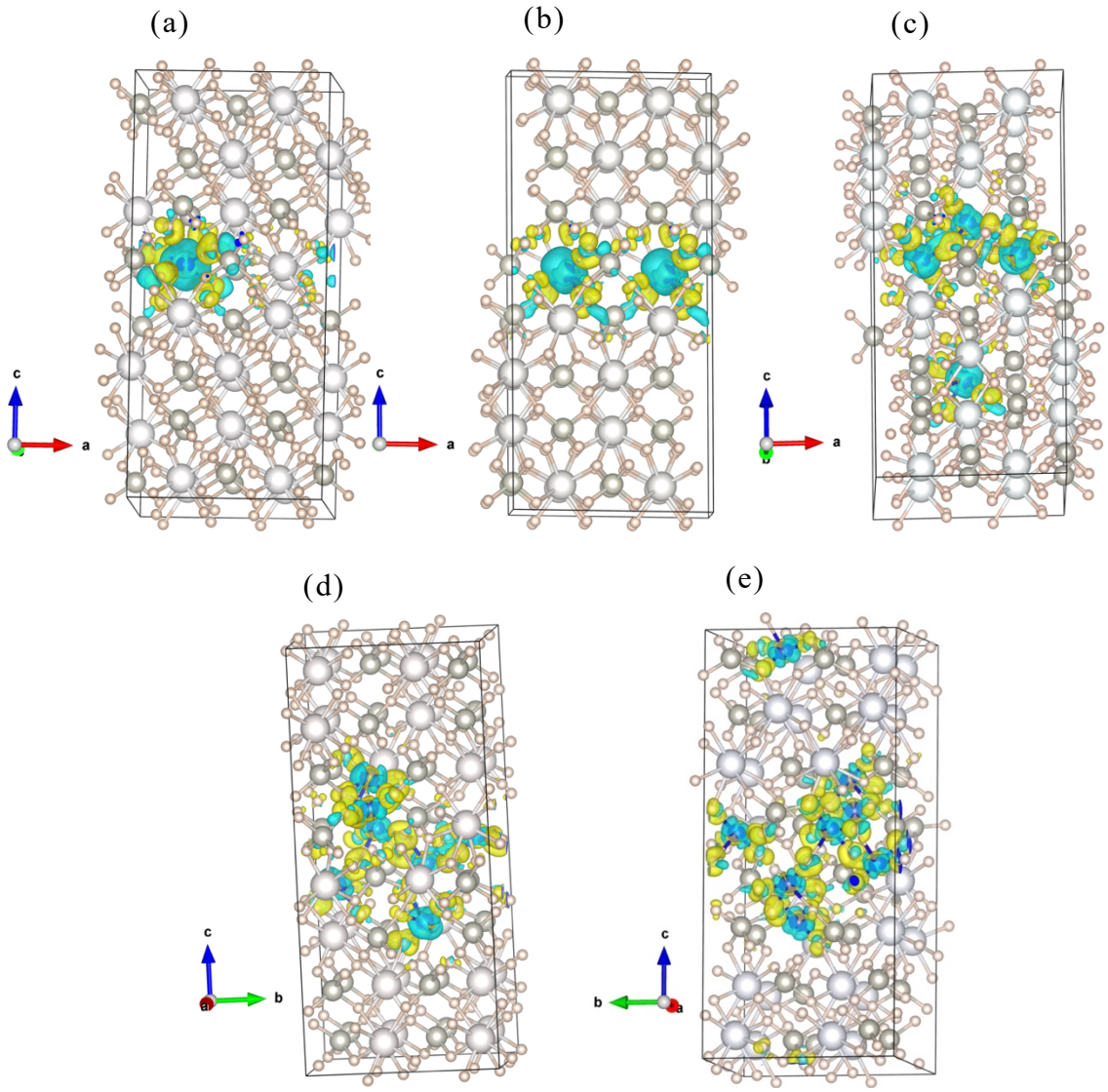

Figure 5.10: The charge density contour plot of (a) $Ca_{31}Cu(WO_4)_{32}$, (b) $Ca_{30}Cu_2(WO_4)_{32}$, (c) $Ca_{28}Cu_4(WO_4)_{32}$, (d) $Ca_{25}Cu_7(WO_4)_{32}$ and (e) $Ca_{24}Cu_8(WO_4)_{32}$

5.4 Conclusion

The computational modelling results of this chapter systematically characterise how the structural, electronic and magnetic properties of the bulk $Ca_{32}(WO_4)_{32}$ are influenced by doing the oxide using various levels of Cu concentration, between

0.0 and 25.0 at.%. It is found that there can be a transition between indirect bandgap semiconductors and direct bandgap semiconductors depending on the Cu doping concentration. For example, as Cu doping increases from 0 to 3.125, 6.25, 12.5, 21.875, and 25.0 at.%, the $Ca_{32-x}Cu_x(WO_4)_{32}$ band type transits from direct band type to indirect, direct, indirect, direct, and indirect band type.

The electronic energy level of the W-5d orbitals has a greater influence on the CBM, making it move closer to the VBM as the concentration of Cu cations rises, whereas the electronic energy level of the Cu-3d orbitals moves to higher levels and the VBM moves towards higher energies. It is evident that the Cu-W interaction is stronger than the Cu-Ca interaction in the $Ca_{32-x}Cu_x(WO_4)_{32}$. It is worth noting that the dopant concentration is also an important factor affecting the alteration of the bandgap. As Cu concentration increases from 0 to 25.0 at.%, the bandgap value of $Ca_{32-x}Cu_x(WO_4)_{32}$ decreases from 4.07 to 3.35, 2.66, 2.35, 2.21, and 2.02 eV for the $Ca_{31}Cu(WO_4)_{32}$, $Ca_{30}Cu_2(WO_4)_{32}$, $Ca_{28}Cu_4(WO_4)_{32}$, $Ca_{25}Cu_7(WO_4)_{32}$, and $Ca_{24}Cu_8(WO_4)_{32}$ systems due to the formation of additional IELs in the VB and bandgap region as well as stronger interaction between Cu-3d and W-5d orbitals. As a result, the absorption edge of $Ca_{32-x}Cu_x(WO_4)_{32}$ is red-shifted towards a greater wavelength as the Cu^{2+} concentration increases from 0 to 25.0 at.%. The volume and bond length of undoped $Ca_{32-x}Cu_x(WO_4)_{32}$ are altered because Cu^{2+} cations have a much smaller ionic radius ($r_{Cu^{2+}}$ = 0.73 Å) than Ca^{2+} ($r_{Ca^{2+}}$ = 1.12 Å). Therefore, Cu^{2+} changes the electronic band structure and of the $Ca_{32}(WO_4)_{32}$.

Chapter 6:

Computational prediction of electronic and photocatalytic properties of $CaWO_4$ thin film and its surface doping with Cu-ion

6.1 Introduction

The contents of Chapter 5 focus on exploring the underlying mechanisms of the photocatalytic properties of bulk $CaWO_4$ when subjected to chemical modification by doping with Cu ions. The modelling results reveal valuable insights into the material's structural, electronic, and optical properties, offering a deeper understanding of the fundamental mechanisms of its photocatalytic behaviour. In Chapter 5, because the periodic boundary condition is employed in all three directions (i.e., the direction of *x*, *y*, and *z*) of the simulation domain, the supercell actually mimics the infinitely large bulk material of the related oxides.

When trying to analyse the interaction between the photocatalysts and organic wastes, the photocatalysts can no longer be assumed to be infinitely large materials because the reactions happen on the surface of the photocatalysts. To obtain a good comprehension of the surface reactions, it is very convenient to assume the photocatalyst is a thin film in computational modelling. Thin films of photocatalysts have high surface area-to-volume ratios[238–240], which significantly enhances the reactivity for photocatalytic applications. Furthermore, the utilization of thin film modelling offers a valuable approach to investigating surface reactions in nano and microparticles.

Thin film catalysts provide several advantages over powder catalysts, including reduced material costs, lower physical damage, and easier recyclability or recollection after the degradation process. Their durability, easy integration into devices, ability to modify material properties, and potential for miniaturization make them increasingly popular in related applications. Numerous researchers have published research on the synthesis of thin film catalysts, which have wide applications in such as solar cells, sensors, metal oxide coatings, solid oxide fuel cells, optoelectronics, gas sensing, self-cleaning surfaces, supercapacitors, antireflective coatings, dielectric applications, biomedical devices, photovoltaics, photocatalysis, and other energy-related technologies[241–248]. It has been found that metal oxide (such as TiO_2, ZnO, CdO, CuO, Fe_2O_3, WO_3, $BiVO_4$, Bi_2WO_6, etc.) and metal sulfide (e.g., ZnS and CdS) thin films have great potential for the

photodegradation of organic compounds[1,10,25,69]. Moreover, the use of chemical modification techniques has shown promise in enhancing their performance under visible light sources[25,249]. Table 6.1 provides a comprehensive list of thin film materials and their photodegradation efficiency on organic pollutants. Semiconducting thin films, in particular, show great potential for organic water treatment and offer improved device efficiency and cost reduction.

Table 6.1: The effectiveness of different metal oxide and metal sulfide thin films in photocatalysis.

Study	Thin film material	Chemical modification in thin film	Model pollutants	Degradation rate (%)	Irradiation source
Experimental Characterisation	TiO_2 [250]	-	Phenol	33.85	UV
	Bi_2WO_6 [251]	-	RhB	100	UV-Vis
	ZnS[252]	-	MB	92	UV-Vis
	$BiVO_4$ [253]	-	MB	97	Visible
	CdS [254]	-	MB	89	UV-Vis
	WO_3 [255]	-	MB	88.5	Visible
	TiO_2 [256]	N-doped	MB	89	Visible
	ZnO [257]	Co-doped	crystal violet	90	UV
	CuO/ZnO[258]	Heterojunction	MB	84	UV-Vis
	SiO_2 [259]	ZnO-doped	MB	60	UV
	Fe_2O_3 [260]	Au-doped	Salicylic acid	60	Visible
	$BiVO_4$ [261]	Si-doped	Phenol	69	Visible
	Bi_2O_3 [262]	Cu-doped	RhB	96	UV-Vis
	Bi_2O_3 [263]	Fe-doped	RhB	98	Visible
	WO_3/TiO_2[264]	Composite	Oxalic acid	83	Visible
	WO_3/ZnO[265]	Composite	Phthalic acid	63.63	Visible

Before computational modelling is employed to characterise the reactions of organic molecules on the surface of photocatalysts, the properties of the photocatalyst thin films without organic molecules need to be computationally predicted. Chapter 6 presents the computational modelling of the pure and Cu-doped $CaWO_4$ thin films, which is focused on predicting the electronic and photocatalytic properties of the materials and interpreting related underlying mechanisms.

6.2 Computational methodology

The structural and electronic properties of the pure and doped $CaWO_4$ thin films are characterised using spin-polarized[266] DFT-D3 (Grimme) [267,268] computations embraced in the Vienna Ab-initio Simulation Package (VASP)[71]. The GGA-PBE approach[76] is used to establish the exchange and correlation (XC) potential, and the PAW method[152] is used to define the electron wave functions and pseudopotentials for the electron-ion interaction. In the self-consistency field (SCF), the energy threshold is set to $1x10^{-6}$ eV per atom, and the force threshold is -0.01meV/Å with 0.05 eV of Gaussian smearing. The expansion of Kohn-Sham wave functions in plane waves was performed up to an energy cut-off of 450 eV.

Using the Atomic Simulation Environment (ASE), the repetitive slab approach is employed to design two-dimensional translational symmetric[269,270] $CaWO_4$ thin films. The slab model utilized in this study consists of four layers of (101) facet (where facet is a primitive cell of $CaWO_4$ with a 101-surface exposed) with Ca-termination, where the bottom two layers are held fixed and the top two layers are left unconstrained as depicted in Figure 6.1a. As shown in Figure 6.1b, a $CaWO_4$ slab is sandwiched between two layers of vacuum. The periodic boundary condition is only employed in the a and b directions. Therefore, such simulation domain mimics an infinitely large thin film of the photocatalyst, the surface of which is the (101) plane.

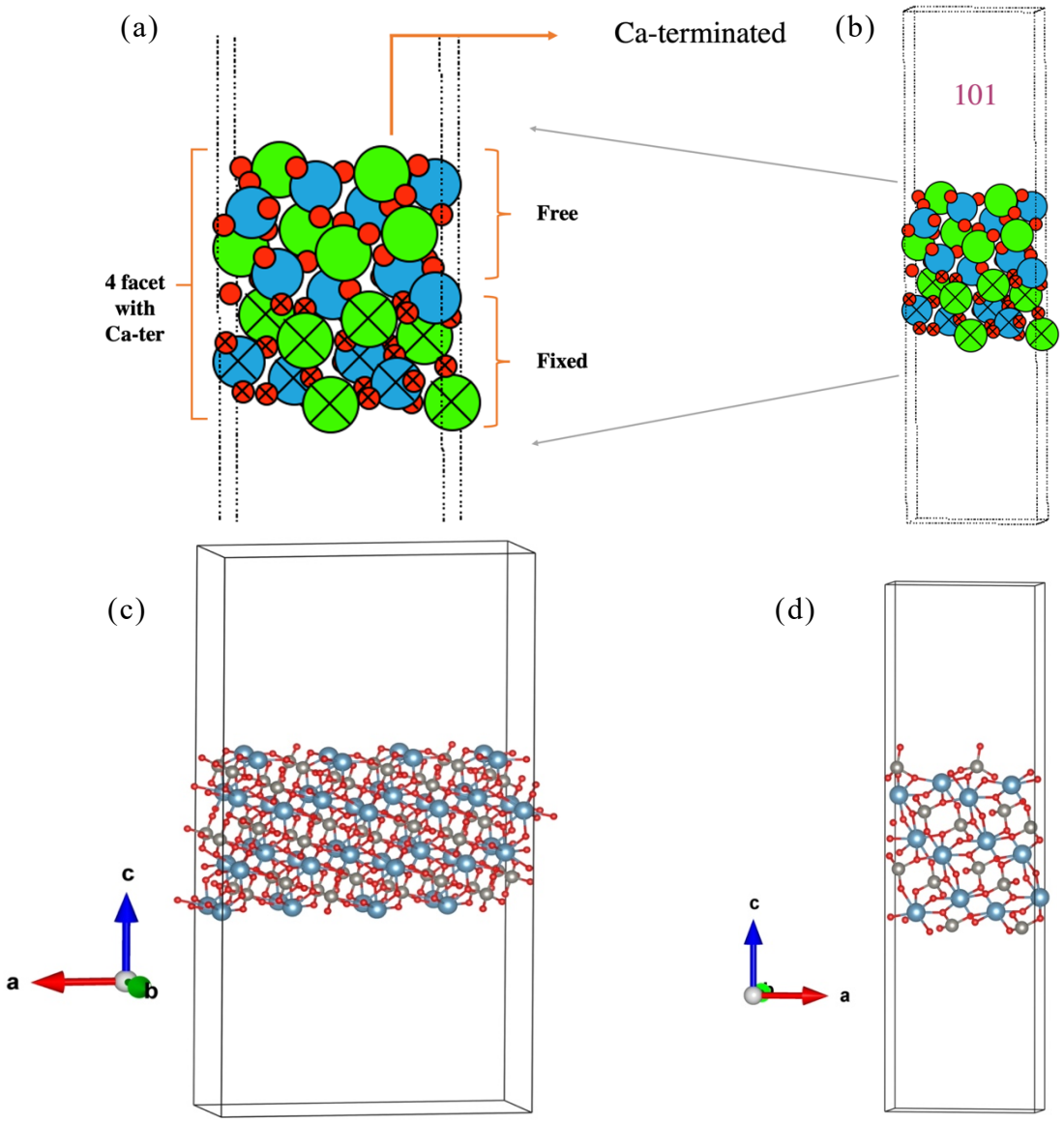

Figure 6.1: Setup of the simulation domain: (a) and (b) are the Ca-terminated $CaWO_4$ slab models with four layers of (101) facet, (c) is $2a \times 2b$ supercell of $CaWO_4$ thin film, and (d) is the W-terminated $CaWO_4$ slab models with three layers of (101) facet.

The dimensions of the photocatalyst slab (i.e., a combination of 4 facets with Ca-terminated which can be seen in Figure 6.1a and b) are: 12.62 Å in the direction of x, 5.28 Å in the direction of y, and a thickness of 13.63 Å in the direction of z. The system has a 30 Å vacuum, achieved by creating two layers of vacuum, each 15 Å in height. As depicted in Figure 6.1c, the $CaWO_4$ slab forms a supercell structure of $2a \times 2b$, which dimensions corresponding to 25.24 Å × 10.56 Å in the x and y directions, respectively, and its thickness is 13.63 Å in the z-direction. The

top and bottom surface of the crystal lattice is the (101) surface[203], which is the most stable surface[110,203] of $CaWO_4$. There are overall 288 atoms in the simulation domain, including 48-Ca, 48-W, and 192-O atoms, accounting for $Ca_{48}(WO_4)_{48}$.

A convergence test was done to determine the minimum thickness of the thin film. Figure 6.2 illustrates the modelling results of the surface energy difference (ΔE_{sur}) among various models with different numbers of layers. In this context, ΔE_{sur} represents the energy difference between any two models. Based on the test results, it was determined that utilizing a minimum of four layers of (101) facets is a feasible approach. This slab model having four layers facilitates a reasonable balance between the accuracy of the modelling results and the associated affordable computational costs.

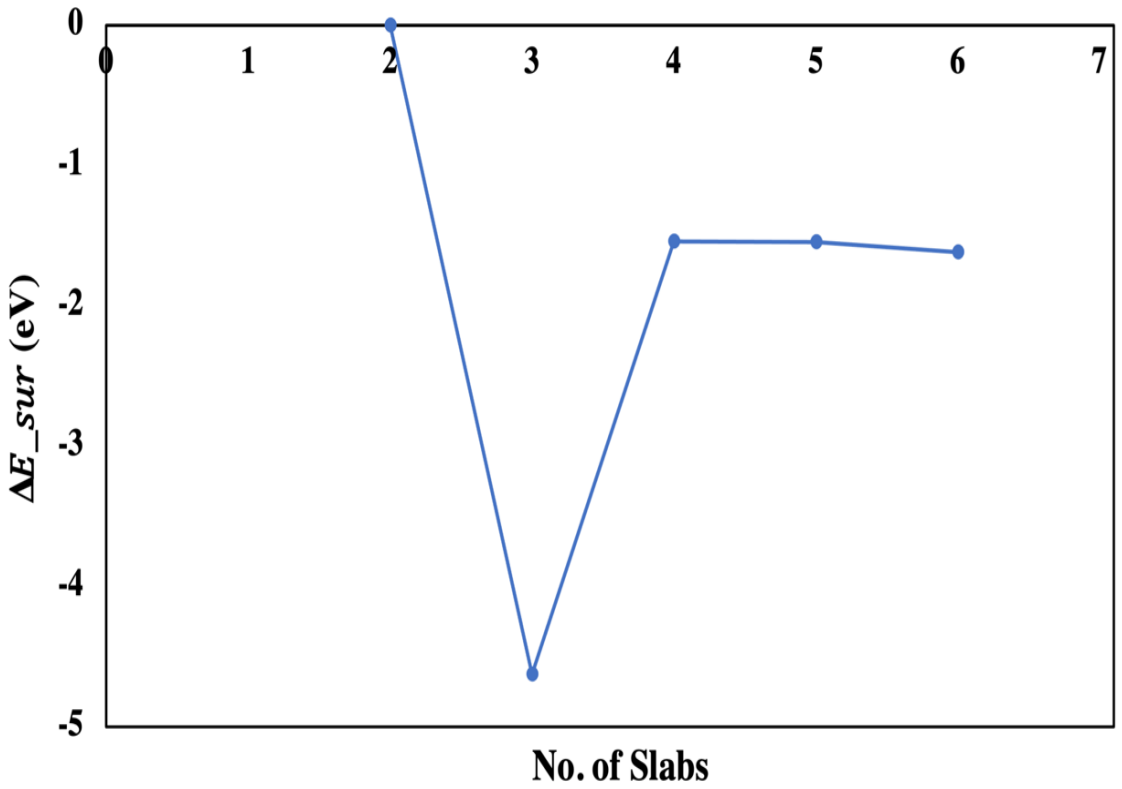

Figure 6.2: Computational modelling results of the convergence test regarding the surface energy difference corresponding to the setups that have different number of layers.

Compared with the WO_4 termination, the Ca termination proves to have better stability since its surface energy is lower than that of the WO_4 termination[203]. Moreover, this work employs the Ca-terminated phase of the $CaWO_4$ (101) surface

because it also exhibits greater stability in the real condition than the WO_4-terminated surface[110]. The surface energy (E_{sur}) of the systems can be calculated using the following formula:

$$E_{sur} = \frac{E_{slab} - nE_{bulk}}{2(a \cdot b)} \qquad 6.1$$

where E_{slab} – the energy of the slab, E_{bulk} – the energy of the bulk material in a unit-cell, n – number of unit-cells in the slab, a and b are the lattice parameters of the slab.

The defect formation energy (E_{form}) is determined using the formula below for the Cu-doped thin film.

$$E_{form} = \sum E_{products} - \sum E_{reactants} \qquad 6.2$$

where,

$$E_{products} = E_{Ca_{47}Cu_1(WO_4)_{48}} + E_{Ca_1}$$
$$E_{reactants} = E_{Ca_{48}(WO_4)_{48}} + E_{Cu_1}$$

where $E_{Ca_{48}(WO_4)_{48}}$ and $E_{Ca_{47}Cu_1(WO_4)_{48}}$ are the total energy of undoped $Ca_{48}(WO_4)_{48}$ and Cu-doped $Ca_{47}Cu_1(WO_4)_{48}$ thin-films respectively, E_{Ca_1} is the total energy of removed Ca-atom from the lattice structure, and E_{Cu_1} is the total energy of Cu-atom which is added to the lattice structure.

The atoms on the lower two layers of the slab are fixed in position while the rest atoms of the slab are allowed to move in the process of relaxation. A 3x5x1 Monkhorst-Pack grid is used, and the Brillouin zone (BZ) was sampled during computations. The VESTA programme[271] was used to make the charge density contour plots and retrieve the information of atom positions. Using the Bader charge analysis method developed by Henkelman, et al.[272], the partial atomic charges are determined. The tetrahedron method with Blöhl corrections was used in the DOS calculation.

6. 3 Results and discussion

6.3.1 Structural properties

The Birch-Murnaghan equation of state was utilized to calculate the lattice parameters of the $CaWO_4$ unit-cell. Based on these parameters, a tetragonal unit-cell with space group $I4_1/a$ was created and then cleaved along the (101) facet [110,203] to ensure a systematic approach to surface cleavage. The implementation of this approach enhances the quality of the findings in the present study. Surface energy (E_{sur}) calculations are used to evaluate material structure stability. In this study, the slab model's Ca-terminated (101) surface (as shown in Figure 6.1a and b) is found to have a lower E_{sur} value of 0.88 J/m^2 compared to the W-terminated (101) surface (2.07 J/m^2) (as shown in Figure 6.1d), indicating greater stability of the slab model with Ca-terminated (101) surface. This is fairly consistent with the reported value from earlier theoretical study[110,203].

Firstly, the most stable doping position for the Cu ion on the uppermost layer of the undoped $Ca_{48}(WO_4)_{48}$ thin film that has the (101) surface exposed is determined by evaluating the total energies of all the potential configurations, in which Cu ions may substitute the Ca atoms at a variety of locations in the supercell, including Ca_9, Ca_{18}, Ca_{21}, Ca_{30}, Ca_{34}, Ca_{36}, Ca_{38}, and Ca_{47}. In the modelling results using the GGA approach, Cu doping at Ca_{36} (Cu_{Ca36}) is found to be the optimum configuration as it is more stable than Cu doping at Ca_9, Ca_{18}, Ca_{21}, Ca_{30}, Ca_{34}, Ca_{38}, and Ca_{47}. In the supercell, one Ca atom is replaced by one Cu ion, accounting for the dopant concentration of 2.08 at. % ($Ca_{47}Cu(WO_4)_{48}$). A similar approach is employed to achieve a doping concentration of 4.16 at.% of Cu in the thin film surface ($Ca_{46}Cu_2(WO_4)_{48}$). This is accomplished by replacing Ca_{36} and Ca_{21} with two Cu ions. The crystal lattice structures of $Ca_{48}(WO_4)_{48}$, $Ca_{47}Cu(WO_4)_{48}$ and $Ca_{46}Cu_2(WO_4)_{48}$ thin film are shown in Figure 6.3.

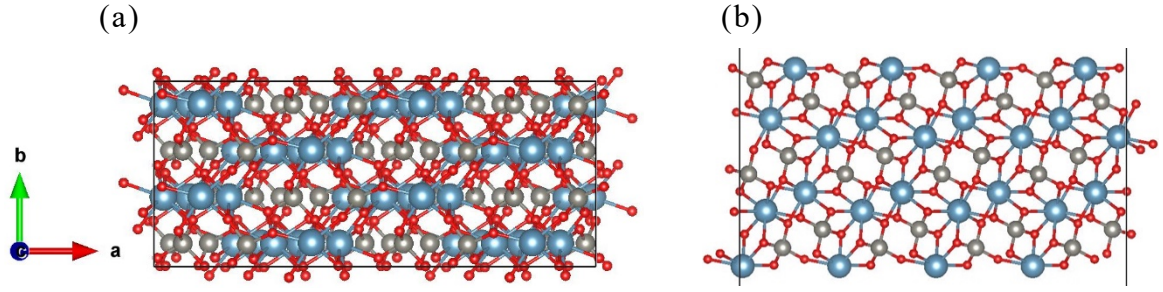

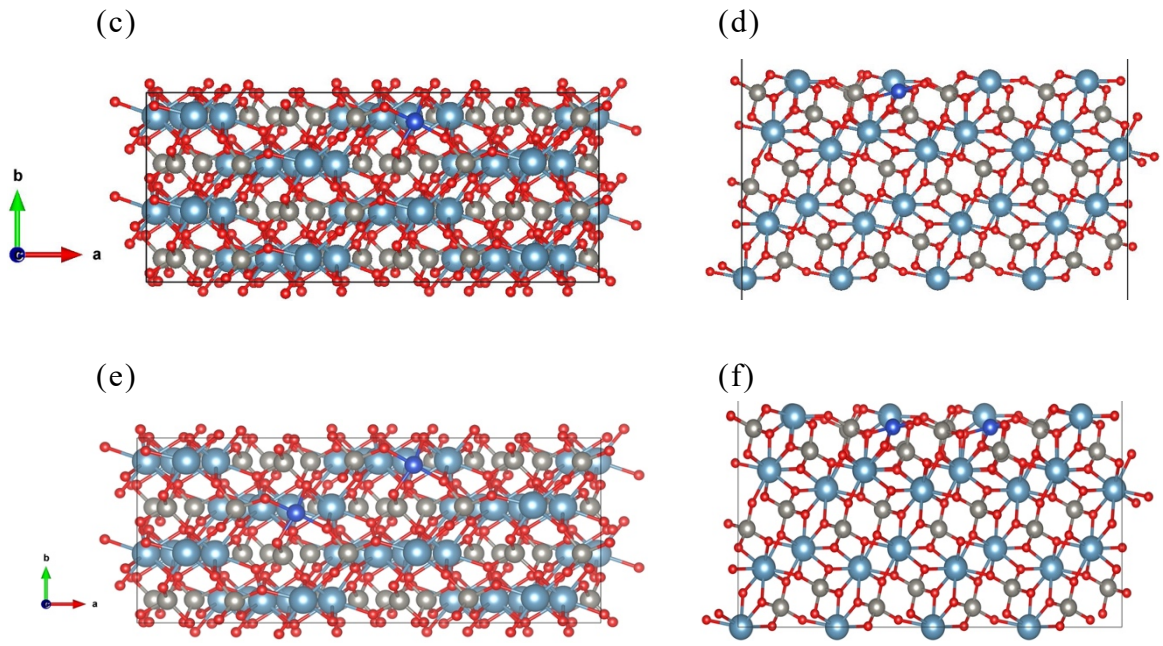

Figure 6.3: Relaxed $Ca_{48}(WO_4)_{48}$ [(a) Top and (b) Side views], $Ca_{47}Cu(WO_4)_{48}$ [(c) Top and (d) Side views] and $Ca_{46}Cu_2(WO_4)_{48}$ [(e) Top and (f) Side views]. The red, grey, light blue and dark blue spheres represent the atoms of oxygen (O), tungsten (W), calcium (Ca), and copper (Cu).

The total energy of the reactants is subtracted from the total energy of the products to calculate the defect formation energy (E_{form}), as explained in section 6.2 (see Eq. 6.2). The computed E_{form} value of 4.42 eV for $Ca_{47}Cu(WO_4)_{48}$ suggests that replacing a Ca atom with a Cu ion (2.08 at.%) incurs a lower energy cost compared to the E_{form} value of 8.91 eV regarding the 4.16 at.% Cu-doping system ($Ca_{46}Cu_2(WO_4)_{48}$). Consequently, doping the thin film surface with 2.08 at.% Cu at the Ca site is energetically favourable. The computed E_{sur} values of $Ca_{48}(WO_4)_{48}$, $Ca_{47}Cu(WO_4)_{48}$, and $Ca_{46}Cu_2(WO_4)_{48}$ thin films are 0.88, 1.01, and 1.14 J/m^2, respectively. These results suggest that the stability of the surface decreases as the concentration of Cu doping increases. Therefore, our focus for the forthcoming investigation will be exclusively on $Ca_{48}(WO_4)_{48}$ and $Ca_{47}Cu(WO_4)_{48}$. It is noteworthy that the modelling result of E_{sur} value of the undoped thin film (as shown in Figure 6.1c), which is 0.88 J/m^2, is identical to the E_{sur} value of the slab model (as shown in Figure 6.1a). This confirms the successful optimization of the thin film, indicating its effective structure and stability.

Furthermore, the interaction between the Ca or Cu and its nearby O atoms is analysed. It is widely acknowledged, in various metal oxides [273,274], that the formation of the metal oxide surface is accompanied by a defect of the ordered oxygen vacancy type[274,275]. Upon analysing the spatial distribution of Ca and W atoms in thin films with (101) facets, it becomes evident that varying degrees of broken chemical bonds exist on the surface, as well as at specific sites within the core of the thin film. In comparison to bulk $CaWO_4$, the positions and bond lengths of WO_4 and CaO_8 remain unchanged within the core of the $Ca_{48}(WO_4)_{48}$ thin film. However, the surface Ca atoms exhibit undercoordinated behaviour. For example, the undoped $Ca_{48}(WO_4)_{48}$ surface which has a Ca-terminated (101) facet exhibits that one Ca coordinates to five O atoms, each has a bond length of 2.26, 2.27, 2.28, 2.35, and 2.42 Å in good agreement with the related theoretical results[110]. The (101) facet of the $Ca_{47}Cu(WO_4)_{48}$ surface shows that one Cu is coordinated with four O atoms, each having a bond length of 1.93, 1.96, 1.99, and 2.00 Å. In contrast to the undoped $Ca_{48}(WO_4)_{48}$ surface, the W atoms of the $Ca_{47}Cu(WO_4)_{48}$ surface display greater variation of their bond lengths on the surface of the thin film. Specifically, these W atoms are coordinated with four neighbouring O atoms, with bond lengths ranging from 1.75 (±1) to 1.83 (±2) Å.

On one hand, the undercoordinated bond length of the Ca-O (i.e., five bonds on the surface) in the undoped $Ca_{48}(WO_4)_{48}$ thin film is between 2.27 and 2.42 Å. The undercoordinated Ca-O bond length (i.e., five bonds on the surface) in the $Ca_{47}Cu(WO_4)_{48}$ thin film varies between 2.27 and 2.44 Å. On the other hand, undercoordinated Cu-O bond length (i.e., four bonds on the surface) in the $Ca_{47}Cu(WO_4)_{48}$ thin-film is between 1.92 and 2.00 Å. The smaller ionic radius of Cu ion ($r_{Cu^{2+}}$ = 0.73 Å) relative to Ca ($r_{Ca^{2+}}$ = 1.12 Å) is the reason for such change of bond length. As a result, the stronger bonds between the Cu and its nearby O atoms imply that this compound has greater stability.

6.3.2 Electronic properties

Figure 6.4a-d illustrates the computational modelling results of the PDOS and TDOS with the up-spin and down-spin of $Ca_{48}(WO_4)_{48}$ and $Ca_{47}Cu(WO_4)_{48}$ thin-

film by using the GGA method. The electron transport among the atoms' orbitals in the system is characterised by the PDOS factor. As seen in Figure 6.4a, The O-2p orbitals predominate in the valence band (VB) of the undoped $Ca_{48}(WO_4)_{48}$ surface. The W-5d orbitals, as well as O-2p and Ca-3d orbitals, predominate in the conduction band (CB). As observed in Figure 6.4c, its band edges, such as the valence band maxima (VBM) and conduction band minima (CBM), are located at -0.09 and 3.58 eV, respectively. These edges are mainly composed of the O-2p orbital and hybridization of the Ca-4s, Ca-3d and W-5d orbitals, respectively. The fundamental bandgap value of the undoped $Ca_{48}(WO_4)_{48}$ surface is 3.68 eV (Figure 6.4c), which is significantly lower than the experimental result of 5.2–5.8 eV[110,276]. The limitation of the standard GGA method of the DFT model causes the bandgap values to be underestimated. Nevertheless, the DOS interpretation provided by GGA is still appropriate for qualitative assessment[277]. Interestingly, the $Ca_{48}(WO_4)_{48}$ thin film that has the (101) surface exposed effectively decreases the bandgap by 0.39 eV when compared to the bulk $Ca_{48}(WO_4)_{48}$.

(a)

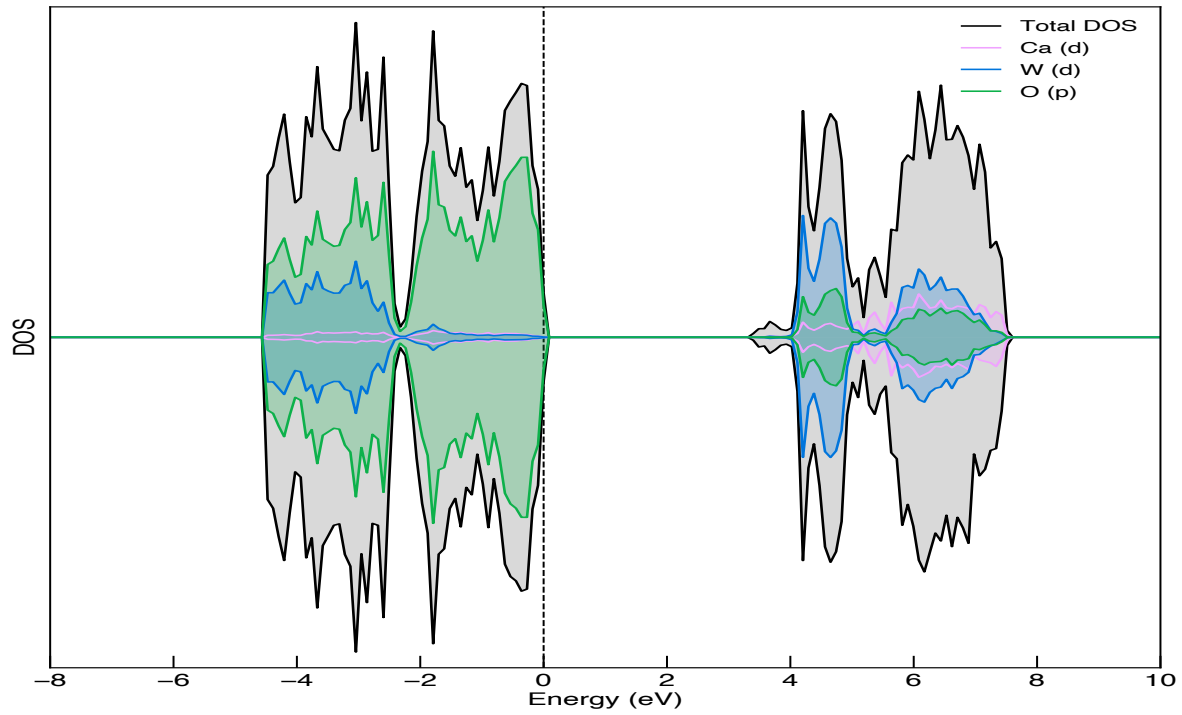

(b)

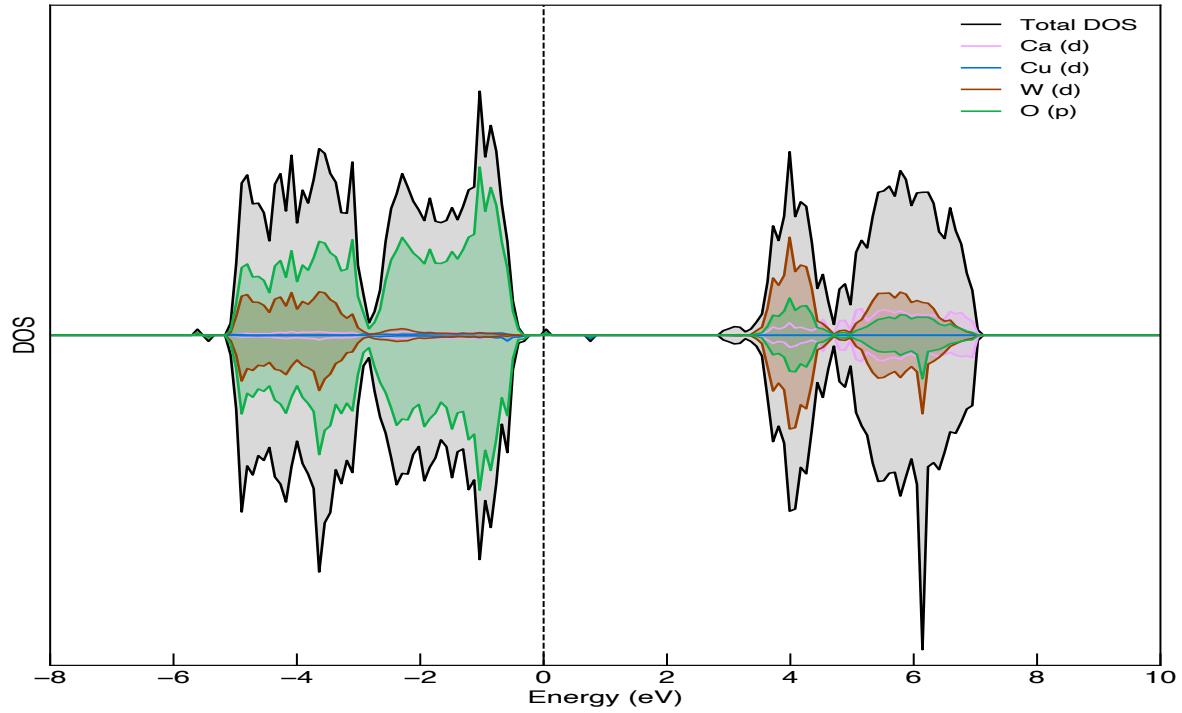
Total DOS
Ca (d)
Cu (d)
W (d)
O (p)
DOS
−8
−6
−4
−2
0
2
4
6
8
10
Energy (eV)

(c)

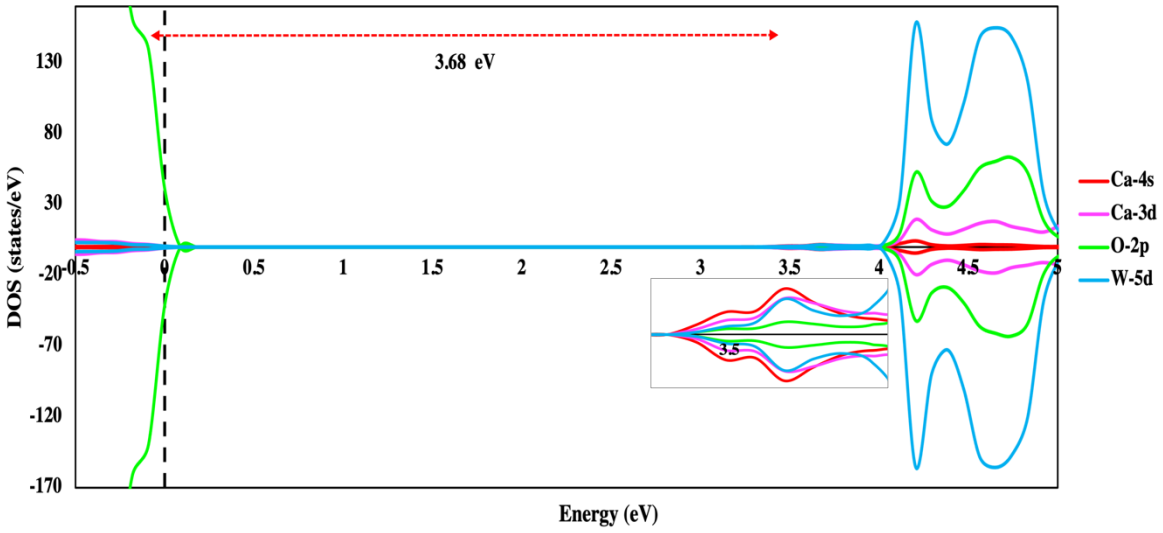
3.68 eV
130
80
30
-20
-70
-120
-170
DOS (states/eV)
-0.5
0
0.5
1
1.5
2
2.5
3
3.5
4
4.5
5
Energy (eV)
Ca-4s
Ca-3d
O-2p
W-5d

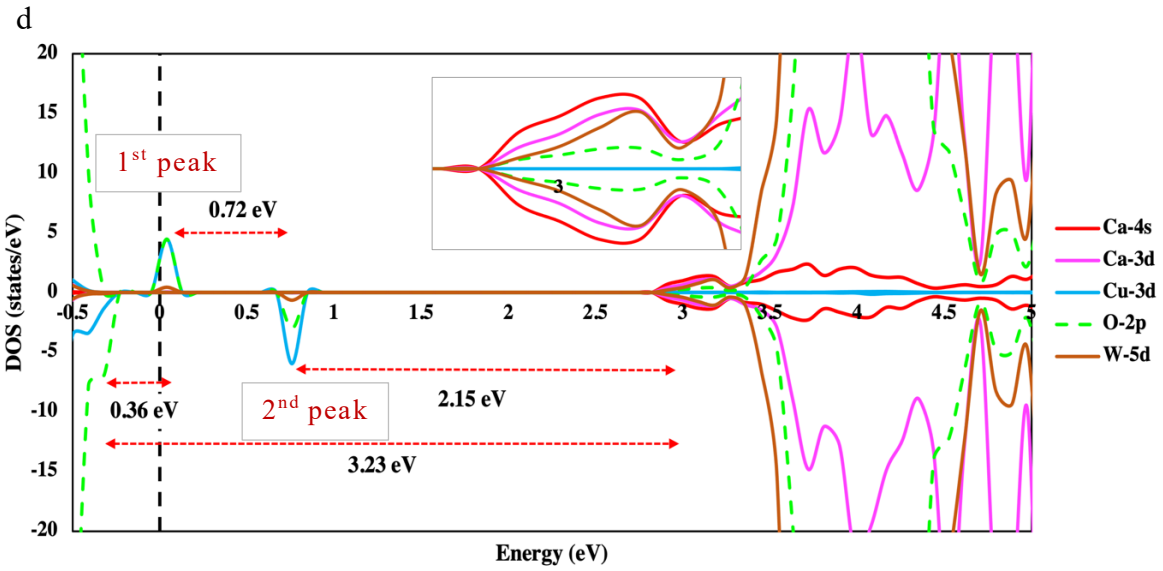

Figure 6.4: Total density of states (TDOS) and partial density of states (PDOS) of $Ca_{48}(WO_4)_{48}$ (a and c) and $Ca_{47}Cu(WO_4)_{48}$ (b and d)with (101) surface exposed

The Cu-doping produces impurity energy levels (IELs) between the band edges of the fundamental bandgap as seen in Figure 6.4b. Being similar to the undoped material, the band edges such as the CBM and VBM of the $Ca_{47}Cu(WO_4)_{48}$ surface are mainly composed of hybridization of the Ca-4s, Ca-3d and W-5d orbitals and the O-2p orbital, respectively. While W-5d orbitals, along with O-2p and Ca-3d orbitals, predominate in its CB, O-2p orbitals are primarily dominant in its VB. When compared to the undoped $Ca_{48}(WO_4)_{48}$ (Figure 6.4c), the fundamental bandgap value of $Ca_{47}Cu(WO_4)_{48}$ is reduced by up to 0.44 eV due to the influence of Cu. The bandgap value of the $Ca_{47}Cu(WO_4)_{48}$ with (101) surface exposed is estimated to be 3.23 eV (Figure 6.4d) since its VBM and CBM are at -0.32 and 2.92 eV, respectively.

Moreover, the Cu doping causes two sub-bandgap states in the fundamental bandgap, such as the first and second peaks arising due to the primary hybridization of Cu-3d with O-2p orbitals, to emerge above the Fermi energy (E_F) which can be clearly seen in Figure 6.4d. These two peaks emerged at 0.04 and 0.76 eV forming sub-bandgaps in the fundamental bandgap region. The photogenerated electron migrates from VBM and reaches CBM easily by approaching the 1st and 2nd peaks step by step. For instance, an electron might

travel from the VBM to the 1st peak, then from the 1st peak to the 2nd peak, and finally from the 2nd peak to the CBM, which corresponds to travelling through three sub-bandgaps separated by 0.36, 0.72, and 2.15 eV (see Figure 6.4d).

As seen in Figure 6.4b, the O-2p orbital completely dominates the whole VB from -5.5 eV up to the VBM, and a significant hybridization between the O-2p and W-5d orbitals occurs below -2.5 eV in the VB region and above ~3 eV in the CB region. The engagement of the orbitals O-2p, Cu-3d, and W-5d is related to the electronic transitions of the $Ca_{47}Cu(WO_4)_{48}$ surface. It is evident, as can be seen in Figure 6.4d, that the Cu-3d and O-2p orbitals strongly hybridise at 0.04 and 0.76 eV (i.e., 1st and 2nd peak, respectively). As a result, the charge transfer from the Cu to O atoms is possible in the 2.08 at.% Cu-doped $Ca_{48}(WO_4)_{48}$ surface. These two sub-bandgaps created by the Cu ion reduces the bandgap value by 1.35 eV in comparison to the undoped material, which also facilitates strong covalent interactions between the Cu–O. In light of all these, the Cu-doping enhances the photogenerated carriers' migration from VBM to CBM and inhibits charge recombination by generating sub-bandgaps, which serve as a trapping centre for the photogenerated carriers.

The VBM and CBM are moved closer to each other by the IELs dispersion in the bands (VB and CB) and bandgap region due to the energy difference of the Ca-3d and Cu-3d orbitals[278]. It results in a bandgap narrowing with significant asymmetrical distribution of the spin-up and spin-down electrons close to the Fermi energy level (E_f) (Figure 6.4b and d), suggesting the presence of induced magnetism in the $Ca_{47}Cu(WO_4)_{48}$ surface. The total magnetic moment (μ_m) is predicted to be $0.94\mu_B$ per supercell, which is inherently missing in the undoped $Ca_{48}(WO_4)_{48}$ surface. The induced μ_m by Cu-doping agrees with earlier GGA-PBE calculations on Cu-doped ZnO monolayer[279,280]. This induced magnetization could be attributed to Cu's significant electronegativity and electronic charge transfer to O[278], as well as the hybridization of their orbitals (Cu-3d and O-2p)[279]. Hence, the orbitals of Cu-3d and O-2p are primarily responsible for this induced magnetism. For an effective photocatalysis process, the efficient e^--h^+ pair separation and surface reaction are required which are facilitated by spin polarization and induced

diluted magnetism (i.e., asymmetric spin distribution)[278,281,282]. As shown in Figure 6.4a and c, the symmetrical distribution of electrons in the spin-up and spin-down of DOS states that the undoped $Ca_{48}(WO_4)_{48}$ with (101) surface exposed is not magnetic.

In addition, the charge profile analysis indicates that Cu possesses a +2 oxidation state (Cu^{2+}) due to the 9.092 electrons in its d orbitals. The Cu^{2+} increases the lifetime of an excited electron by preventing the recombination process[283] since Cu^{2+} acts as an efficient trapping centre (i.e., $Cu^{2+} + e^- \rightarrow Cu^+$) for excited electrons. The formation of a Schottky junction[284,285] upon Cu doping on the surface of $CaWO_4$ facilitates this process. For example, Cu^{2+}'s holes capture the photoexcited electrons which reduces the recombination of e^--h^+ on the surface of the $Ca_{48}(WO_4)_{48}$. As a result, the surface of $Ca_{48}(WO_4)_{48}$ thin film may produce more $OH^{\cdot}$ and $O_2^{\cdot-}$ radicals, which would greatly improve the oxidative decomposition of organic pollutants. These phenomena can be visualized by using the schematic diagram shown in Figure 6.5. In conclusion, Cu-doping greatly improves the electronic properties of $Ca_{48}(WO_4)_{48}$ thin film, resulting in a decreased bandgap value, more efficient e^--h^+ pair separation, and induced magnetism with asymmetrical distribution of the spin-up and spin-down electrons, which makes suitable for photocatalytic applications.

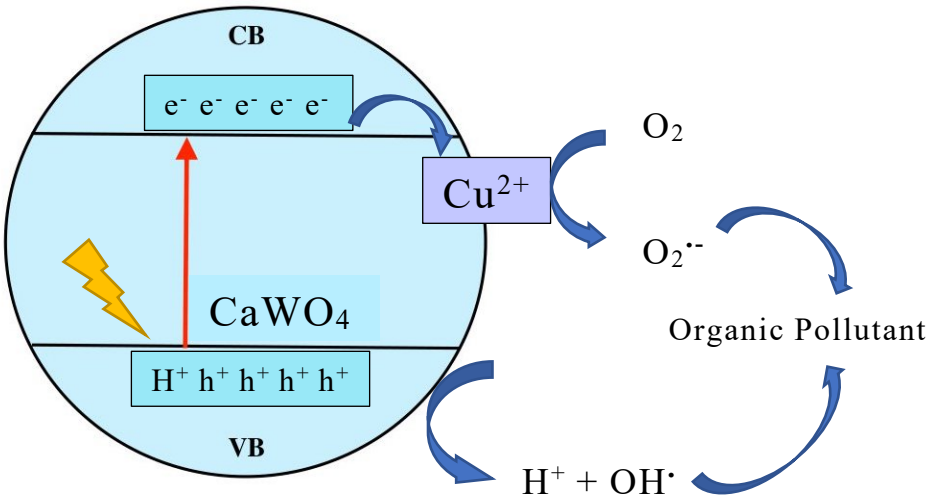

Figure 6.5: A diagram illustrating the mechanism of degradation of organic pollutants.

6.3.3 Absorption spectrum

The material's optical properties are directly related to its electronic properties. For a potentially effective photocatalytic material, the material must have efficient absorption activity. If a photocatalyst can make proper use of visible light, its bandgap value should ideally be between 1.6 eV and 3.2 eV.

The modelling results (using the sumo code[286]) of the absorption spectrum of the $Ca_{48}(WO_4)_{48}$ thin film with (101) surface exposed is displayed in Figure 6.6a.

(a)

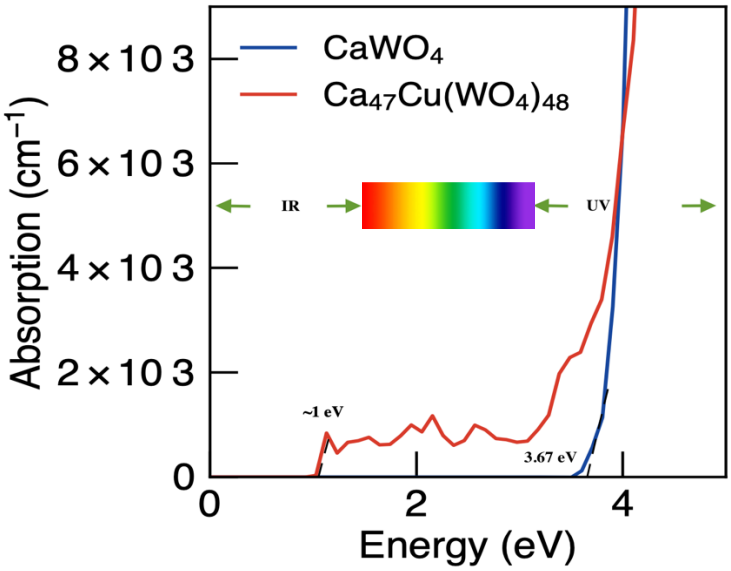

(b)

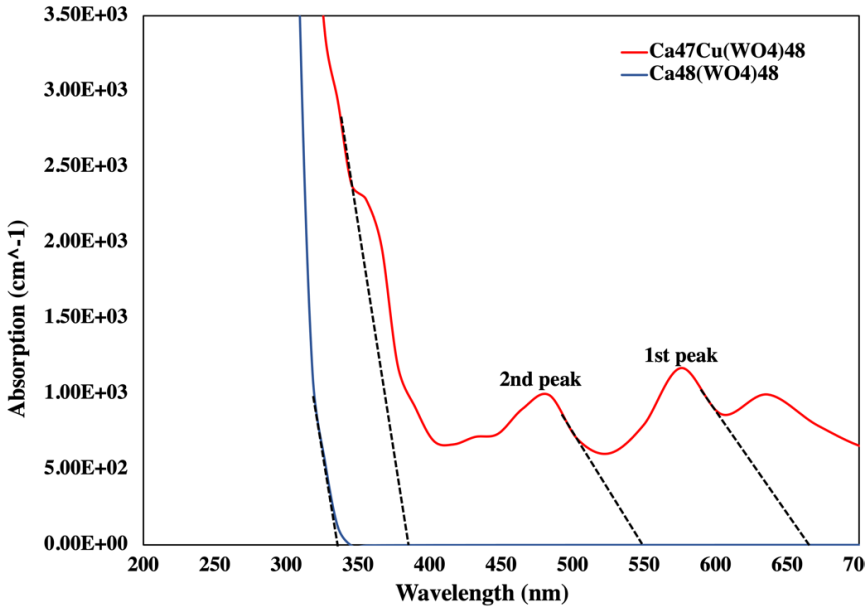

Figure 6.6: Computational modelling results of the absorption spectrum of $Ca_{48}(WO_4)_{48}$ and $Ca_{47}Cu(WO_4)_{48}$ with (101) surface exposed using two different approaches, including (a) Energy (eV) vs Absorption (cm^{-1}) and (b) Wavelength (nm) vs Absorption (cm^{-1}).

The undoped $Ca_{48}(WO_4)_{48}$ surface has an absorption edge at ~3.65 ($\pm$2) eV, which is only sensitive to ultra-violet (UV) radiation, and Cu-doping on the surface shifts it significantly to ~1 eV, which is sensitive to visible-light (VL) as well as some infrared (IR) radiation. This results from a variety of mechanisms. For example, Cu-doping results in an electronic bandgap reduction in the material, causing asymmetric up and down spins that generate sub-bandgaps states. As a result, significant inter-band transitions of the carriers between sub-bandgaps can occur, which lowers adsorption edge values and increases adsorption activity in the IR and VL spectrum. It can be more clearly seen in Figure 6.6b. The multiple adsorption peaks of the Cu-doped material indicate increased optical absorption across the spectrum of wavelengths, from UV to IR. Moreover, this illustrates how a photoexcited charge carrier can transfer from the VBM to CBM through 1st and 2nd peaks of so called sub-bandgap states as was discussed in the previous section 6.3.2. For instance, a photoexcited charge carrier may move stepwise from the first to the second peak and subsequently to the CBM states using corresponding wavelengths 660, 570, and 542 nm as shown in Figure 6.6b. These phenomena can be visualized by using the schematic diagram shown in Figure 6.7.

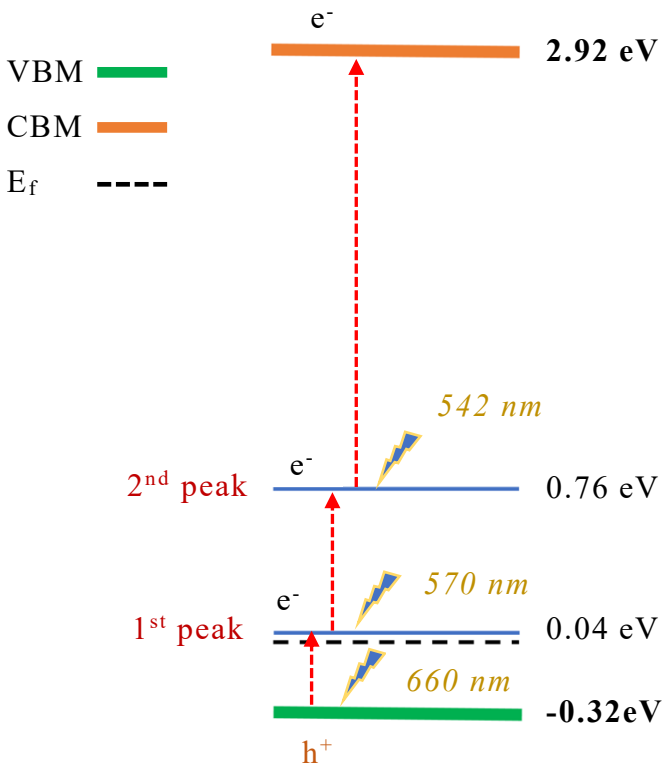

Figure 6.7: Schematic visualization of photoexcited electron transition from VBM to CBM.

Overall, all these demonstrate that the $Ca_{47}Cu(WO_4)_{48}$ thin-film with (101) surface exposed has strong absorption and is sensitive to visible light, which is ideal for effective photocatalytic processes.

6.3.4 Charge density difference analysis

Figure 6.8 illustrates the charge density difference of the $Ca_{47}Cu(WO_4)_{48}$ with (101) surface exposed. It visualises the influence of Cu-dopant on the material in terms of induced magnetism, and electronic and optical properties. The charge density difference $\Delta\rho$ is calculated by using the below formula.

$$\Delta\rho = \rho_{Ca_{47}Cu(WO_4)_{48}} - \rho_{Ca_{47}(WO_4)_{48}} - \rho_{Cu_{gas-phase}} \qquad 6.2$$

where $\rho_{Ca_{47}Cu(WO_4)_{48}}$ is the charge density of $Ca_{47}Cu(WO_4)_{48}$, $\rho_{Ca_{47}(WO_4)_{48}}$ is the charge density of the $Ca_{48}(WO_4)_{48}$ that one Ca atom is replaced by a vacancy, and $\rho_{Cu_{gas-phase}}$ is the charge density of the gas phase Cu. Figure 6.8 illustrates how the

charge density surrounding Cu^{2+} and the O^{2-} can significantly change when Cu^{2+} is doped at the site of Ca^{2+}. As can be seen in Figure 6.8a, the electron charge density of the Cu ion loses while the charge density of its coordinated O ions, such as O_{148}, O_{152}, O_{156}, and O_{172}, gains. The W^{6+} ions that are close to Cu^{2+} have a reduced charge density as well when doping with Cu. The significant difference of electronegativity between O(3.5) and Cu(1.9) or W(1.7) atoms can be attributed to this phenomenon[110]. A significant portion of charges is located around O sites, which accounts for the strong bonds between O-Cu/W atoms.

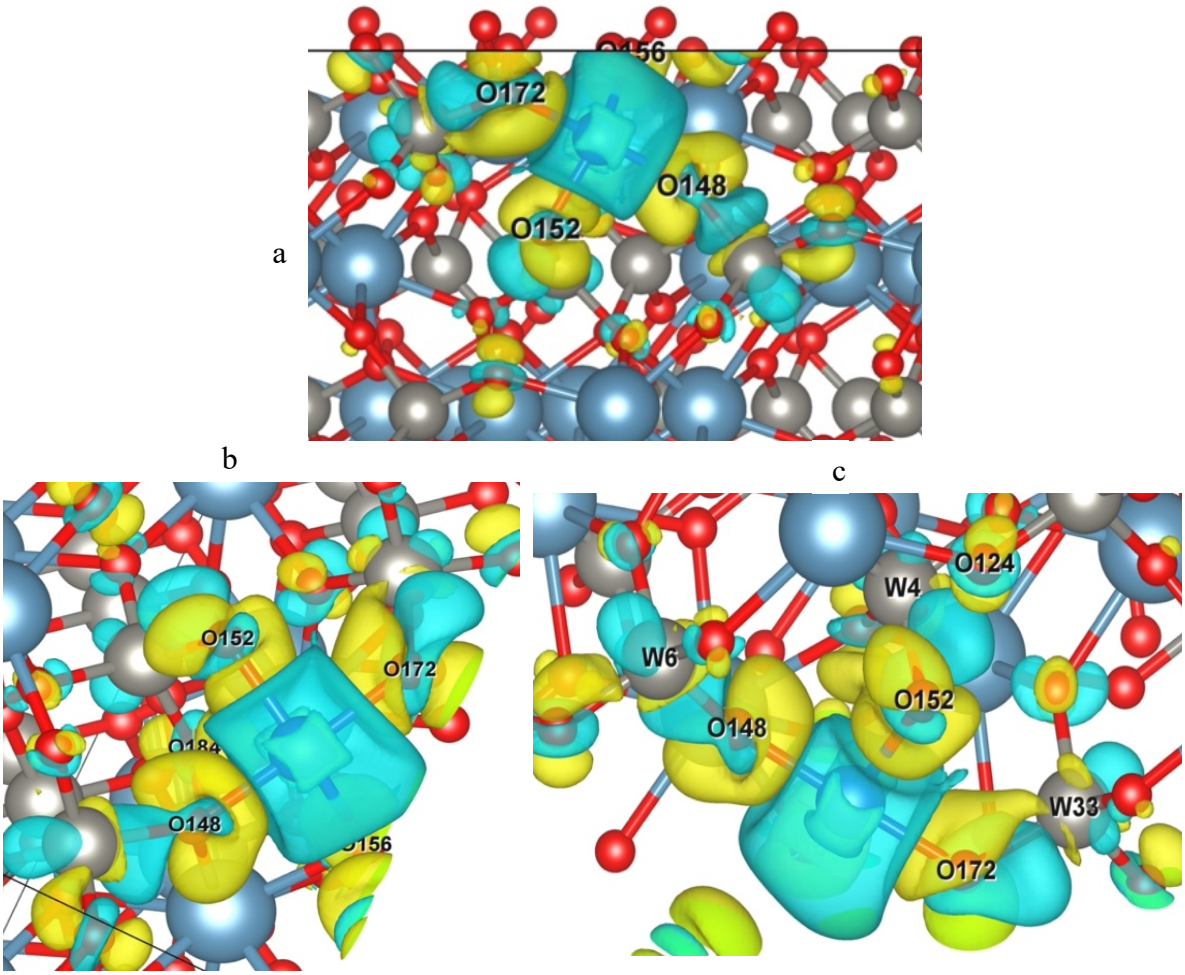

Figure 6.8: Charge density differences of $Ca_{47}Cu(WO_4)_{48}$ with (101) surface exposed: (a) top view of the entire supercell, (b) local zoom-in around the O_{184} as well as Cu's coordinated O atoms, and (c) local zoom-in around the W atoms that are close to Cu. The charge gain and charge loss are represented by yellow color and blue color clouds, respectively.

Besides being distributed around the coordinated O atoms, the charge density is also dispersed to nearby O atoms, particularly O_{184} (Figure 6.8b). The charge

transfer process employing Bader charge analysis can serve as more evidence for this. It confirms a substantial charge loss of 1.13e from Cu, resulting in a cationic state of Cu^{2+}. In addition, Cu has a calculated Bader charge of 9.87 electrons[287], which is compatible with the oxidation state of Cu^{2+}. According to the charge clouds shown in Figure 6.8, the Cu cation and its nearby W cations predominantly contribute to the charge gains of the O anions nearest to Cu, which range from 0.97 to 1.09e. It is important to note that this effect is limited to the Cu and its neighbouring O atoms (i.e., at the top layer), and it is not extended to other layers. The estimated total magnetic moment of a $Ca_{47}Cu(WO_4)_{48}$ thin film is approximately 0.94 μ_B per supercell. Within this structure, the local moment surrounding the Cu atom is estimated to be 0.58 μ_B, while the remaining most of the magnetic moment is predominantly associated with the O atoms (i.e., O148, O152, O156, and O172) that are bonded to Cu. Therefore, the main factors inducing magnetism in $Ca_{47}Cu(WO_4)_{48}$ with (101) surface exposed are the Cu dopant and its nearby O atoms. This study provides additional evidence that the orbitals of Cu-3d and O-2p are primarily responsible for this induced magnetism in Cu-doped $Ca_{48}(WO_4)_{48}$ with (101) surface exposed, as was discussed in section 6.3.2.

6.4 Conclusion

The electronic and optical properties of $Ca_{48}(WO_4)_{48}$ and $Ca_{47}Cu(WO_4)_{48}$ thin film with (101) surface exposed are computationally predicted by using spin-polarized DFT calculations. Interestingly, the $Ca_{48}(WO_4)_{48}$ thin film, with its exposed (101) surface, shows a notable reduction in bandgap by 0.39 eV compared to the bulk $Ca_{48}(WO_4)_{48}$. In contrast, the positions and bond lengths of WO_4 and CaO_8 within the core of the thin film remain unchanged when compared to bulk $Ca_{48}(WO_4)_{48}$. However, it is worth noting that the Ca atoms on the surface display undercoordinated behaviour.

Cu ion is used to substitute Ca_{36} to achieve a 2.08 at.% Cu-doping concentration ($Ca_{47}Cu(WO_4)_{48}$). The computed E_{form} value of 4.42 eV for $Ca_{47}Cu(WO_4)_{48}$ indicates that the energy cost of replacing a Ca atom with a Cu ion is lower

compared to the 8.91 eV of the 4.16 at.% Cu-doping system ($Ca_{46}Cu_2(WO_4)_{48}$). This suggests that doping the thin film surface with 2.08 at.% Cu at the Ca site is energetically favourable. Furthermore, the computed E_{sur} value of $Ca_{48}(WO_4)_{48}$, $Ca_{47}Cu(WO_4)_{48}$, and $Ca_{46}Cu_2(WO_4)_{48}$ thin films reveal that the thermal stability of the surface decreases as the concentration of Cu doping increases.

The Cu-doping creates IELs such as Cu-3d orbitals above the VBM, and they strongly hybridise with O-2p orbitals, indicating a strong covalent interaction. This enables the absorption edge of the material to shift towards the visible light and IR spectrum. Cu-3d states are broadly dispersed above the VBM, which explains why $Ca_{47}Cu(WO_4)_{48}$ with (101) surface exposed can absorb visible light more efficiently. With induced magnetism, Cu-doping lowers the fundamental bandgap value of the undoped $Ca_{48}(WO_4)_{48}$ thin film (3.67 eV) to 3.23 eV for the $Ca_{47}Cu(WO_4)_{48}$ system. These lead to increased optical absorption, efficient e^--h^+ pair separation and reduced recombination by generating sub-bandgaps and induced magnetism, which makes the Cu-doped $Ca_{48}(WO_4)_{48}$ thin film suitable for photocatalytic applications.

Chapter 7:

Computationally predict the interaction between undoped and Cu-doped $CaWO_4$ thin-film with methylene blue.

7.1 Introduction

Chapter 6 presents the computational modelling results of the properties of the $CaWO_4$ thin film as well as the influence of doping the material using Cu.

Chapter 7 is focused on presenting the computational modelling results of the interaction between the undoped and Cu-doped thin films and a model organic waste. Methylene blue (MB) is used as a model organic waste in this chapter.

7.1.1 Why is methylene blue considered a model organic pollutant in this study?

Various organic dyes are being extensively used in the printing, textile, leather, pharmaceutical, food, and cosmetic sectors for the purpose of colouring[288]. They are frequently released into the environment annually, accounting for a source of water pollution[289,290]. Of particular concern are cationic dyes like methylene blue (MB)[291,292], which can have harmful effects on human health, including irregular heartbeat, vomiting, diarrhoea, chest pain and gastritis [293,294]. Exposure to MB can also lead to symptoms of nausea, shock, and mental confusion. Furthermore, it can cause skin irritation upon contact[295]. The dye MB remains extremely mobile and possesses stable chemical properties after being released into the environment, which can have a negative influence on the ecology and especially the growth of aquatic life[296,297].

In general, cationic dyes are more toxic than anionic (i.e., methyl orange, etc.) dyes[298], making the removal of MB from industrial effluents a significant environmental concern[299]. Moreover, the cationic dye MB is water-soluble with poor biodegradability, and it remains in the environment for a long time[294,300]. The presence of organic pollutants like MB is common in all types of wastewater and can have adverse effects on well-being [293,294]. Therefore, the effective elimination of organic dyes such as MB from the water body is needed. As a result, various innovative attempts have been made to decompose organic pollutants (i.e., chemical structure of MB, MO, etc.) using photocatalytic methods. These methods,

which fall under the category of advanced oxidation processes (AOPs), have gained significant attention due to their high efficiency, cost-effectiveness, and environmentally friendly approach[25], as discussed in Section 1.2 of Chapter 1.

7.1.2 Stage-of-the-art research on photocatalytic degradation of MB

Here are some instances of how different types of photocatalyst materials are employed in the treatment of MB. Overall, chemically modified TiO_2 has been widely utilized as a photocatalyst in experimental studies for decomposing the MB:

- Sb-doped TiO_2 for the MB degradation[301],
- Ag, Sn or Zn-doped TiO_2 for the degradation of MB and MO[38],
- N-doped TiO_2 for MB degradation[302],
- Zn-N co-doped TiO_2 for the degradation of MB[42].

Besides the chemical modification of TiO_2, chemical modifications have been conducted on numerous other semiconductor photocatalysts to increase their photocatalytic activity when being exposed to visible light to efficiently degrade the MB. For example, C-doped ZnO exhibited high efficiency in the degradation of MB, with a rate of approximately 96-98%, and exhibited good recyclability [49]. A Sm-doped Fe_2O_3 photocatalyst effectively degraded MB with a remarkable photodegradation efficiency of 99.8% [54]. Both $FeVO_4$ (by 2% Zn^{2+}) and the doped $FeVO_4$ (by 2% Mn^{2+}) showed enhanced photocatalytic activity for MB degradation, with both demonstrating an effective degradation rate of 99% [55].

Despite this, unmodified metal oxide nanoparticles have also demonstrated excellent photodegradation of MB dye in the characterisation studies. For instance, mesoporous $BiVO_4$ nanoparticle[297] and hydroxylated α-Fe_2O_3 nanoplate[303] exhibited high degradation rates of ~98% and ~60%, respectively under visible-light illumination.

Regarding related DFT modelling, when MB is loaded onto the ZnO (0001) facet, the molecule becomes energized and unstable due to the gain or loss of charge,

which enables faster degradation by the photocatalyst compared to a MB unadsorbed[304]. In a different publication, DFT modelling was used to evaluate the degradation capacity of $ZnTiO_3$ oxide photocatalyst against MB dye, by analysing the electronic band structure and adsorption energy when the dye is loaded on the (101) surface[305]. Both experimental and theoretical studies on hydroxylated α-Fe_2O_3 nanoplates were conducted to understand the adsorption behaviour of MB cations on hydroxylated (001) and (012) α-Fe_2O_3 surfaces under vacuum conditions [303].

$CaWO_4$ and its derivatives have gained considerable attention as photocatalytic materials for treating both anionic (such as Acid Red-18[107] and methyl orange[306]) and cationic dyes (such as methylene blue[104,307,308] and Rhodamine B[9,224,309,310]). $CaWO_4$ nanomaterial exhibits excellent properties such as uniform dispersion, photoluminescence, a decreased ratio of photogenerated electron-hole pair recombination and acts as a superior direct semiconductor catalyst[67]. A photocatalytic material needs a favourable bandgap width to enable the redox reaction for the photocatalytic mechanism. The suitable bandgap width of $CaWO_4$ promotes electron excitation and recombination, supporting the continuous progression of the photocatalytic reaction. Moreover, $CaWO_4$ is insoluble in wastewater during the treatment of dye wastewater, facilitating efficient recycling. As a result, $CaWO_4$ is regarded as a highly promising photocatalyst with significant potential for a wide range of applications[67]. It is noteworthy that the use of $CaWO_4$ nanomaterial resulted in the degradation of more than 80% of MB even after five cycles under UV irradiation[67]. Some research was focused on the combined use of UV and visible light and demonstrated a high percentage (93%) of MB dye degradation under UV irradiation[104]. As part of ongoing experimental studies, $CaWO_4$ nanoparticles underwent chemical modification to enhance their capacity for complete MB dye decomposition and to extend the absorption profile to the visible range. For example, the synthesized transition metal (TM) ion (Ag^+ and Zn^{2+}) co-doped $CaWO_4$ nanoparticles were tested regarding the degradation of MB under UV irradiation[70]. It was observed that the doping of Ag to $CaWO_4$ nanoparticles resulted in complete degradation (100%) of MB dye after 120 minutes [70]. Under visible light, the synthesized $CaWO_4$/α-Ag_2WO_4 nanocomposite exhibited a high level of photocatalytic activity, degrading approximately 85% of

MB dye[66]. The synthesized $BaMoO_4/CaWO_4$ nanocomposites (BCCHMNs) exhibited efficient photocatalytic activity and degraded MB dye by 95% under simulated sunlight[308]. Based on the discussion presented above and in Section 6.1 of Chapter 6, it is apparent that chemical modification, specifically through the process of doping, can significantly enhance the photocatalytic capacity of scheelite-based catalysts and enables them to utilize visible light effectively.

7.1.3 Overview of the study

In this chapter, the molecule of organic dye MB is used as a model organic pollutant. The DFT computational modelling is used to characterise how it interacts with the undoped and Cu-doped $CaWO_4$ thin film. Besides computationally predicting the electronic and absorption properties of the photocatalyst, this research also predicts how the model organic pollutant can be concurrently oxidized due to the interaction with the photocatalyst. Furthermore, doping with Cu alters the surface chemistry of the material. Hence, the computational modelling is also used to characterise how the Cu-doping concentration influences the interaction between MB and the photocatalyst thin film.

7.2 Computational methodology

The structural and electronic properties of the undoped and doped $CaWO_4$ are examined using spin-polarized[266] DFT-D3[267,268] computations embraced in the Vienna Ab-initio Simulation Package (VASP)[71]. The GGA-PBE approach[76] is used to formulate the exchange and correlation (XC) potential, and the PAW method[152] is used to define the electron wave functions and pseudopotentials for the electron-ion interaction. To precisely predict the lattice structures, thermodynamics[311] properties, and adsorption energies of the target materials, particularly when physisorption occurs[312–316], the van der Waals (vdW) dispersion correction term is considered in the calculations. The specific setups of the computational modelling are addressed in section 6.2 of Chapter 6. The following equation is used to make the charge density difference ($\Delta\rho$) plots:

$$\Delta\rho = \rho_{system} - \rho_{photocatalyst} - \rho_{MB} \quad 7.1$$

where, ρ_{system}, $\rho_{thin-film}$, and $\rho_{molecule}$ are electron charge density of the MB loaded photocatalyst, photocatalyst, and MB molecule, respectively.

The differential Gibbs free energy (ΔG_{ads}) of surface adsorption can be determined using the equation provided below[269,317–320]. Frequency calculations were carried out to characterize each minimum configuration, enabling the determination of the required partition functions for computing the thermodynamic functions of adsorption[320], namely ΔH_{ads} and ΔS_{ads}. These thermodynamic functions can be connected to ΔG_{ads} through equation 7.2. In particular, the ideal gas model was employed to account for translational, rotational, and vibrational degrees of freedom of the isolated molecules, and compute the corresponding Gibbs corrections. For the thermodynamic corrections of adsorbates, instead, the harmonic model was employed and all 3N degrees of freedom were considered to be vibrational. In all cases, a temperature of 298 K and a pressure of 1 atm were employed. The nuclear motions of the surface atoms were neglected due to their negligible changes upon gas adsorption, resulting in their exclusion from the calculation of (ΔG_{ads})[320].

$$\Delta G_{ads} = \Delta H_{ads} - T\Delta S_{ads} \quad 7.2$$

$$\Delta H_{ads} = \Delta E_{ads} + \Delta E_{ZPE} + \int_0^T C_P \, dT \quad 7.3$$

where the ΔH_{ads} – the enthalpy change; ΔE_{ads} – the total energy of the system (i.e., electronic energy); ΔE_{ZPE} – the zero-point energy (i.e., change of zero-point energy resulting from vibrational frequency calculation); and $\int_0^T C_P \, dT$ – the integral is over the constant-pressure heat capacity. T is temperature (298 K) and ΔS_{ads} is the change of entropy[319].

The following equations are used to calculate the adsorption energy (E_{ads}) of MB on the surface of undoped and Cu-doped photocatalyst:

$$E_{ads} = E_{TF/MB} - E_{TF} - E_{MB} \quad 7.3$$

$$E_{ads} = E_{Cu-TF/MB} - E_{Cu-TF} - E_{MB} \quad 7.4$$

where, $E_{TF/MB}$, and $E_{Cu-TF/MB}$ are total energy of the MB absorbed undoped and Cu-doped photocatalyst, respectively. E_{TF}, E_{Cu-TF}, and E_{MB} represent the total energy of the undoped photocatalyst, Cu-doped photocatalyst, and free MB molecule in a vacuum, respectively. The charge transfer (Q_t) from the MB to the photocatalyst and vice versa is calculated using the equation:

$$Q_t = Q_a - Q_b \quad 7.5$$

where Q_a and Q_b are the quantities of accumulated charge value of the specific atom of the MB that goes for binding after and before adsorption on the photocatalyst as evaluated by using electron population analysis. It is important to note that if the value of Q_t is positive, it implies that charges migrate from the MB to the photocatalyst, whereas if Q_t is negative, charge migration occurs from photocatalyst to MB [312,321].

The method of making the $CaWO_4$ thin film using the slab model, choosing the (101) plane, running the structural optimization as well as other related computational modelling methods for the undoped and Cu-doped $CaWO_4$ thin films are comprehensively addressed in Chapter 6.

7.3 Results and discussion

7.3.1 Structure analysis

The adsorption capacity of the (101) surface of $CaWO_4$ thin film is evaluated using three typically available ions in water, such as H^+, O^-, and OH^- as shown in Figure 7.1.

(a)

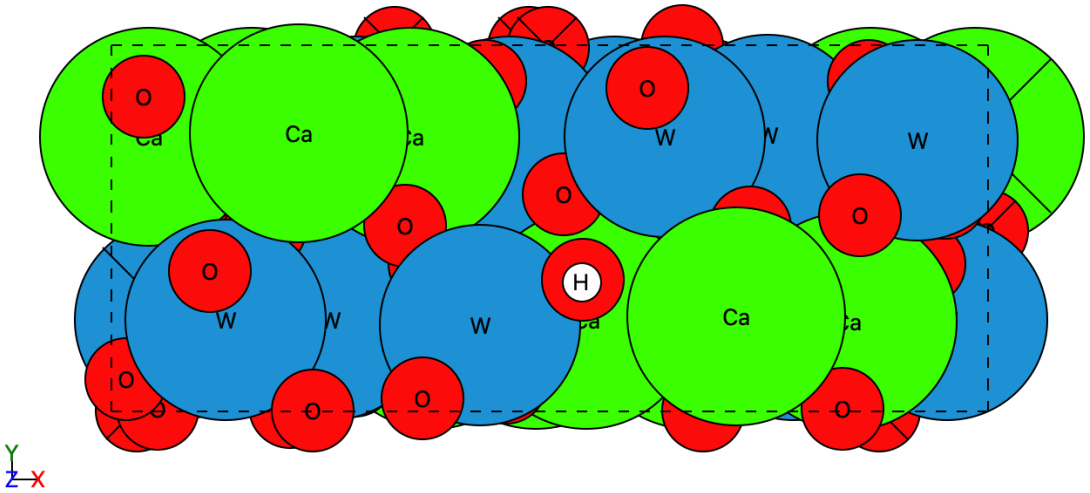

(b)

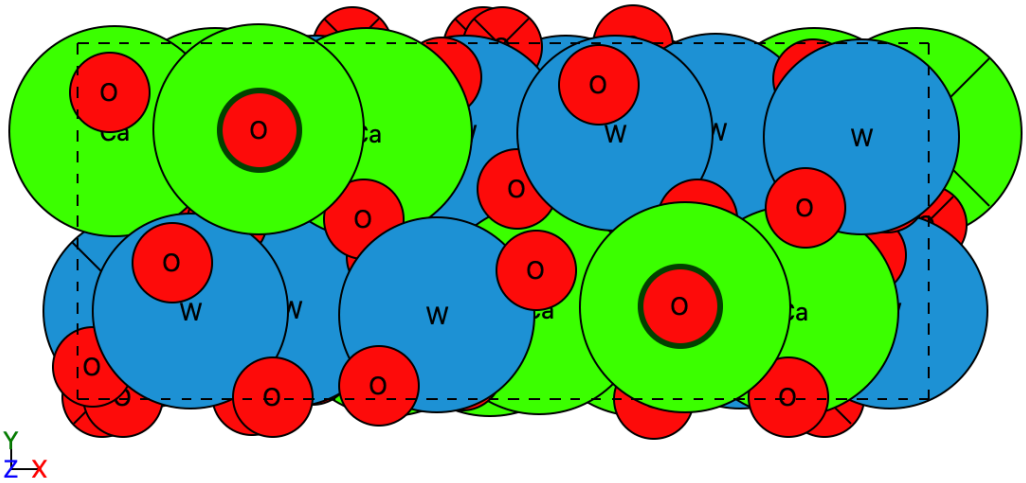

(c)

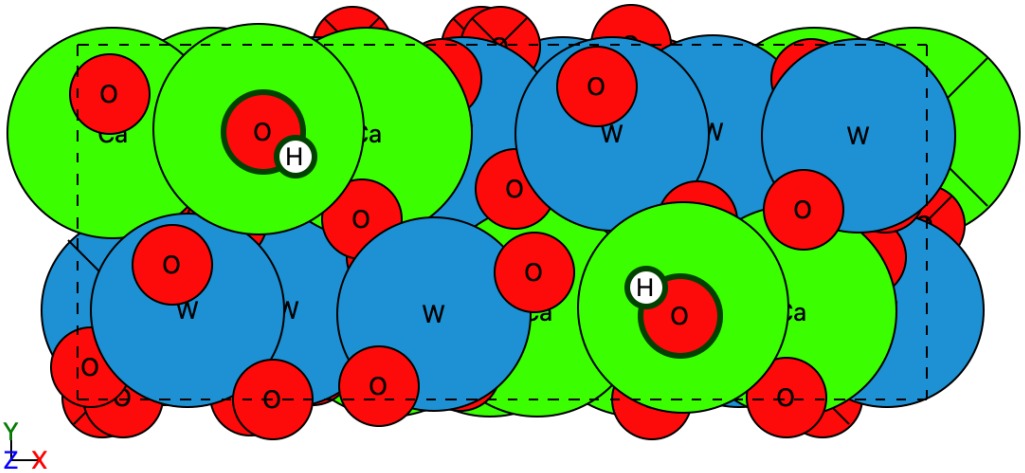

Figure 7.1: Ions' coverage on (101) surface: (a) H^+ ion covers O atom, (b) O^- ions cover Ca atoms, and (c) OH^- ions cover Ca atoms of the $CaWO_4$. Red sphere:

Oxygen (O)-atom, Green sphere: Calcium (Ca)-atom, Blue sphere: Tungsten (W)-atom, White sphere: Hydrogen cation (H^+), Red sphere with a black circle: Oxygen anion (O^-), and Red and White spheres with a black circle: Hydroxide anion (OH^-).

The adsorption of these ions on the surface at various sites is shown in Figure. S7.1-S7.3 of Appendix-C7. To graphically explain the ion's coverage on the surface of the $CaWO_4$, related structural models can be seen in Figure 7.1. In comparison to the adsorption of the MB molecule, the E_{ads} of ions on the surface of the $CaWO_4$ has greater values which can be seen in Table 7.1. For all the setups of the computational modelling, the modelling results of the adsorption energies (E_{ads}) of the MB loaded photocatalyst systems are all negative. It means the MB can stably bond to the (101) surface of $CaWO_4$. All of these results clearly demonstrate that ions in water (such as H^+, O^-, and OH^-) do not significantly compete with the MB molecules regarding the occupancy of the surface-active sites of $CaWO_4$ thin-film when engaging in photocatalytic processes. This type of surface coverage analysis is also conducted for the surfaces of Cu-doped $CaWO_4$, and very similar conclusions can be drawn. Overall, the ability of MB to adsorb on the surface of the $CaWO_4$ (undoped and Cu-doped) is greater than that of ions in water.

In the interest of determining the optimum MB orientation on the $CaWO_4$ surface, below seven different orientations of the MB molecule are tested in the computational modelling.

- Four geometries with MB's perpendicular orientations on ($1a \times 2b$) supercell of thin-film surface, including (I) x-axis, (II) y-axis, (III) diagonal-axis, and (IV) H atoms of the MB covering both O and Ca atoms of surface.
- Three adsorption configurations for the MB's parallel orientations on ($2a \times 2b$) supercell of thin-film surface, including (V) N1 and H atoms of the MB covering the hollow region of surface (i.e., between in-plane oxygens), (VI) N1 and N3 atoms of the MB covering the Ca atoms (i.e., Ca36 and Ca44, respectively) of the surface, and (VII) N1 and H atoms of the MB covering the O atoms of the surface.

As shown in Figure 7.2, two different sizes of the supercell, i.e. ($1a \times 2b$) and ($2a \times 2b$), are used to implement the slab model for establishing the $CaWO_4$ thin film in the simulation domain. This technique involves creating a thin slab of the material, which can then be repeated periodically in the x and y axis to create a larger supercell, as explained in detail in Section 6.2 of Chapter 6. The optimized structure of these seven adsorption orientations can be found in Figure. S7.4 of Appendix-C7 of the thesis. Only one adsorption configuration is depicted in Figure 7.2 for the convenience of discussions.

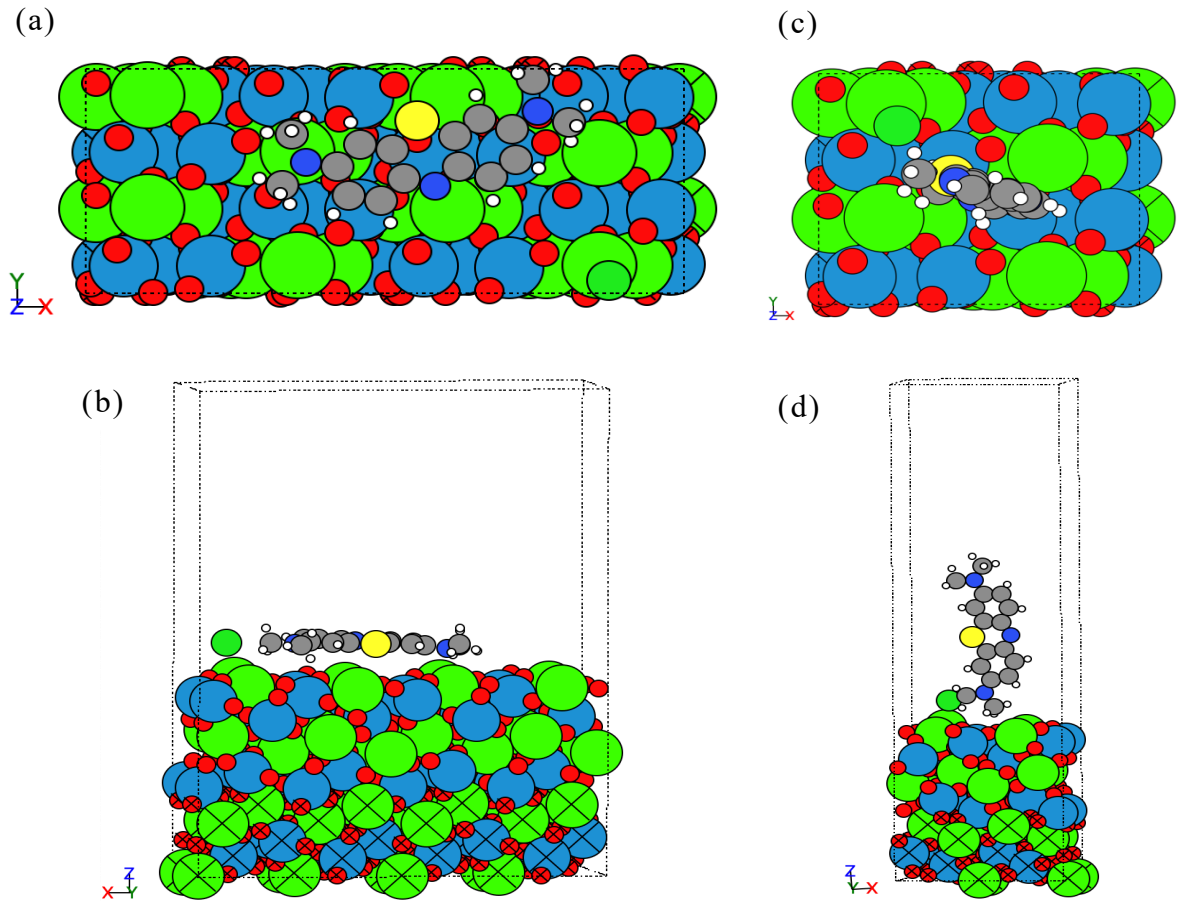

Figure 7.2: Top (a,c) and side view (b,d) of the MB molecule loaded on the (101) surface of $CaWO_4$ thin-film. A layer of vacuum of 20 Å is applied on top of the MB molecule that is parallel to the (101) surface (a,b). A layer of vacuum of 30 Å is applied on top of the MB molecule that is perpendicular to the (101) surface (c,d). The Oxygen (O), Calcium (Ca), Tungsten (W), Hydrogen (H), Carbon (C), Sulfur (S), Nitrogen (N), and Chlorine (Cl) atoms are represented by red, green, mild blue, white, grey, yellow, dark blue, and green-small spheres, respectively.

Overall, a layer of vacuum is applied on top of the MB molecule in the *z*-direction. The periodic boundary condition is applied to the *x* and *y* directions of the simulation domain. The position of atoms of the bottom two slabs are fixed. For the purpose of structural optimization, the H-atoms of the MB molecule are kept at an average distance of 2.16–2.37 Å relative to the (101) surface of the photocatalyst. To avoid the impact of the MB molecules of adjacent computational domains (resulting from the periodic boundary condition in the *x* and *y* directions) on energy calculations, the choice of the $CaWO_4$ supercell is large enough (e.g. (1*a*×2*b*) or (2*a*×2*b*)) on the (101) surface. The distance between the MB molecules of adjacent simulation domains (resulting from the periodic boundary in the *x* and *y* directions) is 7.18 Å (between the atom H5 of MB_1 and the atom H11 of MB_2) or 7.03 Å (between the atom Cl of MB_1 and the atom H1 of MB_2) when the MB molecule is perpendicular to the (101) surface of $CaWO_4$ (Figure 7.3a and b).

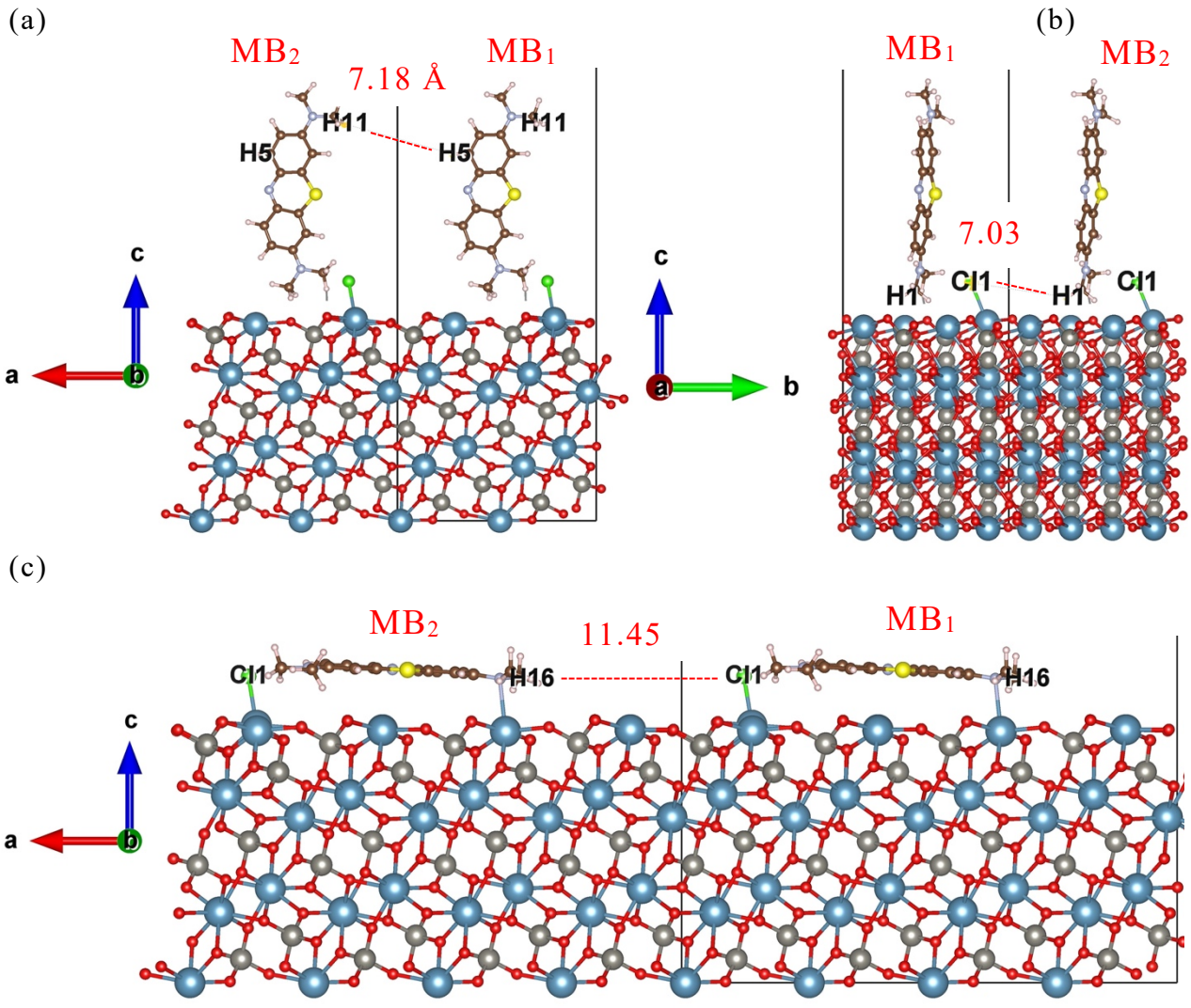

(d)

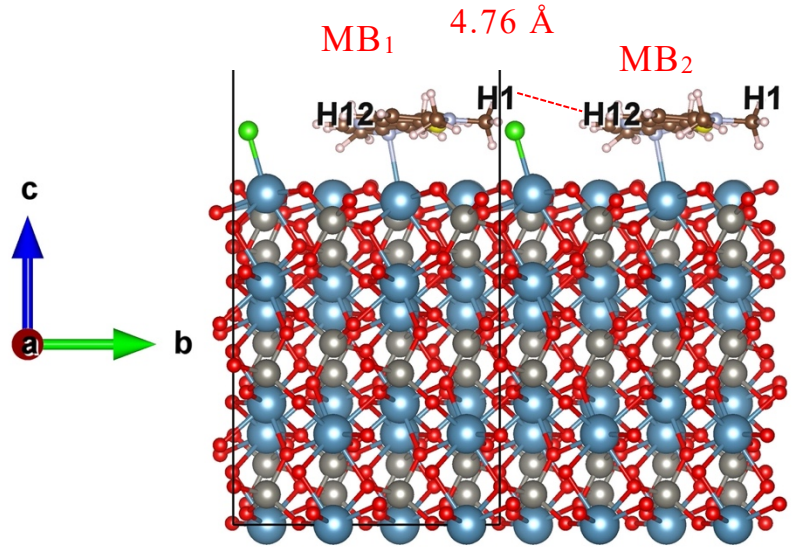

(e)

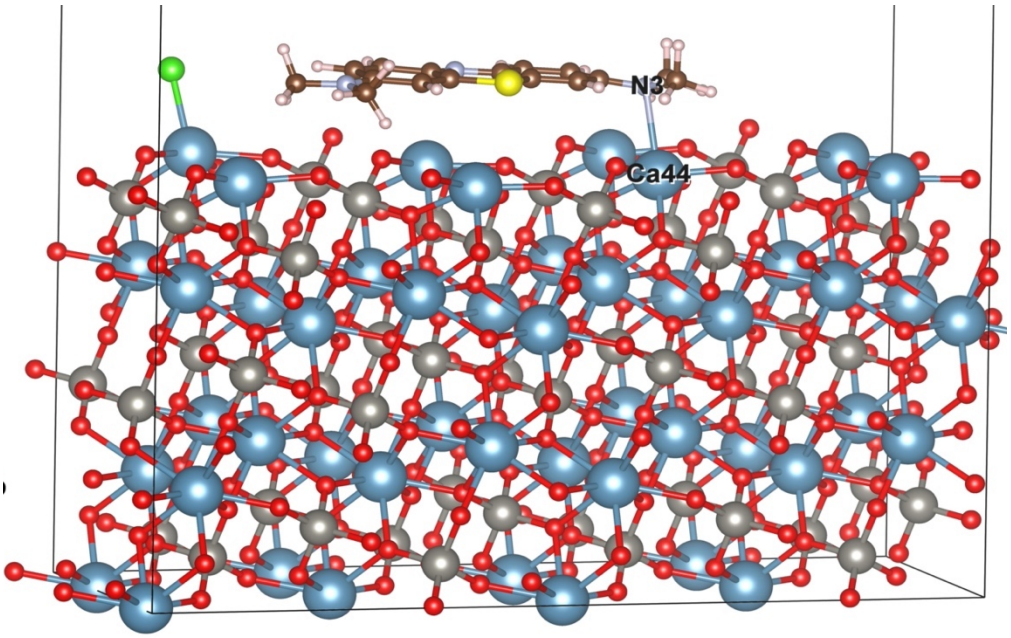

Figure 7.3: The distance between MB molecules in neighbouring simulation domains resulting from the periodic condition. (a) and (b) are the side views in the x and y directions for the perpendicular orientation of the MB molecule, and (c) and (d) are the side views in the x and y directions for the parallel orientation of the MB molecule. (e) is the most stable relaxed structure according to the minimum value of E_{ads}.

The distance is 11.45 Å in the *x* direction (between the atom Cl of MB_1 and the atom H16 of MB_2) or 4.76 Å in the *y* direction (between the atom H1 of MB_1 and the atom H12 of MB_2) when the MB is parallel to the (101) surface of $CaWO_4$ (Figure 7.3c and d). There is a total of 183 atoms in the simulation domain for the MB molecule perpendicular to the (101) surface and there is a total of 327 atoms

in the simulation domain for the MB molecule parallel to the (101) surface. The computational modelling results of the adsorption energy (E_{ads}) of the MB loaded $CaWO_4$ can be seen in Table 7.1. In general, greater negative values of the E_{ads} indicate that the adsorbed systems are more stable, implying a stronger bonding between the MB molecule and the surface of $CaWO_4$ [322].

Table 7.0.1: Computational modelling results of the adsorption energy (E_{ads}), van der waals (vdW) interaction range and charge transfer (Q_t) in the systems of respective configurations

System	Configurations	E_{ads} (eV)	E_{ads} (kJ mol^{-1})	Q_t (e) (From N to surface)	vdW's interaction range (Å)
Coverage test on (101) surface of undoped $CaWO_4$ slab	(H^+) cation	1.18	113.86	-	-
	(O^-) anion	0.70	67.54	-	-
	(OH^-) anion	2.32	223.86	-	-
MB perpendicularly loaded on undoped thin films	I	-0.68	-66.0	-	-
	II	-0.99	-96.1	-	-
	III	-0.79	-76.7	-	-
	IV	-0.71	-68.0	-	-
MB parallelly loaded on undoped thin films	V	-2.46	-237.4	-	-
	VI	-2.54	-245.5	0.836 (N3→Ca44)	2.159-2.908
	VII	-2.45	-236.6	-	-
MB loaded on Cu-doped thin films	$Ca_{47}Cu(WO_4)_{48}$	-2.08	-200.7	0.018 (N1→Ca18)	2.629-2.912
	$Ca_{46}Cu_2(WO_4)_{48}$	-2.74	-264.4	-0.003 (Cu2→N1)	2.539-3.018

When the MB molecule is perpendicular to the (101) surface of the $CaWO_4$, the adsorption energy is between -0.68 eV and -0.99 eV (i.e., about -66 to -96 kJ mol^{-1}). When the MB is parallel to the (101) surface of $CaWO_4$, the adsorption energy is between -2.45 eV and -2.54 eV (i.e., about -236 to -245 kJ mol^{-1}). It means that a strong physisorption exists when the MB molecule is parallel to the $CaWO_4$ surface.

Among the 7 different geometries, configuration VI (N1 and N3 atoms of MB covered the Ca36 and Ca44 of surface atoms respectively, in the parallel

orientations) as shown in Table 7.1 has a substantially stronger binding between the MB and $CaWO_4$ than other configurations. It implies the stronger chemical interaction (i.e., vdW and electrostatic interactions) between the MB molecule and (101) surface of $CaWO_4$. The comparison of all the configurations can be found in Figure. S7.4 of Appendix-C7. Based on the modelling results, it has been determined that the configuration VI has adsorption energy of -2.54 eV (-245 kJ mol^{-1}). This signifies that the adsorption of this configuration is highly efficient compared to the other configurations. Furthermore, since the adsorption strength is greater, it permits a longer duration of energy transfer, leading to a superior degradation of MB when compared to other configurations. These findings highlight that the configuration VI of MB loaded on the (101) surface of undoped and Cu-doped CaWO4 is the most favourable confirmation that can effectively facilitate the photocatalytic degradation of MB on the surface of the photocatalyst. Consequently, this configuration (as shown in Figure 7.3e) has been chosen for further computation modelling and data analysis.

In the configuration as shown in Figure 7.3e (also in Figure 7.4), H and N atoms in MB appear to prefer a location near the surface O and Ca atoms of the $Ca_{48-x}Cu_x(WO_4)_{48}$ due to such the vdW and electrostatic interaction. A N3-Ca44 bond with a bond length of 2.74 Å plays a role in the adsorption mechanism of MB on the (101) surface of $Ca_{48-x}Cu_x(WO_4)_{48}$ because of the electrostatic interaction between the N atom and Ca atom as shown in Figure 7.4b.

(a)

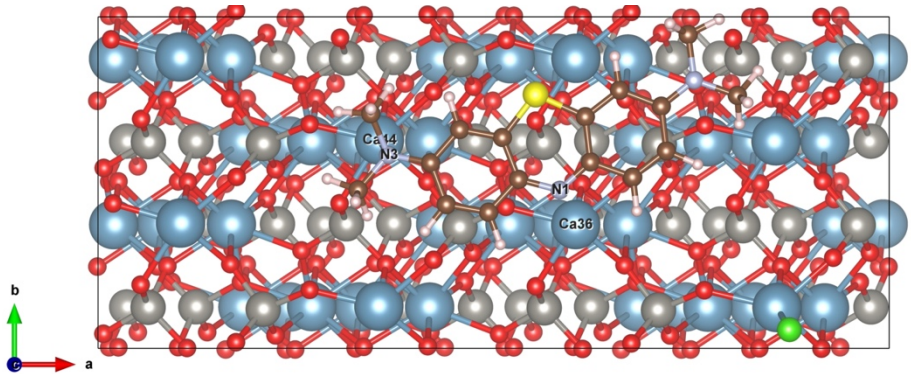

(b)

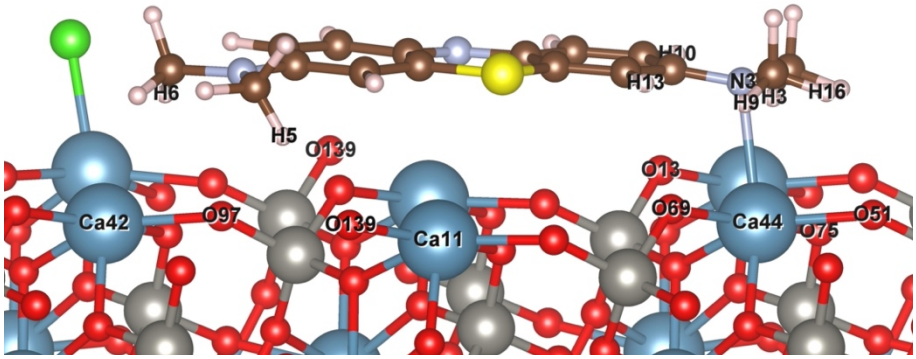
H6
H5
O139
H10
H13
N3
H9
H3
H16
O13
O69
Ca42
O97
O139
Ca11
Ca44
O75
O51

(c)

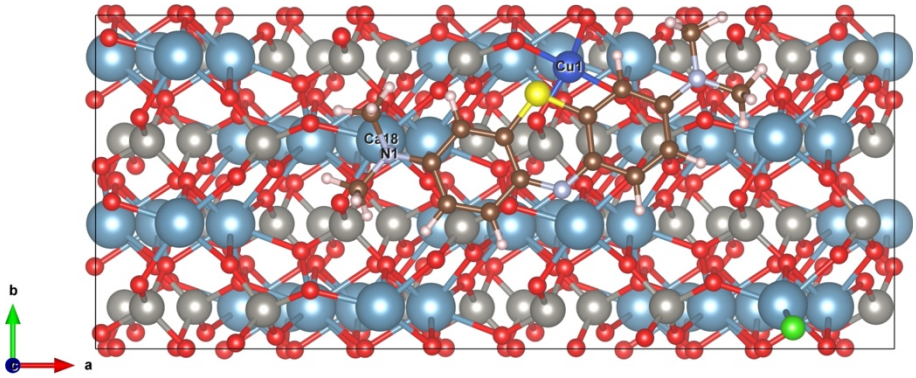
Cu1
Ca18
N1
b
a

(d)

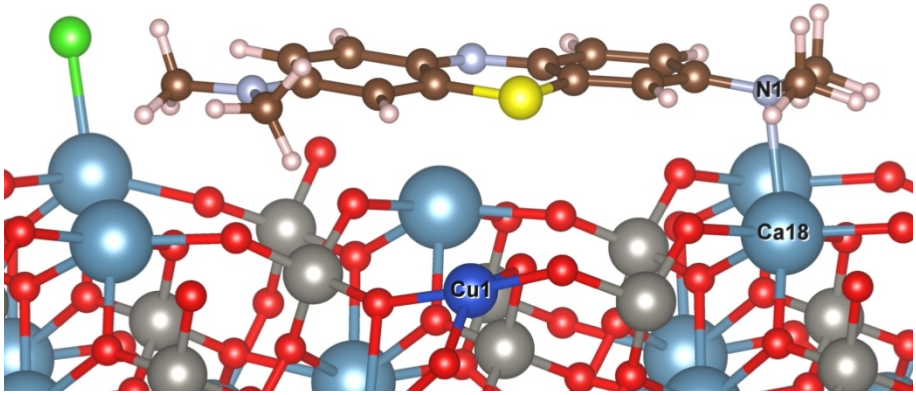
N1
Ca18
Cu1

(e)

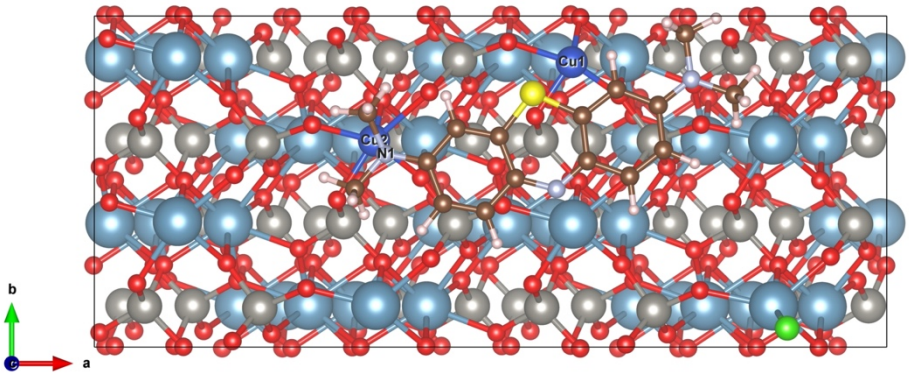
Cu1
N1
b
a

(f)

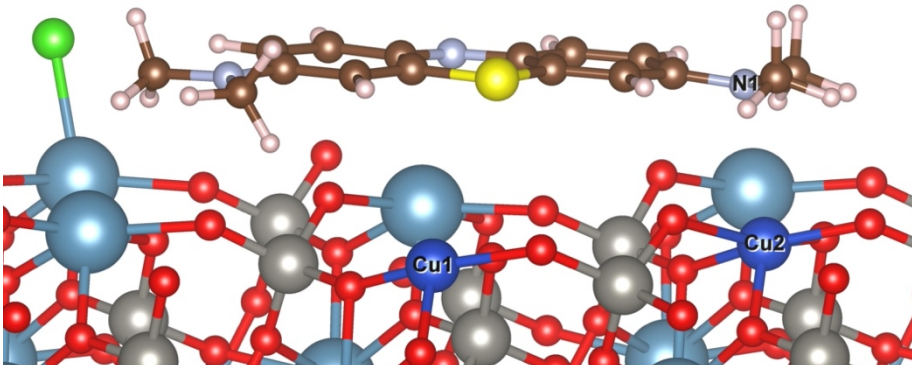

Figure 7.4: MB molecule loaded to the (101) surface of pure $Ca_{48}(WO_4)_{48}$ (a,b), 2.08 at% Cu-doped $Ca_{47}Cu(WO_4)_{48}$ (c,d), and 4.16 at% Cu-doped $Ca_{46}Cu_2(WO_4)_{48}$ (e,f). The Oxygen (O), Calcium (Ca), Tungsten (W), Copper (Cu), Hydrogen (H), Carbon (C), Sulfur (S), Nitrogen (N), and Chlorine (Cl) atoms are represented by using red, mild blue, grey, dark blue, light pink, brown, yellow, silver and green spheres, respectively. (a,c,e) are top views and (b,d,f) are side views.

The quantity of charge transfer (Q_t) from the N3 atom of MB to the surface Ca44 atom is up to 0.836*e*, indicating that the N3-Ca44 interaction is stronger. Based on the Bader charge analysis, the charge of the Ca and O atoms on a clean surface (i.e., undoped (101) surface without MB coverage) is 1.617*e* and -1.062*e*, respectively, whereas the charge of the Ca and O atoms on a surface that is covered by loaded MB molecule (except Cl atom's coverage) is 0.398*e* (up to 0.520*e*) and -0.275*e* (up to -0.617*e*), respectively. In particular, the charge of O51 and Ca11 on the surface loaded with MB drops to -0.066*e* and 0.003*e* (nearly neutral) respectively from their original charge value of -1.062*e* and 1.617*e* on the clean surface. It is important to highlight that, upon MB loading, a reduction in surface Ca^{2+} was observed in $Ca_{48-x}Cu_x(WO_4)_{48}$. These confirm that charges are transferred from the MB molecule to the surface atoms of $Ca_{48-x}Cu_x(WO_4)_{48}$. As a result, due to the process of adsorption, the surface calcium atoms have experienced an augmentation in their electron count, resulting in an altered oxidation state of Ca^{2+} (specifically, transitioning from 6.37 electrons to 7.48 electrons). This transformation has been substantiated through Bader charge

analysis. In conclusion, all of these mean that MB is effectively oxidized on the $Ca_{48-x}Cu_x(WO_4)_{48}$ surface.

Moreover, the vdW interactions between the MB and the $Ca_{48}(WO_4)_{48}$ surface is predominantly created by the H end(s) of the MB molecule connected to the oxygen atom(s) at the top of the surface. As demonstrated in Figure 7.4a, the surface atoms of undoped $Ca_{48}(WO_4)_{48}$ such as O75, O139, O97, O69, O13, O69, and O51 and hydrogen atoms of MB such as H3, H5, H6, H9, H10, H13, and H16 are separated by distances of 2.741, 2.159, 2.908, 2.642, 2.521, 2.578, 2.500, and 2.646 Å, respectively. In addition, the Ca42 is separated from the H6 by 2.908 Å. It is also noteworthy that, as a consequence of the substantial degree of freedom on the (101) surface of $Ca_{48-x}Cu_x(WO_4)_{48}$ that is loaded with MB, the minimum lateral distance among any two Ca atoms on the surface drops by on average 0.014 Å while the bond length between Ca atom and O atom on the surface of $Ca_{48-x}Cu_x(WO_4)_{48}$ nearly remains unchanged in comparison to the clean surface of $Ca_{48}(WO_4)_{48}$ that is not loaded with MB.

Chapter 6 systematically presents the computational modelling research on the $CaWO_4$ with (101) surface exposed that is doped with 2.08 at.% Cu. In Chapter 7, the aim is to investigate how the chemical modification of $CaWO_4$ by doping with Cu can affect the interaction between MB and the modified $CaWO_4$. To achieve this, one or two Ca atoms are replaced with Cu atoms in the supercell in the computational modelling. This is done to account for the doping concentration of 2.08 and 4.16 at.% of Cu, which is denoted as $Ca_{47}Cu(WO_4)_{48}$ and $Ca_{46}Cu_2(WO_4)_{48}$, respectively, in the following sections of the chapter. By using this approach, the modelling results can be used to analyze how increasing the Cu concentration can improve the photocatalytic activity of $CaWO_4$ regarding the interaction with the MB molecule.

In the following sections of this chapter, three systems are analysed. They include the $Ca_{48}(WO_4)_{48}$, $Ca_{47}Cu(WO_4)_{48}$, and $Ca_{46}Cu_2(WO_4)_{48}$, which are loaded with one MB molecule each. Related systems are denoted as MB|$Ca_{48}(WO_4)_{48}$, MB|$Ca_{47}Cu(WO_4)_{48}$, and MB|$Ca_{46}Cu_2(WO_4)_{48}$ respectively (see Figure 7.4). The

computational modelling results of the value of E_{ads} of these systems can be seen in Table 7.1.

Similar to the electrostatic interaction that is observed in the case of MB|$Ca_{48}(WO_4)_{48}$, the Ca18 and N1 separated by 2.688 Å also have electrostatic interaction (i.e., the bond between Ca18-N1) in the MB|$Ca_{47}Cu(WO_4)_{48}$ system as can be seen in Figure 7.4d. However, the bond is not seen in the system of MB|$Ca_{46}Cu_2(WO_4)_{48}$ as shown in Figure 7.4f. In addition, a 3.026 Å distance separates the surface's Cu2 and N1 of the MB (Figure 7.4f), and this distance is larger than that in the case of MB|$Ca_{48}(WO_4)_{48}$ and MB|$Ca_{47}Cu(WO_4)_{48}$. These findings indicate that the higher Cu-doping concentration inhibits the electrostatic interaction between the (101) surface and MB.

In comparison to the system of MB|$Ca_{48}(WO_4)_{48}$, the Q_t from the N1 to Ca18 atom in the MB|$Ca_{47}Cu(WO_4)_{48}$ decreases by 0.818e. This reveals that the electrostatic interaction of N1-Ca18 (Figure 4d) is weaker than the electrostatic interaction of N3-Ca44 (Figure 4b). Ca and O atoms' charges in the MB|$Ca_{47}Cu(WO_4)_{48}$ are 1.121e (up to 1.609e) and -1.009e (up to -1.078e), respectively, while they are 1.607e (up to 1.624e) and -0.929e (up to -1.069e) in the MB|$Ca_{46}Cu_2(WO_4)_{48}$. This clearly demonstrates that in contrast to MB|$Ca_{48}(WO_4)_{48}$, only a small amount of charges transfer from MB to the surface of $Ca_{48-x}Cu_x(WO_4)_{48}$ in the case of MB|$Ca_{47}Cu(WO_4)_{48}$. As a result, Ca18 of MB|$Ca_{47}Cu(WO_4)_{48}$ has the same Ca^{2+} oxidation state (6.40 electrons) as surface Ca-atoms of $Ca_{48}(WO_4)_{48}$ without MB (6.37 electrons). In conclusion, the MB|$Ca_{47}Cu(WO_4)_{48}$ system exhibits slightly weaker adsorption of MB on the surface than the MB|$Ca_{48}(WO_4)_{48}$ system. The distances between Cu and its four coordinated atoms O69, O75, O78, and O82 are 1.933, 1.951, 1.995, and 1.995 Å, respectively. These distances are smaller than those between Ca and its five coordinated O-atoms in MB|$Ca_{48}(WO_4)_{48}$, which range from 2.266 to 2.414 Å. This is caused by the smaller ionic radius of the Cu ion ($r_{Cu^{2+}}$ = 0.73 Å) compared to the Ca^{2+} ($r_{Ca^{2+}}$ = 1.12 Å), which results in the distortion and shrinkage of the lattice of the $Ca_{48-x}Cu_x(WO_4)_{48}$ thin-film.

On the other hand, as surface Cu-doping increases to 4.16 at.% (corresponding to the MB|$Ca_{46}Cu_2(WO_4)_{48}$ system), charges begin to move from the surface of $Ca_{48-x}Cu_x(WO_4)_{48}$ to the MB molecule. The Q_t from the Cu2 to N1 atom is -0.003*e*, indicating MB reduction and surface oxidation (see Figure 7.5c).

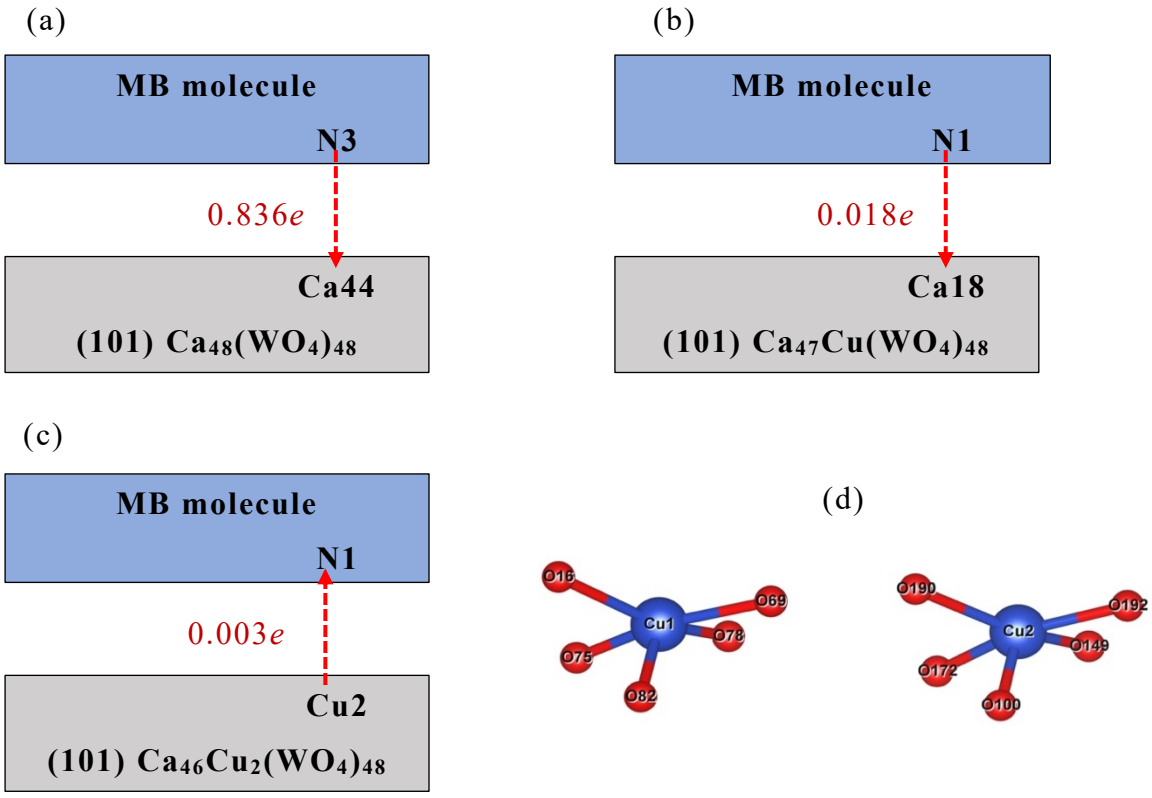

Figure 7.5: Amount of charge transfer between MB and (101) surface of (a) undoped $Ca_{48}(WO_4)_{48}$, (b) 2.08 at% Cu-doped $Ca_{48}(WO_4)_{48}$ and (c) 4.16 at% Cu-doped $Ca_{48}(WO_4)_{48}$. (d) Coordination of Cu with O atoms in the 4.16 at% Cu-doped $Ca_{48}(WO_4)_{48}$ system.

Specifically, the charge of Ca10 in MB|$Ca_{46}Cu_2(WO_4)_{48}$ is slightly raised to 1.624*e* compared to the charges of Ca atoms in $Ca_{48}(WO_4)_{48}$ without MB (1.616*e*), MB|$Ca_{48}(WO_4)_{48}$ (0.398-0.52*e*), and MB|$Ca_{47}Cu(WO_4)_{48}$ (1.597-1.618*e*), indicating charge transfer from Ca10 to MB reflecting the Ca^{2+} oxidation state. The schematic diagram presented in Figure 7.5 provides a clear visual representation of the charge transfer process between MB and photocatalyst surfaces such as $Ca_{48}(WO_4)_{48}$, $Ca_{47}Cu(WO_4)_{48}$, and $Ca_{46}Cu_2(WO_4)_{48}$ (shown in Figure 7.5a, b, and c, respectively). It can help us to better understand how higher Cu-doping concentrations can affect the oxidization of MB molecule.

The Cu dopants such as Cu1 and Cu2 significantly transfer charges to their coordinated and adjacent O-atoms, exhibiting Cu^{2+} oxidation state (i.e., 9.0 and 9.2 Bader electrons, respectively). The distances between Cu1 and its five coordinated atoms O16, O69, O75, O78, and O82 are 2.458, 2.156, 1.930, 2.082, and 2.056 Å, respectively, as well as Cu2 coordinated with five O atoms, and their distances range between 1.981 Å and 2.453 Å (see Figure 7.5d). This lattice distortion and shrinkage can be attributed to the difference in ionic radius between Cu and Ca as seen before in Chapters 5 and 6. All these mean that the tendency of MB reduction reaction becomes more significant when the Cu doping concentration increases. According to the Q_t analysis, it can be concluded that the oxidation of the MB molecule by the $Ca_{48}(WO_4)_{48}$ system is relatively more significant than the other two systems. Therefore, the oxidation strength of the $Ca_{48-x}Cu_x(WO_4)_{48}$ on (101) surface for MB is: MB|$Ca_{48}(WO_4)_{48}$ > MB|$Ca_{47}Cu(WO_4)_{48}$ > MB|$Ca_{46}Cu_2(WO_4)_{48}$.

As observed in the case of MB|$Ca_{48}(WO_4)_{48}$, the vdW predominantly forms between the H ends of the MB molecule and the oxygen atom(s) located on the top of the surface of the photocatalyst, connecting them via vdW interaction. This trend is also evident in the cases of MB|$Ca_{47}Cu(WO_4)_{48}$ and MB|$Ca_{46}Cu_2(WO_4)_{48}$, where the vdW connects the H ends of the MB molecule with the oxygen atoms situated at the top of the surface as shown in Figure 7.6. H-atoms (H2, H3, H6, H9, H13, H16, and H17) of MB|$Ca_{47}Cu(WO_4)_{48}$ (see Figure 7.6a) and H-atoms (H2, H5, H6, H9, H13, H16, and H17) of MB|$Ca_{46}Cu_2(WO_4)_{48}$ (see Figure 7.6b) form vdW with the surface O-atoms of $Ca_{48-x}Cu_x(WO_4)_{48}$ at distances ranging between 2.629 Å and 2.912 Å, and between 2.539 Å and 3.018 Å, respectively. Moreover, the Ca16 atom of MB|$Ca_{47}Cu(WO_4)_{48}$ and MB|$Ca_{46}Cu_2(WO_4)_{48}$ have a vdW with the H13 atom of MB at distances of 2.903 and 2.909 Å, respectively.

(a)

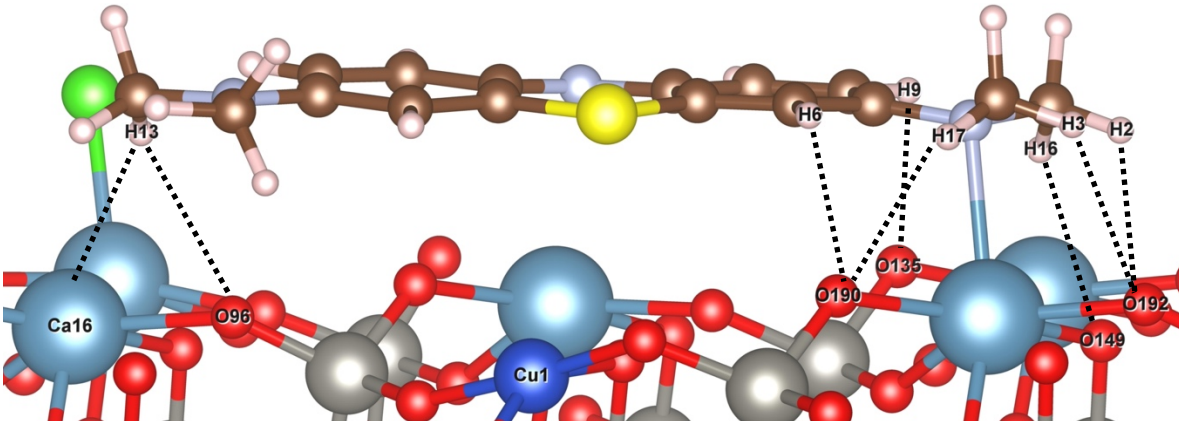

(b)

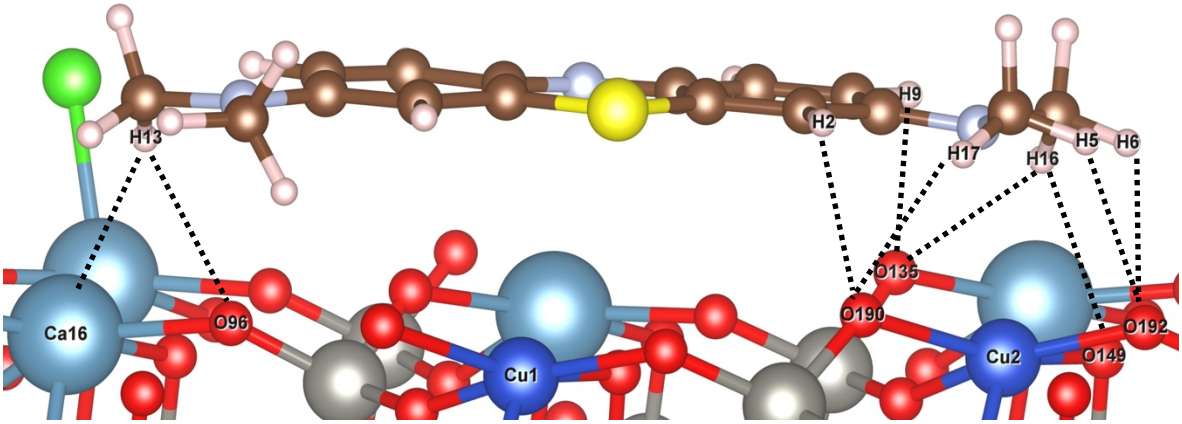

Figure 7.6: MB forms vdW with (101) surface of (a) $Ca_{47}Cu(WO_4)_{48}$ and (b) $Ca_{46}Cu_2(WO_4)_{48}$.

As a consequence of the Cu-doping and substantial degree of freedom on the surface of $Ca_{48-x}Cu_x(WO_4)_{48}$, the lateral distance between Cu1-Ca9 in the MB|$Ca_{47}Cu(WO_4)_{48}$ system dropped by 0.232 Å relative to the lateral distance 5.303 Å of Ca11-Ca36 in MB|$Ca_{48}(WO_4)_{48}$. Similar observations are made for the MB|$Ca_{46}Cu_2(WO_4)_{48}$ system, where the lateral distances between Cu1-Ca10 and Cu2-Ca46 are observed to decrease by 0.118 and 0.038 Å, respectively, as compared to the undoped system. According to the modelling results of E_{ads}, the adsorption energy of the MB|$Ca_{46}Cu_2(WO_4)_{48}$ system is −264.4 kJ/mol, which is considerably less than the adsorption energies of -245.5 and -200 kJ/mol for the MB|$Ca_{48}(WO_4)_{48}$ and MB|$Ca_{47}Cu(WO_4)_{48}$ systems. The observed trend may appear irregular because the project has yet to incorporate the GGA+U calculation, a critical method that provides precise insights into the magnetic ordering (be it ferromagnetism or antiferromagnetism) of the Cu cation. Based on the calculated

E_{ads}, it can be inferred that the interaction between the MB molecule and the $Ca_{46}Cu_2(WO_4)_{48}$ surface is relatively strong. Therefore, the strength of interaction between the MB molecule and the $Ca_{48-x}Cu_x(WO_4)_{48}$ on the (101) surface is: $MB|Ca_{46}Cu_2(WO_4)_{48} > MB|Ca_{48}(WO_4)_{48} > MB|Ca_{47}Cu(WO_4)_{48}$.

7.3.2 Charge Density Difference

The charge density difference (CDD) analysis can be used to support and justify the charge transfer between MB and surface as discussed above. Yellow and blue clouds in Figure 7.7 depict the electron accumulation and depletion, respectively, in the CDD analysis of the MB-loaded $Ca_{48-x}Cu_x(WO_4)_{48}$. These charges are extensively dispersed across the MB molecule, and the charge transfer occurs from the MB molecule to the (101) surface. As shown in Figure 7.7a, dense electrons appear between the N3 of MB and the Ca44 of $Ca_{48-x}Cu_x(WO_4)_{48}$ surface. This demonstrates that the $MB|Ca_{48}(WO_4)_{48}$ forms as the N3 atom of the MB approaches the surface and transfers charges to the Ca44 atom of the $Ca_{48-x}Cu_x(WO_4)_{48}$ surface, contributing to the electrostatic interaction. Moreover, one can also observe charge transfer from MB hydrogen atoms to surface oxygen atoms. Being similar to this, a small amount of electron accumulation appears between the N1-Ca18 (see Figure 7.7b). This charge is more concentrated near the N1 atom of the MB. The transfer of this charge to Ca18 of the $Ca_{48-x}Cu_x(WO_4)_{48}$ surface stabilizes the $MB|Ca_{47}Cu(WO_4)_{48}$ system as can be seen in Figure 7.7b. There is also a charge transfer from MB's interfacial atoms to the surface O atoms of $Ca_{48-x}Cu_x(WO_4)_{48}$. All these mean that loading MB on the (101) surface of $Ca_{48-x}Cu_x(WO_4)_{48}$ leads to a substantial redistribution of charges on the surface, during which charges are primarily transferred from the MB atoms to the atoms on the top layer of the (101) surface. This redistribution of charges helps to stabilize the vdW and electrostatic interactions between MB and the $Ca_{48-x}Cu_x(WO_4)_{48}$ surface. This means that Ca atoms are effectively reduced, and their neighbouring O atoms on the (101) surface stabilize the entire system (i.e. MB loaded $Ca_{48-x}Cu_x(WO_4)_{48}$) by oxidation. These surface O atoms are simultaneously reduced as a result of the MB interfacial hydrogen atoms forming a vdW interaction with them during the adsorption process. It is important to note that the Cu atom is also effectively oxidized by its

coordinated O-atoms in the case of MB|$Ca_{47}Cu(WO_4)_{48}$ as can be seen in Figure 7.7b.

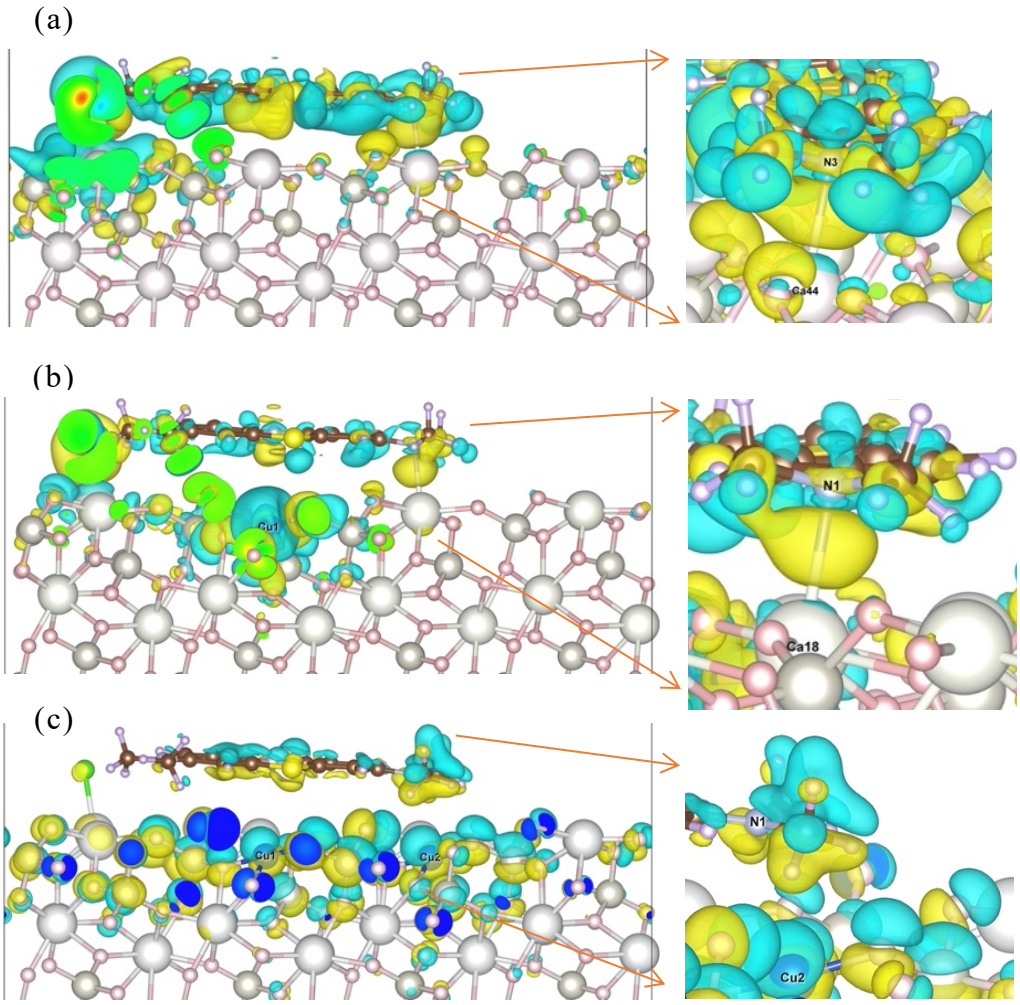

Figure 7.7: Charge density difference (CDD) analysis of (a) MB|$Ca_{48}(WO_4)_{48}$, (b) MB|$Ca_{47}Cu(WO_4)_{48}$, and (MB|$Ca_{46}Cu_2(WO_4)_{48}$).

According to the Bader charge analysis, for the MB|$Ca_{47}Cu(WO_4)_{48}$ system, the top layer atoms on the (101) surface gain electrons, as shown in Figure 7.7b. In MB|$Ca_{47}Cu(WO_4)_{48}$, the top layer O and Ca atoms on the (101) surface of $Ca_{48-x}Cu_x(WO_4)_{48}$ have enriched electron region while most of the interfacial atoms of MB, including H, N, and S atoms, have electron depletion region. For instance, the surface Ca atoms gain -0.25*e* on average during the process of MB adsorption on $Ca_{48-x}Cu_x(WO_4)_{48}$. On the other hand, the higher valence electron capacity of Cu atoms implies their susceptibility to losing their valence electrons readily, as

demonstrated by the electron accumulation across the interface atoms of MB (see Figure 7.7c). This accumulation of electrons suggests that MB can accept charge from the surface atoms, including O, Ca, and Cu of $Ca_{46}Cu_2(WO_4)_{48}$, as illustrated in Figure 7.7c. Hence, increasing the Cu doping concentration from 2.08 to 4.16 at.% on the surface of the $Ca_{48-x}Cu_x(WO_4)_{48}$ results in oxidation of the $Ca_{48-x}Cu_x(WO_4)_{48}$ surface during the MB adsorption process. Consequently, a 4.16 at.% of Cu doping on the surface may not further enhance the breakdown of MB.

All these results demonstrate that there are significant differences among the three systems (i.e. MB|$Ca_{48}(WO_4)_{48}$, MB|$Ca_{47}Cu(WO_4)_{48}$, and MB|$Ca_{46}Cu_2(WO_4)_{48}$) regarding how increasing the Cu doping concentration can affect the MB absorptivity and oxidation. This finding is supported by the analyses of charge transfer, adsorption energy, and electrostatic interactions.

7.3.3 Density of states

The computational modelling results of the electronic properties of MB|$Ca_{48}(WO_4)_{48}$, MB|$Ca_{47}Cu(WO_4)_{48}$ and MB|$Ca_{46}Cu_2(WO_4)_{48}$ are analyzed in this section. Figure 7.8a-c illustrates the spin-up and spin-down of the partial density of states (PDOS) and total density of states (TDOS) for all these three systems, which are calculated using the GGA.

(a)

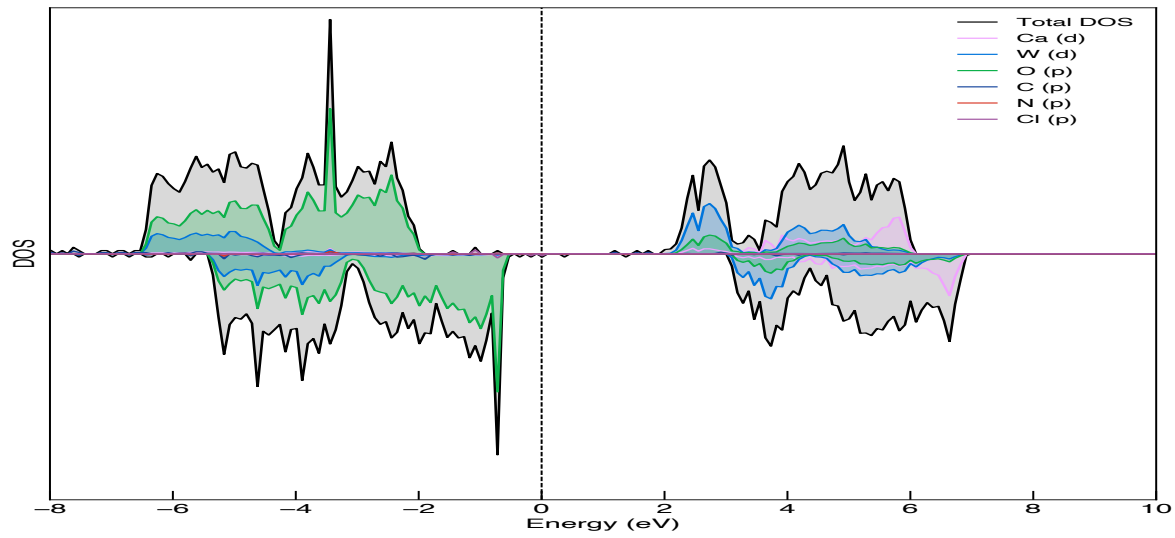

(b)

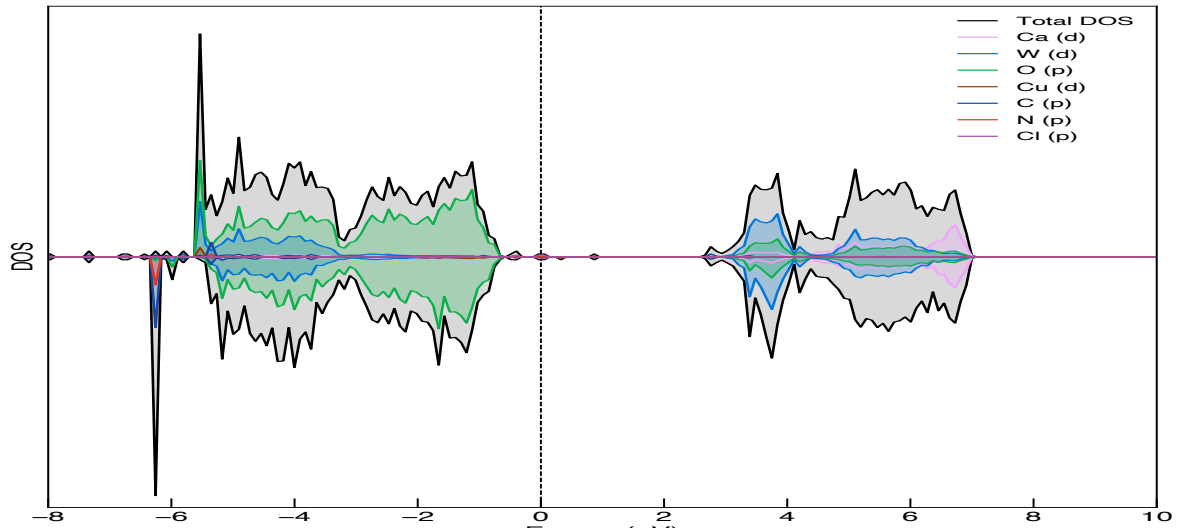
Total DOS
Ca (d)
W (d)
O (p)
Cu (d)
C (p)
N (p)
Cl (p)
DOS
−8
−6
−4
−2
0
2
4
6
8
10

(c)

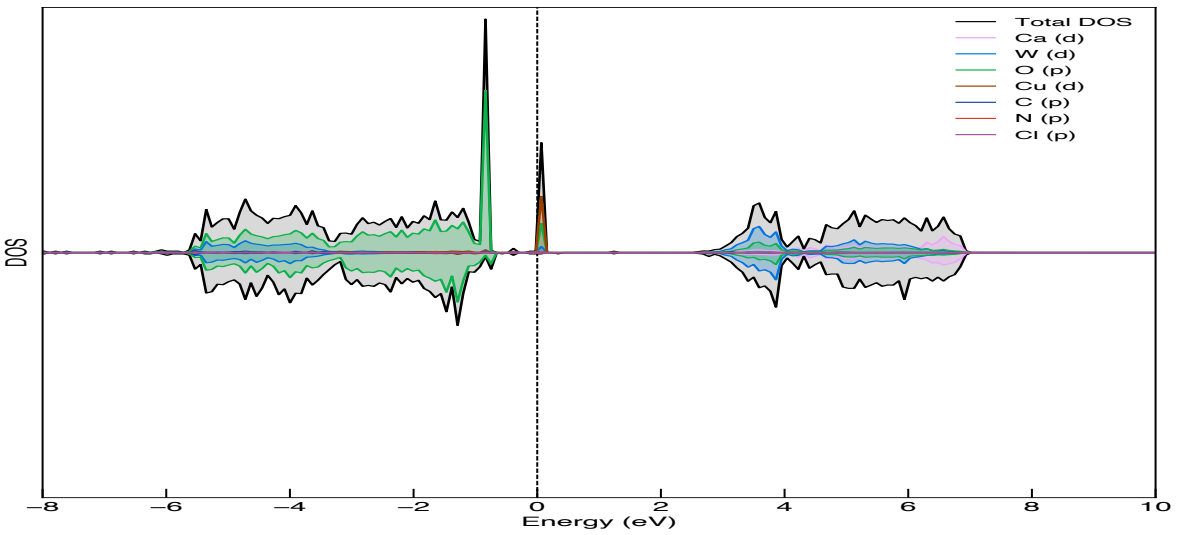
Total DOS
Ca (d)
W (d)
O (p)
Cu (d)
C (p)
N (p)
Cl (p)
DOS
−8
−6
−4
−2
0
2
4
6
8
10
Energy (eV)

(d)

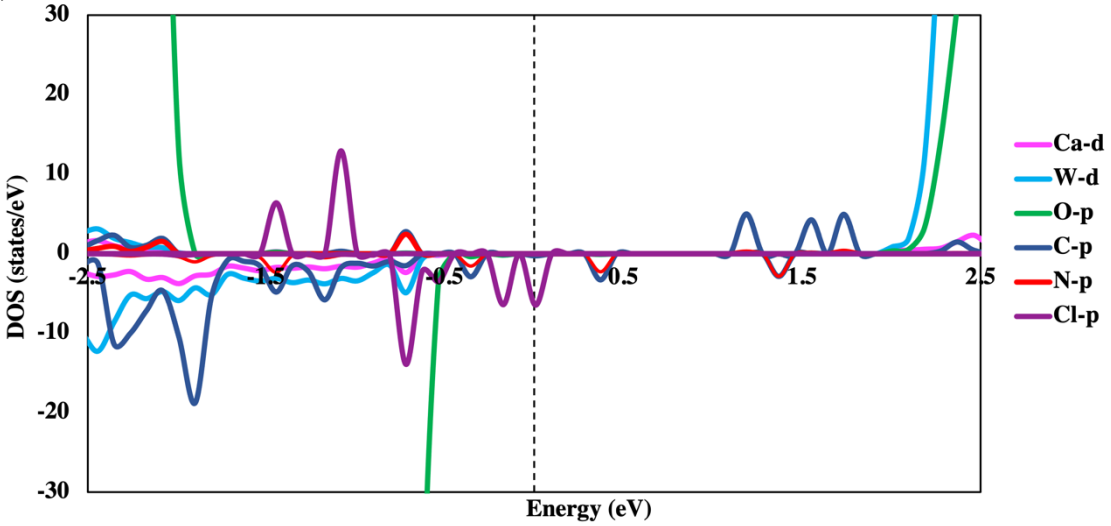
30
20
10
0
-10
-20
-30
-2.5
-1.5
-0.5
0.5
1.5
2.5
DOS (states/eV)
Energy (eV)
Ca-d
W-d
O-p
C-p
N-p
Cl-p

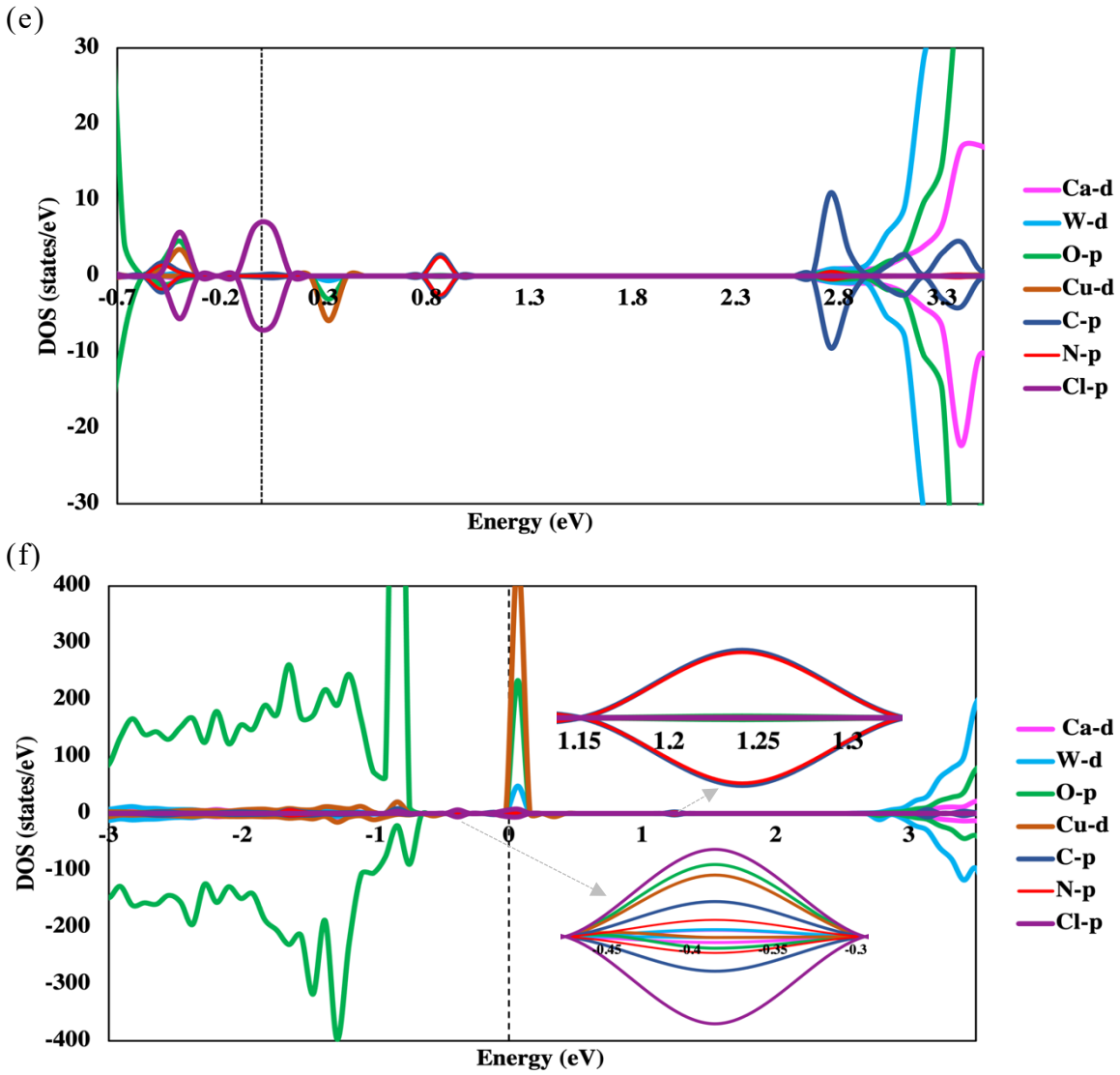

Figure 7.8: Total density of states (TDOS) of (a) MB|$Ca_{48}(WO_4)_{48}$, (b) MB|$Ca_{47}Cu(WO_4)_{48}$ and (c) MB|$Ca_{46}Cu_2(WO_4)_{48}$. (d), (e) and (f) are the partial density of states (PDOS) of MB|$Ca_{48}(WO_4)_{48}$, MB|$Ca_{47}Cu(WO_4)_{48}$ and MB|$Ca_{46}Cu_2(WO_4)_{48}$, respectively. At 0 eV, the Fermi level is displayed by a black dashed line.

In the PDOS profiles, the states that are higher than the Fermi level are considered to be unoccupied. In the configuration such as MB|$Ca_{48}(WO_4)_{48}$, MB|$Ca_{47}Cu(WO_4)_{48}$ and MB|$Ca_{46}Cu_2(WO_4)_{48}$, the O-2p orbitals predominate in the valence band (VB), while W-5d orbitals, accompanied by O-2p and Ca-3d orbitals, predominate in the conduction band (CB) as shown in Figure 7.8a-c. The stable and significant adsorption of MB on the active $Ca_{48-x}Cu_x(WO_4)_{48}$ surface is

reflected by the overlap of the orbitals. For instance, in the VB and CB of MB|$Ca_{48}(WO_4)_{48}$, there is the O-2p and W-5d orbitals hybridization, with their respective energy ranges being roughly -3.1 to -6.4 eV and 2.2 to 6.8 eV as shown in Figure 7.8a. For the MB|$Ca_{47}Cu(WO_4)_{48}$ system as shown in Figure 7.8b, the significant hybridization between the O-2p and W-5d orbitals can be seen below -3.3 eV in the VB region and above 3.4 eV in the CB region. Whereas for the MB|$Ca_{46}Cu_2(WO_4)_{48}$ system as shown in Figure 7.8c, it appears below -3.6 eV in the VB region and above 3.5 eV in the CB region. The presence of dense small DOS peaks around the Fermi energy level (at 0 eV) reveals the potential of $Ca_{48-x}Cu_x(WO_4)_{48}$ to interact with adsorbed species (such as MB) and form electrostatic interactions. The PDOS shown in Figures 7.8d-f demonstrate MB atoms' interaction with surface atoms of $Ca_{48-x}Cu_x(WO_4)_{48}$ in MB|$Ca_{48}(WO_4)_{48}$, MB|$Ca_{47}Cu(WO_4)_{48}$ and MB|$Ca_{46}Cu_2(WO_4)_{48}$. At the Fermi level of MB|$Ca_{48}(WO_4)_{48}$, there are numerous new bands created by spin-down of N-p and C-p orbitals hybridizations (at around -0.35, 0.37, and 1.37 eV), two consecutive spin-down of Cl-p orbitals (at around -0.17 and 0.01 eV, respectively), and spin-up of C-p orbitals (at around 1.18, 1.55, and 1.73 eV). These impurity energy levels (IELs) are schematically depicted in Figure 7.9a. The creation of numerous IELs (i.e., spin up and down) in the MB|$Ca_{48}(WO_4)_{48}$ may facilitate its electron-hole pair recombination.

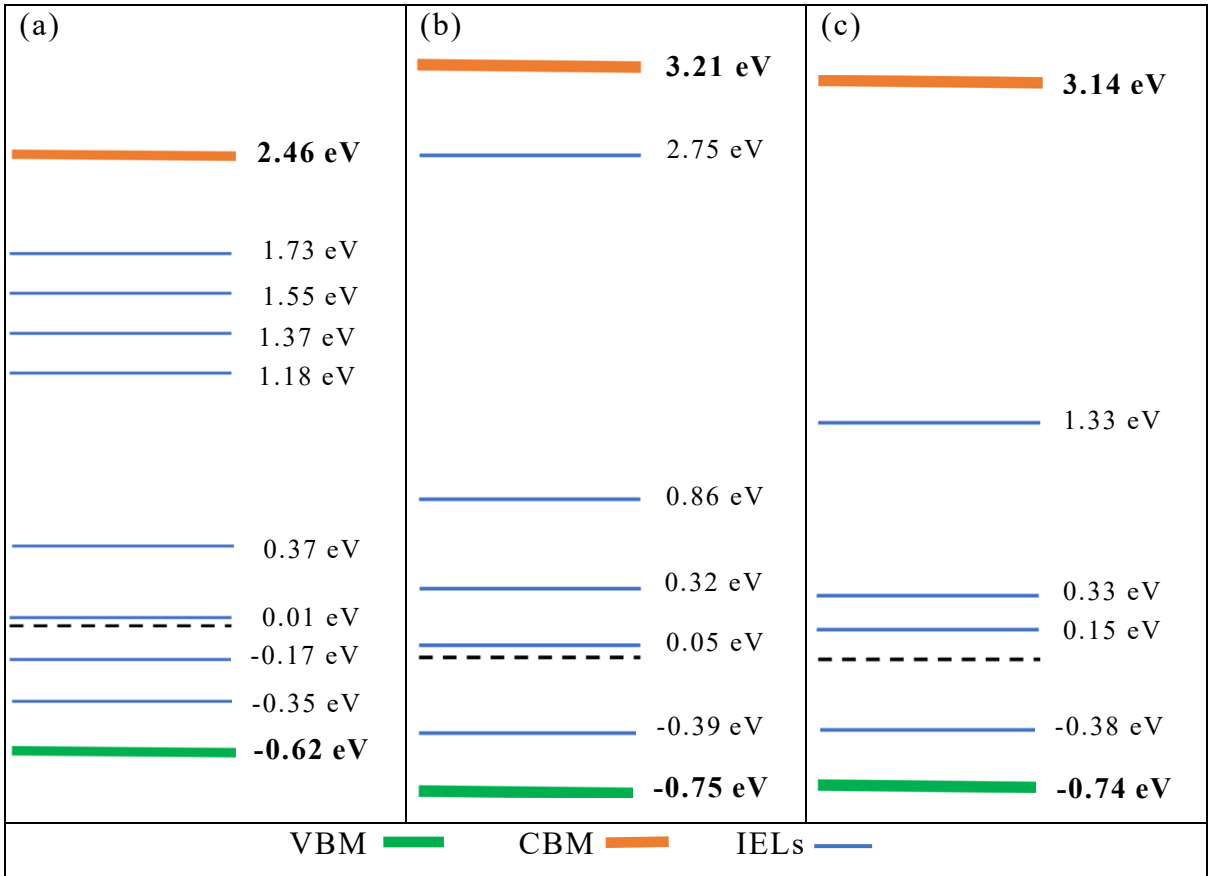

Figure 7.9: Schematic diagram to illustrate the positions of IELs in (a) MB|$Ca_{48}(WO_4)_{48}$, (b) MB|$Ca_{47}Cu(WO_4)_{48}$, and (c) MB|$Ca_{46}Cu_2(WO_4)_{48}$.

In comparison to this, the formation of the new band is much less in MB|$Ca_{47}Cu(WO_4)_{48}$, and they are observed at around -0.39 eV (spin-up: hybridizations of Cl-p, O-p and Cu-d orbitals, and spin-down: Cl-p orbital), 0.05 eV (spin-up and down: Cl-p orbitals), 0.32 eV (spin-down: hybridizations of Cu-d and O-p orbitals), 0.86 eV (spin-up and down: hybridizations of N-p and C-p orbitals), and 2.75 eV (spin-up and down: C-p) which can be seen in Figure 7.9b. In the MB|$Ca_{46}Cu_2(WO_4)_{48}$ system, the formation of new bands is even much less. For example, the emerged bands are observed at around -0.38 eV (spin-up: hybridizations of Cl-p, O-p and Cu-d orbitals, and spin-down: hybridizations of Cl-p and C-p orbitals), 0.15 eV (spin-up: hybridizations of Cu-d, O-p and Ca-d orbitals cause this spike at 0.15 eV in Figure 7.9c), 0.33 eV (spin-down: hybridizations of Cu-d and O-p orbitals), and 1.33 eV (spin-up and down: hybridizations of N-p and C-p orbitals) which can be seen in Figure 7.9c. These modelling results clearly demonstrate that Cu doping at 4.16 at.% or higher may

not result in better adsorption of MB molecule on the (101) surface of $Ca_{48-x}Cu_x(WO_4)_{48}$.

Moreover, the TDOS and PDOS figures of MB|$Ca_{47}Cu(WO_4)_{48}$ and MB|$Ca_{46}Cu_2(WO_4)_{48}$ indicate that the Cu density of states in the two configurations are different. In particular, MB|$Ca_{47}Cu(WO_4)_{48}$ has a low density of Cu-3d orbital which is hybridising with O-2p at 0.32 eV, whereas MB|$Ca_{46}Cu_2(WO_4)_{48}$ has a higher density of Cu-3d orbitals which is hybridising with O-2p and Ca-3d orbitals at 0.15 eV. As a result, the higher Cu dopant (i.e., 4.16 at.%) on the (101) surface of $Ca_{48-x}Cu_x(WO_4)_{48}$ may lead to greater lattice distortion. However, doping with 2.08 at.% Cu has a great beneficial influence on the electronic band structure of the $Ca_{48-x}Cu_x(WO_4)_{48}$. As what is presented in Chapter 6, doping with 2.08 at.% of Cu may enhance the photogenerated carriers' migration and inhibit charge recombination by generating sub-bandgaps (i.e., asymmetric spin distribution due to induced magnetism) in the bandgap region, which serves as a trapping centre for the photogenerated carriers. This enables the effective redox reaction plays an important role in MB photodegradation under visible light. For an effective photocatalysis process, the efficient e^--h^+ pair separation and surface reaction are required which are facilitated by spin polarization and induced magnetism[278,281,282]. The significant asymmetrical distribution of the spin-up and spin-down electrons in DOS of all these three systems implies the presence of induced magnetism. In addition, the presence of numerous IELs (i.e., spin up and down) in MB|$Ca_{48}(WO_4)_{48}$ may enhance the recombination of electron-hole pairs, which could greatly limit the effectiveness of MB|$Ca_{48}(WO_4)_{48}$ in degrading MB under visible light. Overall, it is anticipated that the Cu-doped system such as $Ca_{47}Cu(WO_4)_{48}$ could be very appropriate for MB photodegradation application relative to the other two systems in terms of balanced IELs distribution over the bandgap region. Therefore, the photodegradation ability (i.e., the capacity to facilitate electron-hole pair separation resulting in the formation of radicals for organic pollutant degradation) of the (101) surface of $Ca_{48-x}Cu_x(WO_4)_{48}$ thin films for MB molecule under visible light can follow the order: MB|$Ca_{47}Cu_1(WO_4)_{48}$ > MB|$Ca_{46}Cu_2(WO_4)_{48}$ > MB|$Ca_{48}(WO_4)_{48}$.

7.4 Conclusion

The adsorption of methylene blue (MB) on the pristine $Ca_{48}(WO_4)_{48}$ and Cu-doped surfaces such as $Ca_{47}Cu(WO_4)_{48}$ and $Ca_{46}Cu_2(WO_4)_{48}$ are computationally predicted using spin-polarized DFT-D3 computations embraced in the Vienna ab-initio simulation package (VASP). The structural and electronic properties of related systems are analyzed.

The results demonstrate that MB interacts with the pristine $Ca_{48}(WO_4)_{48}$ by electrostatic interactions and vdW, indicating a strong physisorption mechanism. This structural analysis reveals that the stability of MB loaded $Ca_{48-x}Cu_x(WO_4)_{48}$ system is stronger in MB|$Ca_{48}(WO_4)_{48}$ than in MB|$Ca_{47}Cu(WO_4)_{48}$ or MB|$Ca_{46}Cu_2(WO_4)_{48}$. Therefore, the structural stability of the systems follows the order: MB|$Ca_{48}(WO_4)_{48}$ > MB|$Ca_{47}Cu(WO_4)_{48}$ > MB|$Ca_{46}Cu_2(WO_4)_{48}$.

According to the adsorption energy (E_{ads}) calculation, the adsorption interaction between the MB molecule and the (101) surface of the $Ca_{46}Cu_2(WO_4)_{48}$ system is relatively strong. Therefore, the strength of interaction between the MB molecule and the $Ca_{48-x}Cu_x(WO_4)_{48}$ on the (101) surface are: MB|$Ca_{46}Cu_2(WO_4)_{48}$ > MB|$Ca_{48}(WO_4)_{48}$ > MB|$Ca_{47}Cu(WO_4)_{48}$. In other words, the thermal stability of the MB molecule interacting with the oxides decreases in the order of MB|$Ca_{46}Cu_2(WO_4)_{48}$ > MB|$Ca_{48}(WO_4)_{48}$ > MB|$Ca_{47}Cu(WO_4)_{48}$.

Charge density difference (CDD) and charge transfer (Q_t) analysis revealed that the $Ca_{48}(WO_4)_{48}$ system oxidizes the MB more effectively and has a relatively higher oxidation ability than the other two surfaces. Therefore, the oxidation strength of the (101) surface of $Ca_{48-x}Cu_x(WO_4)_{48}$ thin-film for MB follows the order: MB|$Ca_{48}(WO_4)_{48}$ > MB|$Ca_{47}Cu(WO_4)_{48}$ > MB|$Ca_{46}Cu_2(WO_4)_{48}$.

DOS analysis confirms that doping the photocatalyst with 2.08 at.% Cu (i.e., the $Ca_{47}Cu(WO_4)_{48}$ surface) indicates a more beneficial electronic band structure, while higher Cu dopant concentrations (i.e., 4.16 at.%) may lead to greater lattice distortion. Such electronic band structure enhances the photocatalytic activity of

$Ca_{47}Cu(WO_4)_{48}$ by generating new bands (i.e., IELs) in the bandgap region, which serves as a trapping centre for the photogenerated carriers. In addition to its favourable electronic band structure, $Ca_{47}Cu(WO_4)_{48}$ also demonstrates a relatively strong adsorption strength regarding the MB molecule, indicating higher stability, stronger vdW and electrostatic interactions than MB|$Ca_{46}Cu_2(WO_4)_{48}$. All of this enables the effective redox reaction facilitating the MB photodegradation. Increasing the Cu doping concentration from 2.08 to 4.16 at.% results in oxidation of the $Ca_{48-x}Cu_x(WO_4)_{48}$ surface during the MB adsorption process. Consequently, the surface of $Ca_{46}Cu_2(WO_4)_{48}$ may not better enhance the breakdown of MB compared with $Ca_{47}Cu(WO_4)_{48}$. In addition to this, the DOS analysis clearly reveals that Cu doping of 4.16 at.% is not advantageous regarding the adsorption of MB molecule due to less new band generation around the Fermi level. Furthermore, the presence of numerous IELs in MB|$Ca_{48}(WO_4)_{48}$ may enhance the recombination of electron-hole pairs, which could effectively limit the effectiveness of MB|$Ca_{48}(WO_4)_{48}$ in degrading MB under visible light. Therefore, the photodegradation ability of the (101) surface of $Ca_{48-x}Cu_x(WO_4)_{48}$ thin film for MB molecule under visible light follows the order: MB|$Ca_{47}Cu(WO_4)_{48}$ > MB|$Ca_{46}Cu_2(WO_4)_{48}$ > MB|$Ca_{48}(WO_4)_{48}$.

Overall, the $Ca_{47}Cu(WO_4)_{48}$ may have great application in the photodegradation of MB due to its related beneficial properties such as higher photodegradation ability, more beneficial electronic band structure, more stability, stronger physisorption (i.e., stronger vdW and electrostatic interactions), and good oxidation strength on MB.

Chapter 8:

Conclusions

Chapter 1 and Chapter 2 of the thesis describe the background, aim, objectives and research questions of this PhD project. With the results presented in Chapters 4-7 and the discussions provided, we are confident that we can answer appropriately to the research questions posed at the beginning of the thesis.

What could be the optimal co-doping concentration for bulk anatase TiO_2 with Zn^{2+} and La^{3+}? (Chapter 4)

In the computational modelling as presented in Chapter 4, the TiO_2 was single-doped separately with Zn^{2+} and La^{3+} cations at concentrations ranging from 2.08 to 10.41 at.%. The lowest bandgap values of 1.92 and 1.73 eV were observed when TiO_2 was doped with 2.08 at.% of La^{3+} and separately 6.25 at.% of Zn^{2+}. The modelling results reveal how the Zn ion and La ion may affect the electronic properties of the TiO_2 regarding related underlying mechanisms. The modelling results were also used to verify the computational modelling methods of this project. Co-doping TiO_2 simultaneously with Zn and La was then computationally analysed at concentrations ranging from 4.17 to 10.41 at.%, and the optimal combination was found to be 6.25 at.% of Zn^{2+} plus 2.08 at.% of La^{3+} cations, resulting in the lowest bandgap value of 1.85 eV. It was found that the bandgap value of such co-doped TiO_2 is still greater than the minimum bandgap value of Zn-doped TiO_2, which was interpreted in Chapter 4.

How and why does the co-doping using Zn^{2+} and La^{3+} metal cations influence TiO_2's photocatalytic properties? (Chapter 4)

The modelling results reveal that doping the oxide using elements such as Zn and La can create extra impurity energy levels (IELs) in the electronic band structure of the oxide. On one hand, single doping the oxide with Zn^{2+} or La^{3+} can shift the VBM of the material from -1.4 eV to 0.49 eV or -0.1 eV, compared to pure TiO_2. On the other hand, the co-doped systems VBM is moved to 0.51 eV mainly due to the influence of Zn^{2+}, because of the IELs in the VB. In addition, since this shift of VBM pushes the Fermi level of co-doped materials towards the VB region, Zn^{2+} and La^{3+} co-doping change the TiO_2 from n-type to p-type semiconductors. Due to the synergistic effects of these two metal ions, the co-doped system

($Ti_{12}LaZn_3O_{32}$) has a much less value of bandgap value than pure TiO_2 by 0.27 eV. Since Ti^{2+} (0.86 Å) gets replaced by cations having a different ionic radius, such as Zn^{2+} (0.75 Å) and La^{3+} (1.16 Å), the $Ti_{12}LaZn_3O_{32}$ has a deformed lattice structure relative to pure TiO_2 and there is an overall volume expansion by 6%.

The co-doped system's narrow bandgap allows photoexcited electrons to move from VBM to CBM with less energy than pure TiO_2. The well-dispersed bands at both band edges due to co-doping with Zn^{2+} and La^{3+} take the role of holders for the photoexcited carriers when electron-hole pair separation occurs. It makes their recombination process more difficult and increases the photoinduced charge carrier lifespan. All these factors improve the overall photocatalytic activity of $Ti_{12}LaZn_3O_{32}$. As a result, the photo-absorption nature of the co-doped system $Ti_{12}LaZn_3O_{32}$ expands into the region of visible light. In addition, $Ti_{12}LaZn_3O_{32}$ showed good stability with a formation energy of -1.342 eV.

What could be the impact of Cu-doping on the photocatalytic properties of bulk $CaWO_4$, and what is the underlying mechanism? (Chapter 5)

Chapter 5 systematically describes how the Cu doping concentration) influences the electronic band structure of the bulk $Ca_{32-x}Cu_x(WO_4)_{32}$ system. The bandgap value of 3.125 at.% Cu doped system ($Ca_{31}Cu(WO_4)_{32}$) is 3.35 eV, which is lower than the bandgap value of pure $Ca_{32}(WO_4)_{32}$ (4.07 eV). As a result of the formation of additional IELs within the CB, VB, and energy bandgap, the bandgap value of $Ca_{31}Cu(WO_4)_{32}$, $Ca_{30}Cu_2(WO_4)_{32}$, $Ca_{28}Cu_4(WO_4)_{32}$, $Ca_{25}Cu_7(WO_4)_{32}$, and $Ca_{24}Cu_8(WO_4)_{32}$ is 3.35 eV to 2.66, 2.35, 2.21, and 2.02 eV as the Cu doping concentration increases from 6.25 to 25.0 at.%. Particularly, slightly doping $CaWO_4$ with such as 3.125 at.% and 6.25 at.% Cu has a much more significant influence on the value of bandgap compared with doping with greater Cu concentrations.

The absorption edge of $Ca_{32-x}Cu_x(WO_4)_{32}$ red-shifts towards a greater wavelength as the Cu^{2+} concentration increases from 0 to 25.0 at.%. The volume and bond length (i.e., between Ca/Cu and O atoms) of $Ca_{32-x}Cu_x(WO_4)_{32}$ are different from those of the undoped $Ca_{32}(WO_4)_{32}$ because Cu atoms have a much smaller atomic

radius (r_{Cu} = 145 pm) than Ca atoms (r_{Ca} = 194 pm). Cu^{2+} change the electrical band structure and crystal lattice structure of the $Ca_{32-x}Cu_x(WO_4)_{32}$.

How does Cu-doping affect the electronic properties of $Ca_{48}(WO_4)_{48}$ thin film with the (101) surface exposed, and what is the underlying mechanism? (Chapter 6)

Chapter 6 presents the computational modelling research on the Cu-doped $Ca_{48}(WO_4)_{48}$ thin film that has the (101) surface exposed, regarding such as the photocatalytic properties. The modelling results of the formation energy confirm the thermal stability of the Cu-doped systems. The Cu-doped systems are predicted to be able to efficiently absorb visible light as well as IR radiation due to widely dispersed Cu-3d states, particularly above the VBM of the materials, which form substantial sub-bandgaps. This reduces the size of the native thin film bandgap significantly and induces magnetism, which increases the optical absorption by encouraging e^--h^+ pair separation and reducing the e^--h^+ pair recombination rate.

Interestingly, the $Ca_{48}(WO_4)_{48}$ thin film, with its exposed (101) surface, shows a notable reduction in bandgap by 0.39 eV compared to the bulk $Ca_{48}(WO_4)_{48}$. On one hand, the positions and bond lengths of WO_4 and CaO_8 entities within the core of the thin film remain unchanged in comparison to the bulk $Ca_{48}(WO_4)_{48}$ material. On the other hand, it is significant to observe that the Ca atoms on the thin film surface exhibit undercoordinated behaviour.

What would be the interaction between the MB molecule and Cu-doped $Ca_{48}(WO_4)_{48}$ thin film on the (101) surface? (Chapter 7)

In the computational modelling research as presented in Chapter 7, a MB molecule is loaded on the (101) surface of the $Ca_{48-x}Cu_x(WO_4)_{48}$ thin film. The MB interacts with the $Ca_{48-x}Cu_x(WO_4)_{48}$ thin-film by electrostatic interactions and vdW, indicating a strong physisorption mechanism. The MB|$Ca_{47}Cu(WO_4)_{48}$ system exhibits very significant adsorption behaviour on the (101) surface due to the stronger vdW and electrostatic interaction compared to MB|$Ca_{46}Cu_2(WO_4)_{48}$. This enables the effective redox reaction, which is one of the fundamental mechanisms

for MB photodegradation. Moreover, the heightened physisorption of MB onto the $Ca_{47}Cu(WO_4)_{48}$ surface contributes significantly to the stabilization of MB on the $Ca_{48-x}Cu_x(WO_4)_{48}$ surface, thereby ensuring the overall stability of the system.

Therefore, the photodegradation ability of the (101) surface of $Ca_{48-x}Cu_x(WO_4)_{48}$ thin film for MB molecule under visible light follows the order: $MB|Ca_{47}Cu(WO_4)_{48} > MB|Ca_{46}Cu_2(WO_4)_{48} > MB|Ca_{48}(WO_4)_{48}$.

Overall, the $Ca_{47}Cu(WO_4)_{48}$ may have great application in the photodegradation of MB due to its related beneficial properties such as higher photodegradation ability, more beneficial electronic band structure, more stability, stronger physisorption (i.e., stronger vdW and electrostatic interactions), and good oxidation strength on MB.

How would the doping concentration of Cu affect the photocatalytic and adsorption properties of Cu-doped $Ca_{48}(WO_4)_{48}$ thin film that is loaded with MB? (Chapter 7)

According to the structural analysis presented in Chapter 7, MB interacts with the undoped $Ca_{48}(WO_4)_{48}$ through vdW and electrostatic interactions, pointing to a strong physisorption mechanism. This phenomenon becomes less prevalent when the amount of Cu-doping increases on the (101) surface of the photocatalyst. The surface stability of MB loaded $Ca_{48-x}Cu_x(WO_4)_{48}$ follows the ordered : $MB|Ca_{48}(WO_4)_{48} > MB|Ca_{47}Cu(WO_4)_{48} > MB|Ca_{46}Cu_2(WO_4)_{48}$.

On one hand, the calculations of adsorption energy indicate that the strength of adsorption between the MB molecule and the $Ca_{48-x}Cu_x(WO_4)_{48}$ surface is notably higher in the case of the 4.16 at.% Cu-doped surface ($MB|Ca_{46}Cu_2(WO_4)_{48}$) compared to other configurations. On the other hand, while doing 2.08 at.% Cu improves the MB's photooxidation process, the Bader charge and charge density differential analysis reveal that the MB's photooxidation process deteriorates when the Cu doping concentration further increases from 2.08 to 4.16 at.%. In particular, raising the Cu doping level from 2.08 to 4.16 at.% (i.e. corresponding to the $Ca_{46}Cu_2(WO_4)_{48}$ system) causes oxidation to the $Ca_{46}Cu_2(WO_4)_{48}$ rather than the

MB molecule after loading the MB molecule to the (101) surface of $Ca_{46}Cu_2(WO_4)_{48}$. Consequently, the $Ca_{46}Cu_2(WO_4)_{48}$ system is worse than the $Ca_{47}Cu(WO_4)_{48}$ system regarding breaking down the MB. Moreover, the modelling results of the DOS of related materials reveal that there are fewer new bands generated around the Fermi level in $Ca_{46}Cu_2(WO_4)_{48}$ compared with $Ca_{47}Cu(WO_4)_{48}$. This analysis also confirms that doping the photocatalyst with 2.08 at.% Cu produces a more beneficial electronic band structure, while higher Cu dopant concentrations (i.e., 4.16 at.%) may lead to greater lattice distortion. Therefore, the adsorption properties of MB molecules on the (101) surface of $Ca_{46}Cu_2(WO_4)_{48}$ are worse than those on the (101) surface of the $Ca_{47}Cu(WO_4)_{48}$ system.

Final perspective

Overall, in this project, computational modelling based on the DFT method is employed to systematically predict the influence of doping metal oxide photocatalysts using transition metals on the electronic and photocatalytic properties of the chemically modified oxides. A primary focus is given to examining the interaction between a model organic waste (i.e., MB) and the photocatalysts. TiO_2 and $CaWO_4$ are used as the target materials of the project. The modelling research on the TiO_2 system validates the employment of such modelling methodology in this type of research. The computational prediction of the $CaWO_4$ systems reveals some very interesting properties of the systems. For example, there is a transition between the direct band and the indirect band (as well as vice versa) while the Cu doping concentration increases. Cu doping may induce magnetism in the material. The interaction between the MB molecule and the chemically modified $CaWO_4$ is of great interest in this project. The modelling results show that slightly doping the $CaWO_4$ with Cu can enhance the oxidation of the MB module due to the related charge transition process in the MB loaded $Ca_{48-x}Cu_x(WO_4)_{48}$. However, when over doping the $Ca_{48-x}Cu_x(WO_4)_{48}$ with Cu, the oxidation happens to $Ca_{48-x}Cu_x(WO_4)_{48}$ rather than the MB.

Overall, the computational modelling research of this project found that slightly doping the $CaWO_4$ using Cu can very effectively improve the photocatalytic

properties of the oxide. Specifically, the $Ca_{47}Cu_1(WO_4)_{48}$ system can very effectively use optical light in conjunction with some IR spectrum of solar radiation. It has reasonably good stability, regarding the thermal stability as well as the photogenerated electron-hole pair. It can cause effective oxidation to the model organic waste MB when loading the MB molecule to the (101) surface of $Ca_{47}Cu_1(WO_4)_{48}$. Additionally, the surface's heightened physisorption capability plays a crucial role in stabilizing the adsorption of MB on its surface. It is noted that over doping the $CaWO_4$ with 4.16% (or maybe more) Cu can deteriorate related photocatalytic properties of the $Ca_{48-x}Cu_x(WO_4)_{48}$ system. Conclusively, 2.08 at.% is the optimal Cu doping concentration of $CaWO_4$ according to the computational modelling results of this project.

Appendix

Appendix-C5

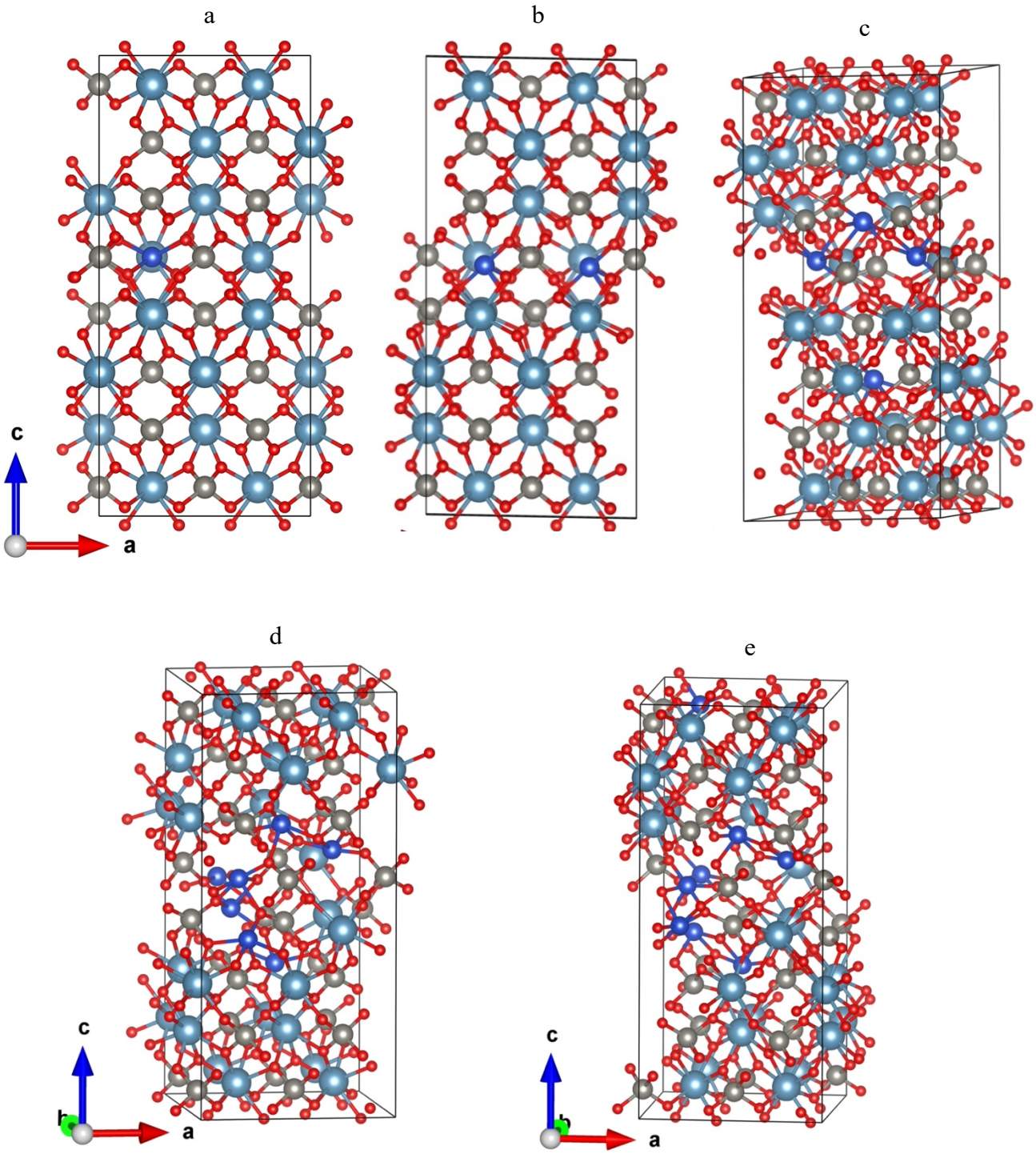

Figure. S5.1: Relaxed crystal structure of Cu^{2+}-doped $Ca_{32}(WO_4)_{32}$: (a) $Ca_{31}Cu(WO_4)_{32}$, (b) $Ca_{30}Cu_2(WO_4)_{32}$, (c) $Ca_{28}Cu_4(WO_4)_{32}$, (d) $Ca_{25}Cu_7(WO_4)_{32}$, (e) $Ca_{24}Cu_8(WO_4)_{32}$.

Table S5.1: Distance range between Cu atoms and its nearby coordinated O atoms in angstrom unit (Å).

Materials	Cu_1-O	Cu_2-O	Cu_3-O	Cu_4-O	Cu_5-O	Cu_6-O	Cu_7-O	Cu_8-O
$Ca_{32}(WO_4)_{32}$	-	-	-	-	-	-	-	-
$Ca_{31}Cu(WO_4)_{32}$	2.22	-	-	-	-	-	-	-
$Ca_{30}Cu_2(WO_4)_{32}$	1.95-2.44	1.95-2.44	-	-	-	-	-	-
$Ca_{28}Cu_4(WO_4)_{32}$	1.98-2.18	1.96-2.23	1.99-2.45	1.99-2.28	-	-	-	-
$Ca_{25}Cu_7(WO_4)_{32}$	1.94-2.33	1.93-1.97	1.88-2.06	1.95-2.25	1.95-2.35	1.95-2.33	2.00-2.24	-
$Ca_{24}Cu_8(WO_4)_{32}$	1.98-2.27	2.04-2.19	1.98-2.05	1.94-1.99	1.96-2.29	1.94-2.23	1.93-2.26	1.92-2.25

Table S5.2: Distance between any nearby Cu atoms within the simulation domain.

Materials	Distance between any nearby Cu atoms	Distance in Å
$Ca_{32}(WO_4)_{32}$	-	-
$Ca_{31}Cu(WO_4)_{32}$	-	-
$Ca_{30}Cu_2(WO_4)_{32}$	Cu_1-Cu_2	5.28
$Ca_{28}Cu_4(WO_4)_{32}$	Cu_1-Cu_2	5.28
	Cu_1-Cu_4	3.27
	Cu_1-Cu_3	7.39
	Cu_2-Cu_4	3.23
	Cu_2-Cu_3	6.92
	Cu_3-Cu_4	8.49
$Ca_{25}Cu_7(WO_4)_{32}$	Cu_3-Cu_4	3.23
	Cu_4-Cu_6	3.81
	Cu_4-Cu_1	4.88
	Cu_4-Cu_2	6.42

	Cu_4-Cu_7	3.23
	Cu_6-Cu_1	5.71
	Cu_1-Cu_7	3.66
	Cu_7-Cu_2	5.25
	Cu_7-Cu_5	3.65
	Cu_5-Cu_2	3.14
$Ca_{24}Cu_8(WO_4)_{32}$	Cu_6-Cu_1	3.21
	Cu_6-Cu_4	5.73
	Cu_6-Cu_7	4.09
	Cu_6-Cu_8	5.17
	Cu_6-Cu_3	3.69
	Cu_3-Cu_5	3.24
	Cu_8-Cu_3	3.98
	Cu_4-Cu_7	3.06
	Cu_7-Cu_2	7.81

Appendix-C6

Table S6.1: Modelling results of the convergence test to determine the optimum thickness of the thin film.

Surface energy (E_{sur}) of Slabs								
Number of Facets	Number of Atoms	Total Energy (eV)	Number of Unit Cell	Energy of Bulk (eV)	lattice a (Å)	lattice b (Å)	E_{sur} (eV)	ΔE_{sur} (eV)
2	48	-394.096	2	-205.639	12.626	5.280	0.128	0
3	72	-599.725	3				-4.497	-4.626
4	96	-805.34	4				-6.039	-1.542
5	120	-1010.99	5				-7.582	-1.542
6	144	-1226.7	6				-9.199	-1.617

Appendix-C7

O atoms of (101) surface is covered by H^+ cation.

(a)

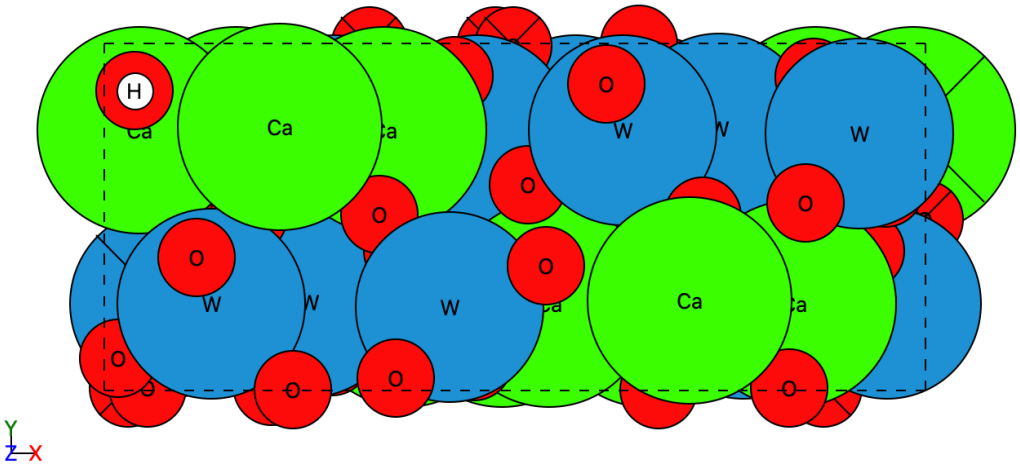

(b)

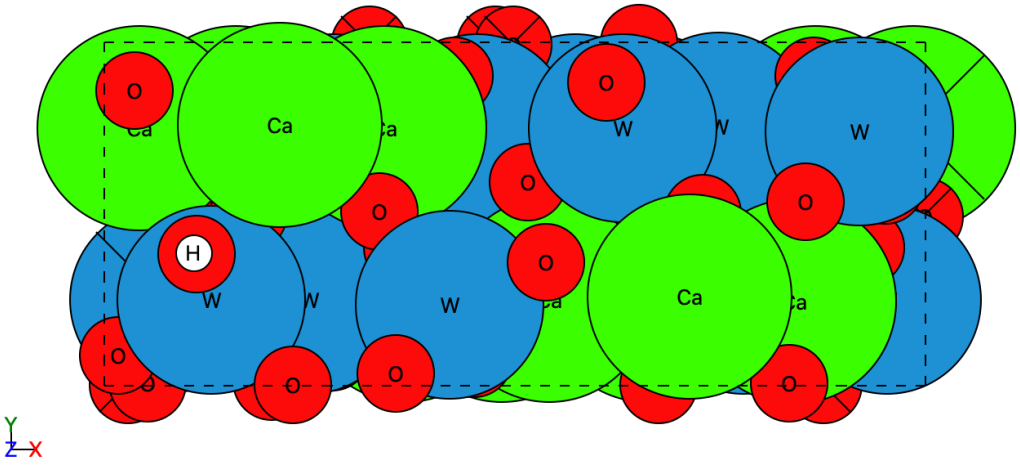

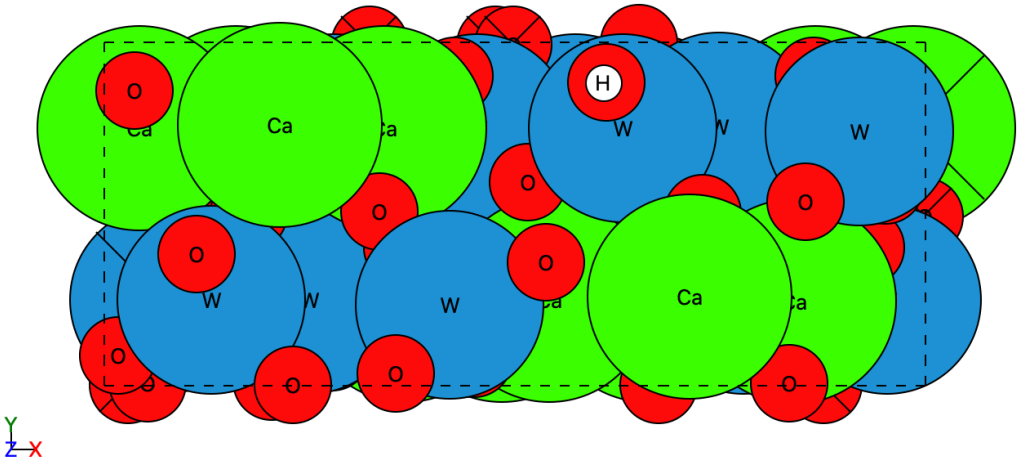

(d)

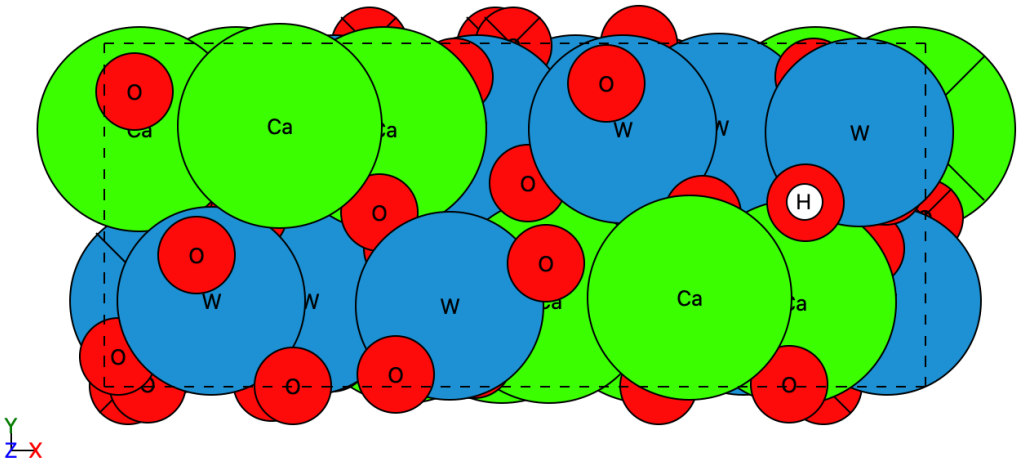

Figure. S7.1: To test the coverage of H^+ ions, all surface oxygens are taken into consideration, with each of the four surface Os individually covered and displayed in (a)-(d). Red sphere: Oxygen (O)-atom, Green sphere: Calcium (Ca)-atom, Blue sphere: Tungsten (W)-atom, White sphere: Hydrogen cation (H^+).

Ca and W atoms of (101) surface is covered by OH^- anion.

(a)

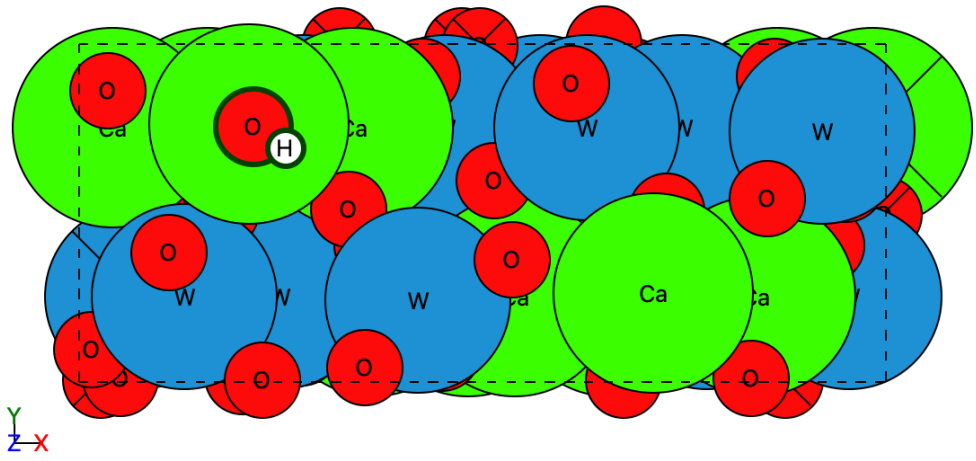

(b)

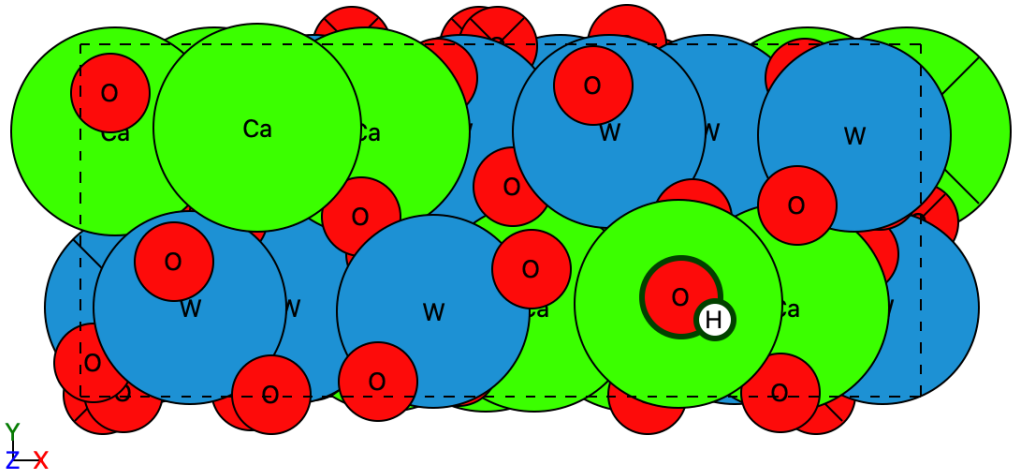

(c)

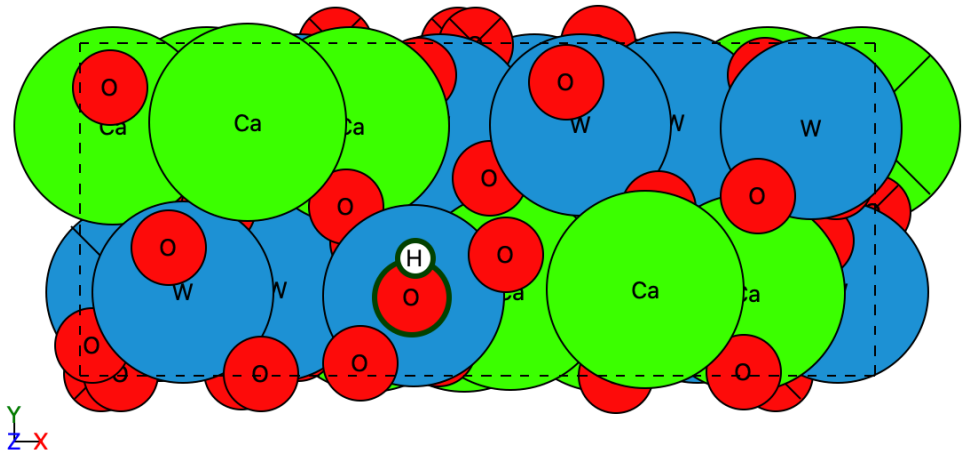

(d)

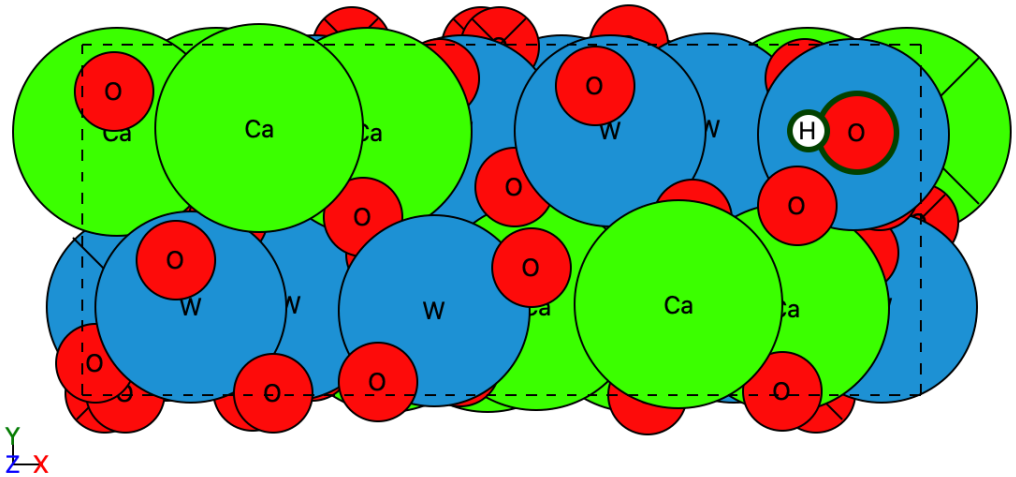

(e)

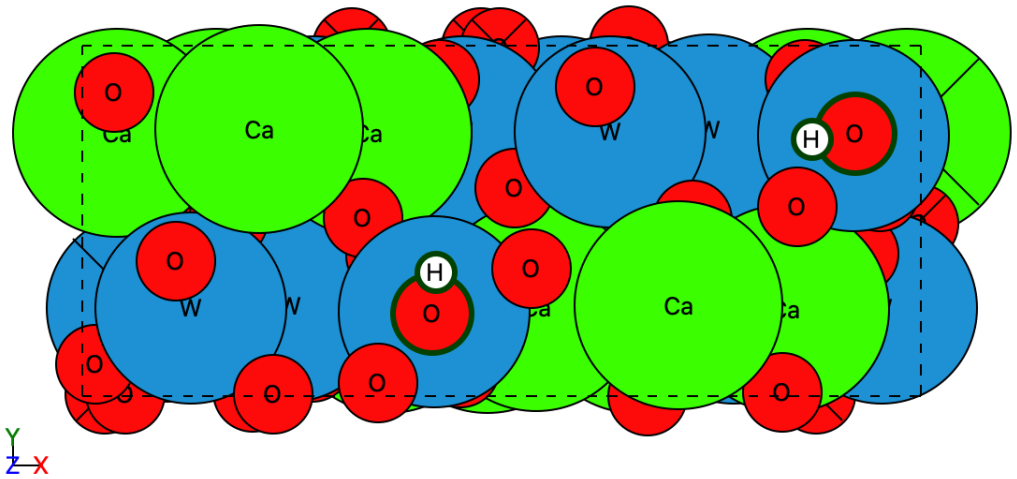

Figure. S7.2: To test the coverage of OH^- ions, all different surface Ca and W atoms are covered and displayed in (a)-(d). Two of the W atoms on surface is covered by OH^- and shown in (e). Red and White spheres with black circle: Hydroxide anion (OH^-).

Ca and W atoms of (101) surface is covered by O-anion.

(a)

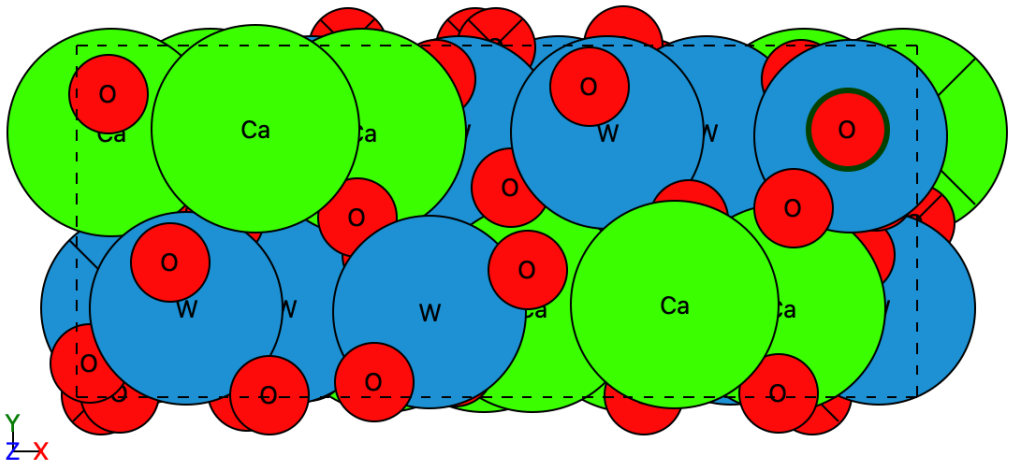

(b)

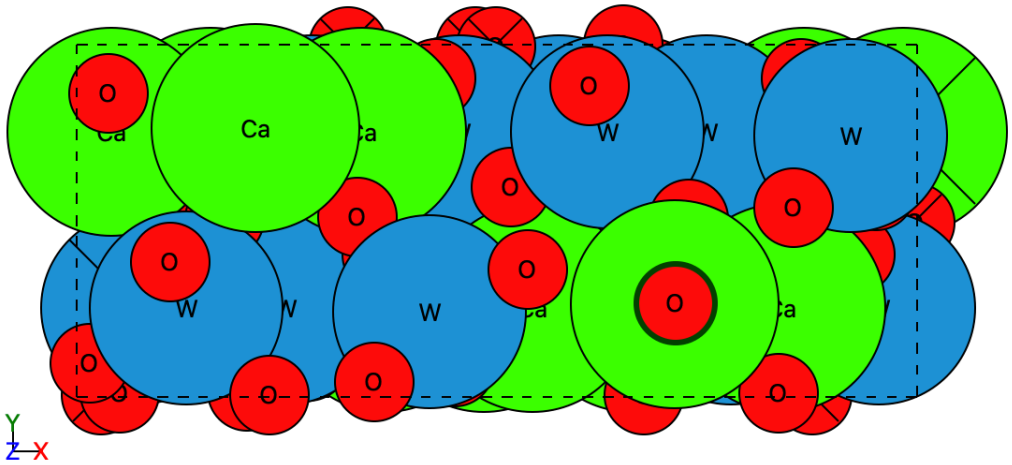

(c)

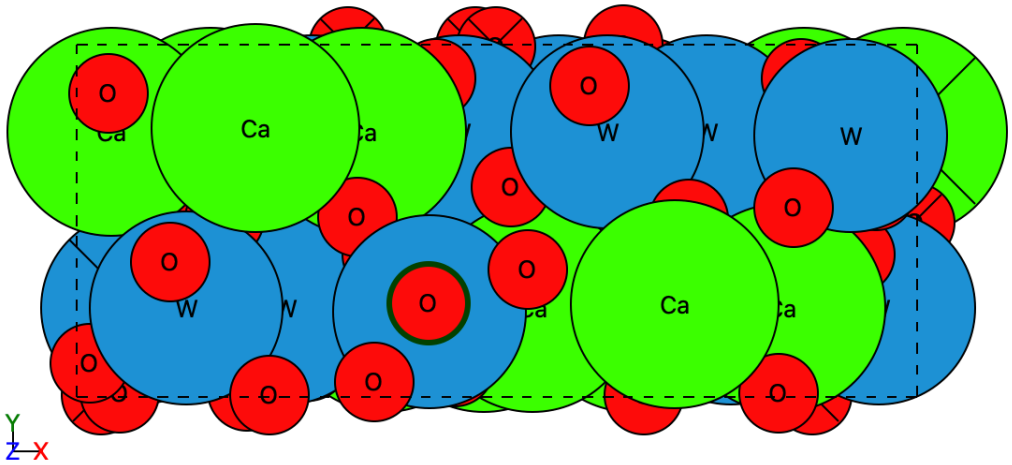

(d)

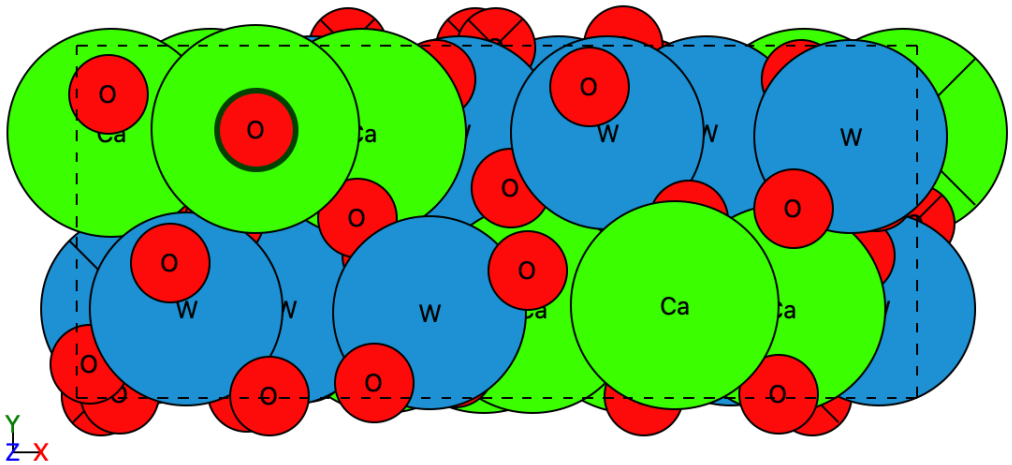

(e)

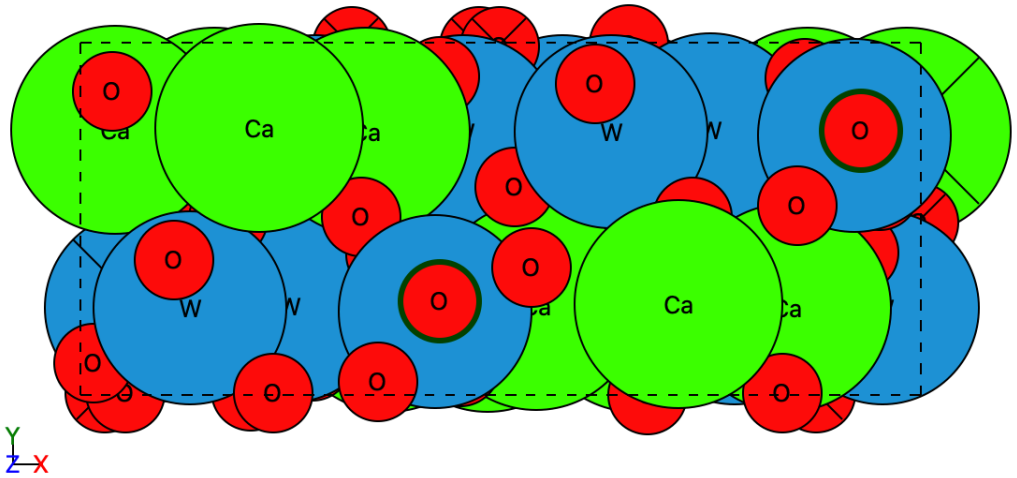

Figure. S7.3: To test the coverage of O^- ions, all different surface Ca and W atoms are covered and displayed in (a)-(d). Two of the W atoms on surface is covered by OH^- and shown in (e). Red sphere with black circle: Oxygen anion (O^-).

Methylene blue (MB) adsorption orientations

(a)

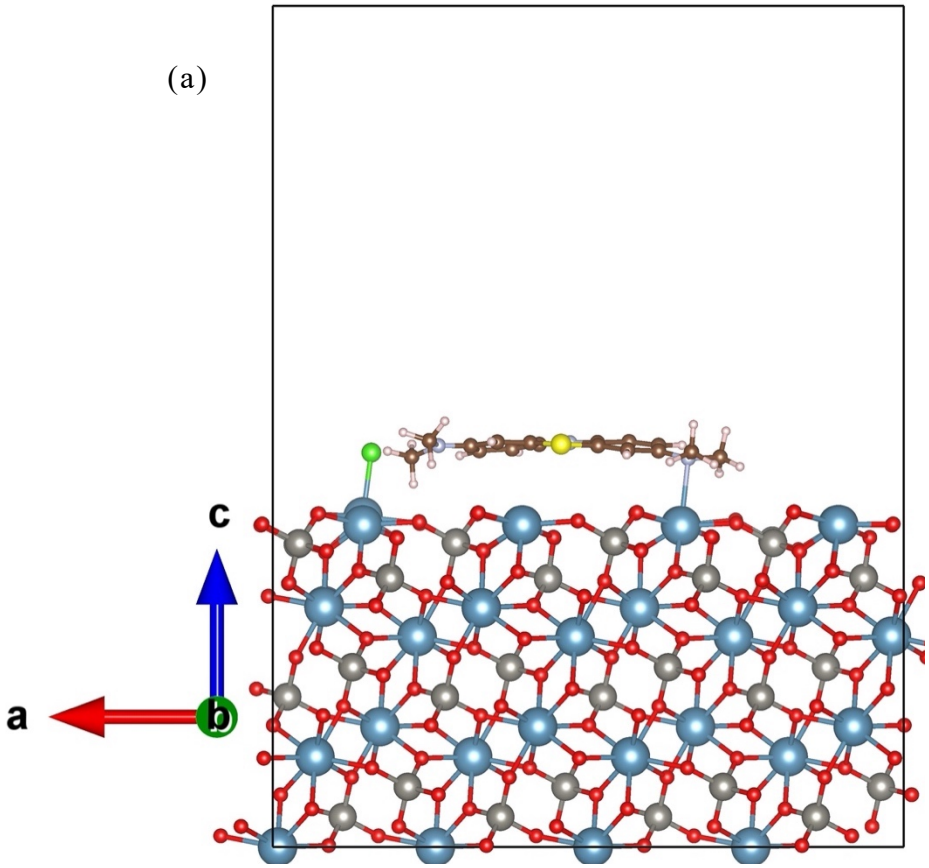

(b)

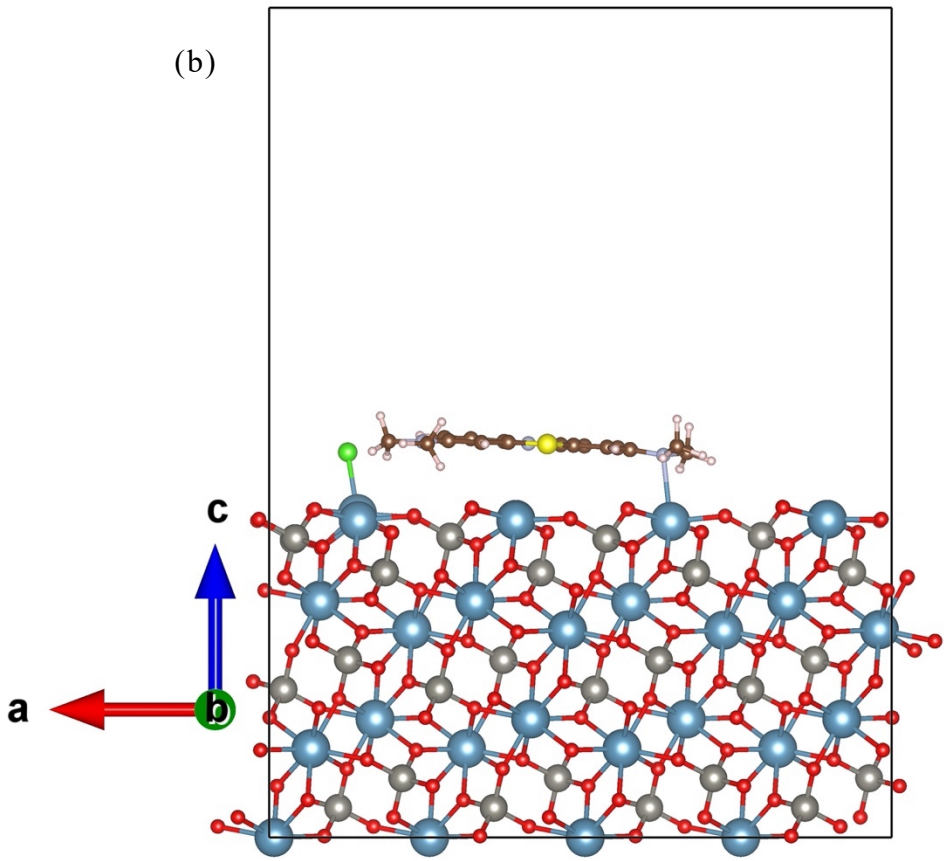

(c)

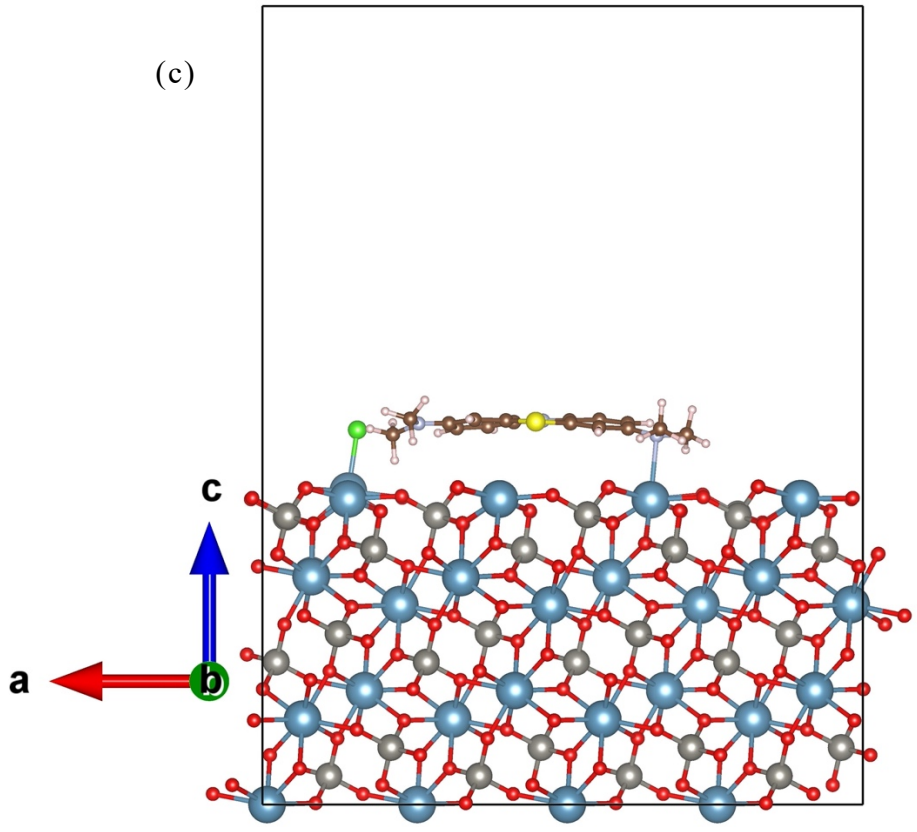

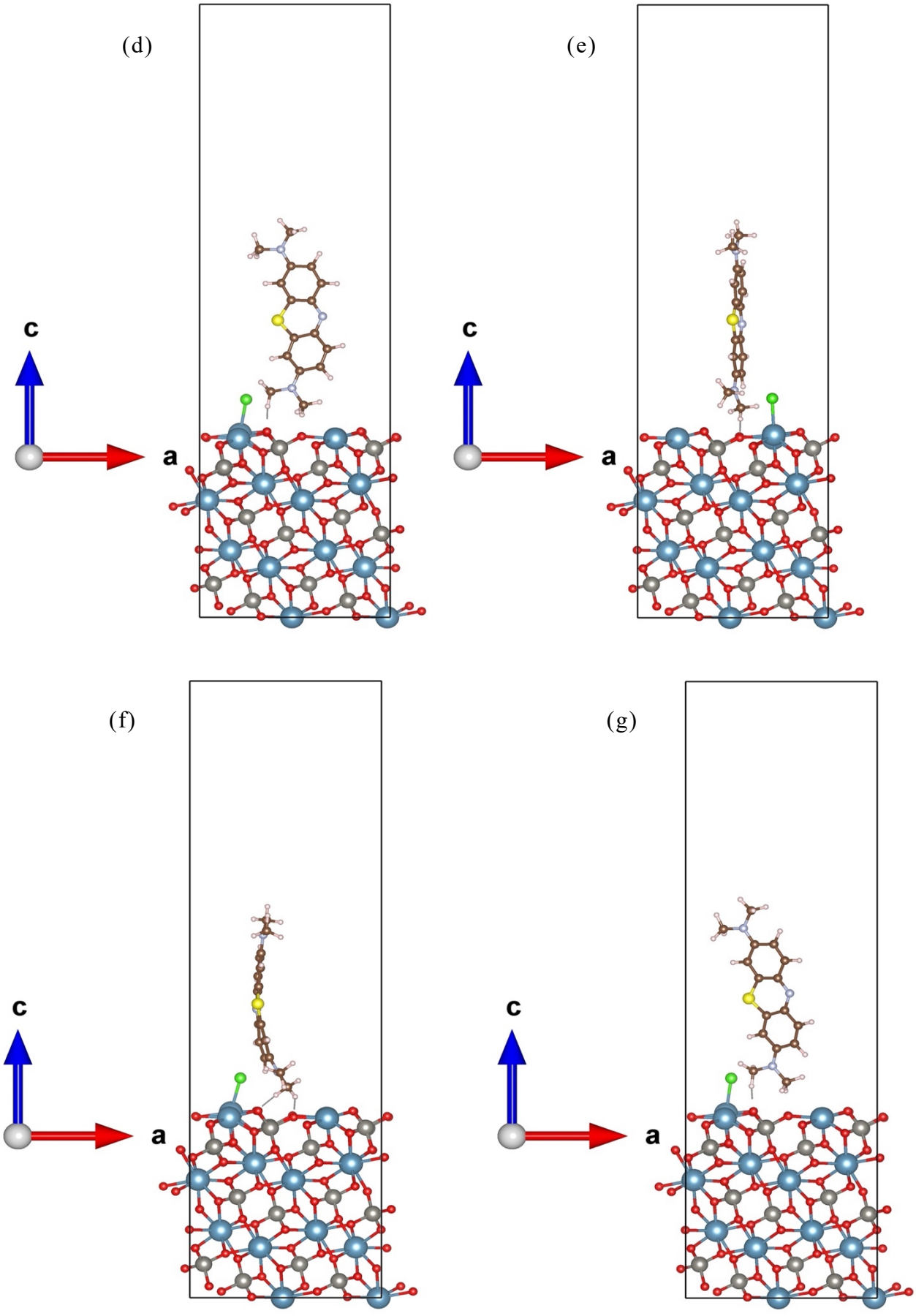
(d)
c
a
(e)
c
a
(f)
c
a
(g)
c
a

Figure. S7.4: MB molecule loaded on the (101) surface in the parallel (a-c) and perpendicular (d-g) orientation. Parallel orientations: (a) N1 and H atoms of the MB covering the hollow of the surface, (b) N1 and N3 atoms of the MB covering the Ca atoms (i.e., Ca36 and Ca44, respectively) of surface, (c) (VII) N1 and H atoms of the MB covering the O atoms of the surface. Perpendicular orientations: (d) MB loaded on the x-axis, (e) y-axis, and (f) diagonal-direction of the surface, and (g) H atoms of the MB covering both O and Ca atoms of surface.

References

1 Z. Jinkai, *Modified titanium dioxide (TiO2) photocatalysts for the degradation of organic pollutants in wastewater*, 2007.

2 Environmental Protection Agency, *Urban Waste Water Treatment in 2020*, 2021.

3 G. Bal and A. Thakur, *Mater Today Proc*, 2022, **50**, 1575–1579.

4 D. Chen, Y. Cheng, N. Zhou, P. Chen, Y. Wang, K. Li, S. Huo, P. Cheng, P. Peng, R. Zhang, L. Wang, H. Liu, Y. Liu and R. Ruan, *J Clean Prod*, 2020, **268**, 121725.

5 S. Shakoor and A. Nasar, *J Taiwan Inst Chem Eng*, 2016, **66**, 154–163.

6 N. Peng, D. Hu, J. Zeng, Y. Li, L. Liang and C. Chang, *ACS Sustain Chem Eng*, 2016, **4**, 7217–7224.

7 A. Demirbas, *J Hazard Mater*, 2009, **167**, 1–9.

8 Z. Cai, Y. Sun, W. Liu, F. Pan, P. Sun and J. Fu, *Environ Sci Pollut Res*, 2017, **24**, 15882–15904.

9 F. X. Nobre, R. Muniz, E. R. do Nascimento, R. S. Amorim, R. S. Silva, A. Almeida, J. A. Moreira, P. B. Tavares, W. R. Brito, P. R. C. Couceiro and Y. Leyet, *Journal of Materials Science: Materials in Electronics*, 2021, **32**, 9776–9794.

10 M. R. Boskabadi, V. Rogé, A. Bazargan, H. Sargazi and E. Barborini, *Photocatalytic Water and Wastewater Treatment*, 2022, 1–36.

11 A. Bazargan and N. Hankins, *Photocatalytic Water and Wastewater Treatment*, 2022.

12 V. Rogé, N. Bahlawane, G. Lamblin, I. Fechete, F. Garin, A. Dinia and D. Lenoble, *J Mater Chem A Mater*, 2015, **3**, 11453–11461.

13 A. H. Navidpour, S. Abbasi, D. Li, A. Mojiri and J. L. Zhou, *Catalysts*, 2023, **13**, 232–260.

14 N. Goodarzi, Z. Ashrafi-Peyman, E. Khani and A. Z. Moshfegh, *Catalysts*, 2023, **13**, 1102–1157.

15 J. Ge, Y. Zhang, Y. J. Heo and S. J. Park, *Catalysts*, 2019, **9**, 122–153.

16 M. A. Fendrich, A. Quaranta, M. Orlandi, M. Bettonte and A. Miotello, *Applied Sciences*, 2019, **9**, 118.

17 A. Fujishima and K. Honda, *Nature*, 1972, **238**, 37–38.

18 Ashwin Kishore M.R, *Chapter-1: Tailoring the Electronic Band Gap and Band Edge Positions of C 2 N Monolayer for Photocatalytic Water Splitting: A First Principles Study*, 2018.

19 C. Belver, J. Bedia and J. J. Rodriguez, *Appl Catal B*, 2015, **176–177**, 278–287.

20 D. Nansheng, W. Feng, L. Fan and X. Mei, *Chemosphere*, 1998, **36**, 3101–3112.

21 D. W. Bahnemann, S. N. Kholuiskaya, R. Dillert, A. I. Kulak and A. I. Kokorin, *Appl Catal B*, 2002, **36**, 161–169.

22 I. M. Arabatzis, T. Stergiopoulos, D. Andreeva, S. Kitova, S. G. Neophytides and P. Falaras, *J Catal*, 2003, **220**, 127–135.

23 K. S. Potter and J. H. Simmons, in *Optical Materials*, Elsevier, 2021, pp. 309–368.

24 X. Chen, S. Shen, L. Guo and S. S. Mao, *Chem Rev*, 2010, **110**, 6503–6570.

25 R. S. Pedanekar, S. K. Shaikh and K. Y. Rajpure, *Current Applied Physics*, 2020, **20**, 931–952.

26 R. Bashiri, N. M. Mohamed, C. F. Kait, S. Sufian and M. Khatani, *J Environ Chem Eng*, 2017, **5**, 3207–3214.

27 S. Deng, J. Yu, C. Yang, J. Chang, Y. Wang, P. Wang and S. Xie, *Appl Phys A Mater Sci Process*, 2017, **123**, 639.

28 X. Liu, L. Cao, W. Sun, Z. Zhou and J. Yang, *Research on Chemical Intermediates*, 2016, **42**, 6289–6300.

29 T. V. Nguyen, J. C. S. Wu and C. H. Chiou, *Catal Commun*, 2008, **9**, 2073–2076.

30 K. S. Yao, D. Y. Wang, C. Y. Chang, K. W. Weng, L. Y. Yang, S. J. Lee, T. C. Cheng and C. C. Hwang, *Surf Coat Technol*, 2007, **202**, 1329–1332.

31 F. Chen, Z. Deng, X. Li, J. Zhang and J. Zhao, *Chem Phys Lett*, 2005, **415**, 85–88.

32 E. Borgarello, J. Kiwi, E. Pelizzetti, M. Visca and M. Grätzel, *J Am Chem Soc*, 1981, **103**, 6324–6329.

33 J. Yin, Z. Zou and J. Ye, *Chem Phys Lett*, 2003, **378**, 24–28.

34 S. Ouyang, Z. Li, Z. Ouyang, T. Yu, J. Ye and Z. Zou, *Journal of Physical Chemistry C*, 2008, **112**, 3134–3141.

35 A. Elfiad, F. Galli, A. Djadoun, M. Sennour, S. Chegrouche, L. Meddour-Boukhobza and D. C. Boffito, *Materials Science and Engineering: B*, 2018, **229**, 126–134.

36 B. Rodríguez-Cabo, I. Rodríguez-Palmeiro, R. Corchero, R. Rodil, E. Rodil, A. Arce and A. Soto, *Water Sci Technol*, 2017, **75**, 128–140.

37 J. Moon, H. Takagi, Y. Fujishiro and M. Awano, *J Mater Sci*, 2001, **36**, 949–955.

38 M. K. Tariq, A. Riaz, R. Khan, A. Wajid, H. U. Haq, S. Javed, M. A. Akram and M. Islam, *Mater. Res. Express*, 2019, **6**, 106435.

39 C. Liu, L. Zhang, R. Liu, Z. Gao, X. Yang, Z. Tu, F. Yang, Z. Ye, L. Cui, C. Xu and Y. Li, *J Alloys Compd*, 2016, **656**, 24–32.

40 J. Li, X. Xu, X. Liu, C. Yu, D. Yan, Z. Sun and L. Pan, *J Alloys Compd*, 2016, **679**, 454–462.

41 Liu Baojiang, Cheng Xubang and He Jinxin, in *IEEE, 2009 3rd International Conference on Bioinformatics and Biomedical Engineering*, [IEEE], 2009.

42 H. Zhang, Y. Liang, X. Wu and H. Zheng, *Mater Res Bull*, 2012, **47**, 2188–2192.

43 S. Sreekantan, S. Mohd Zaki, C. W. Lai and T. Wah Tzu, *Eur. Phys. J. Appl. Phys.*, 2014, **67**, 10404.

44 I. M. Arabatzis, T. Stergiopoulos, D. Andreeva, S. Kitova, S. G. Neophytides and P. Falaras, *J Catal*, 2003, **220**, 127–135.

45 G. Odling, A. Ivaturi, E. Chatzisymeon and N. Robertson, *ChemCatChem*, 2018, **10**, 234–243.

46 X. Sun, H. J. Li, N. Ou, B. Lyu, B. Gui, S. Tian, D. Qian, X. Wang and J. Yang, *Molecules*, 2019, **24**, 344.

47 M. Xue, L. Huang, J. Q. Wang, Y. Wang, L. Gao, J. H. Zhu and Z. G. Zou, *Nanotechnology*, 2008, **19**, 185604.

48 C. Chen, W. Cai, M. Long, B. Zhou, Y. Wu, D. Wu and Y. Feng, *ACS Nano*, 2010, **4**, 6425–6432.

49 X. Zhang, J. Qin, R. Hao, L. Wang, X. Shen, R. Yu, S. Limpanart, M. Ma and R. Liu, *Journal of Physical Chemistry C*, 2015, **119**, 20544–20554.

50 R. Saffari, Z. Shariatinia and M. Jourshabani, *Environmental Pollution*, 2020, **259**, 113902.

51 R. Ebrahimi, K. Hossienzadeh, A. Maleki, R. Ghanbari, R. Rezaee, M. Safari, B. Shahmoradi, H. Daraei, A. Jafari, K. Yetilmezsoy and S. H. Puttaiah, *J Environ Health Sci Eng*, 2019, **17**, 479–492.

52 V. H. T. Thi and B. K. Lee, *Mater Res Bull*, 2017, **96**, 171–182.

53 N. Suganthi and K. Pushpanathan, *International Journal of Environmental Science and Technology*, 2019, **16**, 3375–3388.

54 H. A. Alburaih, S. Aman, N. Ahmad, S. R. Ejaz, R. Y. Khosa, A. G. Abid, S. Manzoor, H. M. T. Farid, M. S. Waheed and T. A. Taha, *Chinese Journal of Physics*, 2023, **83**, 637–649.

55 D. P. Dutta, M. Ramakrishnan, M. Roy and A. Kumar, *J Photochem Photobiol A Chem*, 2017, **335**, 102–111.

56 B. Czech and K. Tyszczuk-Rotko, *Sep Purif Technol*, 2018, **206**, 343–355.

57 F. Su, P. Li, J. Huang, M. Gu, Z. Liu and Y. Xu, *Sci Rep*, 2021, **11:85**, 1–13.

58 L. Li, X. Yin and Y. Sun, *Sep Purif Technol*, 2019, **212**, 135–141.

59 X. Hu, X. Meng and Z. Zhang, *International Journal of Photoenergy*, 2016, **2016**, 8730806.

60 S. Sharma, G. Sharma, A. Kumar, M. Naushad, G. T. Mola, A. Kumar, F. A. Al-Misned, H. A. El-Serehy and F. J. Stadler, *Top Catal*, 2020, **63**, 1302–1313.

61 N. Abbas, G. N. Shao, M. S. Haider, S. M. Imran, S. S. Park and H. T. Kim, *Journal of Industrial and Engineering Chemistry*, 2016, **39**, 112–120.

62 Y. Zhang, D. Ma, J. Wu, Q. Zhang, Y. Xin and N. Bao, *Appl Surf Sci*, 2015, **353**, 1260–1268.

63 P. L. Truong, A. Kidanemariam and J. Park, *Journal of Industrial and Engineering Chemistry*, 2021, **100**, 19–39.

64 A. Saravanan, P. S. Kumar, S. Jeevanantham, M. Anubha and S. Jayashree, *Environmental Pollution*, 2022, **298**, 118844.

65 S. Huang, Z. Lou, A. Shan, N. Zhu, K. Feng and H. Yuan, *J Mater Chem A Mater*, 2014, **2**, 16165–16174.

66 C. Ayappan, B. Palanivel, V. Jayaraman, T. Maiyalagan and A. Mani, *Mater Sci Semicond Process*, 2019, **104**, 104693.

67 C. Yuan, F. Sun, H. Liu, T. Chen, Z. Chu, H. Wang, X. Zou, P. Zhai and D. Chen, *Processes*, 2023, **11**, 1050.

68 Y. J. Zhang, L. Zhang, L. Kang, M. Y. Yang and K. Zhang, *Int J Hydrogen Energy*, 2017, **42**, 3690–3697.

69 A. Syed, H. A. AL-Shwaiman, M. M. Al Khulaifi, R. R. Al Zahrani, F. N. Almajhdi and A. M. Elgorban, *Mater Sci Semicond Process*, 2021, **133**, 105921.

70 N. F. A. Neto, B. P. Dias, R. L. Tranquilin, E. Longo, M. Li, M. R. D. Bomio and F. V. Motta, *J Alloys Compd*, 2020, **823**, 153617.

71 G. Kresse and J. Furthmüller, *Comput Mater Sci*, 1996, **6**, 15–50.

72 S. J. Clark, M. D. Segall, C. J. Pickard Ii, P. J. Hasnip, M. I. J. Probert, K. Refson and M. C. Payne, *Z. Kristallogr*, 2005, **220**, 567–570.

73 M. C. Payne, M. P. Teter, D. C. Ailan, T. A. Arias and J. D. Joannopouios, *Rev Mod Phys*, 1992, **64**, 1045.

74 R. Dovesi, V. Saunders, C. Roetti, R. Orlando, C. M. Zicovich-Wilson, F. Pascale, B. Civalleri, K. Doll, N. Harrison, I. Bush and M. Llunell, *CRYSTAL06 User's Manual*, 2008.

75 P. Giannozzi, S. Baroni, N. Bonini, M. Calandra, R. Car, C. Cavazzoni, D. Ceresoli, G. L. Chiarotti, M. Cococcioni, I. Dabo, A. Dal Corso, S. De Gironcoli, S. Fabris, G. Fratesi, R. Gebauer, U. Gerstmann, C. Gougoussis, A. Kokalj, M. Lazzeri, L. Martin-Samos, N. Marzari, F. Mauri, R. Mazzarello, S. Paolini, A. Pasquarello, L. Paulatto, C. Sbraccia, S. Scandolo, G. Sclauzero, A. P. Seitsonen, A. Smogunov, P. Umari and R. M. Wentzcovitch, *Journal of Physics: Condensed Matter*, 2009, **21**, 395502.

76 J. P. Perdew, K. Burke and M. Ernzerhof, *Phys Rev Lett*, 1996, **77**, 3865.

77 V. I. Anisimov, J. Zaanen and O. K. Andersen, *Phys Rev B*, 1991, **44**, 943–954.

78 J. Heyd, G. E. Scuseria and M. Ernzerhof, *J Chem Phys*, 2003, **118**, 8207.

79 M. Z. Fidelis, Y. B. Favaro, A. S. G. G. dos Santos, M. F. R. Pereira, R. Brackmann, G. G. Lenzi, O. S. G. P. Soares and O. A. B. Andreo, *J Environ Chem Eng*, 2023, **11**, 110690–1106104.

80 T. Iwasaki, Y. Shimamura, Y. Makino and S. Watano, *Optik (Stuttg)*, 2016, **127**, 9081–9087.

81 A. Panahi, R. Monsef, S. A. Hussein, S. A. Hammood, W. K. Al-Azzawi, D. E. Raffik, F. S. Hashim and M. Salavati-Niasari, *Int J Hydrogen Energy*, 2023, **48**, 33155–33165.

82 B. Munisha, B. Mishra, J. Nanda, N. K. Sahoo, D. Ghosh, K. J. Sankaran and S. Suman, *Journal of Rare Earths*, 2023, **41**, 1541–1550.

83 O. Kamoun, A. Gassoumi, M. Shkir, N. E. Gorji and N. Turki-Kamoun, *Coatings*, 2022, **12**, 823–832.

84 S. Vishwanathan, S. Laxmi, S. Nandan, S. Jayan, M. Lijo and S. Das, *Environmental Science and Pollution Research*, 2023, **30**, 8448–8463.

85 A. Al Baroot, K. A. Elsayed, S. A. Haladu, S. M. Magami, M. Alheshibri, F. Ercan, E. Çevik, S. Akhtar, A. A.Manda, T. S. Kayed, N. A. Altamimi, A. A. Alsanea and A. L. Al-Otaibi, *Opt Laser Technol*, 2023, **157**, 108734–108744.

86 S. Sasikala, M. Balakrishnan, M. Kumar and J. H. Chang, *Inorg Chem Commun*, 2023, **153**, 110854–110866.

87 M. Sheng, C. Gan, Y. Li, Z. Hu, Y. Zhang, X. Gao, X. Wang and H. Jiang, *Chemical Engineering Journal*, 2022, **446**, 136919–136929.

88 S. Shen, X. Li, Y. Zhou, L. Han, Y. Xie, F. Deng, J. Huang, Z. Chen, Z. Feng, J. Xu and F. Dong, *J Mater Sci Technol*, 2023, **155**, 148–159.

89 C. Han, C. Cheng, F. Liu, X. Li, G. Wang and J. Li, *Nanotechnol Rev*, 2023, **12**, 20220503–20220512.

90 M. M. Sajid, H. Assaedi and H. Zhai, *Journal of Materials Science: Materials in Electronics*, 2023, **34**, 539–554.

91 Y. Liu, Y. Su, H. Han and X. Wang, in *Journal of Nanoscience and Nanotechnology*, 2013, vol. 13, pp. 853–857.

92 P. Promdet, C. J. Carmalt and I. P. Parkin, *Mater Adv*, 2023, **4**, 910–916.

93 L. Gracia, V. M. Longo, L. S. Cavalcante, A. Beltrn, W. Avansi, M. S. Li, V. R. Mastelaro, J. A. Varela, E. Longo and J. Andrés, *J Appl Phys*, 2011, **110**, 043501.

94 K. Tanji, I. El Mrabet, Y. Fahoul, A. Soussi, M. Belghiti, I. Jellal, Y. Naciri, A. El Gaidoumi and A. Kherbeche, *Reaction Kinetics, Mechanisms and Catalysis*, 2023, **136**, 1125–1142.

95 B. Liu, L. J. Wu, Y. Q. Zhao, L. Z. Wang and M. Q. Cai, *RSC Adv*, 2016, **6**, 92473–92478.

96 K. H. Van, P. V. R. K. Ramacharyulu, D. H. Youn and C. W. Kim, *Comput Mater Sci*, 2023, **219**, 112024–112032.

97 M. A. Lahmer, *Physica B Condens Matter*, 2023, **669**, 415322–415330.

98 S. K. Matta, T. Liao and S. P. Russo, *J Mater Sci Technol*, 2023, **155**, 142–147.

99 J. Lin, B. Zhang, T. Zhang and X. Chen, *Physical Chemistry Chemical Physics*, 2023, **25**, 15052–15061.

100 R. K. Mahmoud, M. Taha, A. Zaher and R. M. Amin, *Sci Rep*, 2021, **11**, 21365–21383.

101 R. Haounati, H. Ighnih, R. E. Malekshah, S. Alahiane, F. Alakhras, E. Alabbad, H. Alghamdi, H. Ouachtak, A. A. Addi and A. Jada, *Mater Today Commun*, 2023, **35**, 105915–105925.

102 W. Z. Liang, J. Huang, J. Sun, P. Zhang and A. Li, *Wiley Interdiscip Rev Comput Mol Sci*, 2023, **13**, 1665–1699.

103 A. Masood, T. Iqbal, S. Afsheen, K. N. Riaz, G. Nabi, M. I. Khan, N. Al-Zaqri, I. Warad and H. Ahmed, *Biomass Convers Biorefin*, 2023, 1–13.

104 K. Manjunath and C. G. Thimmanna, *Mater Res Express*, 2018, **5**, 035030.

105 P. B. de Sousa, A. F. Gouveia, J. C. Sczancoski, I. C. Nogueira, E. Longo, M. A. San-Miguel and L. S. Cavalcante, *J Alloys Compd*, 2021, **855**, 157377.

106 A. Sobhani-Nasab and M. Sadeghi, *Journal of Materials Science: Materials in Electronics*, 2016, **27**, 7933–7938.

107 K. Li, C. Dong, Y. Zhang, H. Wei, F. Zhao and Q. Wang, *J Mol Catal A Chem*, 2014, **394**, 105–113.

108 I. P. Carvalho, A. F. Lima and M. V. Lalic, *Opt Mater (Amst)*, 2019, **92**, 187–194.

109 A. Benmakhlouf, D. Errandonea, A. Bouhemadou, A. Bentabet, S. Maabed, M. Bouchenafa and S. Bin-Omran, *Int J Mod Phys B*, 2017, **31**, 1750086.

110 V. M. Longo, L. Gracia, D. G. Stroppa, L. S. Cavalcante, M. Orlandi, A. J. Ramirez, E. R. Leite, J. Andrés, A. Beltrán, J. A. Varela and E. Longo, *Journal of Physical Chemistry C*, 2011, **115**, 20113–20119.

111 D. Errandonea, J. Pellicer-Porres, F. J. Manjón, A. Segura, C. Ferrer-Roca, R. S. Kumar, O. Tschauner, P. Rodríguez-Hernández, J. López-Solano, S. Radescu, A. Mujica, A. Muñoz and G. Aquilanti, *Phys Rev B Condens Matter Mater Phys*, 2005, **72**, 174106.

112 E. Orhan, M. Anicete-Santos, M. A. M. A. Maurera, F. M. Pontes, A. G. Souza, J. Andrès, A. Beltràn, J. A. Varela, P. S. Pizani, C. A. Taft and E. Longo, *J Solid State Chem*, 2005, **178**, 1284–1291.

113 J. A. S. Laranjeira, G. S. L. Fabris, A. R. Albuquerque, M. M. Ferrer and J. R. Sambrano, *Mater Today Commun*, 2022, **33**, 104178.

114 H. Wu, P. Niu, R. Pei, Y. Zheng, W. Jin, X. M. Li and R. Jiang, *J Lumin*, 2021, **236**, 118146.

115 C. Leforestier, R. H. Bisselinc, C. Cerjan, M. D. Feit, R. Friesner, A. Guldberg, A. Hammerich, G. Jolicard, W. Karrlein, H.-D. Meyer, N. Lipkin, O. A. Roncero and R. Kosloff, *J Comput Phys*, 1991, **94**, 59–80.

116 V. J. Härkönen, R. Van Leeuwen and E. K. U. Gross, *Phys Rev B*, 2020, **101**, 235153–235172.

117 Y. R. Xie, Y. F. Wang, W. Wang, T. Wang, D. X. Dai, C. L. Xiao and X. M. Yang, *Chinese Journal of Chemical Physics*, 2020, **33**, 135–138.

118 Y. Zhang, *First-principles Statistical Mechanics Approach to Step Decoration at Solid Surfaces*, 2008.

119 J. Flick, H. Appel, M. Ruggenthaler and A. Rubio, *J Chem Theory Comput*, 2017, **13**, 1616–1625.

120 I. Mayer, *Int J Quantum Chem*, 1983, **XXIII**, 341–363.

121 X. S. Liu, L. W. Su and P. Z. Ding, *Int J Quantum Chem*, 2002, **87**, 1–11.

122 X. S. Liu, X. Y. Liu, Z. Y. Zhou, P. Z. Ding and S. F. Pan, *Int J Quantum Chem*, 2000, **79**, 343–349.

123 L. P. Ginzburg, *Theoretical and Mathematical Physics*, 1999, **121**, 1641–1653.

124 Abdullah Mohmmed Alotaibi, *Aerosol-Assisted Chemical Vapour Deposition of Doped Titania films; Characterisation and Functional Properties Department of Chemistry*, 2019.

125 Paul Robert Tulip, *Dielectric and lattice dynamical properties of molecular crystals via density functional perturbation theory: implementation within a rst principles code*, 2004.

126 K. T. Ngeywo, *Mid-Gap States In Defective Anatase TiO2: A Density Functional Theory Study Plus A Hubbard Term (DFT+U)*, 2016.

127 F. Opoku, *First–principles studies on the development of semiconductor–based photocatalyst materials for applications in photocatalytic water splitting and degradation of pollutants*, 2018.

128 W. Kohn, *Rev Mod Phys*, 1999, **71**, 1253–1266.

129 S. K. Iyemperumal, *Conversion of Carbon Dioxide to Fuels using Dispersed Atomic-Size Catalysts*, Worcester Polytechnic Institute, 2018.

130 T. Francese, *Rationalization of the Mechanism of Bistability in Dithiazolyl-based Molecular Magnets*, 2019.

131 L. H. Thomas, *Mathematical Proceedings of the Cambridge Philosophical Society*, 1927, **23**, 542–548.

132 P. Hohenberg and W. Konnt, *Physicsl Review*, 1964, **136**, B864–B871.

133 B. C. Zhou and Z. K. Liu, *Diffusion Foundations*, 2016, **8**, 1–30.

134 L. Mederos, E. Velasco, Y. Martínez-Ratón and A. K. Theophilou, *Journal of Physics C: Solid State Physics*, 1979, **12**, 5419.

135 W. Koch and M. C. Holthausen, *A Chemist's Guide to Density Functional Theory*, Wiley, 2001.

136 W. Kohn and L. J. Sham, *Physical Review*, 1965, **140**, A1133.

137 Navid Abedi Khaledi, *Linear response functions of solids within time-dependent density functional theory (TDDFT)*, 2011.

138 Timothy James Callow, *Systematic routes to improved approximations in Kohn-Sham theory*, 2020.

139 K. Choudhary, *Computational Design of Surfaces, Nanostructures And Optoelectronic Materials*, 2015.

140 R. O. Jones and O. Gunnarsson, *Rev Mod Phys*, 1989, **61**, 689.

141 D.J. Singh and L. Nordstrom, *Planewaves, Pseudopotentials, and the LAPW Method - David J. Singh, Lars Nordstrom - Google Books*, 2006.

142 Ralf Gehrke, *First-Principles Basin-Hopping for the Structure Determination of Atomic Clusters*, 2008.

143 C. Adamo and V. Barone, *J Chem Phys*, 1999, **110**, 6158–6170.

144 M. Ernzerhof and G. E. Scuseria, *J Chem Phys*, 1999, **110**, 5029–5036.

145 C. Lee, W. Yang and R. G. Parr, *Phys Rev B*, 1988, **37**, 785.

146 K. Raghavachari, *Theor Chem Acc*, 2000, **103**, 361–363.

147 J. Paier, M. Marsman, K. Hummer, G. Kresse, I. C. Gerber and J. G. Angyán, *Journal of Chemical Physics*, 2006, **124**, 154709.

148 L. Hedin, *Physical Review*, 1965, **139**, A796.

149 P. Giannozzi, O. Andreussi, T. Brumme, O. Bunau, M. Buongiorno Nardelli, M. Calandra, R. Car, C. Cavazzoni, D. Ceresoli, M. Cococcioni, N. Colonna, I. Carnimeo, A. Dal Corso, S. De Gironcoli, P. Delugas, R. A. Distasio, A.

Ferretti, A. Floris, G. Fratesi, G. Fugallo, R. Gebauer, U. Gerstmann, F. Giustino, T. Gorni, J. Jia, M. Kawamura, H. Y. Ko, A. Kokalj, E. Kücükbenli, M. Lazzeri, M. Marsili, N. Marzari, F. Mauri, N. L. Nguyen, H. V. Nguyen, A. Otero-De-La-Roza, L. Paulatto, S. Poncé, D. Rocca, R. Sabatini, B. Santra, M. Schlipf, A. P. Seitsonen, A. Smogunov, I. Timrov, T. Thonhauser, P. Umari, N. Vast, X. Wu and S. Baroni, *Journal of Physics Condensed Matter*, 2017, **29**, 465901.

150 M. Rasukkannu, *Modelling and Simulation of materials for Photovoltaic applications*, 2019.

151 Ravindran Vidya, *Theoretical Investigations on Mixed-valence Transition-metal Oxides*, 2005.

152 P. E. Blöchl, *Phys Rev B*, 1994, **50**, 17953.

153 G. Kresse and D. Joubert, *Phys Rev B*, 1999, **59**, 1758.

154 R. Dronskowski and P. E. Blochl, *J. Phys. Chem*, 1993, **97**, 8617–8624.

155 D. J. Chadi and M. L. Cohen, *Phys Rev B*, 1973, **8**, 5747.

156 P. Blaha, K. Schwarz, G. K. H. Madsen, D. Kvasnicka, J. Luitz, R. Laskowski, F. Tran and L. D. Marks, 2018.

157 S. Sharma, Pramod Kumar and Rakesh Chandra, Molecular dynamics simulation of nanocomposites using BIOVIA materials studio, Lammps and Gromacs, 2019, vol. 141.

158 C. Di Valentin, E. Finazzi, G. Pacchioni, A. Selloni, S. Livraghi, M. C. Paganini and E. Giamello, *Chem Phys*, 2007, **339**, 44–56.

159 A. Suresh, N. Soundararajan and A. B. M. Ahmed, *Int J Chemtech Res*, 2014, **6**, 5246–5251.

160 T. Tachikawa and T. Majima, *NPG Asia Mater*, 2014, **6**, e100.

161 F. Spadavecchia, G. Cappelletti, S. Ardizzone, M. Ceotto and L. Falciola, *Journal of Physical Chemistry C*, 2011, **115**, 6381–6391.

162 C. Chen, W. Ma and J. Zhao, *Chem Soc Rev*, 2010, **39**, 4206–4219.

163 T. Luttrell, S. Halpegamage, J. Tao, A. Kramer, E. Sutter and M. Batzill, *Sci Rep*, 2015, **4**, 4043.

164 X. Wu, J. Wang, G. Zhang, K. ichi Katsumata, K. Yanagisawa, T. Sato and S. Yin, *Appl Catal B*, 2017, **201**, 128–136.

165 M. Sotoudeh, M. Abbasnejad and M. R. Mohammadizadeh, *Eur. Phys. J. Appl. Phys.*, 2014, **67**, 30401.

166 C. Di Valentin, G. Pacchioni and A. Selloni, *Journal of Physical Chemistry C*, 2009, **113**, 20543–20552.

167 Y. Cong, B. Tian and J. Zhang, *Appl Catal B*, 2011, **101**, 376–381.

168 H. Peng, J. Li, S. S. Li and J. B. Xia, *Journal of Physics Condensed Matter*, 2008, **20**, 1–6.

169 A. Kubacka, M. J. Muñoz-Batista, M. Ferrer and M. Fernández-García, *Appl Catal B*, 2013, **140–141**, 680–690.

170 F. Liu, N. Feng, L. Yang, Q. Wang, J. Xu and F. Deng, *Journal of Physical Chemistry C*, 2018, **122**, 10948–10955.

171 M. Xue, L. Huang, J. Q. Wang, Y. Wang, L. Gao, J. H. Zhu and Z. G. Zou, *Nanotechnology*, 2008, **19**, 185604.

172 A. A. Ismail, L. Robben and D. W. Bahnemann, *ChemPhysChem*, 2011, **12**, 982–991.

173 Z. Chen, J. Zhao, X. Yang, Q. Ye, K. Huang, C. Hou, Z. Zhao, J. You and Y. Li, *Ind Eng Chem Res*, 2016, **55**, 80–85.

174 L. Xu, C. Q. Tang, J. Qian and Z. Bin Huang, *Appl Surf Sci*, 2010, **256**, 2668–2671.

175 G. Liu, X. Zhang, Y. Xu, X. Niu, L. Zheng and X. Ding, *Chemosphere*, 2005, **59**, 1367–1371.

176 L. Jing, B. Xin, F. Yuan, L. Xue, B. Wang and H. Fu, *Journal of Physical Chemistry B*, 2006, **110**, 17860–17865.

177 Y. Huang, J. J. Cao, F. Kang, S. J. You, C. W. Chang and Y. F. Wang, *Aerosol Air Qual Res*, 2017, **17**, 2555–2565.

178 J. Liqiang, S. Xiaojun, X. Baifu, W. Baiqi, C. Weimin and F. Honggang, *J Solid State Chem*, 2004, **177**, 3375–3382.

179 Y. Huo, J. Zhu, J. Li, G. Li and H. Li, *J Mol Catal A Chem*, 2007, **278**, 237–243.

180 Liu Baojiang, Cheng Xubang and He Jinxin, in *IEEE, 2009 3rd International Conference on Bioinformatics and Biomedical Engineering*, [IEEE], 2009.

181 J. J. Zou, B. Zhu, L. Wang, X. Zhang and Z. Mi, *J Mol Catal A Chem*, 2008, **286**, 63–69.

182 Pseudopotential Ti.pbe-spn-rrkjus_psl.1.0.0.UPF, https://www.quantum-espresso.org/upf_files/Ti.pbe-spn-rrkjus_psl.1.0.0.UPF (accessed July, 2019).

183 Pseudopotential O.pbe-n-rrkjus_psl.1.0.0.UPF, https://www.quantum-espresso.org/upf_files/O.pbe-n-rrkjus_psl.1.0.0.UPF (accessed July, 2019).
184 Pseudopotential Zn.pbe-dnl-rrkjus_psl.1.0.0.UPF, https://www.quantum-espresso.org/upf_files/Zn.pbe-dnl-rrkjus_psl.1.0.0.UPF (accessed July, 2019).
185 Pseudopotential La.pbe-spfn-rrkjus_psl.1.0.0.UPF, https://www.quantum-espresso.org/upf_files/La.pbe-spfn-rrkjus_psl.1.0.0.UPF (accessed July, 2019).
186 E. Baldini, L. Chiodo, A. Dominguez, M. Palummo, S. Moser, M. Yazdi-Rizi, G. Auböck, B. P. P. Mallett, H. Berger, A. Magrez, C. Bernhard, M. Grioni, A. Rubio and M. Chergui, *Nat Commun*, 2017, **8:13**, 1–27.
187 I. Timrov, N. Vast, R. Gebauer and S. Baroni, *Comput Phys Commun*, 2015, **196**, 460–469.
188 M. H. Samat, A. M. M. Ali, M. F. M. Taib, O. H. Hassan and M. Z. A. Yahya, *Results Phys*, 2016, **6**, 891–896.
189 Z. Zhao and Q. Liu, *J Phys D Appl Phys*, 2008, **41**, 1–9.
190 J. K. Burdett, T. Hughbanks, G. J. Miller, J. V. Smith and J. W. Richardson, *J Am Chem Soc*, 1987, **109**, 3639–3646.
191 Y. Wang, R. Zhang, J. Li, L. Li and S. Lin, *Nanoscale Res Lett*, 2014, **9**, 1–8.
192 Q. Meng, T. Wang, E. Liu, X. Ma, Q. Ge and J. Gong, *Physical Chemistry Chemical Physics*, 2013, **15**, 9549–9561.
193 Q. Zhang, Y. Fu, Y. Wu and T. Zuo, *Eur. J. Inorg. Chem.*, 2016, **2016**, 1706–1711.
194 R. Chauhan, A. Kumar and R. P. Chaudhary, *J Solgel Sci Technol*, 2012, **61**, 585–591.
195 M. R. Ashwin Kishore and P. Ravindran, *Journal of Physical Chemistry C*, 2017, **121**, 22216–22224.
196 H. C. Wu, Y. S. Lin and S. W. Lin, *International Journal of Photoenergy*, 2013, **2013**, 289328.
197 K. Yang, Y. Dai and B. Huang, *Journal of Physical Chemistry C*, 2007, **111**, 12086–12090.
198 C. Zhang, Z. Li and W. Wang, *Materials*, 2021, **14**, 5161.
199 R. Long and N. J. English, *Mol Simul*, 2010, **36**, 618–632.

200 T. Yang, S. Park, T. G. Kim, D. S. Shin, K. Suh and J. Park, *Opt Express*, 2017, **25**, 30843.

201 Y. Yu, Z. Lan, L. Guo, E. Wang, J. Yao and Y. Cao, *New Journal of Chemistry*, 2018, **42**, 483–488.

202 F. X. Nobre, I. C. Nogueira, G. D. S. Souza, J. M. E. De Matos, P. R. D. C. Couceiro, W. R. Brito, J. P. De La Cruz and Y. Leyet Ruiz, *Inorg Chem*, 2020, **59**, 6039–6046.

203 T. G. Cooper and N. H. De Leeuw, *Langmuir*, 2004, **20**, 3984–3994.

204 S. Huang, Z. Lou, A. Shan, N. Zhu, K. Feng and H. Yuan, *J Mater Chem A Mater*, 2014, **2**, 16165–16174.

205 E. S. Kim, S. H. Kim and B. I. Lee, *J Eur Ceram Soc*, 2006, **26**, 2101–2104.

206 N. Faure, C. Borel, M. Couchaud, G. Basset, R. Templier and C. Wyon, *Appl. Phys. B*, 1996, **63**, 593–598.

207 A. A. Kaminskii, H. J. Eichler, K.-I. Ueda, N. V Klassen, B. S. Redkin, L. E. Li, J. Findeisen, D. Jaque, J. García-Sole, J. Ferná Ndez and R. Balda, *Appl Opt*, 1998, **38**, 4533.

208 M. J. Treadaway and R. C. Powell, *Phys Rev B*, 1975, **11**, 862.

209 Y. Yang, X. Wang and B. Liu, *World Scientific Publishing Company*, 2014, **9**, 1450008.

210 V. Nagirnyi, E. Feldbach, L. Jönsson, M. Kirm, A. Lushchik, C. Lushchik, L. L. Nagornaya, V. D. Ryzhikov, F. Savikhin, G. Svensson and I. A. Tupitsina, *Radiat Meas*, 1998, **29**, 247–250.

211 K. Nitsch, M. Nikl, S. Ganschow, P. Reiche and R. Uecker, *J Cryst Growth*, 1996, **165**, 163–165.

212 C. Michail, I. Valais, G. Fountos, A. Bakas, C. Fountzoula, N. Kalyvas, A. Karabotsos, I. Sianoudis and I. Kandarakis, *Measurement*, 2018, **120**, 213–220.

213 G. Xinmin and W. Sue, *Imaging Science Journal*, 1999, **47**, 29–35.

214 N. J. Welham, *J Mater Res*, 1999, **14**, 619–627.

215 S. Gürmen, S. Timur, C. Arslan and I. Duman, *Scandinavian Journal of Metallurgy*, 2002, **31**, 221–228.

216 D. Spassky, V. Mikhailin, M. Nazarov, M. N. Ahmad-Fauzi and A. Zhbanov, *J Lumin*, 2012, **132**, 2753–2762.

217 C. Ayappan, B. Palanivel, V. Jayaraman, T. Maiyalagan and A. Mani, *Mater Sci Semicond Process*, 2019, **104**, 104693.

218 Y. Song, S. Liang, F. Li, X. Wang, C. You and Y. Yang, *Mater Lett*, 2015, **161**, 100–103.

219 R. Chai, Y. Liu, G. Zhang, J. Feng and Q. Kang, *J Lumin*, 2018, **202**, 65–70.

220 E. Palmieri, A. Marcucci, G. Marcheselli, A. De Stefanis and R. Polini, *Int J Refract Metals Hard Mater*, 2016, **59**, 93–99.

221 W. Hu, W. Tong, L. Li, J. Zheng and G. Li, *Physical Chemistry Chemical Physics*, 2011, **13**, 11634–11643.

222 S. Huang, Z. Lou, N. Zhu and H. Yuan, *Catal Commun*, 2015, **61**, 6–10.

223 W. Feng, J. Li, Z. Lei, Y. Liu, Y. Shen and Z. Chen, *Journal of Materials Science: Materials in Electronics*, 2019, **30**, 16049–16055.

224 S. Mohammadi-Aghdam, *Journal of Materials Science: Materials in Electronics*, 2017, **28**, 17161–17167.

225 S. Huang, Z. Lou, N. Zhu and H. Yuan, *Catal Commun*, 2015, **61**, 6–10.

226 N. L. M. Tri, D. S. Duc, D. Van Thuan, T. Al Tahtamouni, T. D. Pham, D. T. Tran, N. Thi Phuong Le Chi and V. N. Nguyen, *Chem Phys*, 2019, **525**, 110411.

227 L. S. Cavalcante, V. M. Longo, J. C. Sczancoski, M. A. P. Almeida, A. A. Batista, J. A. Varela, M. O. Orlandi, E. Longo and M. S. Li, *CrystEngComm*, 2012, **14**, 853–868.

228 R. Lacomba-Perales, D. Errandonea, A. Segura, J. Ruiz-Fuertes, P. Rodríguez-Hernández, S. Radescu, J. López-Solano, A. Mujica and A. Muñoz, *J Appl Phys*, 2011, **110**, 43703.

229 C. Zhang, X. Chen, B. Cao, H. Duan, Q. Sun and F. Ouyang, *Appl Surf Sci*, 2022, **579**, 152190.

230 Y. Zhang, N. A. W. Holzwarth and R. T. Williams, *Phys Rev B*, 1998, **57**, 12738.

231 Z. Shao, Q. Zhang, T. Liu and J. Chen, *Nucl Instrum Methods Phys Res B*, 2008, **266**, 797–801.

232 L. Li, Y. Su and G. Li, *Appl. Phys. Lett*, 2007, **90**, 54105.

233 R. M. Hazen, L. W. Finger and J. W. E. Mariathasan, *Journal of Physics and Chemistry of Solids*, 1985, **46**, 253–263.

234 A. M. Alotaibi, B. A. D. Williamson, S. Sathasivam, A. Kafizas, M. Alqahtani, C. Sotelo-Vazquez, J. Buckeridge, J. Wu, S. P. Nair, D. O. Scanlon and I. P. Parkin, *ACS Appl Mater Interfaces*, 2020, **12**, 15348–15361.

235 X. Gonze and C. Lee, *Phys Rev B*, 1997, **55**, 16.

236 Z. H. Levine and D. C. Allan, *Phys Rev Lett*, 1989, **63**, 16.

237 X. X. Liu, L. Z. Liu, X. L. Wu and P. K. Chu, *Phys Lett A*, 2015, **379**, 1384–1390.

238 V. Scuderi, G. Impellizzeri, L. Romano, M. Scuderi, G. Nicotra, K. Bergum, A. Irrera, B. G. Svensson and V. Privitera, *Nanoscale Res Lett*, 2014, **9**, 495.

239 A. Di Mauro, M. E. Fragalà, V. Privitera and G. Impellizzeri, *Mater Sci Semicond Process*, 2017, **69**, 44–51.

240 M. E. Fragalà, Y. Aleeva and G. Malandrino, *Thin Solid Films*, 2011, **519**, 7694–7701.

241 S. Rahemi Ardekani, A. Sabour Rouh Aghdam, M. Nazari, A. Bayat, E. Yazdani and E. Saievar-Iranizad, *J Anal Appl Pyrolysis*, 2019, **141**, 104631.

242 N. C. Maile, S. K. Shinde, R. R. Koli, A. V. Fulari, D. Y. Kim and V. J. Fulari, *Ultrason Sonochem*, 2019, **51**, 49–57.

243 C. Ravichandiran, A. Sakthivelu, R. Davidprabu, S. Valanarasu, A. Kathalingam, V. Ganesh, M. Shkir, H. Algarni and S. AlFaify, *Microelectron Eng*, 2019, **210**, 27–34.

244 M. R. Das and P. Mitra, *Chemical Papers*, 2019, **73**, 1605–1619.

245 C. Martinet, V. Paillard, A. Gagnaire and J. Joseph, *J Non Cryst Solids*, 1997, **216**, 77–82.

246 M. Zhang, L. E, R. Zhang and Z. Liu, *Surfaces and Interfaces*, 2019, **16**, 194–198.

247 W. Yang and C. A. Wolden, *Thin Solid Films*, 2006, **515**, 1708–1713.

248 H. Szymanowski, A. Sobczyk, M. Gazicki-Lipman, W. Jakubowski and L. Klimek, *Surf Coat Technol*, 2005, **200**, 1036–1040.

249 B. H. Lee, S. Park, M. Kim, A. K. Sinha, S. C. Lee, E. Jung, W. J. Chang, K. S. Lee, J. H. Kim, S. P. Cho, H. Kim, K. T. Nam and T. Hyeon, *Nat Mater*, 2019, **18**, 620–626.

250 S. Wardhani, D. Purwonugroho, C. W. Fitri and Y. P. Prananto, *AIP Conf Proc*, 2018, **2021**, 50009.

251 B. Y. Alfaifi, H. Bayahia and A. A. Tahir, *Nanomaterials*, 2019, **9**, 755.

252 J. Santos, D. Santos Cruz, F. De Moure-Flores, J. S. Cruz, D. S. Cruz, M. C. Arenas-Arrocena, F. De Moure Flores and S. A. Mayén Hernández, *Chalcogenide Letters*, 2015, **12**, 277–285.

253 M. Chahkandi and M. Zargazi, *J Hazard Mater*, 2020, **389**, 121850.

254 K. Ravichandran and S. Porkodi, *Mater Sci Semicond Process*, 2018, **81**, 30–37.

255 H. Li, Z. X. Mu, S. G. Liu and J. L. Zhang, *Mater Sci Semicond Process*, 2019, **99**, 99–105.

256 H. K. Lee, T. Fujiwara, T. Okada, T. Fukushima and S. W. Lee, *The Chemical society of Japan*, 2018, **47**, 628–631.

257 S. Ben Ameur, H. BelHadjltaief, B. Duponchel, G. Leroy, M. Amlouk, H. Guermazi and S. Guermazi, *Heliyon*, 2019, **5**, e01912.

258 L. Xu, J. Su, G. Zheng and L. Zhang, *Materials Science and Engineering: B*, 2019, **248**, 114405.

259 A. M. Ali, A. A. Ismail, R. Najmy and A. Al-Hajry, *J Photochem Photobiol A Chem*, 2014, **275**, 37–46.

260 M. A. Mahadik, S. S. Shinde, S. S. Kumbhar, H. M. Pathan, K. Y. Rajpure and C. H. Bhosale, *J Photochem Photobiol B*, 2015, **142**, 43–50.

261 X. Zhang, X. Quan, S. Chen and Y. Zhang, *J Hazard Mater*, 2010, **177**, 914–917.

262 W. Qin, J. Qi and X. Wu, *Vacuum*, 2014, **107**, 204–207.

263 W. Xiaohong, Q. Wei, L. Li, G. Yun and X. Zhaoyang, *Catal Commun*, 2009, **10**, 600–604.

264 Y. M. Hunge, M. A. Mahadik, A. V. Moholkar and C. H. Bhosale, *Ultrason Sonochem*, 2017, **35**, 233–242.

265 Y. M. Hunge, M. A. Mahadik, A. V. Moholkar and C. H. Bhosale, *Appl Surf Sci*, 2017, **420**, 764–772.

266 D. Bokhan and R. J. Bartlett, *Chem Phys Lett*, 2006, **427**, 466–471.

267 B. Van Troeye, M. Torrent and X. Gonze, *Phys Rev B*, 2016, **93**, 144304.

268 V. Caciuc, N. Atodiresei, M. Callsen, P. Lazić and S. Blügel, *Journal of Physics: Condensed Matter*, 2012, **24**, 424214.

269 D. Bahamon, M. Khalil, A. Belabbes, Y. Alwahedi, L. F. Vega and K. Polychronopoulou, *RSC Adv*, 2021, **11**, 2947–2957.

270 A. A. AlKhoori, K. Polychronopoulou, A. Belabbes, M. A. Jaoude, L. F. Vega, V. Sebastian, S. Hinder, M. A. Baker and A. F. Zedan, *Appl Surf Sci*, 2020, **521**, 146305.

271 K. Momma and F. Izumi, *J. Appl. Cryst.*, 2011, **44**, 1272–1276.

272 G. Henkelman, A. Arnaldsson and H. Jónsson, *Comput Mater Sci*, 2006, **36**, 354–360.

273 E. Antipov, *Advanced Materials*, 1997, **9**, 274–274.

274 H. Tanaka, T. Matsumoto, T. Kawai and S. Kawai, *Jpn J Appl Phys*, 1993, **32**, 1405–1409.

275 T. Kubo and H. Nozoye, *Surf Sci*, 2003, **542**, 177–191.

276 V. B. Mikhailik, H. Kraus, D. Wahl, M. Itoh, M. Koike and I. K. Bailiff, *Phys. Rev. B*, 2004, **69**, 205110.

277 N. Mardirossian and M. Head-Gordon, *J Chem Phys*, 2014, **140**, 18A527.

278 Sharma Shambhu Bhandari, Qattan I. A., Jaoude Maguy Abi and Abedrabbo Sufian, *Comput Mater Sci*, 2023, **218**, 111952.

279 L. Chen, X. Zhang, Z. Xiong, Y. Liu, Y. Cui and B. Liu, *J Alloys Compd*, 2019, **798**, 149–157.

280 J. Ren, H. Zhang and X. Cheng, *Int J Quantum Chem*, 2013, **113**, 2243–2250.

281 L. Pan, M. Ai, C. Huang, L. Yin, X. Liu, R. Zhang, S. Wang, Z. Jiang, X. Zhang, J. J. Zou and W. Mi, *Nat Commun*, 2020, **11**, 418.

282 C. Peng, W. Fan, Q. Li, W. Han, X. Chen, G. Zhang, Y. Yan, Q. Gu, C. Wang, H. Zhang and P. Zhang, *J Mater Sci Technol*, 2022, **115**, 208–220.

283 C. S. Turchi and D. F. Ollis, *J Catal*, 1990, **122**, 178–192.

284 G. Sukhadeve, Shaileshkumar, Y. Janbandhu, R. Kumar and R. S. Gedam, *ChemistrySelect*, 2021, **6**, 12873–12883.

285 X. Li, J. Yu, S. Wageh, A. A. Al-Ghamdi and J. Xie, *Small*, 2016, **12**, 6640–6696.

286 A. M Ganose, A. J Jackson and D. O Scanlon, *J Open Source Softw*, 2018, **3**, 717.

287 C. Byrne, L. Moran, D. Hermosilla, N. Merayo, Á. Blanco, S. Rhatigan, S. Hinder, P. Ganguly, M. Nolan and S. C. Pillai, *Appl Catal B*, 2019, **246**, 266–276.

288 Z. Mulushewa, W. T. Dinbore and Y. Ayele, *Environ Anal Health Toxicol*, 2021, **36**, e2021007.

289 S. Nikfar, A. Parsa, N. Bahaloo-Horeh and S. M. Mousavi, *J Clean Prod*, 2020, **264**, 121622.

290 B. Ismail, S. T. Hussain and S. Akram, *Chemical Engineering Journal*, 2013, **219**, 395–402.

291 M. H. Dehghani, A. Naghizadeh, A. Rashidi and E. Derakhshani, *Desalination Water Treat*, 2013, **51**, 7655–7662.

292 M. S. Atas, S. Dursun, H. Akyildiz, M. Citir, C. T. Yavuz and M. S. Yavuz, *RSC Adv*, 2017, **7**, 25969–25977.

293 Z. Yuan, J. Wang, Y. Wang, Q. Liu, Y. Zhong, Y. Wang, L. Li, S. F. Lincoln and X. Guo, *RSC Adv*, 2019, **9**, 21075–21085.

294 H. Hosseini, A. Zirakjou, D. J. McClements, V. Goodarzi and W. H. Chen, *J Hazard Mater*, 2022, **421**, 126752.

295 S. A. Umoren, U. J. Etim and A. U. Israel, *J. Mater. Environ. Sci*, 2013, **4**, 75–86.

296 X. Li, C. Ni, C. Yao and Z. Chen, *Appl Catal B*, 2012, **117–118**, 118–124.

297 G. Xie, H. Wang, Y. Zhou, Y. Du, C. Liang, L. Long, K. Lai, W. X. Li, X. Tan, Q. Jin, G. Qiu, D. Zhou, H. Huo, X. Hu and X. Xu, *J Taiwan Inst Chem Eng*, 2020, **112**, 357–365.

298 M. Doltabadi, H. Alidadi and M. Davoudi, *Environ Prog Sustain Energy*, 2016, **35**, 1078–1090.

299 M. Mahmoud, A. El-Latif, M. Elkady, M. M. Abd El-Latif, A. M. Ibrahim and M. F. El-Kady, *Journal of American Science*, 2010, **6**, 267–283.

300 A. B. Albadarin, M. N. Collins, M. Naushad, S. Shirazian, G. Walker and C. Mangwandi, *Chemical Engineering Journal*, 2017, **307**, 264–272.

301 Y. Y. Gurkan, E. Kasapbasi and Z. Cinar, *Chemical Engineering Journal*, 2013, **214**, 34–44.

302 C. Di Valentin, E. Finazzi, G. Pacchioni, A. Selloni, S. Livraghi, M. C. Paganini and E. Giamello, *Chem Phys*, 2007, **339**, 44–56.

303 M. Zong, D. Song, X. Zhang, X. Huang, X. Lu and K. M. Rosso, *Environ Sci Technol*, 2021, **55**, 677–688.

304 M. Irani, T. Mohammadi, S. Mohebbi, M. Irani, T. Mohammadi and S. Mohebbi, *J Mex Chem Soc*, 2016, **60**, 218–225.

305 X. Jaramillo-Fierro, L. F. Capa, F. Medina and S. González, *Molecules 2021*, 2021, **26**, 3780.

306 S. M. Ghoreishi, *Journal of Materials Science: Materials in Electronics*, 2017, **28**, 14833–14838.

307 H. Gao, S. Wang, Y. Wang, H. Yang, F. Wang, S. Tang, Z. Yi and D. Li, *Colloids Surf A Physicochem Eng Asp*, 2022, **642**, 128642.

308 H. Gao, S. Wang, Y. Wang, H. Yang, L. Fang, X. Chen, Z. Yi and D. Li, *J Electron Mater*, 2022, **51**, 5230–5245.

309 A. Vosoughifar, *Journal of Materials Science: Materials in Electronics*, 2018, **29**, 3194–3200.

310 Y. Guo, G. Zhang, H. Gan and Y. Zhang, *Dalton Transactions*, 2012, **41**, 12697–12703.

311 M. Kim, W. J. Kim, T. Gould, E. K. Lee, S. Lebègue and H. Kim, *J Am Chem Soc*, 2020, **142**, 2346–2354.

312 H. Wei, Y. Gui, J. Kang, W. Wang and C. Tang, *Nanomaterials*, 2018, **8**, 646.

313 D. Farmanzadeh and S. Ghazanfary, *Journal of the Serbian Chemical Society*, 2013, **78**, 75–83.

314 S. Posada-Pérez, D. Santos-Carballal, U. Terranova, A. Roldan, F. Illas and N. H. De Leeuw, *Physical Chemistry Chemical Physics*, 2018, **20**, 20439–20446.

315 M. J. Ungerer, D. Santos-carballal, A. Cadi-essadek, C. G. C. E. van Sittert and N. H. de Leeuw, *Catalysts*, 2020, **10**, 558.

316 N. Y. Dzade, A. Roldan and N. H. De Leeuw, *J Chem Phys*, 2015, **143**, 094703.

317 Z. Zhou, F. Han, L. Guo and O. V. Prezhdo, *Physical Chemistry Chemical Physics*, 2016, **18**, 16862–16869.

318 W. Zhang and Y. Xiao, *Energy and Fuels*, 2020, **34**, 2425–2434.

319 D. H. Lim, J. H. Jo, D. Y. Shin, J. Wilcox, H. C. Ham and S. W. Nam, *Nanoscale*, 2014, **6**, 5087–5092.

320 G. Alonso, D. Bahamon, F. Keshavarz, X. Giménez, P. Gamallo and R. Sayós, *Journal of Physical Chemistry C*, 2018, **122**, 3945–3957.

321 C. Fonseca Guerra, J. W. Handgraaf, E. J. Baerends and F. M. Bickelhaupt, *J Comput Chem*, 2004, **25**, 189–210.

322 H. Wei, Y. Gui, J. Kang, W. Wang and C. Tang, *Nanomaterials*, 2018, **8**, 646.